

Doctoral Thesis

Mechanical Reliability of Sintered Nano  
Silver for Power Device Packaging

Keisuke WAKAMOTO

March 2023

Graduate School of Engineering  
Kyoto University of Advanced Science



# Mechanical Reliability of Sintered Nano Silver for Power Device Packaging

Keisuke WAKAMOTO

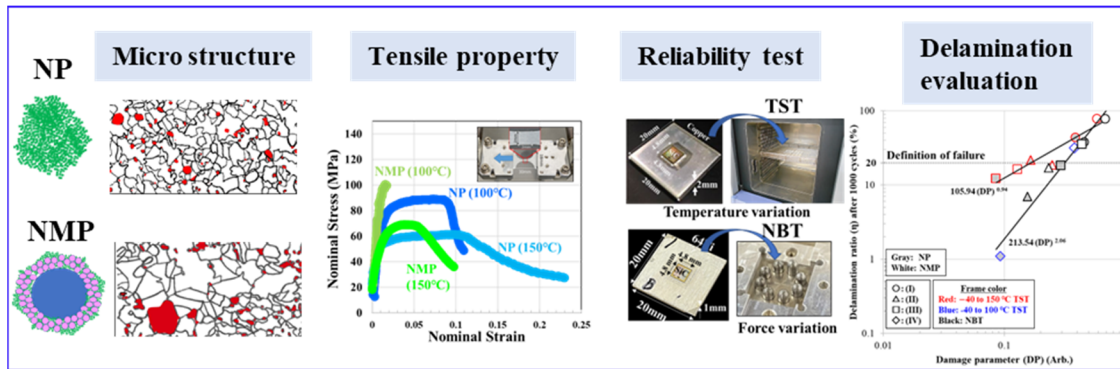
## *Summary*

A new die bonding technique that can provide good stability despite severe thermal density is necessary to maximize the performance of WBG devices. Considering its high heat conductivity of over 200 W(m/K) and a high melting point of 961°C, a sintered silver (s-Ag) material has been considered as a strong die-attach material candidate for WBG devices. However, for the practical use of products, the s-Ag die layer is commonly assessed with a thermal shocked test (TST) that evaluates material degradation by heating and cooling. During TST, thermal and mechanical stresses are generated in the die layer because materials with different coefficients of thermal expansion can cause thermal warpage around a bonded part. Consequently, the die layer fractures. In achieving long-term mechanical and thermal durability, the failure mechanism should be clarified experimentally.

This study aims to establish a packaging reliability design flow with s-Ag die assemblies based on the mechanical reliability evaluation of the s-Ag material. As shown in the figure with a blue frame, this research covers s-Ag microstructure analysis, film mechanical property evaluation, bonding reliability evaluation of mechanical bending test, thermal cycling test, and degradation evaluation using an original damage parameter (DP).

Two types of s-Ag paste (NP, nanosized paste; NMP, nano-to-micro-sized paste) were used. The sintering condition was set to 300°C for 10 min with pressure of 60 MPa. After sintering, each mean porosity ( $pr$ ) of NP and NMP was 5% and 8%, respectively. In addition, the grain size of NP was about half of the grain size of NMP. In addition, NP has large ductility, showing plastic deformation above 100°C, whereas NMP has little ductility. That is, a finer microstructure provides better durability of s-Ag. With regard to the mechanical bending test, a new bending test technique, namely, nine-point bending test (NBT), has been proposed, which provides out-of-plane deformation with s-Ag die-attached assemblies (DAAs) such as TST. In comparing NBT with TST, an experimental condition of each test was determined on the basis of the finite element analysis calculation results with averaged accumulated von Mises plastic strain (APS) at the s-Ag die layer as a general engineering parameter. A similar degradation ratio between NBT and TST was obtained in scanning acoustic tomography (SAT), which indicates that mechanical stress plays a significant role in deteriorating the s-Ag die layer during TST. However, TST with a high

APS region shows large dispersion of delamination ratio compared with NBT with the same region. Cross-sectional microanalysis indicates that s-Ag material aging and mechanical cracking coexisted in the case of large APS condition with TST. Finally, the DP is defined as the ratio of APS value to plastic strain value obtained from tensile test results. The delamination ratio after 1000 cycles of TST and NBT could be separately fitted by two linear approximation lines with “Aging case” and “non-Aging case” in a double logarithmic graph. Molecular dynamics (MD) simulation and classical pore growth discussion indicate that a pore can grow under only a tensile stress state at a high temperature, which would lead to the difference between the two degradation mechanisms.



# Contents

List of Figures .....	VI
List of Tables .....	X
1. Introduction .....	1
1-1. Wide band gap semiconductor device & packaging.....	1
1-2. Die bonding technique overview .....	7
1-3. Sintered silver (s-Ag) characterization .....	12
1-4. Thermal impedance calculation.....	14
1-5. Die bonding reliability evaluation .....	17
1-6. Scope of this study .....	21
References .....	24
2. Sintered Silver (s-Ag) Film Mechanical property .....	33
2-1. s-Ag material.....	33
2-1-1. Introduction of s-Ag paste .....	33
2-1-2. Nano paste (NP) and nano-micro paste (NMP).....	33
2-1-3. Silver particle size distribution .....	35
2-1-4. Organic component.....	38
2-2. Tensile test methodology .....	43
2-2-1. Specimen fabrication methodology .....	43
2-2-2. Uniaxial tensile tester .....	46
2-3. Pressure dependences on tensile mechanical property of s-Ag film.....	49
2-3-1. Microstructure .....	49
2-3-2. Stress-strain curve .....	51
2-3-3. Fractography .....	53
2-4. Temperature dependences on tensile mechanical properties of s-Ag film.....	55
2-4-1. Stress-strain curve .....	55
2-4-2. Fractography .....	59
2-5. NP and NMP tensile mechanical properties of s-Ag film.....	62
2-5-1. Microstructure .....	62
2-5-2. Stress-strain curve .....	64

2-5-3. Crack propagation & fractography .....	69
2-6. Conclusion.....	77
References .....	78
<b>3. Sintered Silver Die Bonding Reliability .....</b>	<b>82</b>
3-1. Thermal shocked test (TST) and four-point bending test .....	82
3-1-1. Experimental methodology .....	82
3-1-2. Fracture mode.....	86
3-1-3. Stress direction.....	88
3-1-4. Failure mechanism .....	90
3-2. TST and nine-point bending test (NBT) .....	94
3-2-1. Experimental methodology .....	94
3-2-2. Experimental condition.....	98
3-2-3. Results of TST and NBT .....	100
3-2-4. Delamination analysis.....	106
3-2-5. Damage parameter validation .....	109
3-3. Conclusion.....	115
References .....	116
<b>4. Sintered Silver Degradation Mechanism .....</b>	<b>119</b>
4-1. Pore growth condition .....	119
4-1-1. MD simulation.....	119
4-1-2. Stress direction.....	122
4-2. Degradation criterion .....	124
4-2-1. Classical pore growth physics .....	124
4-2-2. Pore growth criterion map .....	126
4-3. In-situ s-Ag pore growth observation.....	129
4-4. Overall s-Ag die layer degradation mechanism .....	135
4-5. Conclusion.....	138
References .....	139
<b>5. Conclusions .....</b>	<b>141</b>
Appendix .....	145

Achievements.....169  
Acknowledgements .....174

# List of Figures

Fig. 1-1 (a) Power modules market and (b) Power conversion system in EVs. ....	2
Fig. 1-2 Power module of (a) Representative outlook photograph and (b) Cross-section image. ....	4
Fig. 1-3 Electric field distribution in the depletion layer. ....	5
Fig. 1-4 Thermal distribution image from the semiconductor device. ....	6
Fig. 1-5 Bonding temperature vs. Thermal conductivity. ....	8
Fig. 1-6 Low temperature s-Ag bonding mechanism. ....	10
Fig. 1-7 Representative s-Ag die bonding procedure step. ....	13
Fig. 1-8 Thermal fluid simulation model overview of (a) Simulation model schematic image and (b) Cross section image together with input parameter for each component. ....	14
Fig. 1-9 Thermal fluid simulation results of (a) Chip to water thermal impedance as a function of copper substrate thickness and (b) Surface temperature distribution results with each condition. ....	15
Fig. 1-10 Target packaging structure for power module products with high power density. ....	16
Fig. 1-11 Thermal distribution image at the initial state and after the thermal shocked test (TST) together with out-of-plane deformation image during TST [60]. ....	17
Fig. 1-12 Previous competitor’s research attempt summary for evaluating TSTs. ....	20
Fig. 1-13 Chapter flowchart. ....	23
Fig. 2-1 Paste size analysis methodology schematic view of dynamic light scattering (DLS) methodology. ....	36
Fig. 2-2 Tester photograph together with the sample photograph. ....	37
Fig. 2-3 Ag particle diameter distributions of NP and NMP. ....	37
Fig. 2-4 Chemical analysis overview of Fourier transform infrared spectroscopy (FT-IR). ....	38
Fig. 2-5 FT-IR spectrum results of NP and NMP. ....	39
Fig. 2-6 Gas chromatography-mass spectrometry (GC/MS) schematic view. ....	40
Fig. 2-7 GC/MS spectrum results of NP and NMP after dry and sintering state together with mass spectrum assignment results. ....	41
Fig. 2-8 Specimen preparation process for tensile testing. ....	44
Fig. 2-9 Original tensile tester system with the micron-scale specimen in tests No. 1 and 2. (Left side:	



Overall photograph and right side: Magnified tester of measurement part.).....	46
Fig. 2-10 Original tensile tester system with the millimeter-scale specimen in test No. 3.....	48
Fig. 2-11 Cross-section SEM images with varying process pressure of (a) 60 MPa, (b) 30 MPa, (c) 10 MPa, and (d) 5 MPa [12].....	50
Fig. 2-12 <i>S-S</i> curves for each material [12]. (Red: 60 MPa s-Ag. Orange: 30 MPa s-Ag. Dark blue: 10 MPa s-Ag. Light blue: 5 MPa s-Ag. Black: Bulk Ag.).....	51
Fig. 2-13 (A) Apparent Young's modulus (B) Ultimate tensile strength and (C) Breaking strain as a function of <i>pr</i> . The red, orange, dark-blue, and pale-blue dots denote the data for s-Ag specimens of (a), (b), (c) and (d), respectively. The black dot denotes the data for bulk Ag specimen of (e) [12]. .....	52
Fig. 2-14 SEM images of the fractured surface in s-Ag specimens after tensile tests with (a) 60 MPa, (b) 30 MPa, (c) 10MPa, and (d) 5 MPa [12].....	54
Fig. 2-15 <i>S-S</i> curves for each temperature with (a) s-Ag and (b) bulk Ag [14]. .....	56
Fig. 2-16 (a) E, (b) UTS, and (c) BS as a function of temperature [14]. .....	57
Fig. 2-17 (a-c) Representative SEM images of bulk Ag fracture surface after tensile tests at RT, 60°C, and 120°C. (a'-c') Enlarged SEM images of each area denoted by white square shown in (a-c) [14]. .....	59
Fig. 2-18 Representative SEM images of the s-Ag fracture surface together with the magnified images after tensile tests at (a) RT, (b) 60°C, and (c) 120°C [14]. .....	60
Fig. 2-19 Cross-section SEM observation results of NP and NMP. ....	63
Fig. 2-20 <i>S-S</i> curves for NP (blue colors) and NMP (green colors). ....	65
Fig. 2-21 (a) Young's Modulus: E (b) Ultimate tensile strength: UTS (c) Breaking strain: BS. ....	65
Fig. 2-22 (a) E, (b) UTS, and (c) BS as a function of pore size, crystal size, <i>pr</i> , and pore shape factor ( <i>psf</i> ) for NP and NMP. ....	67
Fig. 2-23 Strain distribution results from FEA with NP and NMP during tensile tests. ....	68
Fig. 2-24 CCD photographs of s-Ag specimen surface during the tensile test at RT of (a) NP and (b) NMP. ....	69
Fig. 2-25 CCD photographs of s-Ag specimen surface during the tensile test at 100°C of (a) NP and (b) NMP.....	70
Fig. 2-26 CCD photographs of s-Ag specimen surface during the tensile test at 150°C of (a) NP and	

(b) NMP.....	72
Fig. 2-27 Crack length during the tensile test as a function of time at (a) 100°C and (b) 150°C for NP and NMP. ....	73
Fig. 2-28 Representative SEM images of s-Ag fracture surface at RT, 100°C, and 150°C for NP and NMP. ....	75
Fig. 3-1 Experiment schematic view of TST, CBT, and SBT [5]. ....	83
Fig. 3-2 Schematic of specimen fabrication for each test together with the photograph [5].....	84
Fig. 3-3 TST chamber. ....	85
Fig. 3-4 Representative scanning acoustic tomography (SAT) images at 100 cycles intervals in 0~500 cycles for TST along with cross-sectional scanning electron microscopy (SEM) images after 500 cycles for TST and after 190,000 cycles for CBT and 46,000 cycles for SBT, respectively [5]. ....	87
Fig. 3-5 Representative FEA results along with the models [5]. (Upper side: Modeling overview. Downside: Maximum principal stress and sheared stress direction distribution in the s-Ag die layer. Thick annotation means representative direction for each test.).....	89
Fig. 3-6 Crack length as a function of the number of cycles (a) Out-of-plane crack length (OCL) (b) In-plane crack length (ICL) [5]. ....	92
Fig. 3-7 Representative fracture surface at the inclined and horizontal portions after TST and SBT [5]. ....	93
Fig. 3-8 Schematic of TST and NBT along with out-of-plane deformation distribution. ....	95
Fig. 3-9 Photographs of (a) NBT experiment components and (b) Cross section sketch view of NBT together with the s-Ag assemble. ....	97
Fig. 3-10 Representative SAT images after (a) TST and (b) NBT. ....	102
Fig. 3-11 Representative cross-section SEM analysis results after 1000 cycles of (a) TST, (b) NBT, and (c) Microstructure image analysis results in red frame regions depicted in the SEM cross-section images (Red: Pore).....	104
Fig. 3-12 Delamination ratio as a function of the number of cycles of (a) TST and (b) NBT. ....	106
Fig. 3-13 Weibull plot of delamination ratio after 1000 cycles of (a) TST and (b) NBT. ....	109
Fig. 3-14 FEA geometry, mesh configuration, boundary condition, and FEA calculation results of averaged APS value in the evaluation area. ....	111

Fig. 3-15 Damage parameter numerical results of all experiments. ....	112
Fig. 3-16 Delamination ratio after 1000 cycles as a function of APS (Upper graph) and DP (Downside graph). ....	114
Fig. 4-1 MD calculation condition.....	119
Fig. 4-2 Molecular dynamics simulation of (a) 0.1 and (b) 3 ns. (Upper side image: Pore configuration. Downside image: Hydrostatic stress distribution. Bar graph: Pore size growth ratio as a function of applied strain.).....	121
Fig. 4-3 Stress distribution at around a crack tip along with representative stress component and direction inside the s-Ag layer. ....	122
Fig. 4-4 Classical pore growth physical model overview. ....	125
Fig. 4-5 Pore growth criterion plane together with plots of each test condition as a function of initial pore size $r$ , and diffusivity with $Dt/T$ —showing s-Ag die attach reliability criterion.....	128
Fig. 4-6 In-situ SEM tensile tester photographs (a) Overall photograph (b) Specimen attachment appearance. ....	130
Fig. 4-7 Specimen fabrication steps.....	131
Fig. 4-8 In-situ SEM observation results.....	133
Fig. 4-9 Fracture surface SEM images (Upper side: Overall SEM image. Downside: Fracture surface image with local area).....	134
Fig. 4-10 Microstructure image analysis comparison results of initial, after TST 1000 cycles (–40 to 150°C), and after the In-situ tensile testing at 300°C. (Red: Pore.).....	135
Fig. 4-11 Representative cross-section SEM image of TST (I) with NP after 200, 500, and 1000 cycles. Microstructure image analysis results in red frame regions depicted in the SEM cross-section images (Red: Pore).....	136
Fig. 4-12 Overall fracture mode schematic images as a function of cycles (Upper side: Thermal and mechanical stress. Lower side: Mechanical stress.) ....	137
Fig. 5-1 Conventional production flow overview.....	142
Fig. 5-2 New production flow overview. ....	144

## List of Tables

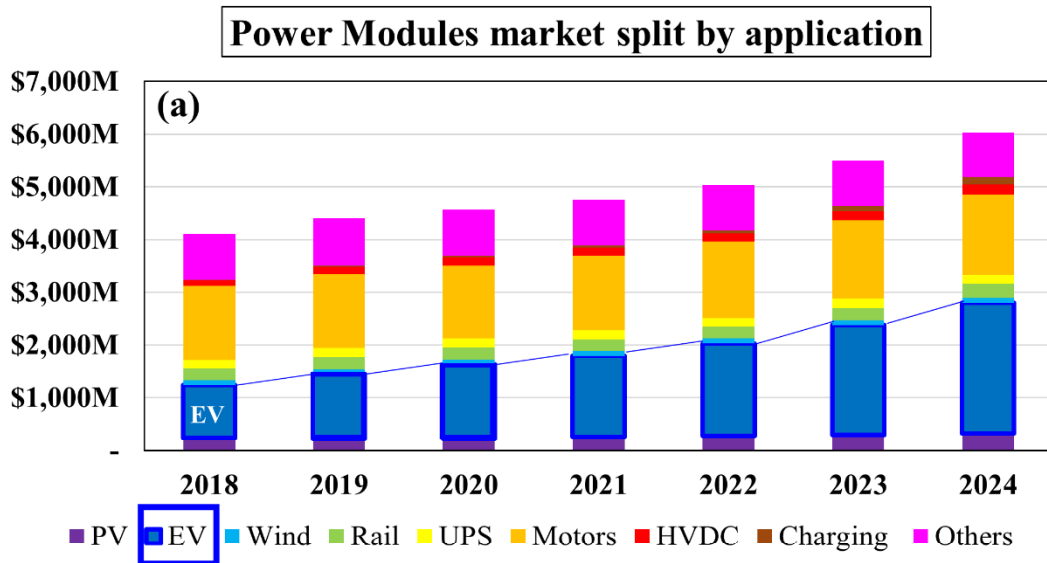
Table 1-1 Physical property of semiconductor material property. ....	4
Table 1-2 Die attach material property overview.....	11
Table 2-1 NP and NMP.....	34
Table 2-2 Analysis methodology after each process step of Ag paste, dry, and sintering. ....	35
Table 2-3 Paste analysis results summary. ....	42
Table 2-4 Tensile tests condition overview. ....	43
Table 2-5 Test No.1 condition. ....	49
Table 2-6 Test No.2 condition. ....	55
Table 2-7 Test No.3 condition. ....	62
Table 3-1 Reliability test condition [5]. ....	85
Table 3-2 Material mechanical properties used in FEA [5]. ....	90
Table 3-3 Experiment condition. ....	99
Table 3-4 DP parameter derivation list. ....	112
Table 4-1 Input parameter for deriving the equation (15).....	126
Table 4-2 Input parameter for plotting.....	128
Table 4-3 Experiment condition .....	129
Table 4-4 FIB process condition .....	132

# 1. Introduction

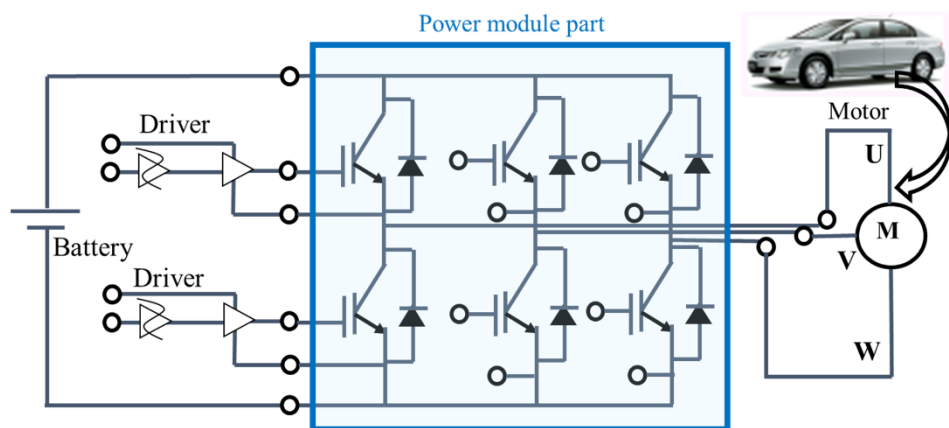
## 1-1. Wide band gap semiconductor device & packaging

Power modules have been widely used for power conversion systems in many industries. The high power density of systems is required year by year. The power modules product market split by application is shown in Fig. 1-1 (a). Nowadays, reducing CO<sub>2</sub> emissions has been one of the most special issues for safe ecology in the world. Especially in the automobile industry, replacing fuel vehicles with electric vehicles (EVs) is progressing. The demand for EVs is increasing, and the power modules market in EVs will keep increasing from 1000 million to 2500 million dollars by the 2024 year, as is shown in Fig. 1-1 (a). Therefore, many semiconductor makers have devoted their human, material, and technical resources to realize the de facto standard power module products for dominating the big EVs market. Rohm co. Ltd. (Japan, Kyoto) also started developing power module products in the 2010s using originally designed silicon carbide (SiC) devices. Since they did not have the proper power module design methodology, the Research and Development (R&D) center started to study power module design skills for providing reliable products in 2017.

Fig. 1-1 (b) shows a representative DC to AC power inverter system for a three-phase (UVW) motor equipped in EVs. The blue frame part represents the power module parts in this system. In power modules, metal oxide semiconductor field effect transistors (MOS-FETs) install, which act as a switch function by external driver signal voltage. During the run operation of EVs, DC from the battery can be translated to AC by switching the timing control of MOS-FET devices to supply energy to the UVW motor. When EVs operate in braking mode, regenerative energy from the UVW motor conducts through a freewheel diode in MOS-FETs. During the energy exchange in this system, the energy consumption is inevitably generated. Therefore, energy management in this system should consider reliable systems. Moreover, EVs have been demanded with high power density systems to minimize car bodies and expand interior living spaces [1]. In other words, power modules have required that can be converted into significant power even if the size is small. Nowadays, the power module product trends show “High power density” for the EVs market.



**(b) DC-AC inverter system in EVs**



**Fig. 1-1 (a) Power modules market and (b) Power conversion system in EVs.**

Fig. 1-2 depicts a representative power module product photograph and its cross-section schematic illustration. The size of power modules depends on their voltage and current specifications. For example, the typical size measures 62mm in length, 152 mm in width, and 10 mm in height for 1200 V / 400 A, as illustrated in Fig. 1-2 (a). Power modules are mainly equipped with the following three functions in one packaging product, as illustrated in Fig. 1-2 (b):

1. Electric circuit
2. Thermal diffusion

### 3. Insulation

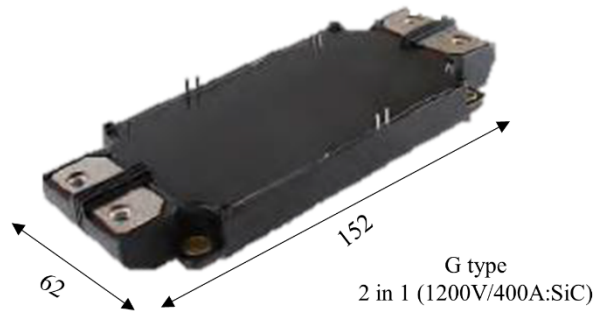
For the electric circuit function, semiconductor devices employ the switching part to control the current flow from the battery, as depicted in Fig. 1-1 (b). Si devices have been widely utilized in this part. However, nowadays, the wide bandgap semiconductor (WBG) material represented as silicon carbide (SiC) and gallium nitride (GaN) have started adopting owing to their excellent device properties with high bandgap energy, breakdown electric field, and saturated electron drift velocity. [3-6]. Si device's power conversion efficiency is reaching its theoretical material limitations. In addition, the operation temperature of Si devices is restricted from 150 to 200°C due to a loss of switching function in devices under harsh temperatures [2]. Therefore, Si devices cannot operate without a heavy and complicated cooling system. By contrast, WBG devices can operate with compact cooling systems because WBG devices can attain low energy loss but operate at high temperatures.

For thermal diffusion, copper (Cu) substrate has been one of the common materials due to its high heat conductivity and availability. Cu substrate bonded with a ceramic plate called "DBC (Direct Bonded Copper) substrate" has been frequently used for thermal diffusion and insulation function. However, due to production regulations, Cu in DBC has been generally restricted to around 0.8 mm in thickness. Two DBC substrates are recently bonded chips not only bottom side but also top side to compensate for the limitation of thermal diffusivity in a single DBC substrate [7-11]. Even though manufacturing double-side bonded configuration still has difficulties from the viewpoint of production accuracies. Alternatively, a substrate based on Cu thick lead frame with a thin-film insulation layer has been developed for enough heat spread even in single-side cooling [12].

For insulation, high glass transformation temperature ( $T_g$ ) plastic material is required. When the plastic material exceeds  $T_g$ , the coefficient of thermal expansion (CTE) and Young's modulus of the plastic are drastically changed, which deteriorates strength, insulation, and adhesivity. Epoxy plastic with an aromatic ring structure possesses high  $T_g$ , which has been widely adopted as an insulator in power modules. Each material is bonded together, acting as power module functions, as seen in Fig. 1-2 (b). The packaging appearance and cross-section configuration are referred at Appendix A.

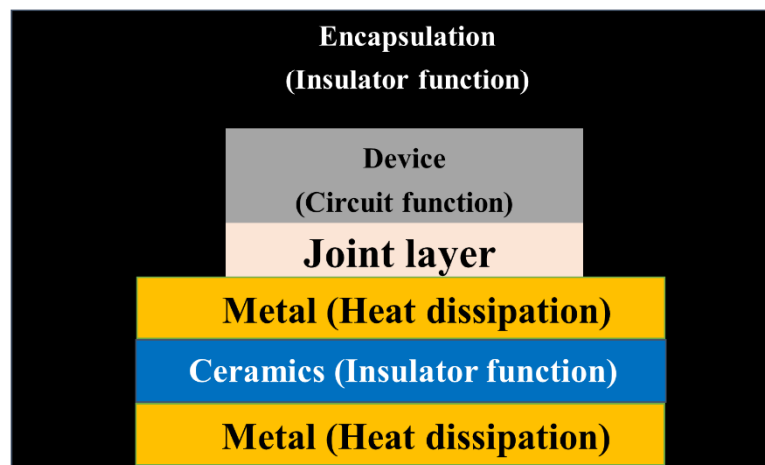
Table 1-1 lists the material characteristics of Si, SiC, and GaN. SiC and GaN have a higher band gap and breakdown electric field values than Si. A high band gap value can reduce thermal carriers during high temperatures operation, which enables us to operate the devices in a high-temperature environment. A high breakdown electric field can reduce energy loss during power conversion.

(a)



[Power module products photograph]

(b)



[Representative power module cross section image]

Fig. 1-2 Power module of (a) Representative outlook photograph and (b) Cross-section image.

Table 1-1 Physical property of semiconductor material property.

Material	Si	SiC (4H)	GaN
Band gap energy (eV)	1.12	3.26	3.39
Break down electric field (kV/cm)	300	2500	3300



The device breakdown voltage is derived from integrating the electric field value along the epitaxial layer depicted as a skin-colored part in Fig. 1-3. The value equals the area of the triangular portion of the graph, as illustrated in Fig. 1-3. Since Si's electric breakdown field strength is low, the epitaxial layer should be set to be thickened configuration as shown in the left side of Fig. 1-3 for achieving the required breakdown voltage. On the other hand, the electric field strength of the WBG device possesses about ten times higher than the electric field strength of the Si device. As a result, even if the thickness of the epilayer is 1/10 compared to the thickness of Si, the same breakdown voltage can be secured. The slope of the line means the carrier density, which indicates that WBG material carrier density is about 100 times higher than the Si value. Since the WBG device can maintain the same breakdown voltage as that of the Si device, even if the WBG device epi layer is thin, the electric resistance in the epilayer can be reduced to attain low energy loss during the power conversion. In addition, the saturated electron drift velocity of SiC and GaN is about two times larger than Si, which can reduce switching loss energies due to high-speed switching. By fully utilizing the WBG device's excellent features for allowing the power module products to be safely operated under high-temperature operation, bonding techniques surrounding chips are fundamental.

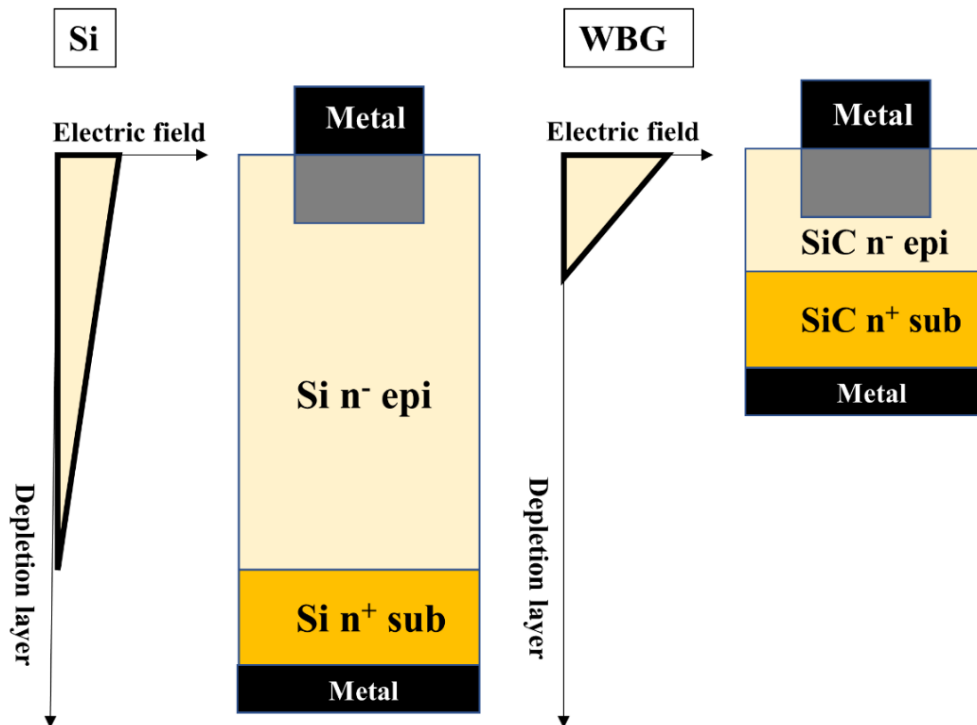
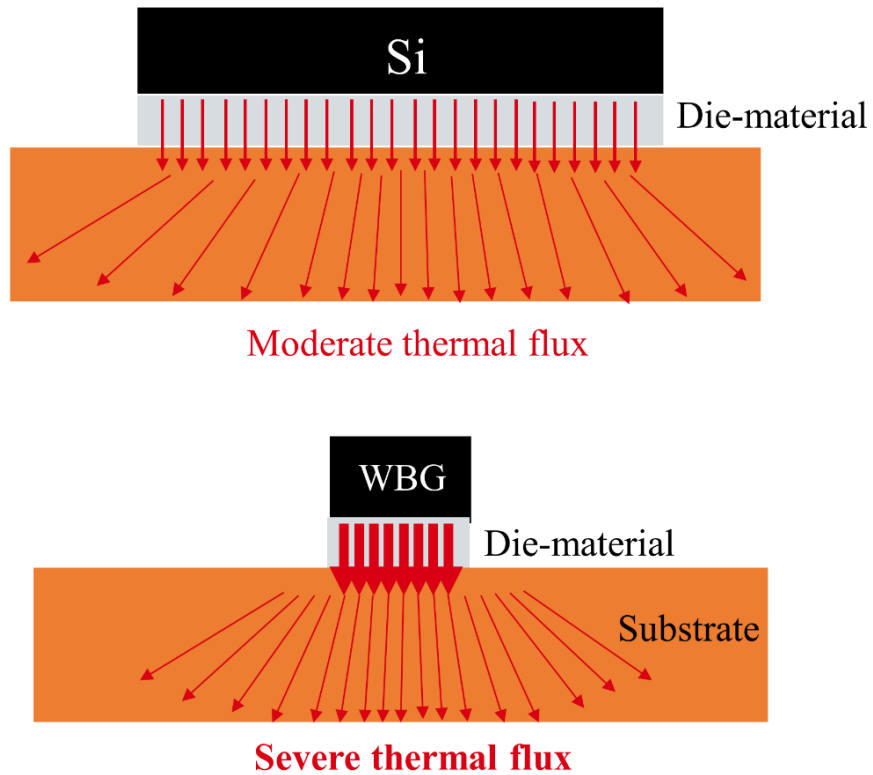


Fig. 1-3 Electric field distribution in the depletion layer.

Fig. 1-4 depicts the thermal spread illustration from the Si and WBG material die to the cooling area located at the substrate's bottom. For Si, a large device size can allow low thermal density. By contrast, due to the downsizing of semiconductor devices in SiC, the thermal density becomes more severe as the size of the chip decreases compared with the conventional large size of Si devices. Therefore, the heat generated from the WBG device must immediately diffuse to spread in the substrate through the die material placed under the WBG device.

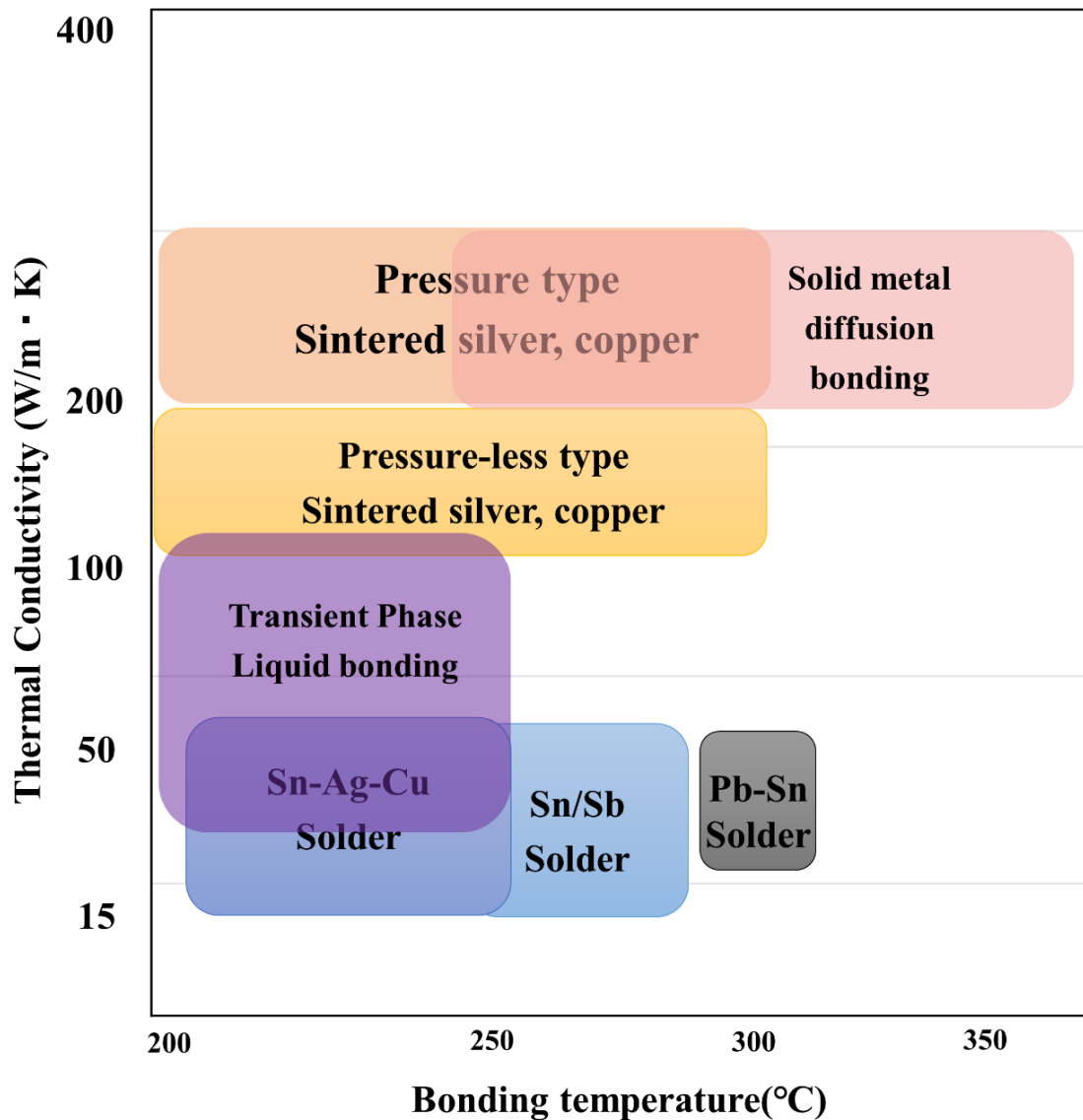


**Fig. 1-4 Thermal distribution image from the semiconductor device.**

## 1-2. Die bonding technique overview

Fig. 1-5 shows the relationship between thermal conductivity and the bonding temperature of each material. The solder bonding technique has been commonly utilized for semiconductor devices [13, 14]. Solders containing Sn are diffused to form an alloy with another metal (Cu, Ni, *etc.*) in a liquid phase under enough temperature elevation. After cooling, the intermediate diffusion layer becomes a solid state, followed by a bonding layer. Pb-Sn solder materials have been expected to be utilized as WBG die bonding material owing to their high melting point, which is close to 300°C. However, in recent years, applying Pb-free solder material (Sn-Ag-Cu system and Sn-Sb system) has changed to be the mainstream solder material from the flow of hazardous material use restriction by RoHS directive. The melting point of the Pb-free solder is restricted to around 220 to 250°C. On the other hand, it has been reported that high temperature operation using WBG devices can retain electric circuit function even at 250 to 300°C [15]. The Pb-free solders are unsuitable because the solders melt and lose functions under the high-temperature operation in WBG devices, which can not extract the excellent high-temperature characteristics from the WBG devices. Moreover, the thermal conductivity of solders is limited to around 60 W/mK in any composite type of materials [16, 17]. Therefore, solders could not be employed for WBG power modules with high power density.

Alternatively, the transient liquid phase (TLP) bonding technique has developed as a potential die bonding technique for WBG devices [18-21]. In the TLP bonding process, a complete intermetallic compounds (IMCs) bonding can be made at low temperatures through the diffusion reaction between the high melting point of the metal substrates such as silver (Ag) material and low-melting-point of interlayer such as Sn-based solders. When the temperature exceeds the value of the lower temperature melting point of the substrate, which allows that the metal diffusion with each other metal powerfully acts to form an inter-metallic phase. The typical process temperature has been set at around 250°C under pressure assist to reduce pores in the bonding layer. Once the TLP bonding process is completed, the alloy's melting point reaches the substrate's high temperature melting point. At that point, there is no limitation for operating with a high temperature of WBG devices. However, the IMCs layer prevents heat conductivity, reducing equivalent thermal conductivity in the TLP layer.



**Fig. 1-5 Bonding temperature vs. Thermal conductivity.**

“Solid-phase diffusion bonding” has attracted so much attention as a game-changer material owing to its excellent physical properties of high melting point and thermal conductivity. Solid phase diffusion bonding has been known as the only process to be preserved the properties inherent in monolithic materials in metal-to-metal joints. For establishing strong bonding, each bonded layer should be brought together within the atomic space to make it diffuse inactively. Unfortunately, actual surfaces are never ideally smooth within atomic scale roughness. The application of pressure can deform each metal layer in plasticity, which increases the contact surface of the area to promote diffusion and densification of the bonding layer. For instance, Chu-Hsuan, *et al.* used Ag foil with a gold (Au) sputtered layer to the alumina

substrate. The foil plays a ductile deformation during the die bonding process for quickly making Ag and Au atoms position within atomic distance. The bonding could be attained under 260°C at a process pressure of 6.9 MPa [22]. Katuaki Suganuma *et al.* proposed utilizing cold rolled Ag sheets as a new die attach material [23]. This technique induces active diffusivity by grain refinement down to a submicron level, which can derive enough diffusivity for intimate bonding. 300°C under the process pressure of 1 MPa was chosen for the bonding process in this study. Also, they initially developed flexible Al sheets sputtered by a thin Ti and Ag to make good contact with any kinds of substrate's surface. An initial die shear strength of 33.4 MPa was achieved under 300°C [24]. However, the die layer reliability has only been assessed by shear tests of chip die-attached assemblies. The assessment was not still performed under the practical reliability test illustrated as a practical operation in products. Above 350°C and 80 MPa pressure is still a mainstream process condition, which is a severe condition from the production side. Above all, solid-phase diffusion bonding through Ag or Cu nano metallic particles has been actively studied toward the realization of WBG die attach implementation [8, 11, 25-43]. If the volume is the fixed amount of material volume with  $V$  when sphere particle size  $d$  decreases, then the total surface area  $A$  increases drastically in accordance with the function of  $6V/d$ , as shown in Fig. 1-6. It is inversely proportional to that of the particle size, which indicates the driving force for sintering is inversely proportional to the particle diameter. When the particle size decreases at a certain level, the total surface area drastically enhances. Consequently, the required temperature for bonding becomes lower than bulk silver because of the large assistance of surface energy originating from the geometric property in nano-silver as illustrated in the bottom image of Fig. 1-6. The production cost of sintered Cu (s-Cu) die material is smaller than that of sintered Ag (s-Ag) die material [41-43]. However, the process should be implemented under reduced atmosphere to prevent Cu oxidation and maintain a high bonding strength value [44]. As a feature, sintered Ag (s-Ag) die bonding can be attained at low temperatures around 200~300°C [22, 24, 26, 33, 36, 45]. Moreover, the s-Ag melting point is comparable to that of bulk Ag, 961°C. The thermal conductivity has been reported that exceeds 150 W(m/K) [46-48], which is superior to the solder's characteristics, 60 W(m/K). The die bonding property overview is listed in Table 1-2. From the viewpoint of the process and physical property, s-Ag die bonding is the most excellent methodology of all bonding methodologies.

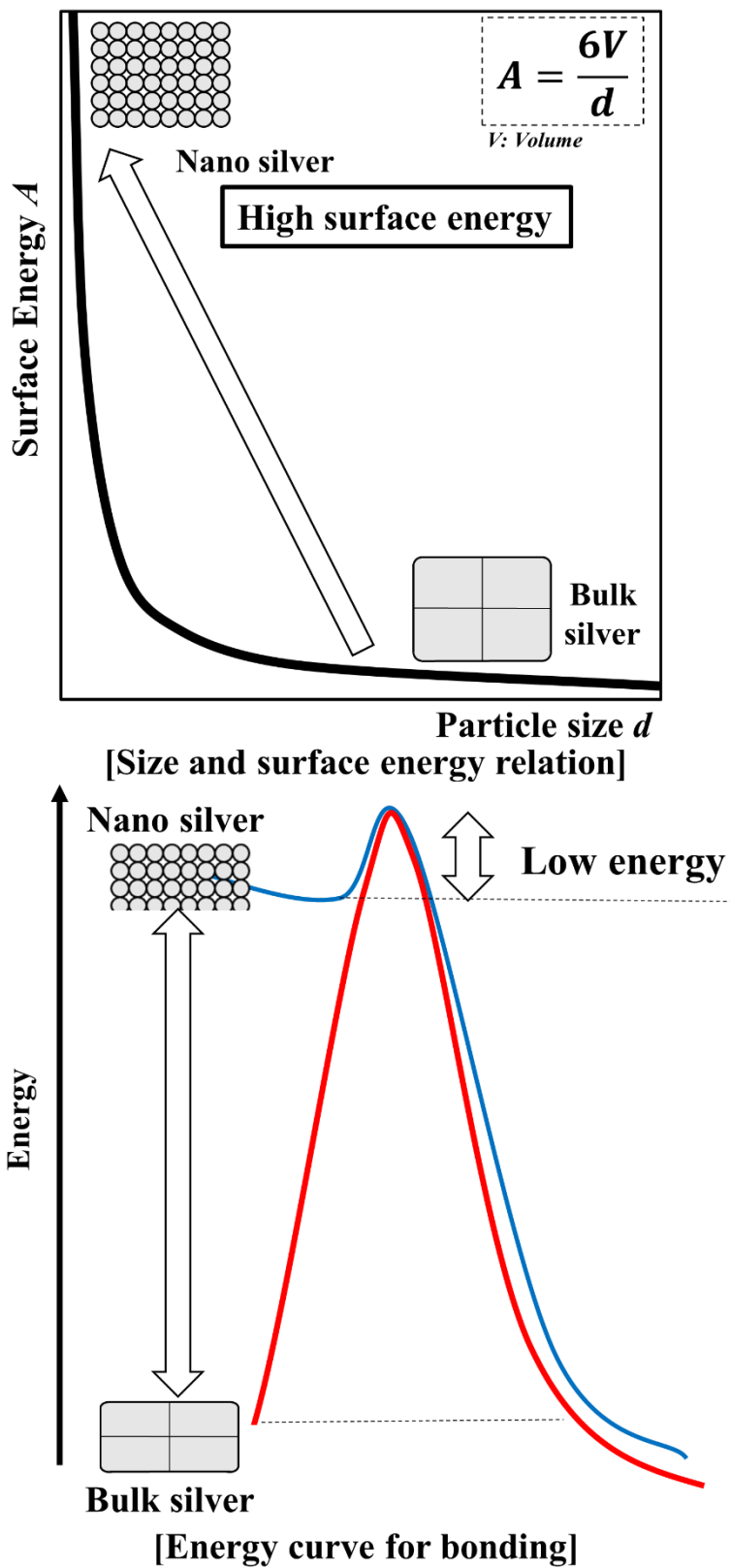
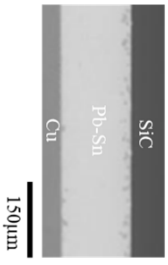
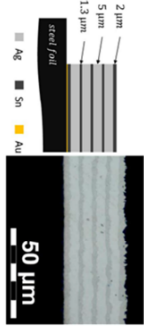
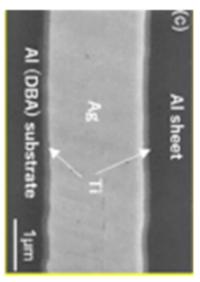
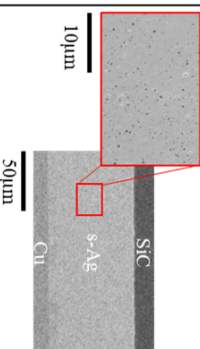


Fig. 1-6 Low temperature s-Ag bonding mechanism.

Table 1-2 Die attach material property overview.

Bonding methodology	Liquid phase bonding		Solid state bonding	
	Solder	Transient liquid phase bonding	Metal sheet bonding	Sintered metal bonding
Bonded layer				
Material	Pb-Sn, Sn-Ag-Cu, Sn-Sb	Ag-Sn, (Cu-Sn, Ni-Sn)	Ag, Al	Ag, Cu
Representative Process	200~300°C (Reduction atmosphere)	300°C (Reduction atmosphere) (Pressure assist needs (SMPa~))	350°C~ (Pressure assist needs (80MPa~))	200°C~ (Pressure assist recommend)
Melting point	200~300°C	Over 300°C (Ag <sub>3</sub> Sn: 480°C, Ag <sub>8</sub> Sn <sub>13</sub> : 600-724°C)	Over 300°C (Ag: 962°C, Al: 660°C)	Over 300°C (Ag: 962°C, Cu: 1083°C)
Thermal conductivity	~60 W/mK	? (Due to the existence of IMC, pore area)	200 W/mK~	200 W/mK~
Remark	Low melting point Low thermal conductivity Reduction atmosphere	Difficult to process optimization	Need high process pressure	(Cu case: Reduction atmosphere)

Red literature: Unfavorable Blue literature: Favorable

### 1-3. Sintered silver (s-Ag) characterization

Fig. 1-7 shows the typical s-Ag die bonding process. First, a paste including an Ag particle coated with organic stabilizer is stencil printed on the substrate. Then, the organic solvent is evaporated from the Ag paste with temperature elevation. In that process, Ag particles start to be coarsened. The figure of the dried paste layer is still shown in particle shape, as illustrated in the middle scanning electron microscopy (SEM) photograph of Fig. 1-7. Then, the dried paste is sintered under the temperature elevation with a specific pressure assist. The typical process temperature is over 200°C, and the typical process pressure ranges from 0 to 60 MPa [22, 24, 26, 33, 36, 45]. However, pores are inevitably included in the s-Ag layer to make gas pathways for outside during the sintering process, as illustrated in the bottom SEM photograph in Fig. 1-7. Pore influences s-Ag mechanical durability because it acts as a stress concentration area. Also, pore prevents thermal passing due to the existence of air. Many researchers have studied the controllability of pores with s-Ag up to date [32, 36, 46, 49-57].

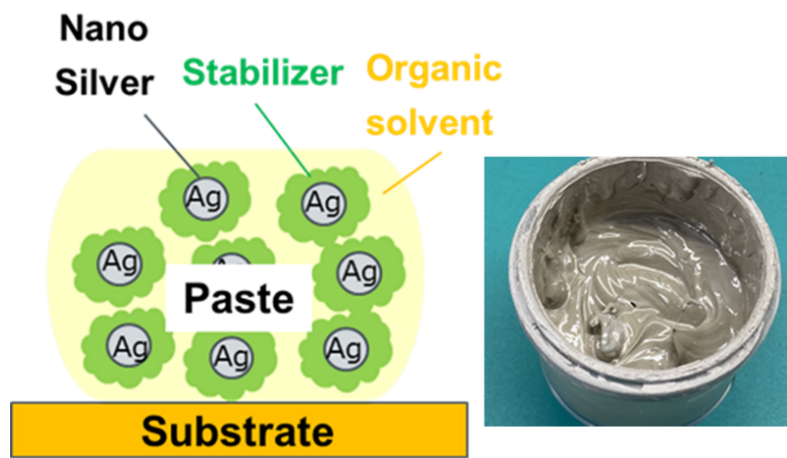
Mackenzie and Shuttleworth's model can express the Ag particle coarsening during the sintering process as following equation:

$$\frac{d\rho}{dt} = \frac{3}{2} \left( \frac{\gamma}{r} + P_{applied} \right) (1 - \rho) \left( 1 - \alpha \left( \frac{1}{\rho} - 1 \right)^{1/3} \ln \left( \frac{1}{1 - \rho} \right) \right) \frac{1}{\eta} \quad (1)$$

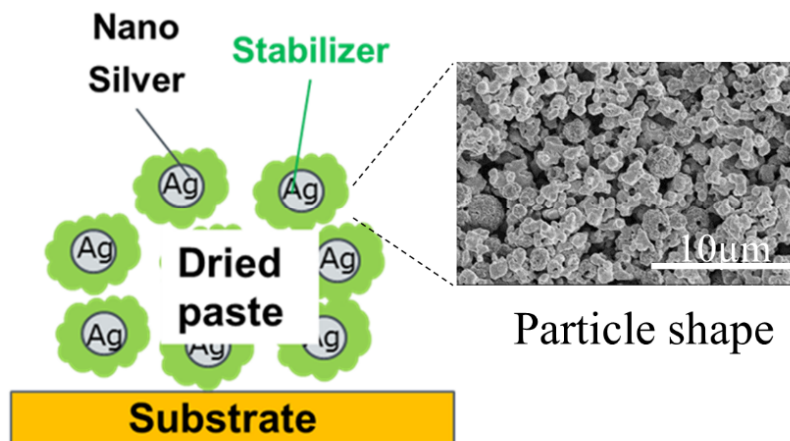
Where  $d\rho/dt$  is the densification rate,  $\gamma$  is the surface energy,  $r$  is the Ag particle diameter,  $P_{applied}$  is the external pressure,  $\rho$  is the density, and  $\eta$  is the densification viscosity. According to the equation, increasing the externally applied pressure can positively influence enhancing this intrinsic driving force. Increasing the temperature reduces the densification viscosity of  $\eta$ , accelerating the coarsening of Ag particles. From the viewpoint of material characteristics, decreasing the particle size can increase the total surface energy as a driving force of densification. Typical paste diameter size ranges from nano to micro size. However, only nano-sized Ag particle is favorable for densification.



# 1. Screen printing



# 2. Dry process



# 3. Sintering

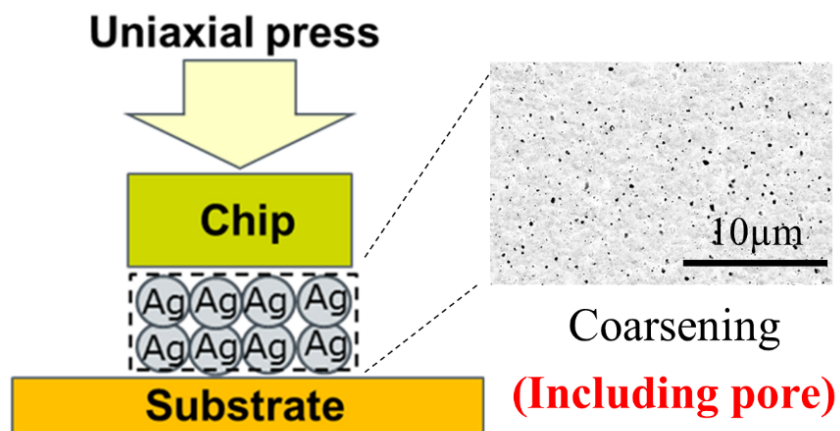
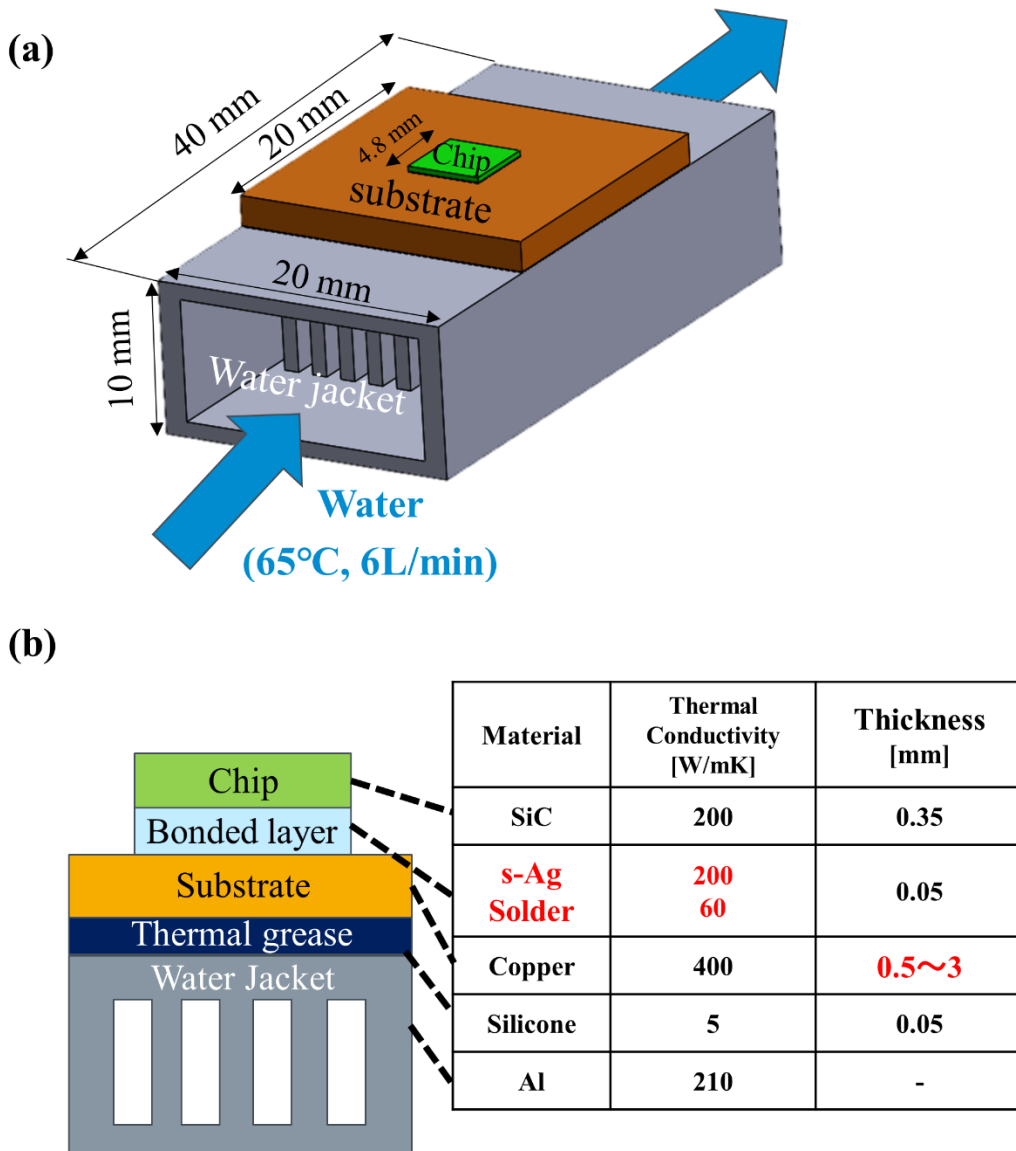


Fig. 1-7 Representative s-Ag die bonding procedure step.

#### 1-4. Thermal impedance calculation

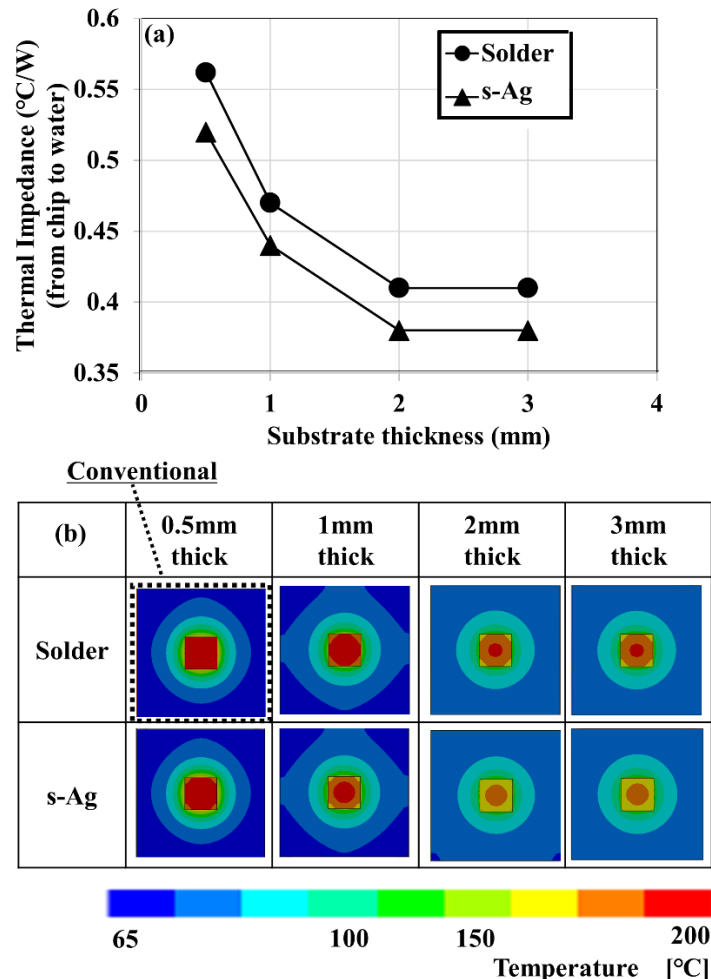
Thermal fluid simulations were performed to seek the target packaging structure with low thermal impedance. Fig. 1-8 shows the calculation model together with the material property used in this calculation. The calculation model comprised a chip, substrate, water jacket, and two bonding layers. s-Ag or solder was adopted as a bonding layer at the bottom of the chip part. The adhesive layer between the substrate and water jacket was adopted with silicone as thermal grease. The Model configuration is shown in Fig. 1-8 (a).



**Fig. 1-8 Thermal fluid simulation model overview of (a) Simulation model schematic image and (b) Cross section image together with input parameter for each component.**

The model configuration parameter was set at substrate thickness ranging from 0.5 to 3 mm. An inflow condition of 6 L/min at 65°C was set on the inlet surface of the cooling channel. The opposite surface was set to the pressure opening condition. Heat conduction to the surroundings was ignored. 300 W of heat was given to the whole part of the chip. Steady-state thermal analysis was performed.

Fig. 1-9 (a) shows a simulation result with thermal impedance as a function of substrate thickness in s-Ag compared to solder die-bonded structure. Thermal impedance value is referred to the difference between averaged chip temperature and inlet water of 65°C divided by the heat of 300 W. The thermal impedance value is decreased by 30% with increasing the substrate thickness from 0.5 mm to 2 mm, then the value saturates up to 3 mm in the substrate thickness. By replacing the solder layer with the s-Ag layer, the thermal impedance value of each structure is decreased by about 10%.



**Fig. 1-9 Thermal fluid simulation results of (a) Chip to water thermal impedance as a function of copper substrate thickness and (b) Surface temperature distribution results with each condition.**

Fig. 1-9 (b) shows the temperature distribution on the surface of the chip and substrate. In the case of a small thickness substrate, the temperature around the chip is high due to the small heat diffusion into the Cu substrate. By contrast, for thick substrates, the heat generated from the chip can be efficiently diffused into the adjacent substrate as much as possible through the die-attached material.

The target structure in this study is summarized as illustrated in Fig. 1-10. Three main points follow the adoption reason.

1. SiC chip can achieve to reduce conduction and switching energy loss during power conversion.
2. s-Ag die bonding can fully extract the SiC excellent device properties by its high heat conductivity and melting point.
3. A thick Cu substrate with 2mm thick can spread thermal flux from the chip to the bottom side to get low thermal impedance packaging.

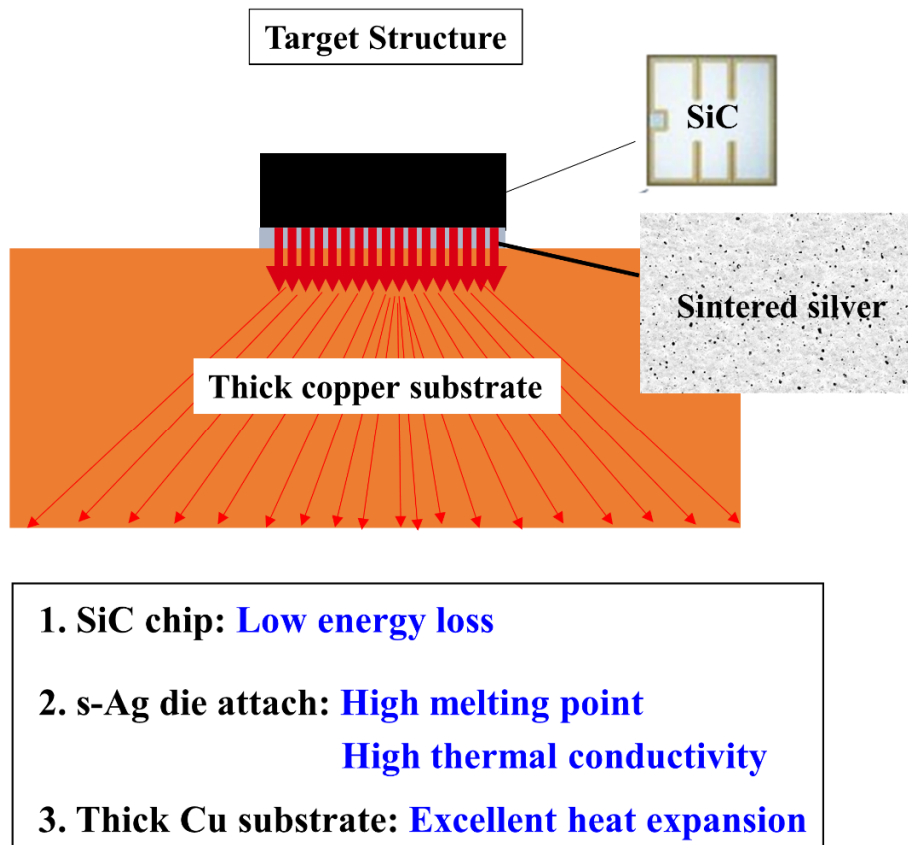
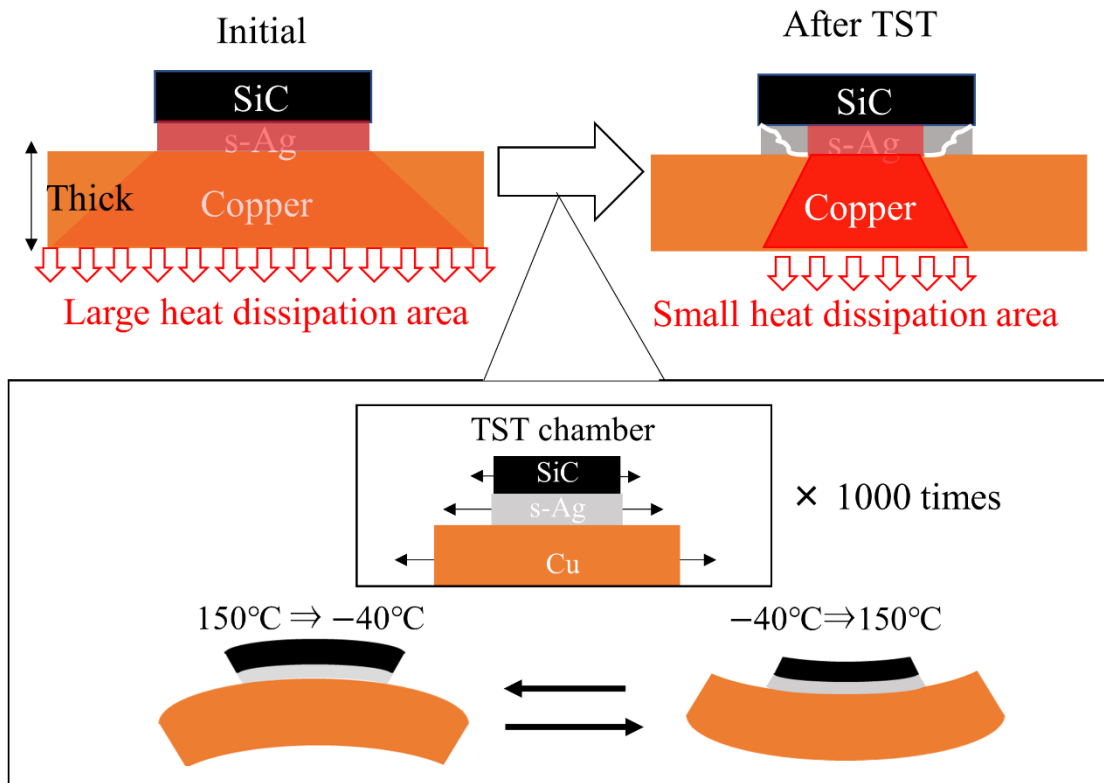


Fig. 1-10 Target packaging structure for power module products with high power density.

### 1-5. Die bonding reliability evaluation

Regarding the practical use of products, s-Ag die layer is commonly assessed by a thermal shocked test (TST), which evaluates material durability against heating and cooling between low and high temperatures set in a heat chamber. The chamber temperature commonly varies between  $-40$  and  $150^{\circ}\text{C}$  with a duration time of 30 min according to the standard testing condition in automobile companies [35, 55, 58-60]. During TST, thermal and mechanical stresses are generated in the die layer because materials with different coefficients of thermal expansion (CTE) cause thermal warpage around a bonded part, as illustrated in the bottom image of Fig. 1-11 [61]. In the case of the s-Ag layer, a fracture starts at the top corner of the s-Ag layer, then the crack propagates horizontally along the substrate surface [55, 60]. After TST, the thermal path area from the SiC chip to the substrate decreases, which makes a smaller heat dissipation area than the heat dissipation area in the initial state. As a result, increased thermal impedance accelerates products to failure. The lifetime of the s-Ag die layer is typically defined as the delamination area percentage of 20% after 1000 cycles in TST for not affecting the thermal impedance with worsen from an originate thermal impedance value.



**Fig. 1-11 Thermal distribution image at the initial state and after the thermal shocked test (TST) together with out-of-plane deformation image during TST [60].**

For a safe and reliable design of s-Ag die toward long-term durability, the thermal and mechanical stresses on degradation should be independently understood with one another. In addition, the relation between applied damage in the s-Ag layer and delamination ratio during thermal and mechanical cyclic tests should be quantitatively clarified. To date, the correlation has been clarified by other researchers, as shown in Fig. 1-12.

As for the first group, shear stress experiments were utilized for evaluating the degradation in thermal shocked tests (TST) [24, 48, 58-60]. A shear test is designed to apply parallel stress to the DAAs; thus, the die layer can be experienced with a sliding failure. Therefore, the bonding strength against the shear stress can roughly be evaluated. Generally, over 30 MPa value in shear force is a standard criterion value, which indicates that the bonding strength showed enough strength for evaluating TSTs. This experiment uses simple experimental units. Considering that TST assessment requires a long time, the shear test has been conventionally adopted as a screening experiment for TST. However, the shear test is not a cyclic load test as TST, which means unclear relation between shear test results associated with bonding strength and TST results associated with die delamination by repeated thermal-mechanical stress.

As for the second group, the degradation assessment of the s-Ag layer during TST has been conducted by combining numerical calculations with experiments. SiC chips were s-Ag bonded with substrates, which were conducted by TST to check the delamination ratio as a function of cycles. The average accumulated von Mises plastic strain (APS) at the s-Ag layer was calculated from finite element analysis (FEA), and then the APS has been utilized for ordering the fracture driving force among performed TSTs [31, 55, 59, 61, 65-73]. In deriving APS, the s-Ag film tensile mechanical property was investigated on the basis of the TST environmental temperature. APS can describe the plastic flowability in the s-Ag die layer, which had a positive correlation against the delamination ratio of the s-Ag layer after TSTs. Considering that the flow resistance difference among s-Ag layers is not included in the APS, the validity of s-Ag layer degradation after TSTs has yet to be entirely revealed by only taking APS into s-Ag layer degradation evaluation after TST.

As for the third group, mechanical fatigue bending tests were also utilized to evaluate s-Ag layer degradation during TST. The mechanical bending test aims to precisely control the test mode with bending test speed, temperature, and frequency. If the s-Ag layer delamination ratio can be associated between the fast mechanical bending test and TST results, then the TST assessment period will be shortened. For example, J. Heilmann *et al.* have developed an original three-point bending tester for applying bending

stress to the s-Ag DAAs to understand the die failure during TST [67, 73]. The experiments at 1 Hz and 125°C showed a 20% s-Ag die layer delamination ratio after 7000 cycles, in which the cycle was about seven times larger than the TST from -40°C to 150°C at 0.0056 Hz. That is, this three-point bending test delamination speed per time is higher than the speed with TST. Further studies should be implemented to obtain the same physics of failure between the bending test and TST by appropriate damage parameter (DP). In addition, the deformation in the conventional set up was restricted to one deformation direction with only one longitudinal direction because of the rectangular configuration of DAAs, as depicted in the bottom of Fig. 1-12.

For achieving the overall understanding of s-Ag die degradation during TST, further experiments of TSTs and appropriate mechanical bending tests should be developed. In addition, s-Ag degradation differences after TSTs and mechanical bending tests should be validated by the modified APS, including plastic flow resistance among different s-Ag types. For validation, at least two types of s-Ag DAAs should be performed by TSTs and mechanical bending tests.

For TSTs, sufficient fundamental experiment result data should be performed to verify whether the modified APS would be suitable for s-Ag die layer degradation assessments or not. Furthermore, the degradation mode of TST should be carefully investigated from the viewpoint of microscopic structural analysis. TSTs should be performed by multiple types of configurations and temperature variations. Notably, s-Ag degradation should implement not only s-Ag delamination ratio evaluation but also failure mode evaluation by cross-sectional scanning electron microscopy (SEM) observations. Cracking mode and s-Ag microstructure differences should be carefully investigated to grasp the failure physics of s-Ag die layer during TSTs. For mechanical bending tests, an advanced mechanical bending test is required to provide out-of-plane deformation with s-Ag DAAs as TST like. By comparing new bending tests and TSTs, the degradation mechanism of the s-Ag layer can be experimentally understood from thermal and mechanical aspects.

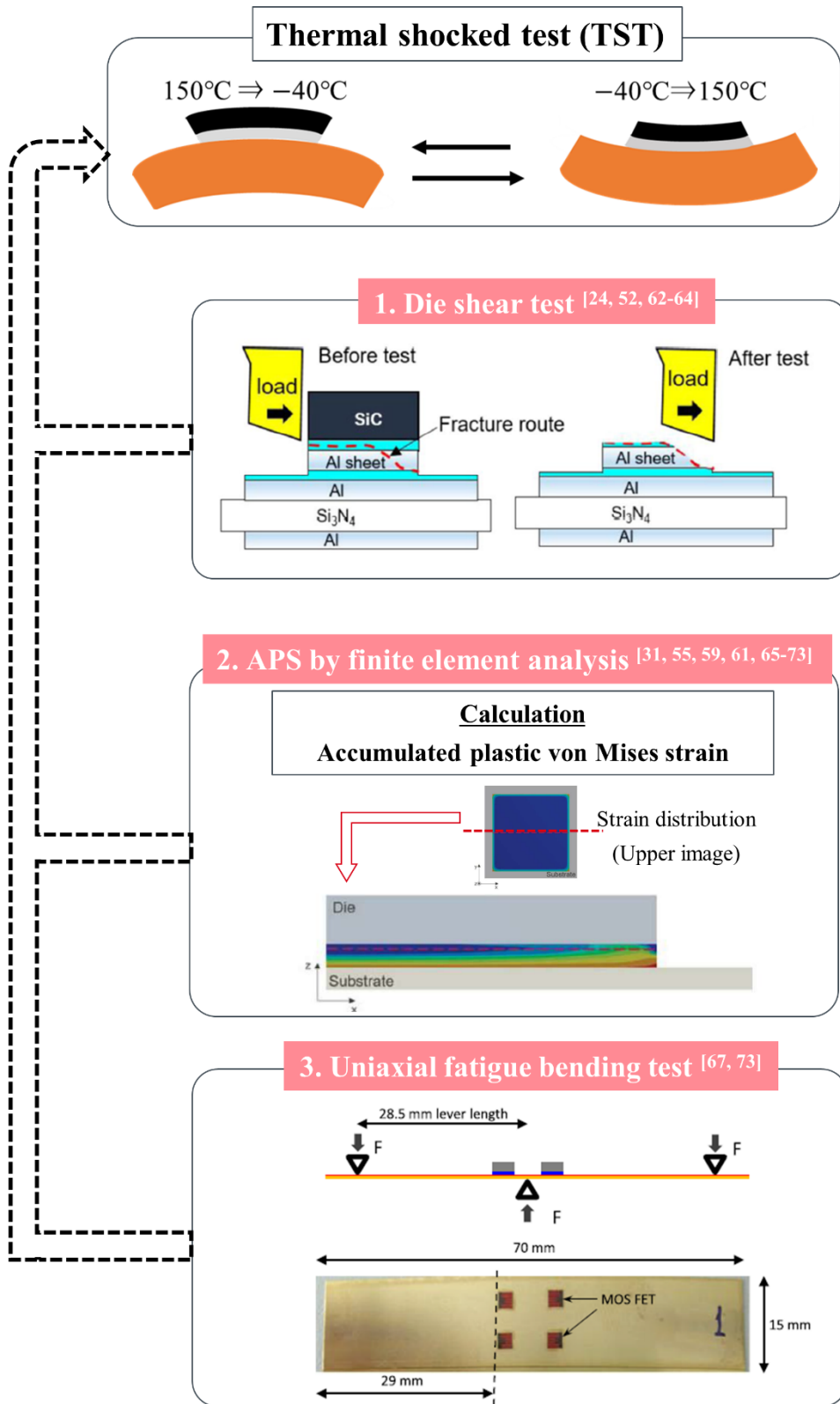


Fig. 1-12 Previous competitor's research attempt summary for evaluating TSTs.



## 1-6. Scope of this study

A new die bonding technique of s-Ag has shown great application potential because of its high heat conductivity and melting point to fully extract excellent WBG device characteristics with low energy loss during power conversion. s-Ag die attachment with WBG devices can achieve high-power-density products for future EV market. However, for practical use in products, s-Ag die layer degradation is commonly assessed with TST, which evaluates material degradation between low and high temperature. The distinct coefficients of thermal expansion (CTE) of each material causes thermal and mechanical stresses in the s-Ag die layer, which leads to failure in the s-Ag die layer. The thermal and mechanical stresses on degradation should be independently understood to clarify the main degradation during TST. The new mechanical bending test should be proposed for focusing on mechanical stress dependence on s-Ag die layer degradation. Moreover, an appropriate degradation criterion should be proposed after a comprehensive understanding of the degradation mechanism of the s-Ag die layer based on the TST and new mechanical bending test results.

This study aims to experimentally clarify the overall s-Ag die degradation mechanism during TST. After achieving the objective of this thesis, the author will propose the reliability design flow of s-Ag DAAs, which can be satisfied with the degradation criterion condition. That is, each geometric parameter of chip, die layer, and substrate size can be properly determined for an appropriate reliable packaging design by the requirement of TST. The Chapter flow chart is shown in Fig. 1-13.

In this thesis, in Chapter 1, the background of die-attach materials for achieving high-power-density power module packaging is explained from device trends, die-attach trends, low thermal impedance packaging structure, and die reliability issue. Then, the scope of this study for clarifying the s-Ag die layer failure mechanism is stated.

In Chapter 2, s-Ag paste characterization is first introduced. Two types of s-Ag pastes (NP, nanosized paste; NMP, nano-to-micro-sized paste) are used as a representative. Each Ag paste is analyzed by dynamic light scattering (DLS) for Ag particle-size distributions and by Fourier transform infrared spectroscopy for organic solvent components. Dried Ag paste and sintered Ag paste are investigated by gas chromatography mass spectrometry (GC/MS) to clarify the protective organic component surrounding Ag particles after each process. Then, the tensile mechanical property of the s-Ag film is investigated to obtain fundamental

data with stress–strain (*S-S*) curves and clarify the s-Ag mechanical characteristics about the pore and tensile mechanical property relations. The appropriate process condition for improving the s-Ag mechanical property is clarified. In addition, by comparing between NP and NMP *S-S* curves, favorable paste characterization for improving the mechanical property is also concluded. The fracture characteristic differences between NP and NMP are discussed based on CCD observations for cracking behavior and cross-sectional SEM observations for understanding the fracture mechanism with microscale.

In Chapter 3, s-Ag die layer degradation is assessed by comparing mechanical bending tests with TST. First, a four-point bending test (FBT) at room temperature (RT) and TST are compared to determine the decisive stress components in the s-Ag layer during TST. As for the advanced step, developed mechanical bending test, namely, NBT, is proposed. NBT can provide out-of-plane deformation with s-Ag DAAs such as TST. s-Ag die layer degradation is assessed by comparing NBTs (0–300 N) at 150°C with 3 min period and TSTs (–40°C–150°C) with 60 min period. SAT and cross-sectional SEM observations are used to assess s-Ag layer failure mode between TSTs and NBTs. Thus, new DP is proposed to obtain a comprehensive understanding of the degradation mechanism classification for the s-Ag die layer. The DP is defined as the conventional evaluation parameter of APS divided by the plastic strain of s-Ag material originating from uniaxial tensile testing at the highest temperature in each condition. DP indicates the ratio of plastic flowability to plastic resistance, which can assess the cracking propagation probability irrespective of test type and material difference. The delamination ratio after 1000 cycles of each TST and NBT is assessed by the DP.

In Chapter 4, the pore growth condition is explored by MD simulation to comprehensively understand s-Ag material degradation. Classical pore growth is described to identify the aging criterion of the s-Ag material. The DP effectiveness for separately evaluating the s-Ag degradation phenomena is discussed on the basis of pore growth. In addition, the pore growth transition is observed by the In-situ SEM tensile testing system for understanding overall s-Ag die layer degradation mechanism during TST and NBT including pore growth phenomena.

In Chapter 5, the research achievement of this study is summarized. In particular, the progress of conventional production flow is described in accordance with the new production flow methodology. Finally, the validation studies provide methods in achieving reliable high-power-density modules.

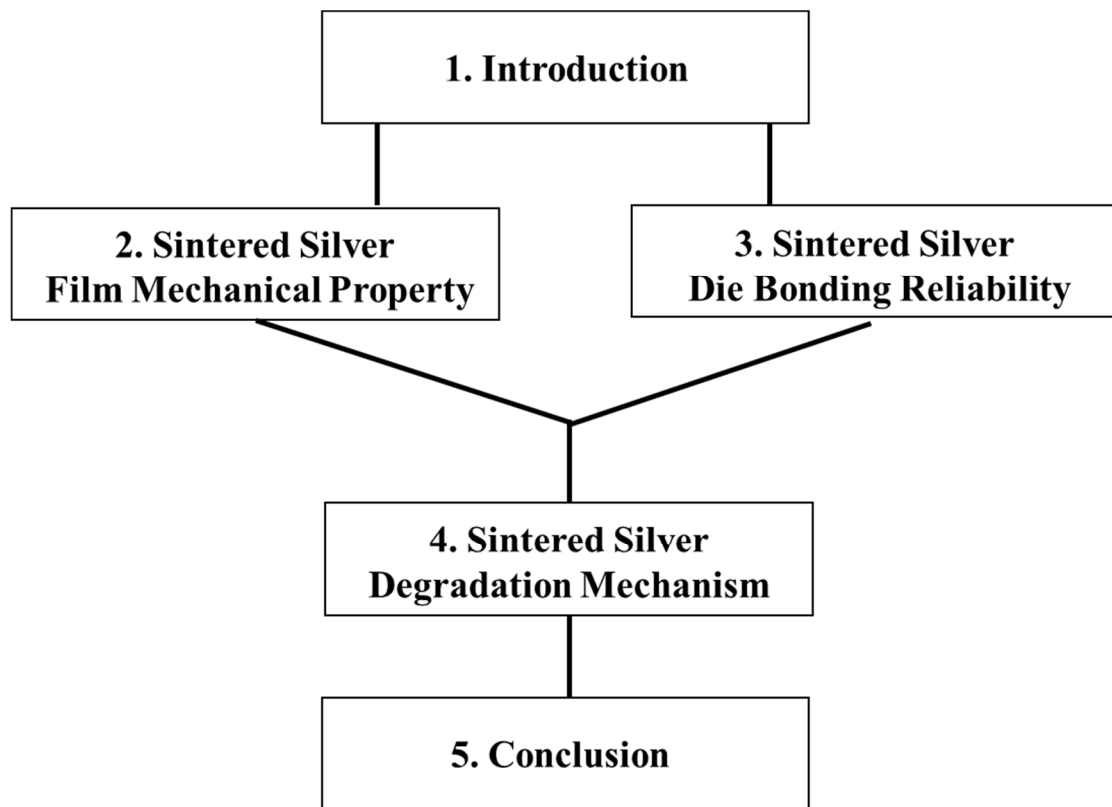


Fig. 1-13 Chapter flowchart.

## References

- [1] F. C. Lee, J. D. van Wyk, D. Boroyevich, G. Q. Lu, Z. Liang, and P. Barbosa, "Technology trends toward a system-in-a-module in power electronics," *IEEE Circuits Syst Mag.*, vol. 2, no. 4, pp. 4-22, 2002, doi: 10.1109/MCAS.2002.1173132.
- [2] B. Wunderle, C. A. Manier, M. Abo Ras, M. Springborn, D. May, H. Oppermann, M. Toepper, R. Mrossko, T. Xhonneux, T. Caroff, W. Maurer, and R. Mitova, "Double-Sided Cooling and Thermo-Electrical Management of Power Transients for Silicon Chips on DCB-Substrates for Converter Applications: Design, Technology and Test," in *Proc. 19th International Workshop on Thermal Investigations of ICs and Systems (THERMINIC)*, Berlin, Germany, 25-27 Sep., 2013, doi: 10.1109/THERMINIC.2013.6675189.
- [3] X. She, A. Q. Huang, O. Lucia, and B. Ozpineci, "Review of Silicon Carbide Power Devices and Their Applications," *IEEE Transactions on Industrial Electronics*, vol. 64, no. 10, pp. 8193-8205, 2017, doi: 10.1109/tie.2017.2652401.
- [4] J. L. Hudgins, G. S. Simin, E. Santi, and M. A. Khan, "An assessment of wide bandgap semiconductors for power devices," *IEEE Transactions on Power Electronics*, vol. 18, no. 3, pp. 907-914, 2003, doi: 10.1109/tpel.2003.810840.
- [5] K. J. Chen, O. Haaberlen, A. Lodow, C. L. Tsai, T. Ueda, Y. Uemoto, and Y. Wu, "GaN-on-Si Power Technology: Devices and Applications," *IEEE Transactions on Electron Devices*, vol. 64, no. 3, pp. 779-795, 2017, doi: 10.1109/ted.2017.2657579.
- [6] J. Biela, M. Schweizer, S. Waffler, and J. W. Kolar, "SiC versus Si—Evaluation of Potentials for Performance Improvement of Inverter and DC–DC Converter Systems by SiC Power Semiconductors," *IEEE Transactions on Industrial Electronics*, vol. 58, no. 7, pp. 2872-2882, 2011, doi: 10.1109/tie.2010.2072896.
- [7] C. Chen, S. Nagao, H. Zhang, T. Sugahara, K. Suganuma, T. Iwashige, K. Sugiura, and K. Tsuruta, "Low-Stress Design for SiC Power Modules with Sintered Porous Ag Interconnection," in *Proc. 66th Electronic Components and Technology Conference (ECTC)*, Las Vegas, NV, USA, Aug., 2016, doi: 10.1109/ECTC.2016.59.
- [8] C. Ding, H. Liu, K. D. T. Ngo, R. Burgos, and G.-Q. Lu, "A Double-Side Cooled SiC MOSFET Power Module With Sintered-Silver Interposers: I-Design, Simulation, Fabrication, and

- Performance Characterization," *IEEE Transactions on Power Electronics*, vol. 36, no. 10, pp. 11672-11680, 2021, doi: 10.1109/tpel.2021.3070326.
- [9] Y. H. Mei, J. Y. Lian, X. Chen, G. Chen, X. Li, and G.-Q. Lu, "Thermo-Mechanical Reliability of Double-Sided IGBT Assembly Bonded by Sintered Nanosilver," *IEEE Transactions on Device and Materials Reliability*, vol. 14, no. 1, pp. 194-202, 2014, doi: 10.1109/tdmr.2013.2280668.
- [10] J. Yan, "A Review of Sintering-Bonding Technology Using Ag Nanoparticles for Electronic Packaging," *Nanomaterials*, vol. 11, no. 4, Apr., 2021, doi: 10.3390/nano11040927.
- [11] M. I. Khalid Hussein, N. Miyamoto, Y. Nakata, and T. Nakano, "New Compact, High Performance 7th Generation IGBT Module with Direct Liquid Cooling for EV/HEV Inverters," in *Proc. 30th Applied Power Electronics Conference and Exposition (APEC)*, Charlotte, USA, March, 2015, doi: 10.1109/APEC.2015.7104522.
- [12] M. A. Huque, L. M. Tolbert, B. J. Blalock, and S. K. Islam, "A High-Temperature, High-Voltage SOI Gate Driver IC with High Output Current and On-Chip Low-Power Temperature Sensor," *Doctor dissertation*, Tennessee university, USA, 2009, URL: [https://trace.tennessee.edu/utk\\_graddiss/706](https://trace.tennessee.edu/utk_graddiss/706).
- [13] V. R. Manikam and C. Kuan Yew, "Die Attach Materials for High Temperature Applications: A Review," *IEEE Transactions on Components, Packaging and Manufacturing Technology*, vol. 1, no. 4, pp. 457-478, 2011, doi: 10.1109/tcpmt.2010.2100432.
- [14] G. Q. Lu, Guangyin Lei, Jesus N. Calata, Xu Chen, and Susan Luo, "Emerging Lead-free, High-temperature Die-Attach Technology Enabled by Low-temperature Sintering of Nanoscale Silver Pastes," *2009 International Conference on Electronic Packaging Technology & High Density Packaging*, Beijing, China, Aug., 2009, doi: 10.1109/ICEPT.2009.5270709.
- [15] D. R. M. Woo, H. H. Yuan, J. A. J. Li, L. J. Bum, and Z. Hengyun, "Miniaturized Double Side Cooling Packaging for High Power 3 Phase SiC Inverter Module with Junction Temperature over 220°C," in *Proc. 66th Electronic Components and Technology Conference (ECTC)*, Las Vegas, USA, Aug., 2016, doi: 10.1109/ECTC.2016, doi: 10.1109/ECTC.2016.396.396.
- [16] C. J. Chen, C. M. Chen, R. H. Horng, D. S. Wu, and J. S. Hong, "Thermal Management and Interfacial Properties in High-Power GaN-Based Light-Emitting Diodes Employing Diamond-Added Sn-3 wt.%Ag-0.5 wt.%Cu Solder as a Die-Attach Material," *Journal of Electronic Materials*, vol. 39, no. 12, pp. 2618-2626, 2010, doi: 10.1007/s11664-010-1354-6.
- [17] F. P. McCluskey, M. Dash, Z. Wang, and D. Huff, "Reliability of high temperature solder

- alternatives," *Microelectronics Reliability*, vol. 46, no. 9-11, pp. 1910-1914, 2006, doi: 10.1016/j.microrel.2006.07.090.
- [18] N. Saud, R. M. Said, "Transient liquid phase bonding for solder-a short review," in *Proc. IOP Conference Series: Materials Science and Engineering*, Penang, Malaysia, November, 2019, vol. 701, doi: 10.1088/1757-899X/701/1/012050.
- [19] M. Feißt, A. Schumacher, I. Spies, and J. Wilde, "Process Optimization of Foil Based Transient Liquid Phase Bonding for Die Attachment," in *Proc. 42nd International Spring Seminar on Electronics Technology (ISSE)*, Wroclaw, Poland, Aug., 2019, doi: 10.1109/ISSE.2019.8810295.
- [20] A. Bajwa, Y. Qin, R. Reiner, R. Quay, and J. Wilde, "Assembly and Packaging Technologies for High-Temperature and High-Power GaN Devices," *IEEE Transactions on Components, Packaging and Manufacturing Technology*, vol. 5, no. 10, pp. 1402-1416, 2015, doi: 10.1109/tcpmt.2015.2468595.
- [21] H. A. Mustain, W. D. Brown, and S. S. Ang, "Transient Liquid Phase Die Attach for High-Temperature Silicon Carbide Power Devices," *IEEE Transactions on Components and Packaging Technologies*, vol. 33, no. 3, pp. 563-570, 2010, doi: 10.1109/tcapt.2010.2046901.
- [22] C. H. Sha and C. C. Lee, "Low-Temperature Solid-State Silver Bonding of Silicon Chips to Alumina Substrates," *IEEE Transactions on Components, Packaging and Manufacturing Technology*, vol. 1, no. 12, pp. 1983-1987, 2011, doi: 10.1109/tcpmt.2011.2170425.
- [23] S. Noh, C. Choe, C. Chen, and K. Suganuma, "Heat-resistant die-attach with cold-rolled Ag sheet," *Applied Physics Express*, vol. 11, no. 1, pp. 016501-1-4, 2018, doi: 10.7567/apex.11.016501.
- [24] C. Chen and K. Suganuma, "Low temperature SiC die-attach bonding technology by hillocks generation on Al sheet surface with stress self-generation and self-release," *Scientific Report*, vol. 10, no. 1, pp. 9042-9952, Jun., 2020, doi: 10.1038/s41598-020-66069-8.
- [25] R. Z. Adeel, A. Bajwa, and J. Wilde, "Process Optimization and Characterization of a Novel Micro-Scaled Silver Sintering Paste as a Die-Attach Material for High Temperature High Power Semiconductor Devices," in *Proc. 36th International Spring Seminar on Electronics Technology*, Alba Iulia, Romania, May, 2013, doi: 10.1109/ISSE.2013.6648214.
- [26] J. G. Bai, Z. Z. Zhang, J. N. Calata, and G. Q. Lu, "Low-Temperature Sintered Nanoscale Silver as a Novel Semiconductor Device-Metallized Substrate Interconnect Material," *IEEE Transactions on Components and Packaging Technologies*, vol. 29, no. 3, pp. 589-593, 2006, doi:

10.1109/tcapt.2005.853167.

- [27] M. Calabretta, A. Sitta, S. M. Oliveri, and G. Sequenzia, "Silver Sintering for Silicon Carbide Die Attach: Process Optimization and Structural Modeling," *Applied Sciences*, vol. 11, no. 15, pp.7012-7023, 2021, doi: 10.3390/app11157012.
- [28] C. Chen and K. Suganuma, "Microstructure and mechanical properties of sintered Ag particles with flake and spherical shape from nano to micro size," *Materials & Design*, vol. 162, pp. 311-321, 2019, doi: 10.1016/j.matdes.2018.11.062.
- [29] J. Dai, J. Li, P. Agyakwa, M. Corfield, and C. M. Johnson, "Comparative Thermal and Structural Characterization of Sintered Nano-Silver and High-Lead Solder Die Attachments During Power Cycling," *IEEE Transactions on Device and Materials Reliability*, vol. 18, no. 2, pp. 256-265, 2018, doi: 10.1109/tdmr.2018.2825386.
- [30] J. Fan, D. Xu, H. Zhang, C. Qian, X. Fan, and G. Zhang, "Experimental Investigation on the Sintering Kinetics of Nanosilver Particles Used in High-Power Electronic Packaging," *IEEE Transactions on Components, Packaging and Manufacturing Technology*, vol. 10, no. 7, pp. 1101-1109, 2020, doi: 10.1109/tcpmt.2020.2995634.
- [31] F. Forndran, J. Heilmann, M. Metzler, M. Leicht, and B. Wunderle, "A Parametric Simulative Study for Lifetime Prediction of Sintered Silver Die Attach Under Different Accelerated Testing Conditions," in *Proc. 22nd International Conference on Thermal, Mechanical and Multi-Physics Simulation and Experiments in Microelectronics and Microsystems (EuroSimE)*, St. julian, Marta, Apr., 2021, doi: 10.1109/EuroSimE52062.2021.9410830.
- [32] S. Fu, Y. Mei, X. Li, P. Ning, and G. Q. Lu, "Parametric Study on Pressureless Sintering of Nanosilver Paste to Bond Large-Area ( $\geq 100 \text{ mm}^2$ ) Power Chips at Low Temperatures for Electronic Packaging," *Journal of Electronic Materials*, vol. 44, no. 10, pp. 3973-3984, 2015, doi: 10.1007/s11664-015-3842-1.
- [33] A. Hu., J. Y. Guo, H. Alarifi, G. Patane, Y. Zhou, G. Compagnini, and C. X. Xu, "Low temperature sintering of Ag nanoparticles for flexible electronics packaging," *Applied Physics Letters*, vol. 97, no. 15, pp.153117-1-3, 2010, doi: 10.1063/1.3502604.
- [34] Y. Gao, C. Chen, S. Nagao, K. Suganuma, A. S. Bahman, and F. Iannuzzo, "Highly Reliable Package using Cu Particles Sinter Paste for Next Generation Power Devices," in *Proc. International Exhibition and Conference for Power Electronics (PCIM Europe)*, Intelligent Motion,

Renewable Energy and Energy Management, Nuremberg, Germany, July, 2019, ISBN: 978-3-8007-4938-6.

- [35] M. Schaal, M. Klingler, and B. W. M. Klingler, "Silver Sintering in Power Electronics: The State of the Art in Material Characterization and Reliability," in *Proc. 7th Electronic System-Integration Technology Conference (ESTC)*, Dresden, Germany, Sept., 2018, doi: 10.1109/ESTC.2018.8546498.
- [36] P. Peng, A. Hu, A. P. Gerlich, G. Zou, L. Liu, and Y. N. Zhou, "Joining of Silver Nanomaterials at Low Temperatures: Processes, Properties, and Applications," *ACS Appl Mater Interfaces*, vol. 7, no. 23, pp. 12597-12618, 2015, doi: 10.1021/acsami.5b02134.
- [37] K. S. Siow, "Are Sintered Silver Joints Ready for Use as Interconnect Material in Microelectronic Packaging?," *Journal of Electronic Materials*, vol. 43, no. 4, pp. 947-961, 2014, doi: 10.1007/s11664-013-2967-3.
- [38] J. Yeom, S. Nagao, C. Chen, T. Sugahara, H. Zhang, C. Choe, Cai-Fu Li, and K. Sugauma, "Ag particles for sinter bonding: Flakes or spheres?," *Applied Physics Letters*, vol. 114, no. 25, 2019, doi: 10.1063/1.5099140.
- [39] Y. Zuo, S. Carter-Searjeant, M. Green, L. Mills, and S. H. Mannan, "High bond strength Cu joints fabricated by rapid and pressureless in situ reduction-sintering of Cu nanoparticles," *Materials Letters*, vol. 276, 2020, doi: 10.1016/j.matlet.2020.128260.
- [40] Y. Zuo, S. Carter-Searjeant, M. Green, L. Mills, and S. H. Mannan, "Low temperature Cu joining by in situ reduction-sintering of CuO nanoparticle for high power electronics," *Advanced Powder Technology*, vol. 31, no. 10, pp. 4135-4144, 2020, doi: 10.1016/j.appt.2020.08.019.
- [41] W. Li, H. Zhang, Y. Gao, J. Jiu, C-F Li, C. Chen, D. Hu, Y. Goya, Y. Wang, H. Koga, S. Nagao, and K. Sugauma, "High reliable and high conductive submicron Cu particle patterns fabricated by low temperature heat-welding and subsequent flash light sinter-reinforcement," *Journal of Materials Chemistry C* vol. 5, no. 5, pp. 1155-1164, 2017, doi: 10.1039/C6TC04892G.
- [42] J. Niittynen, E. Sowade, H. Kang, R. R. Baumann, and M. Mantysalo, "Comparison of laser and intense pulsed light sintering (IPL) for inkjet-printed copper nanoparticle layers," *Scientific Reports*, vol. 5, no. 8832, pp. 1-10, 2015, doi: 10.1038/srep08832.
- [43] J. Liu, H. Ji, S. Wang, and M. Li, "The low temperature exothermic sintering of formic acid treated Cu nanoparticles for conductive ink," *Journal of Materials Science: Materials in Electronics*, vol. 27,



- no. 12, pp. 13280-13287, 2016, doi: 10.1007/s10854-016-5476-3.
- [44] Y. Gao, S. Tanaka, C. Chen, S. Nagao, K. Suganuma, A. S. Bahman, and F. Iannuzzo, "Reliability analysis of sintered Cu joints for SiC power devices under thermal shock condition," *Microelectronics Reliability*, vol. 100-101, pp. 113456, 2019, doi: 10.1016/j.microrel.2019.113456.
- [45] H. Alarifi, A. Hu, M. Yavuz, and Y. N. Zhou, "Silver Nanoparticle Paste for Low-Temperature Bonding of Copper," *Journal of Electronic Materials*, vol. 40, no. 6, pp. 1394-1402, 2011, doi: 10.1007/s11664-011-1594-0.
- [46] W. Rmili, N. Vivet, S. Chupin, T. Le Bihan, G. Le Quilliec, and C. Richard, "Quantitative Analysis of Porosity and Transport Properties by FIB-SEM 3D Imaging of a Solder Based Sintered Silver for a New Microelectronic Component," *Journal of Electronic Materials*, vol. 45, no. 4, pp. 2242-2251, 2016, doi: 10.1007/s11664-015-4288-1.
- [47] J. Ordonez-Miranda, M. Hermens, I. Nikitin, V. G. Kouznetsova, O. V. D. Sliuis, M. A. Ras, J. S. Reparaz, M. R. Wagner, M. Sledzinska, J. Gomis-Bresco, C.M. Sotomayor Torres, B. Wunderle, and S. Volz, "Measurement and modeling of the effective thermal conductivity of sintered silver pastes," *International Journal of Thermal Sciences*, vol. 108, pp. 185-194, 2016, doi: 10.1016/j.ijthermalsci.2016.05.014.
- [48] N. Alayli, F. Schoenstein, A. Girard, K. L. Tan, and P. R. Dahoo, "Spark Plasma Sintering constrained process parameters of sintered silver paste for connection in power electronic modules: Microstructure, mechanical and thermal properties," *Materials Chemistry and Physics*, vol. 148, no. 1-2, pp. 125-133, 2014, doi: 10.1016/j.matchemphys.2014.07.021.
- [49] J. Carr, X. Milhet, P. Gadaud, S. A. E. Boyer, G. E. Thompson, and P. Lee, "Quantitative characterization of porosity and determination of elastic modulus for sintered micro-silver joints," *Journal of Materials Processing Technology*, vol. 225, pp. 19-23, 2015, doi: 10.1016/j.jmatprotec.2015.03.037.
- [50] P. Gadaud, V. Caccuri, D. Bertheau, J. Carr, and X. Milhet, "Ageing sintered silver: Relationship between tensile behavior, mechanical properties and the nanoporous structure evolution," *Materials Science and Engineering: A*, vol. 669, no. 4, pp. 379-386, 2016, doi: 10.1016/j.msea.2016.05.108.
- [51] K. P. Ivan Nikitin, "Mechanical Properties of Porous Silver Materials Depending on Sintering Parameters," in *Proc. 20th International Workshop on thermal Investigations of ICs and systems* Greenwich, UK, 24-26 Sept. 2014: IEEE, doi: 10.1109/THERMINIC.2014.6972536.

- [52] Y. Liu, H. Zhang, L. Wang, X. Fan, G. Zhang, and F. Sun, "Effect of Sintering Pressure on the Porosity and the Shear Strength of the Pressure-Assisted Silver Sintering Bonding," *IEEE Transactions on Device and Materials Reliability*, vol. 18, no. 2, pp. 240-246, 2018, doi: 10.1109/tdmr.2018.2819431.
- [53] W. C. W. Ng, K. Seatman, K. Kumagai, K. Takamura, T. Nishimura, S. Letz, and A. Schletz, "The correlation between sintered silver joint reliability and pressure assisted sintering parameters," in *Proc. 19th Electronics Packaging Technology Conference (EPTC)*, Shingapor, Dec., 2017, doi: 10.1109/EPTC.2017.8277441
- [54] K. Wakamoto, Y. Mochizuki, T. Otsuka, K. Nakahara, and T. Namazu, "Tensile mechanical properties of sintered porous silver films and their dependence on porosity," *Japanese Journal of Applied Physics*, vol. 58, no. SD, pp. SDDL08-1-5, 2019, doi: 10.7567/1347-4065/ab0491.
- [55] T. Herboth, M. Guenther, A. Fix, and J. Wilde, "Failure Mechanisms of Sintered Silver Interconnections for Power Electronic Applications " in *Proc. 63rd Electronic Components and Technology Conference*, Las Vegas, USA, May, 2013, doi: 10.1109/ECTC.2013.6575789.
- [56] S. Zabihzadeh, S. Van Petegem, M. Holler, A. Diaz, L. I. Duarte, and H. Van Swygenhoven, "Deformation behavior of nanoporous polycrystalline silver. Part I: Microstructure and mechanical properties," *Acta Materialia*, vol. 131, no.1, pp. 467-474, 2017, doi: 10.1016/j.actamat.2017.04.021.
- [57] H. Zhang, Y. Liu, L. Wang, F. Sun, J. Fan, M. D. Placette, X. Fan, and G. Zhang, "Effects of Sintering Pressure on the Densification and Mechanical Properties of Nanosilver Double-Side Sintered Power Module," *IEEE Transactions on Components, Packaging and Manufacturing Technology*, vol. 9, no. 5, pp. 963-972, 2019, doi: 10.1109/tcpmt.2018.2884032.
- [58] T. Herboth, M. Guntherl, M. Gunther, and J. Wilde, "Assessment of Thermo-Mechanical Stresses in Low Temperature Joining Technology," in *Proc. 13th International Conference on Thermal, Mechanical and Multi-Physics Simulation and Experiments in Microelectronics and Microsystems (EuroSimE)*, Cascais, Portugal, April, 2012, doi: 10.1109/ESimE.2012.6191762.
- [59] M. Schaal, M. Klinger, B. Metais, R. Grüniger, S. Hoffmann, and B. Wunderle, "Reliability Assessment of Ag Sintered Joints Using a SiC Semiconductor and Determination of Failure Mechanism in the Field of Power Electronics," in *Proc. 21st International Conference on Thermal, Mechanical and Multi-Physics Simulation and Experiments in Microelectronics and Microsystems (EuroSimE)*, Cracow, Poland, July, 2020, doi: 10.1109/EuroSimE48426.2020.9152674.

- [60] K. Wakamoto, T. Otsuka, K. Nakahara, and T. Namazu, "Degradation Mechanism of Pressure-Assisted Sintered Silver by Thermal Shock Test," *Energies*, vol. 14, no. 17, pp. 5532-5546, 2021, doi: 10.3390/en14175532.
- [61] A. Mathew, R. Dudek, A. Otto, C. Scherf, S. Rzepka, N. Subbiah, K. A. Rane, and J. Wilde, "Lifetime modelling of sintered silver interconnected power devices by FEM and experiment," in *Proc. 22nd International Conference on Thermal, Mechanical and Multi-Physics Simulation and Experiments in Microelectronics and Microsystems (EuroSimE)*, st. Julian, Marta, Apr. 2021, doi: 10.1109/EuroSimE52062.2021.9410877.
- [62] S.T. Chua, K. S. Siow, and A. Jalar, "Effect of sintering Atmosphere on the Shear Properties of Pressureless Sintered Silver Joint," in *Proc. 36th International Electronic Manufacturing Technology Conference, 2014*, Johor, Malaysia, Nov., 2014, doi: 10.1109/IEMT.2014.7123119.
- [63] Y. Tan, X. Li, Y. Mei, G. Chen, and X. Chen, "Temperature-Dependent Dwell-Fatigue Behavior of Nanosilver Sintered Lap Shear Joint," *Journal of Electronic Packaging*, vol. 138, no. 2, pp. 021001-021008, 2016, doi: 10.1115/1.4032880.
- [64] Y. Tan, X. Li, Y. Mei, G. Chen, and X. Chen, "Effect of bonding temperature on shear strength of joints using micro-sized Ag particles for high temperature packaging technology," in *Proc. 22nd European Microelectronics and Packaging Conference & Exhibition (EMPC)*, Pisa, Italy, 16-19 Sept., 2019, doi: 10.23919/EMPC44848.2019.8951855.
- [65] T. Herboth, M. Guenther, R. Zeiser, and J. Wilde, "Investigation of Stress States in Silicon Dies Induced by the Low Temperature Joining Technology," in *Proc. 14th International Conference on Thermal, Mechanical and Multi-Physics Simulation and Experiments in Microelectronics and Microsystems (EuroSimE)*, Wroclaw, Poland, April, 2013, doi: 10.1109/EuroSimE.2013.6529945.
- [66] D. J. Yu, X. Chen, G. Chen, G. Q. Lu, and Z. Q. Wang, "Applying Anand model to low-temperature sintered nanoscale silver paste chip attachment," *Materials & Design*, vol. 30, no. 10, pp. 4574-4579, 2009, doi: 10.1016/j.matdes.2009.04.006.
- [67] J. Heilmann, K. Pressel, and B. Wunderle, "Accelerated reliability testing and modeling of subsystems based on sintered silver thermal interface materials.," in *Proc. 20th International Workshop on Thermal Investigations of ICs and Systems*, Greenwich, UK, Sept., 2014, doi: 10.1109/THERMINIC.2014.6972540.
- [68] P. Rajaguru, H. Lu, and C. Bailey, "Sintered silver finite element modelling and reliability based

- design optimisation in power electronic module," *Microelectronics Reliability*, vol. 55, no. 6, pp. 919-930, 2015, doi: 10.1016/j.microrel.2015.03.011.
- [69] C. Weber, M. Hutter, C. Ehrhardt, and K-D. Lang, "Failure Analysis of Ag Sintered Joints After Power Cycling Under Harsh Temperature Conditions From + 30°C up to + 180°C," in *Proc. 2015 European Microelectronics Packaging Conference (EMPC)*, Friedrichshafen, Germany, Sept., 2015, ISBN: 978-0-9568-0862-2.
- [70] T. Suzuki, T. Terasaki, Y. Kawana, D. Ishikawa, M. Nishimura, H. Nakako, and K. Kurafuchi, "Effect of Manufacturing Process on Micro-Deformation Behavior of Sintered-Silver Die-Attach Material," *IEEE Transactions on Device and Materials Reliability*, vol. 16, no. 4, pp. 588-596, 2016, doi: 10.1109/tdmr.2016.2614510.
- [71] T. Suzuki, T. Terasaki, T. Morita, Y. Kawana, D. Ishikawa, M. Nishimura, H. Nakako, and K. Kurafuchi, "Thermal Cycling Lifetime Estimation of Sintered Metal Die Attachment," in *Proc. International Conference on Electronics Packaging (ICEP)*, Hokkaido, Japan, April, 2016, doi: 10.1109/ICEP.2016.7486856.
- [72] C. Weber, H. Walter, M. Van Dijk, M. Hutter, O. Wittler, and K.-D. Lang, "Combination of Experimental and Simulation Methods for Analysis of Sintered Ag Joints for High Temperature Applications," in *Proc. 66th Electronic Components and Technology Conference (ECTC)*, Las Vegas, USA, June, 2016, 10.1109/ECTC.2016.394.
- [73] J. Heilmann, I. Nikitin, U. Zschenderlein, D. May, K. Pressel, and B. Wunderle, "Reliability experiments of sintered silver based interconnections by accelerated isothermal bending tests," *Microelectronics Reliability*, vol. 74, pp. 136-146, 2017, doi: 10.1016/j.microrel.2017.04.016.

## **2. Sintered Silver (s-Ag) Film Mechanical property**

### **2-1. s-Ag material**

#### **2-1-1. Introduction of s-Ag paste**



Sintered silver (s-Ag) material has developed in the late 1980s using the original patent from H. Schwabauer in Siemens Co. Ltd., as a new die-attach material replacing solders [1-3]. In the early phase of development in s-Ag, micron-sized Ag particle was sintered at 250°C under process pressure of 9–40 MPa as a reference process condition [4]. Micron-sized Ag filler size typically ranged less than 15 μm mixed with an organic solvent to control their viscosity for printing well on the substrate. However, the high die bonding strength caused by the small amount of surface energy should be addressed. In the mid-2000s, nano Ag particle has developed to enhance the total surface energy for achieving low-temperature bonding [5]. The diameter of Ag particle could be maintained at less than 100 nm [6]. However, Ag nanoparticles are strongly self-sintered without their capping agents. In preventing self-sintering, nano Ag particles are covered with a strong chemical ligament. In general, attaching a strong ligament surrounding nano Ag particle during production is expensive. Therefore, the cost of nanoparticle Ag paste was relatively higher than the micron-sized Ag paste cost. Similarly, the hybrid paste, which consists of micro- and nanosized Ag particles, has been developed to coexist with the low material production cost and high sintering performance [7]. In general, the s-Ag paste is categorized as either “Pressure” or “Pressure-less” based on the presence or absence of applied pressure during sintering. From the view point of assembly, a pressure-less type of s-Ag is favorable for not loading semiconductor devices. In addition, the large number of products can be processed in only one process, which accelerates the production cycle time. On the contrary, the densification of the s-Ag layer is low because of the insufficient diffusion of each micro-sized Ag particle, which results in low bonding strength.

#### **2-1-2. Nano paste (NP) and nano-micro paste (NMP)**

This study adopted two commercial s-Ag pastes, as illustrated in Table 2-1. Nano paste called “NP” viscosity ranges from 30 to 40/sec at room temperature (RT). Ag content is about 78% in NP. Nano to a micro-sized paste called “NMP” viscosity exceeds 100/sec at RT. Ag content is about 90% in NMP. The low-viscosity paste avoids air bubbles under paste screen printing, even if the printing thickness is high. The optimum sintering process flow differs between NP and NMP, originating from the different amounts of organic components. For NP, after screen printing on the substrate, the drying process to remove the

organic solvent should be set at 140°C for 90 min. For NMP, the drying process needs to be only 70°C for 30 min. That is, the reduction amount of organic solvent during the drying process is small in NMP. After that, both types of dried Ag paste were sintered under the optimized condition. In order to examine the NP and NMP specifications in more detail, this study conducted several analyses, as listed in Table 2-2.

**Table 2-1 NP and NMP.**

	Nano paste (NP)	Nano-Micro paste (NMP)
<b>Photograph</b>		
<b>Silver content (%)</b>	78	90
<b>Paste viscosity (1/sec)</b>	30-40	Over 100
<b>Process condition</b>	1. Paste screen printing (200 μm thick) ↓ 2. Dry process (140°C 90min) ↓ 3. Sinter process	1. Paste screen printing (100 μm thick) ↓ 2. Dry process (70°C 30min) ↓ 3. Sinter process

**Table 2-2 Analysis methodology after each process step of Ag paste, dry, and sintering.**

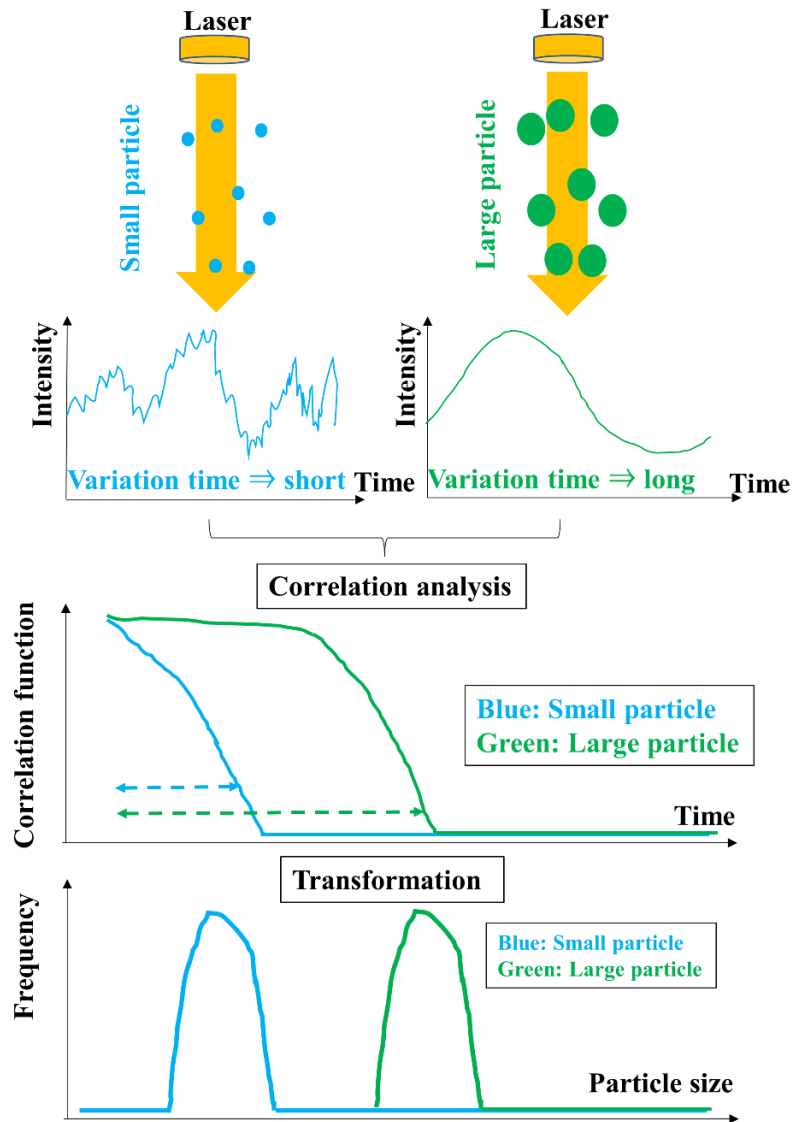
<b>Condition</b>	<b>Analysis method</b>	<b>Analysis item</b>
<b>Paste</b>	<b>Dynamic light scattering (DLS)</b>	<b>Particle size distribution</b>
	<b>Fourier transform infrared spectroscopy (FT-IR)</b>	<b>Chemical component (Organic solvent of paste)</b>
<b>Dry</b>	<b>Gas Chromatography Mass Spectrometry (GC/MS)</b>	<b>Chemical component (Organic protective)</b>
<b>Sinter</b>		

The analyses were performed after each Ag paste, dry, and sinter process step. Dynamic light scattering (DLS) measurements were performed in the paste condition to investigate Ag particle size distributions. Fourier transform infrared spectroscopy (FT-IR) measurements were employed to reveal the chemical component in the paste state. Gas chromatography-mass spectrum (GC/MS) analyses were employed to reveal the organic protective component surrounding Ag particles. GC/MS measurements can reveal whether organic components existed or not after the dry and sintering process.

### 2-1-3. Silver particle size distribution

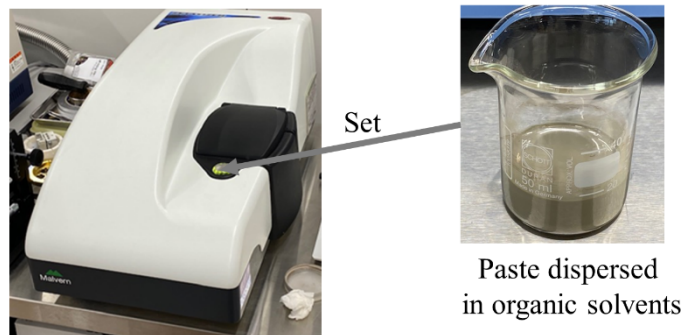
Fig. 2-1 shows a schematic view of DLS methodology for clarifying inherent Ag particle size distributions in NP and NMP. When nano to micro-sized Ag particles is dispersed in an organic solvent, the Ag particles are freely moved to be floated by interactions against organic molecule in the paste solvent. The motion is called “Brownian motion,” which is a specific property with the nano to micro particle solved in the solution. The motion speed turns out to be fast with decreasing the particle size. DLS is utilized for investigating the Ag particle distributions in the paste. When the phase-matched laser light irradiates the paste, the laser light fluctuates according to the “Brownian motion” of the Ag particle. Since the small particles are constantly moving in position due to Brownian motion, the intensity of light is also constantly fluctuating as pale blue. By contrast, for large particles with slow motion, irradiated light

fluctuated over extended period time, as illustrated in the right side of the green waveform. Finally, the degree of fluctuation is converted by the auto correlation function to get the time and correlation function relationship. Various numerical calculations are fitted on the autocorrelation function to obtain a diffusion coefficient, which can clarify the particle size distributions. This study dispersed the NP and NMP paste in the isopropyl alcohol for DLS samples. The solutions were set to the Zetasizer Nano ZS (Malvern Panatycal), as illustrated in Fig. 2-2.



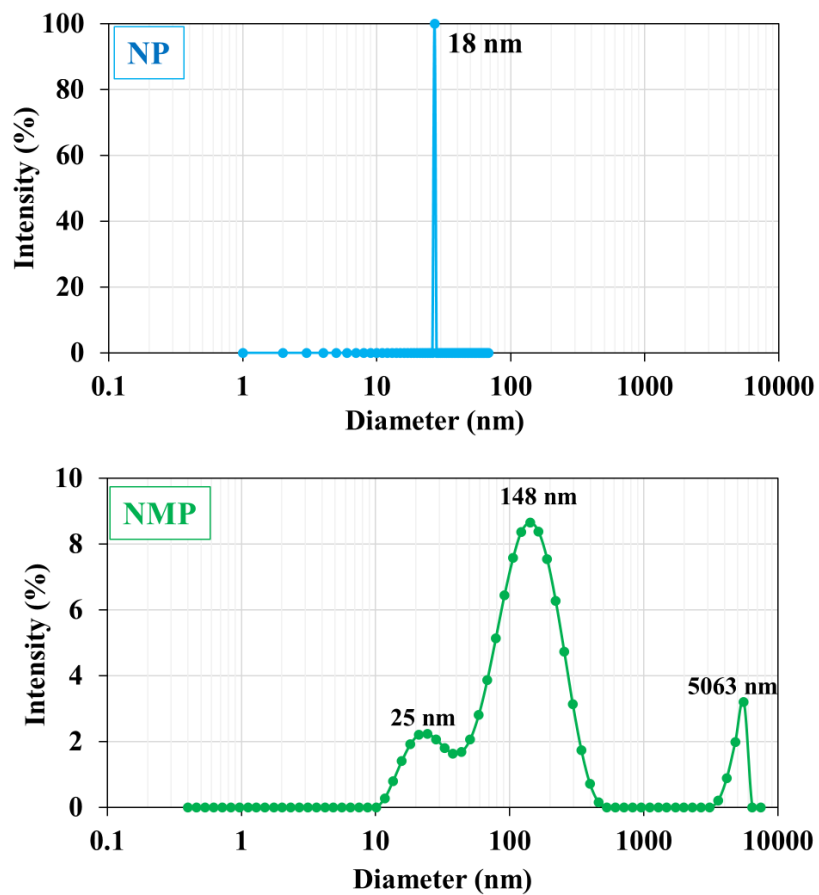
**Fig. 2-1 Paste size analysis methodology schematic view of dynamic light scattering (DLS) methodology.**





**Fig. 2-2 Tester photograph together with the sample photograph.**

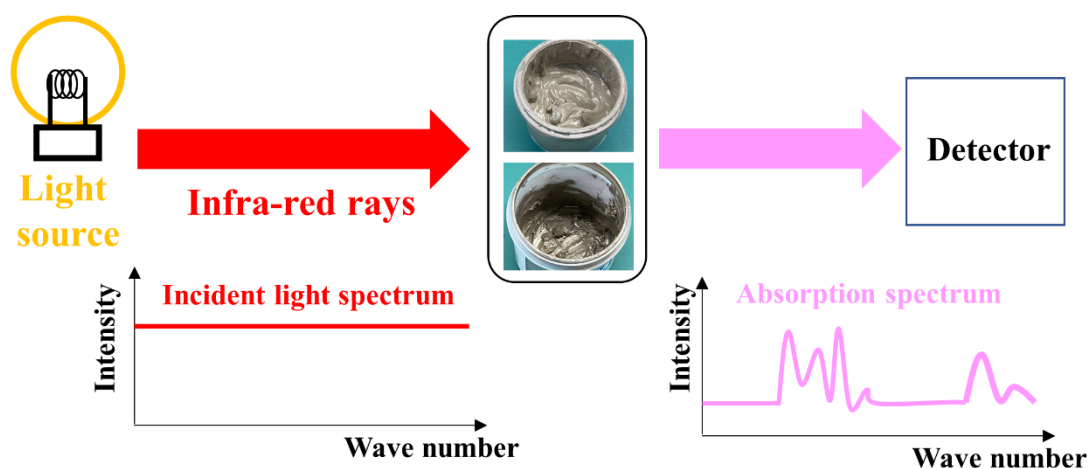
Fig. 2-3 shows the Ag particle size distributions of NP and NMP obtained from DLS measurements. For NP, only one sharp peak around 18nm in diameter is detected. By contrast, NMP has a broader peak than the peak of NP, and the peak value is detected at 25, 148, and 5063 nm in diameter.



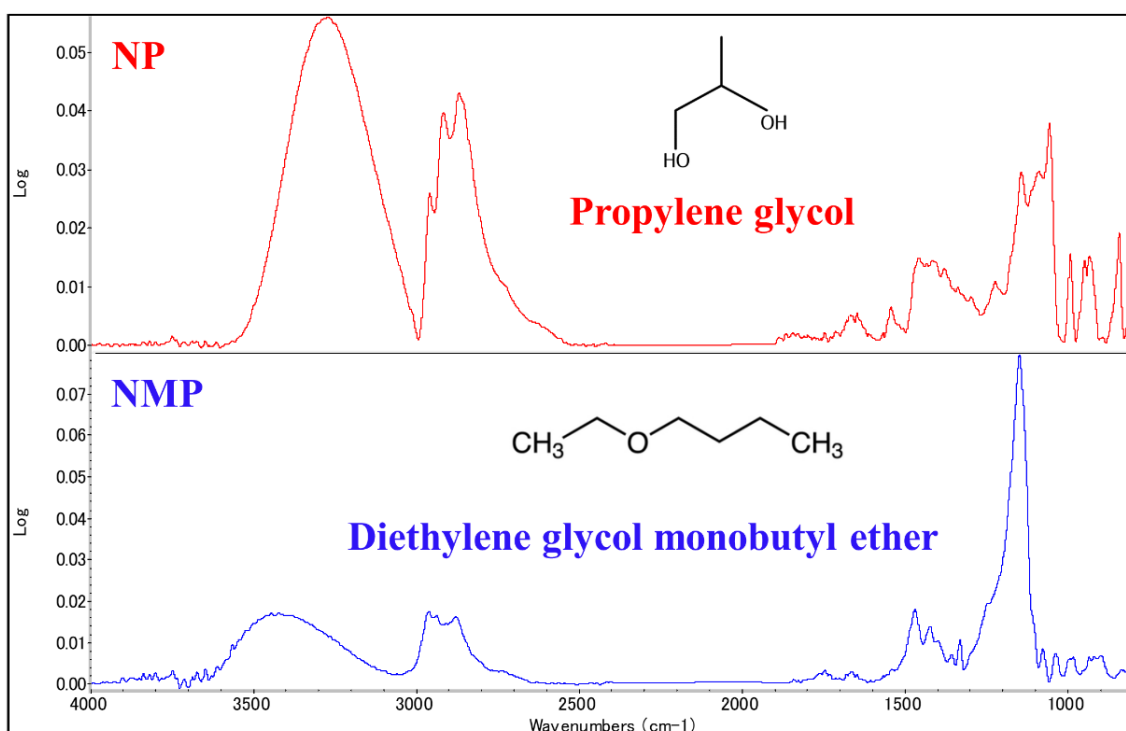
**Fig. 2-3 Ag particle diameter distributions of NP and NMP.**

#### 2-1-4. Organic component

FT-IR measurements were employed for exposing the chemical component in the Ag paste of NP and NMP. Fig. 2-4 shows the schematic overview of FT-IR. Infrared spectroscopy is a spectroscopic technique that can be utilized by light with the infrared region from 0.8 to 1000  $\mu\text{m}$ . Since molecular vibration occurs within a mid-infrared region from 2.5 to 25  $\mu\text{m}$ , which is commonly adopted that molecular vibration accompanies dipole momentum variations. When infrared rays irradiate a molecule, the individual atoms or atomic clusters absorb energy according to their respective periods. Consequently, their absorption appears in the spectrum after infrared rays. Since atoms have their vibrations depending on their molecule structure, the absorption spectra analysis can clarify the chemical molecule structure in the Ag paste. NP and NMP pastes were analyzed by an FT-IR tester (Thermo Fisher SCIENTIFIC, Nicolet™ iNTM 10). FT-IR spectrum results of NP and NMP paste are obtained as shown in Fig. 2-5. Library data in organic material fitted the obtained spectrum. As a result, NP organic solvent component was assigned as the butyl ether alcohol ( $\text{C}_3\text{H}_8\text{O}_2$ ; Boiling point of 188.2°C). In general, butyl ether alcohol showed high productivity due to the polyol reductive chemical reduction way [8, 9]. NMP organic solvent was assigned as the diethylene glycol mono butyl ether ( $\text{C}_8\text{H}_{18}\text{O}_3$ ; Boiling point of 230°C). Monobutyl ether, used in NMP, is characterized as a high solvent property due to the existence of an ether group.

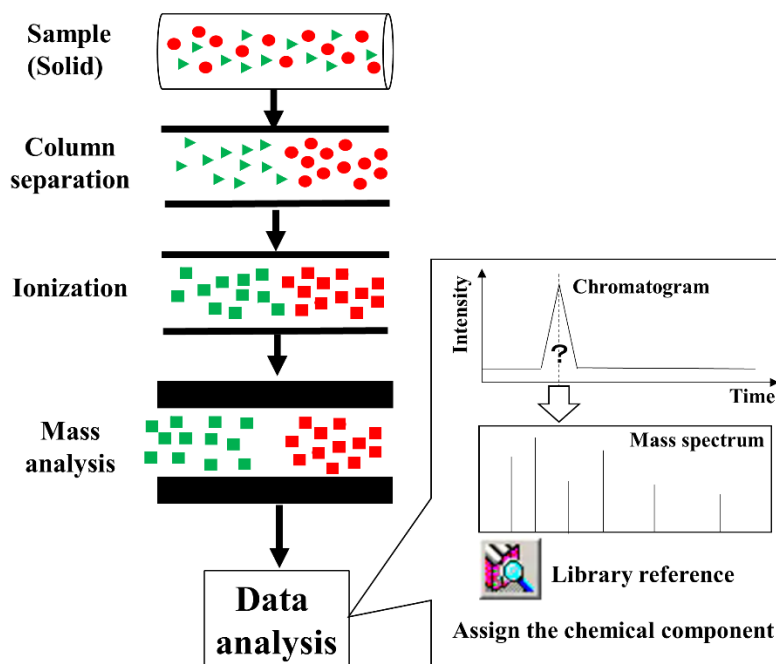


**Fig. 2-4 Chemical analysis overview of Fourier transform infrared spectroscopy (FT-IR).**



**Fig. 2-5 FT-IR spectrum results of NP and NMP.**

GC/MS analysis was employed to clarify the organic protective component with the dry state and sintering state of NP and NMP (Shimazu, GC/MS-QP2020NX). A schematic overview is depicted in Fig. 2-6. Gas chromatography (GC) is classified for separating organic components by utilizing the difference in absorption or distribution coefficient of gas to the stationary phase. Then, separated organic components are utilized by the mass spectrometer. Mass spectrometer composes ionization and mass separation section. In the ionization part, the ionizer charges the molecule to be in a gaseous state. For mass separation, ions can be separated in a vacuum vessel by electric and magnetic fields. Since ions have an electric charge, they are moved by the electric and magnetic fields in the vacuum. Their mass-to-charge ratio determines the motion. Separated ions are detected by electron multipliers, which are converted into visual signals. Mass spectroscopy is analyzed with library data to assign the chemical component. GC/MS characterizes the quantification of organic components with high sensitivity, which can be expected to detect the signal originating from the organic protective covered with the Ag particle.



**Fig. 2-6 Gas chromatography-mass spectrometry (GC/MS) schematic view.**

Fig. 2-7 shows the GC/MS mass spectrum results of NP and NMP after the dry and sinter process, together with the mass spectrum that can be assigned with library reference data. For NP after the dry process, fatty acid components ( $C_{13}H_{26}O_2$ ,  $C_{14}H_{28}O_2$ ,  $C_{15}H_{30}O_2$ ) and amid components ( $C_{19}H_{37}NO$ ,  $C_{14}H_{28}O_2$ ) are detected. NP included a high molecule organic protective. For NP, after the sintering process, amid components completely disappeared. However, fatty acid components are retained. The protective binding force in NP was high to prevent nano Ag self-sintering originating from its high surface energy. Note that the Ag particle of NP contained only nano-size with narrow distributions, which would make narrow pathways of organic binder escape outside during the pressure-assist sintering process. Consequently, the organic binder remained after the sintering of NP. For NMP, after the dry process, amid component ( $C_6H_{12}O_4$ ) is detected. The molecular weight is smaller than the molecule weight in NP. For NMP, after the sintering process, the amid component peak disappears. NMP of surface energy is lower than the surface energy of NP because NMP consists of micro-sized Ag particles. In addition, the binder escape pathway became significant due to the geometric characterization originating from the wide Ag particle size distribution of NMP. Therefore, organic protection would be disappeared with ease after the sintering of NMP. The paste analysis results summary is summarized in Table 2-3.

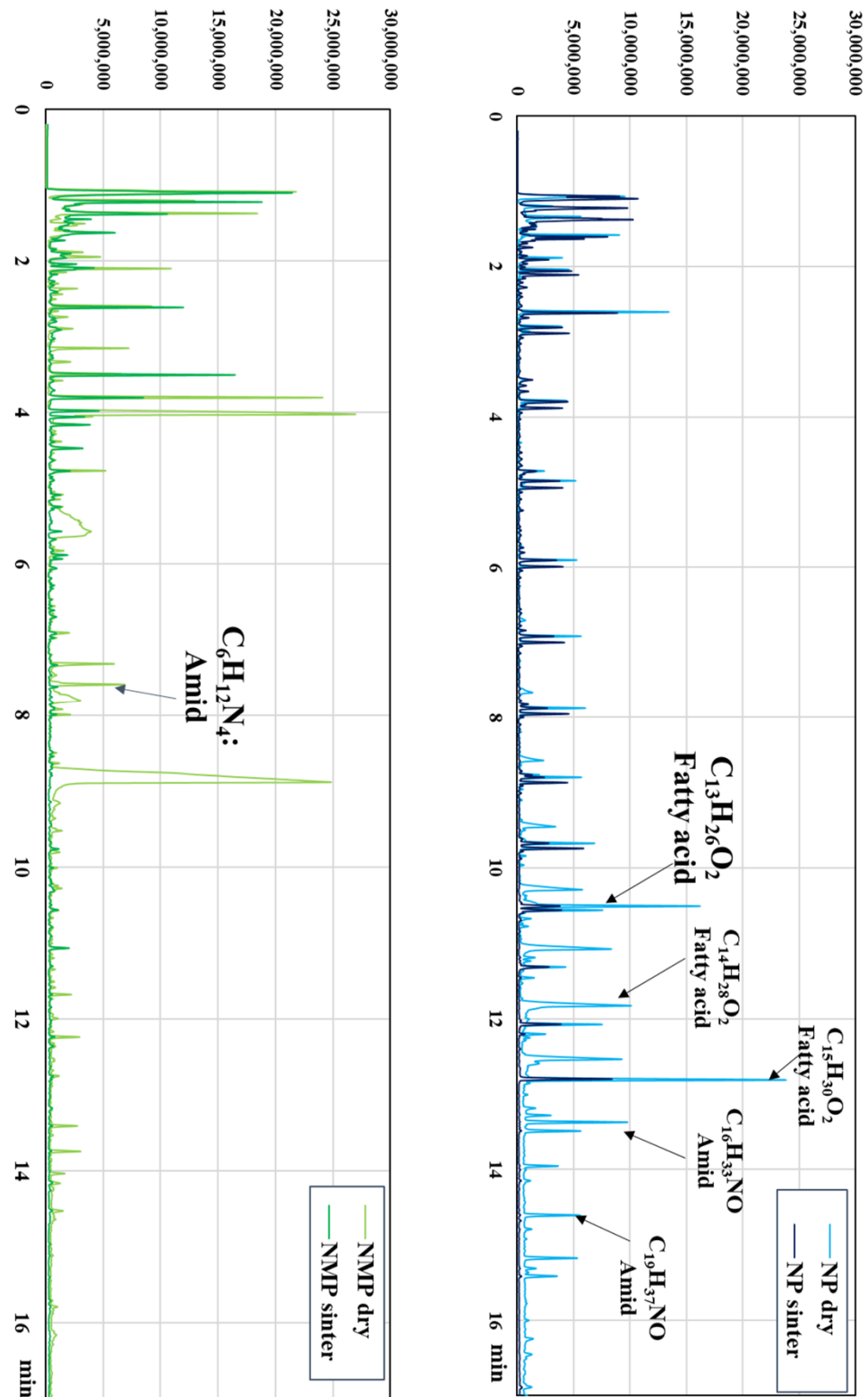
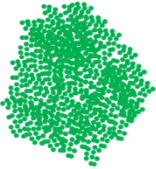
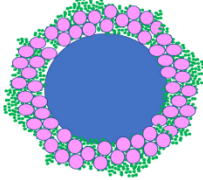
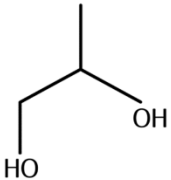

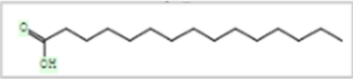
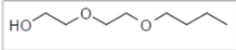
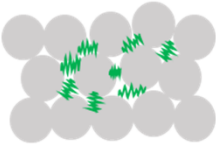



Fig. 2-7 GC/MS spectrum results of NP and NMP after dry and sintering state together with mass spectrum assignment results.

Table 2-3 Paste analysis results summary.

		NP	NMP
Physical property	Diameter	<p>20 nm</p> 	<p>25, 148, and 5063 nm</p> 
	Paste	<p>Propylene glycol</p> 	<p>Diethylene glycol monobutyl ether</p> 
Chemical property	Dry film	<p><math>C_{16}H_{33}NO</math> (Amid) <math>C_{15}H_{30}O_2</math> (Fatty)</p>  <p>High molecules</p>	<p><math>C_6H_{12}N_4</math> (Amid)</p>  <p>Small molecules</p>
	Sintered film	 <p>Green chain: Organic component</p> <p>Residual organic components</p>	 <p>No organic components</p>

## 2-2. Tensile test methodology

### 2-2-1. Specimen fabrication methodology

**Table 2-4 Tensile tests condition overview.**

No.	Specimen	Scope	Aim
1	100 × 500 μm (10 μm thick)	Pore dependences	Favorable sintering condition
2		Temperature dependences	
3	2 × 2 mm (60 μm thick)	Paste dependences	Favorable paste

To understand the s-Ag tensile mechanical properties, three patterns of tensile tests were examined as listed in Table 2-4. As for tests No. 1 and No.2, specimen size was adopted as 100 μm × 500 μm with ten μm in thickness. Test No.1 and No.2 results clarified the favorable sintering process condition for the s-Ag film. Then, the tensile test specimen size was enlarged to 2 mm square with 60 μm thickness, which accorded with the actual die layer delamination size. Ag pastes were sintered under the favorable sintering condition determined by test No.1 to examine the paste type differences in tensile mechanical properties.

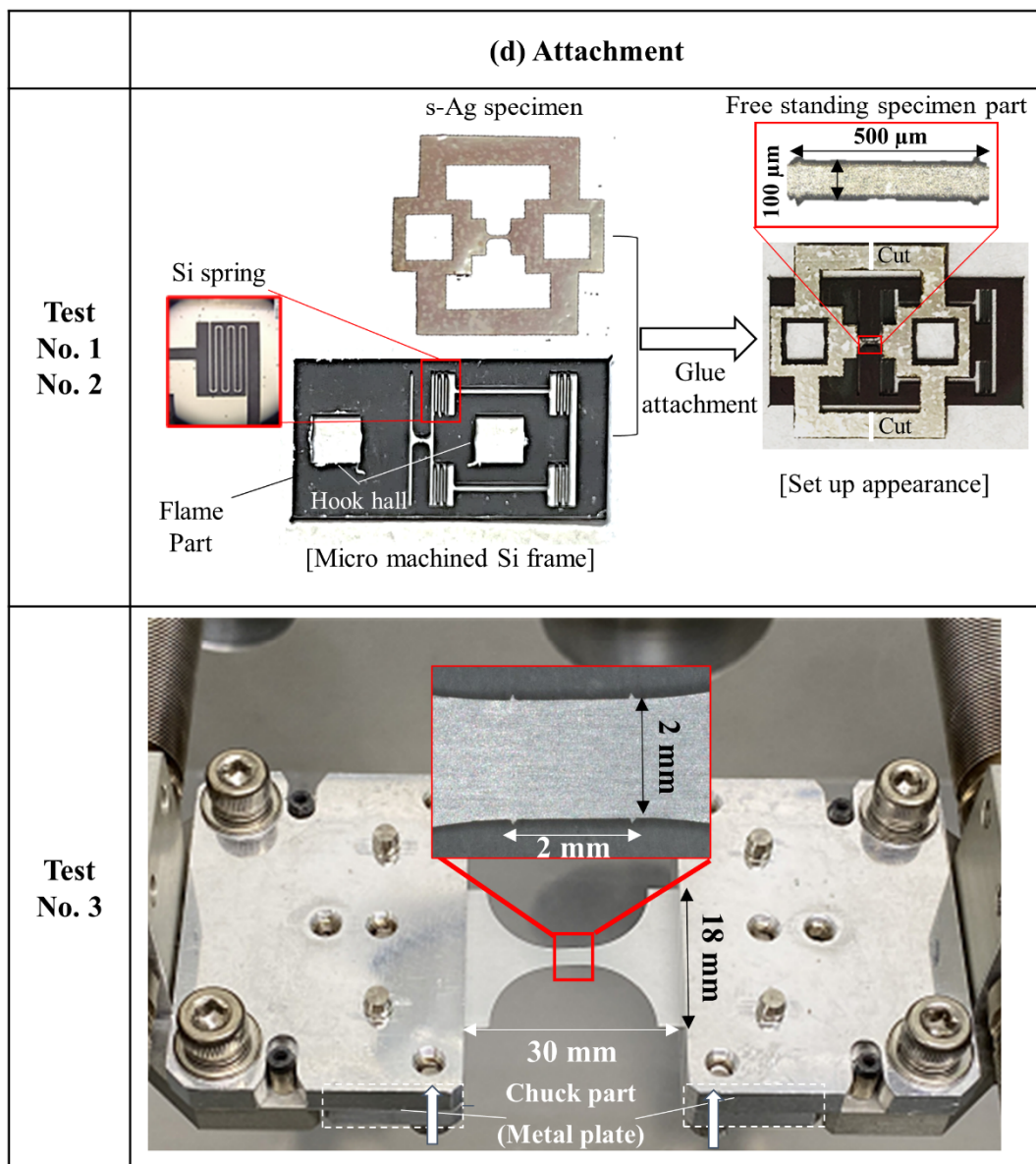
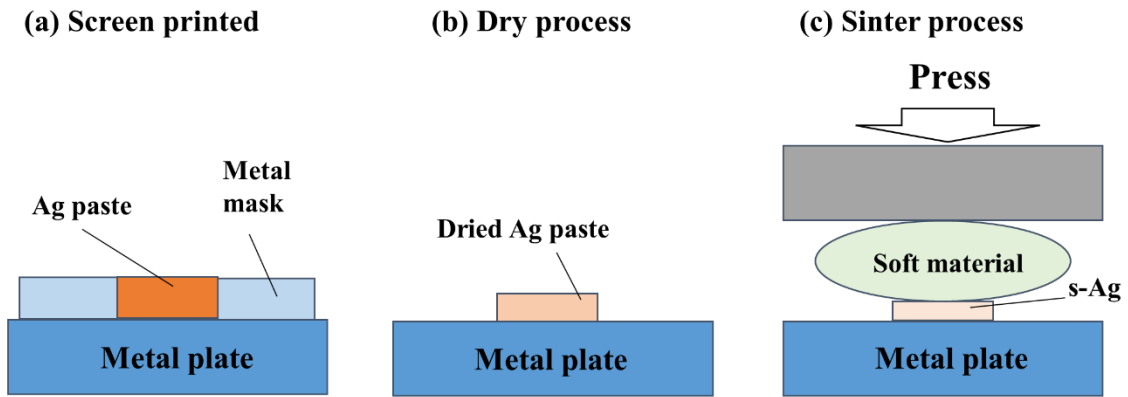


Fig. 2-8 Specimen preparation process for tensile testing.



The fabrication flow for making the s-Ag specimen is illustrated in Fig. 2-8. First, a paste was stencil printed on a metal plate, as shown in Fig. 2-8 (a). This study used a 70 mm square stainless-steel plate with 0.7mm in thickness as a metal plate. Then, the organic solvent was evaporated in the heating chamber according to the condition in Table 2-1. Finally, the dried Ag paste was sintered by temperature elevation under the specific pressure with vertical direction via a buffer sheet to get a uniform pressure distribution on the s-Ag die area, as shown in Fig. 2-8 (c). The buffer sheet was used as a carbon sheet (TOYO TANSO Japan, VVF30). The buffer sheet size was 10 mm square with 0.5 mm in thickness. s-Ag film was detached from the metal substrate as a self-standing film after sintering. The s-Ag film was formed by an ultraviolet laser marker (KEYENCE Japan, 3-Axis UV Laser Marker MD-U1000) to fit the tensile test system used in this study, as shown in Fig. 2-8 (d). Two types of original testers were employed. As for No.1 and 2, the specimen consists of two parts, a freestanding s-Ag thin film, and a micromachined Si frame. The s-Ag film specimen comprises a dog-bone shape section, two hooking holes, and two bridges supporting the center section. The dog-bone section is divided into a parallel portion and a curvature portion. At the boundary between the two portions, a semicircle-shaped gauge mark having a radius of 5  $\mu\text{m}$  was made. The length and width of the parallel part were 500  $\mu\text{m}$  and 100  $\mu\text{m}$ , respectively. The Si frame micromachined by deep reactive ion etching comprises a specimen stage section, two hooking holes, four springs, and a frame. The four springs support the one-side sample stage only, which is able to move along the tensile direction. To precisely stretch a film specimen in the tensile direction only, each Si spring measuring 100  $\mu\text{m}$  in width and 300  $\mu\text{m}$  in thickness was designed to be a leaf spring suspension configuration whose spring constant value in the tensile direction is much smaller than that in the transversal direction. The tensile test of a freestanding film can be prepared by combining the two parts by glue attachment, as shown in Fig. 2-8 (d). Just before the test, the support portion of the test specimen is cut. As for the millimeter scale specimen, the specimen was mechanically chucked by a flat plate at both specimen sides and fastened from the backside via screw as shown in the bottom side of Fig. 2-8 (d) depicted as two white arrows.

2-2-2. Uniaxial tensile tester

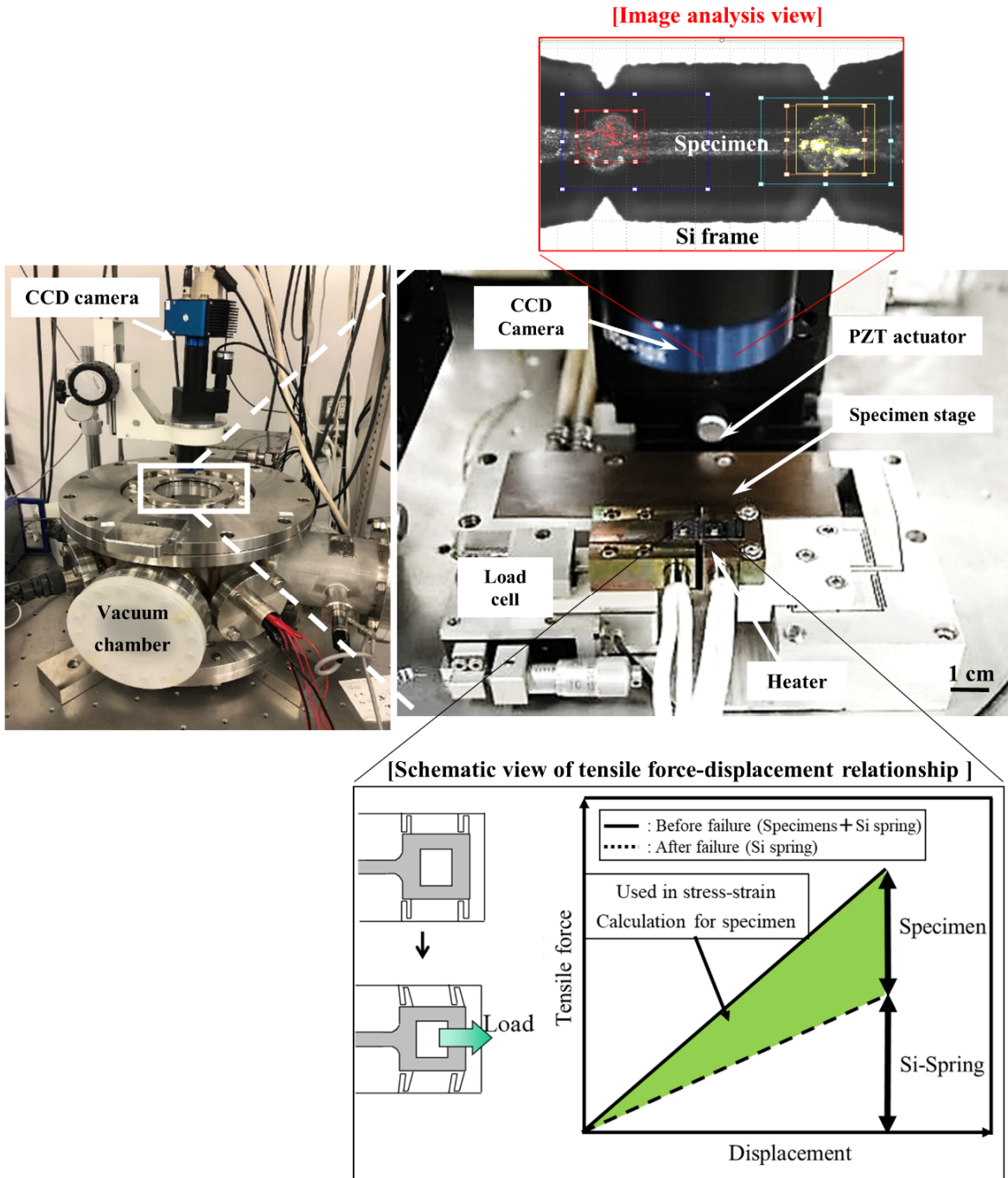
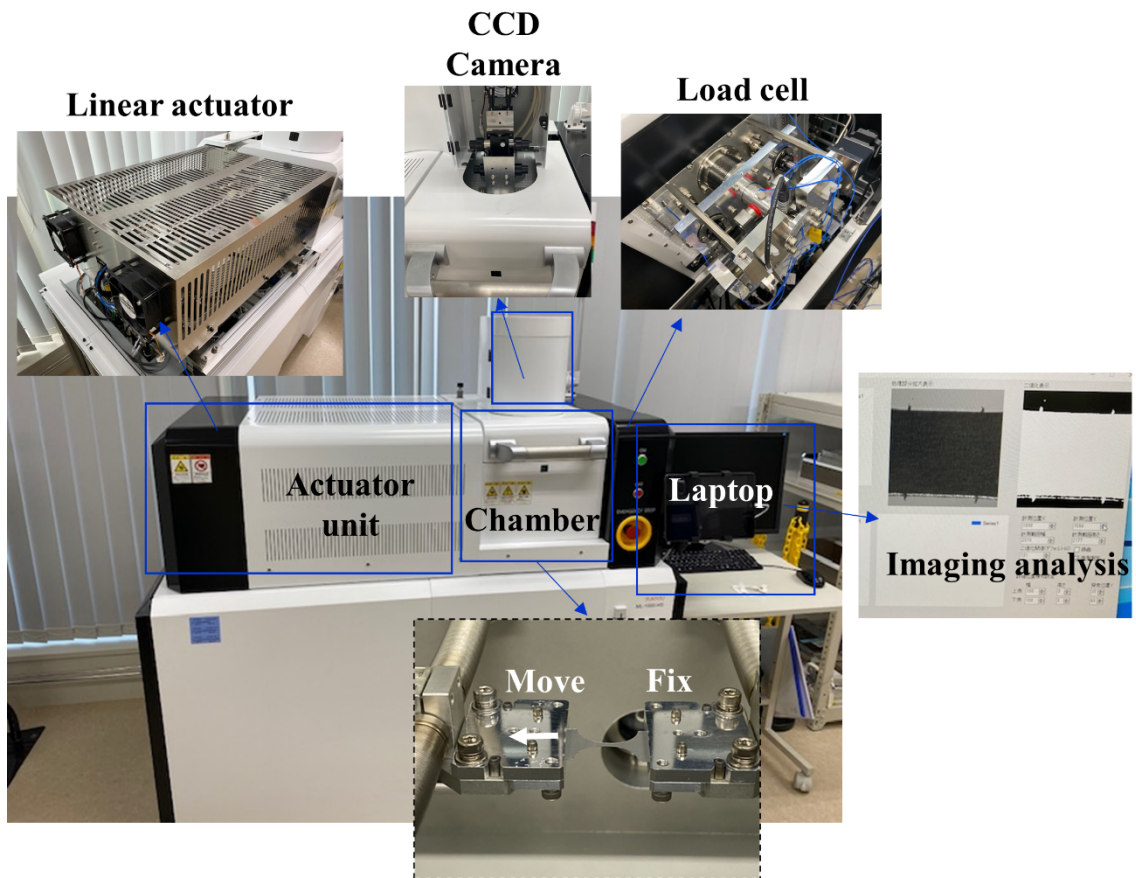


Fig. 2-9 Original tensile tester system with the micron-scale specimen in tests No. 1 and 2. (Left side: Overall photograph and right side: Magnified tester of measurement part.)

The tensile tester used for tests No.1 and 2 is shown in Fig. 2-9. The tensile tester was initially designed to obtain thin films of mechanical properties [10]. The tester consists of the piezoelectric actuator (PI Japan, P-843.40V) for applying tensile force, the load cell ( $0-2\text{ N}\pm 0.339\text{ mN}$ ) (Tech Gihan, DGRV10-2N) for tensile force measurement, the micro heater (Hakko Electric Machine Works Co. Ltd., HLK1151) for temperature control, and CCD camera is utilized for specimen elongation measurement. The system memorizes a semicircular gauge mark on a film specimen, and then the position of the two gauge marks on the tensile axis is measured during the tensile test, as is shown in the top right photograph in Fig. 2-9. The distance between the two marks and the displacement at the time is obtained from the difference in coordinates between the two marks. The optical resolution of the system is calculated to be around 100 nm/pixel. By using a subpixel algorithm, the resolution can take a small value of approximately 15 nm/pixel. The actuator can apply a tensile load to the thin film through a lever-like displacement expanding mechanism (amplification factor of 3~7). When a tensile force is applied to the specimen, both the film and four springs deform. Consequently, a force value measured using a load cell is the sum of applied force to both two elements. To measure the applied force to the specimen, a tensile test was performed twice to obtain the specimen's force-displacement relation, as shown in the right bottom schematic image of the force-displacement relation during tensile testing in Fig. 2-9. The measured force value includes a force applied to a film and Si springs. After the film rupture, the same program runs to measure a force applied to Si springs only. Lastly, the force applied to the film is only obtained by subtracting the second signal from the first. To employ the combination of a thin film and Si substrate, a thin film can be easily handled until just before the test, which is one of the advantages of this method presented.

Fig. 2-10 shows photographs of the tensile testing system (SUNYOU, ML1000-HS) for test No.3. This system comprises a linear actuator, CCD camera, load cell, laptop computer installed imaging software, and temperature controller. The fabricated specimen is mechanically chucked, as depicted in the photograph of the test chamber unit. The attached specimen is moved according to the white arrow line during the tensile test, as depicted in Fig. 2-10 by the linear actuator motion. The motion is controlled by the external software installed on the laptop. The load cell (0-500 N $\pm$ 62.5 mN) measures the applied force to the specimen during tests. Specimen elongation is directly captured by the CCD camera, where placed above the specimen to take an image analysis by the imaging software. The image resolution is 0.5  $\mu$ m/pixel. The test chamber atmosphere can be replaced by nitrogen to prevent the oxidation of the specimen. The atmosphere temperature in the test chamber can be controlled from -5 to 175°C. For thermal saturation, the tensile testing was performed after 120 min when the chamber atmosphere reached the target temperature.



**Fig. 2-10 Original tensile tester system with the millimeter-scale specimen in test No. 3.**

## 2-3. Pressure dependences on tensile mechanical property of s-Ag film

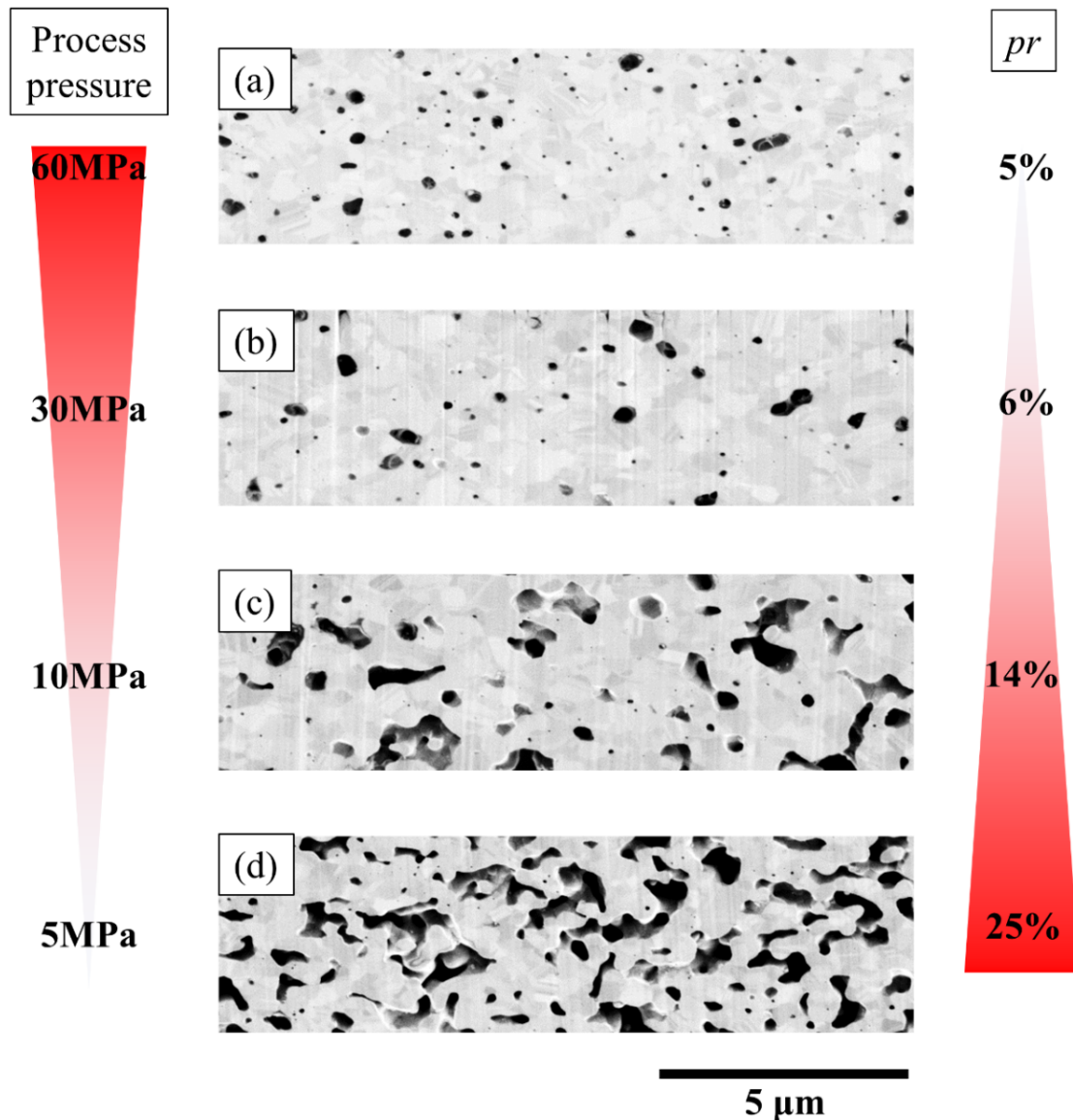
**Table 2-5 Test No.1 condition.**

<b>Sample</b>	<b>Material</b>	<b>Sintering process</b>
<b>(a)</b>	<b>NP s-Ag</b>	<b>300 °C 10 min 60MPa</b>
<b>(b)</b>		<b>300 °C 10 min 30MPa</b>
<b>(c)</b>		<b>300 °C 10 min 10MPa</b>
<b>(d)</b>		<b>300 °C 10 min 5 MPa</b>
<b>(e)</b>	<b>Bulk Ag</b>	<b>-</b>

This section describes test No.1 results for seeking the appropriate sintering process pressure with a suitable tensile mechanical property of the s-Ag film. The test condition is listed in Table 2-5. The NP was sintered by four levels of process pressure with 5, 10, 30, and 60 MPa at 300°C for 10 min. To quantify each porous structure of s-Ag specimen,  $pr$  was defined as the ratio of the pore area to the observation area. The pore area was determined by the binarization image analysis results of each layer. A bulk Ag specimen was also prepared as a reference material to discuss the influence of pores on the s-Ag specimen of the mechanical characteristic. The bulk Ag sheet's purity and mean grain size are 99.99% and 0.8  $\mu\text{m}$ , respectively. The tensile tests were performed under room temperature (RT) at the strain speed of  $10^{-4}$  /sec, equal to the strain speed with the thermal shock test in the Lv324 standard [11].

### 2-3-1. Microstructure

The focused ion beam (FIB) technique (Hitachi High-Technology, SMI3050) was utilized to expose the cross-section of the s-Ag specimens. The FIB acceleration voltage and beam current were 30 kV and 2400 pA, respectively. A scanning electron microscopy (SEM) tester (Hitachi High-Technology, S-4800) was used to confirm the s-Ag microstructure. The electron acceleration voltage of 1.5 kV and a magnification rate of 5000 times were used in this observation.



**Fig. 2-11 Cross-section SEM images with varying process pressure of (a) 60 MPa, (b) 30 MPa, (c) 10 MPa, and (d) 5 MPa [12].**

Fig. 2-11 shows the cross-section SEM images of s-Ag films with varying process pressure from 5 to 60 MPa. The observation window was set to  $4\ \mu\text{m} \times 20\ \mu\text{m}$ . The pores in specimens 10 MPa and 5 MPa pressure are not round and have a peanut-shell form, whereas the pores in samples 60 MPa and 30 MPa pressure are close to the sphere figure, showing a discrete distribution. The  $pr$  is controlled according to the applied pressure value, which ranges from 25 to 5%, with increased pressure from 5 to 60 MPa.

### 2-3-2. Stress-strain curve

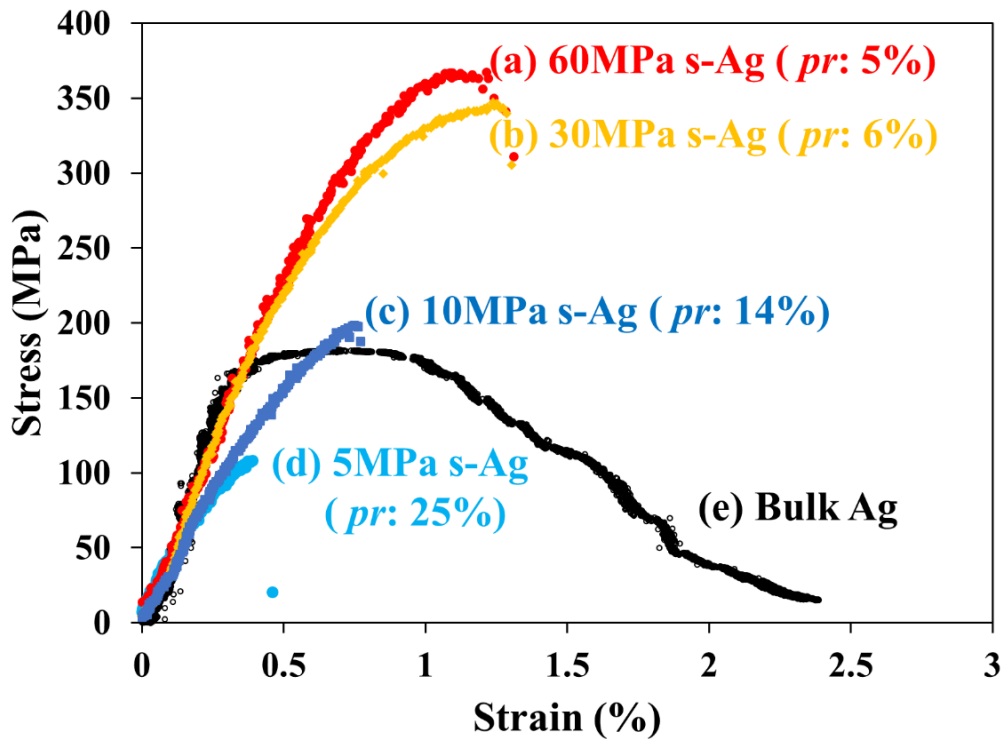


Fig. 2-12 *S-S* curves for each material [12]. (Red: 60 MPa s-Ag. Orange: 30 MPa s-Ag. Dark blue: 10 MPa s-Ag. Light blue: 5 MPa s-Ag. Black: Bulk Ag.)

Fig. 2-12 shows the measured stress-strain (*S-S*) curves of 60, 30, 10, and 5 MPa with s-Ag and bulk Ag. Color differences are indicative of material differences. The *S-S* curve of bulk Ag typifies the mechanical property of a metal, exhibiting a clear yielding point (around 150 MPa), and shows a plateau region before the necking region. On the other hand, *S-S* curves of s-Ag exhibit no yielding point and plateau region regardless of process pressure. Tensile strength increased with increasing pressure. The value reaches 330 MPa for 30 MPa s-Ag and 370 MPa for 60 MPa s-Ag. These values correspond to about twice that of bulk Ag. A little sublinear region is found in the *S-S* curves of high-pressed s-Ag specimens with 30 and 60 MPa. The fracture strain remains at about 1.2% even in the 60 MPa s-Ag specimen, which indicates that the s-Ag is a "High strength but brittle" characteristic even under the high press condition. The tensile strength of 10 MPa s-Ag is almost identical to that of bulk Ag. The tensile strength of 5 MPa s-Ag shows about 110 MPa, about 65% of that of bulk Ag.

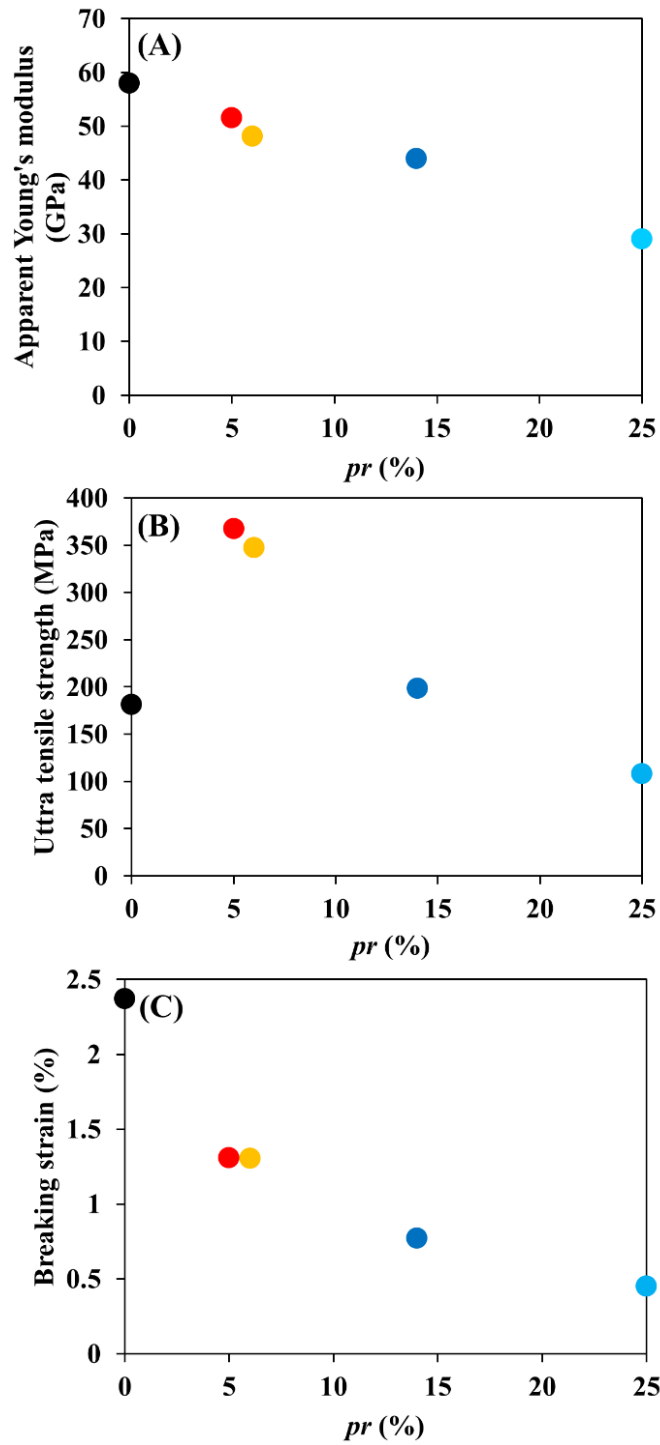


Fig. 2-13 (A) Apparent Young's modulus (B) Ultimate tensile strength and (C) Breaking strain as a function of  $pr$ . The red, orange, dark-blue, and pale-blue dots denote the data for s-Ag specimens of (a), (b), (c) and (d), respectively. The black dot denotes the data for bulk Ag specimen of (e) [12].

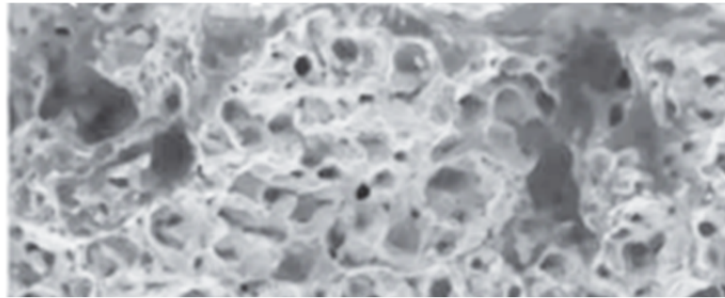


Apparent Young's modulus ( $E$ ), breaking strain ( $BS$ ), and ultimate tensile strength ( $UTS$ ) were extracted from the obtained  $S$ - $S$  curves as a function of  $pr$  as depicted in Fig. 2-13. The plot color differences are identical to those of Fig. 2-12. Note that the data of bulk Ag is plotted at  $p = 0\%$  in the graphs. For  $E$ , as shown in Fig. 2-13 (A), bulk Ag exhibits around 60 GPa. Then, the  $E$  value negatively correlates with  $pr$  at the decreasing rate of approximately  $1\text{GPa}/pr (\%)$  in all plots. This tendency indicates that increasing  $pr$  deformed with ease against applied tensile stress. For  $UTS$ , the value also negatively correlates with  $pr$ , as shown in Fig. 2-13 (B), except for the bulk Ag specimen. The decreasing rate of  $UTS$  against  $pr$  shows around  $10\text{MPa}/pr (\%)$  in s-Ag plots. For  $BS$ , as shown in Fig. 2-13 (C), the value negatively correlates with  $pr$  at the decreasing rate of approximately  $0.08\%/pr (\%)$  in all plots. Augmented ultimate tensile strength and smaller breaking strain occur at  $p = 6\sim 14\%$ . These results prove that over 30 MPa pressure of s-Ag is desirable for reducing  $pr$  and improving mechanical stress durability.

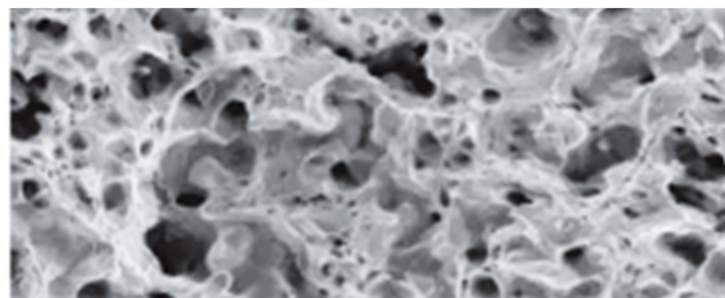
### 2-3-3. Fractography

Fig. 2-14 shows a representative SEM fractography after tensile tests of s-Ag specimens. High-pressure s-Ag specimens show several dimple-like protrusions, such as whiskers, as is seen in Fig. 2-14 (a) and (b). This morphology can be explained by the fact that the high-pressure samples of 30 MPa and 60 MPa showed a nonlinear behavior of about 0.2~0.3% just before the fracture. On the contrary, low-pressure s-Ag specimens show particle aggregation, as is seen in Fig. 2-14 (c) and (d). This tendency indicates that the nano-Ag particles were sintered by contacting each other only at the local part of the surface under low pressure, as indicated by white arrows. That agrees with the tensile test result, broken under the low mechanical force load. Sintering under the condition of a high-pressure atmosphere in the possible range was indispensable to making the s-Ag film with the excellent mechanical property. In this study, s-Ag is decided to fabricate under  $300^\circ\text{C}$  for ten minutes at 60 MPa. A 60 MPa pressure is higher than practically used pressure values [13]. Such high pressure might provide unwanted brittle fracture with a die. Provided that the die fracture does not happen, a low porosity is obtained from the high-pressure process, which gives rise to produce stabilized s-Ag die attached assemblies. That is necessary for investigating the degradation mechanism under various thermal and mechanical conditions described later. Therefore, the author chose 60 MPa as a sintering pressure here.

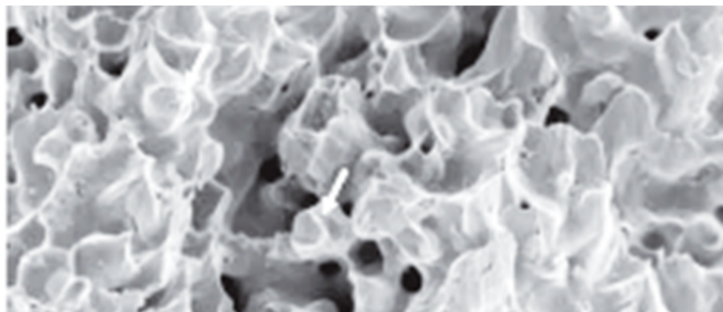
**(a) 60MPa (*pr*: 5%)**



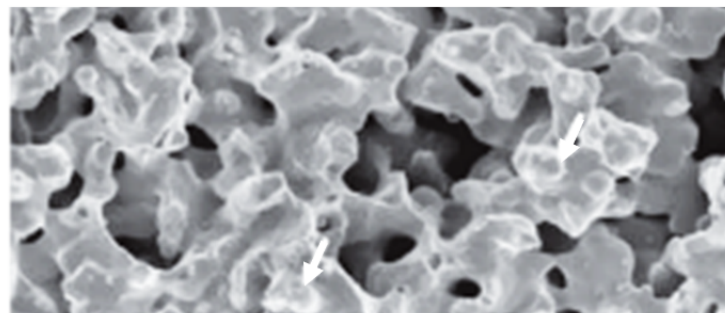
**(b) 30MPa (*pr*: 6%)**



**(c) 10MPa (*pr*: 14%)**



**(d) 5MPa (*pr*: 25%)**



**3  $\mu$ m**

**Fig. 2-14 SEM images of the fractured surface in s-Ag specimens after tensile tests with (a) 60 MPa, (b) 30 MPa, (c) 10MPa, and (d) 5 MPa [12].**

## 2-4. Temperature dependences on tensile mechanical properties of s-Ag film

**Table 2-6 Test No.2 condition.**

Material	Process	Temperature (°C)	Strain speed (s <sup>-1</sup> )
NP s-Ag	300 °C 10 min 60 MPa	RT, 60, 80, 120, and 150 °C	1 × 10 <sup>-4</sup>
Bulk Ag	-	RT, 60, and 120 °C	

As for the next step, temperature dependences on s-Ag mechanical characteristics were investigated to get fundamental data for designing the WBG power modules, as listed in Table 2-6. The specimen configuration, tester, and test motion conditions are identical to those used in sections 2-3. The test temperature varied from RT to 150°C. The NP was sintered under applied 60 MPa pressure with 300°C for 10 min. A bulk Ag specimen was also prepared to investigate the pore influences on the mechanical properties.

### 2-4-1. Stress-strain curve

Fig. 2-15 (a) shows representative *S-S* curves of s-Ag at a temperature ranging from RT to 150°C. Color differences are indicative of measurement temperature differences. The *S-S* curve of s-Ag at RT shows almost linear until failure, which indicates that the specimen fractured in a brittle manner during elastic deformation, as stated in section 2.3. With temperature elevation, a non-linear region can be found. At 60°C, *S-S* curves show a sublinear curve yielded around 200 MPa. Then, the sublinear region could be seen by a strain of a few% just before fracture, which is considered a plastic deformation region. At 80°C, the *S-S* curve characteristic shows almost the same tendency as the 60°C in that the curve showed a non-linear region before fracture. The yield stress of 80°C decreases compared to the yield stress at 60°C. At 120°C, the *S-S* curve shows a plateau region around 10% before fracture. That is, the specimen is wholly fractured in ductile. Dislocation slip motion accompanied by plastic deformation mainly occurred. At 150°C, the *S-S* curve also shows a plateau region around 5% before fracture. The *S-S* curves of s-Ag indicate that the apparent brittle-ductile transition of s-Ag existed at around 80-120°C.

Fig. 2-15 (b) shows the bulk Ag representative *S-S* curves for RT, 60°C, and 120°C. All the *S-S* curves

of bulk Ag indicate ductile behaviors that possessed necking region and large plastic region irrespective of the temperature ranging from RT to 120°C. The plateau region increases with increasing temperature. The tensile strength is almost constant irrespective of the RT to 120°C.

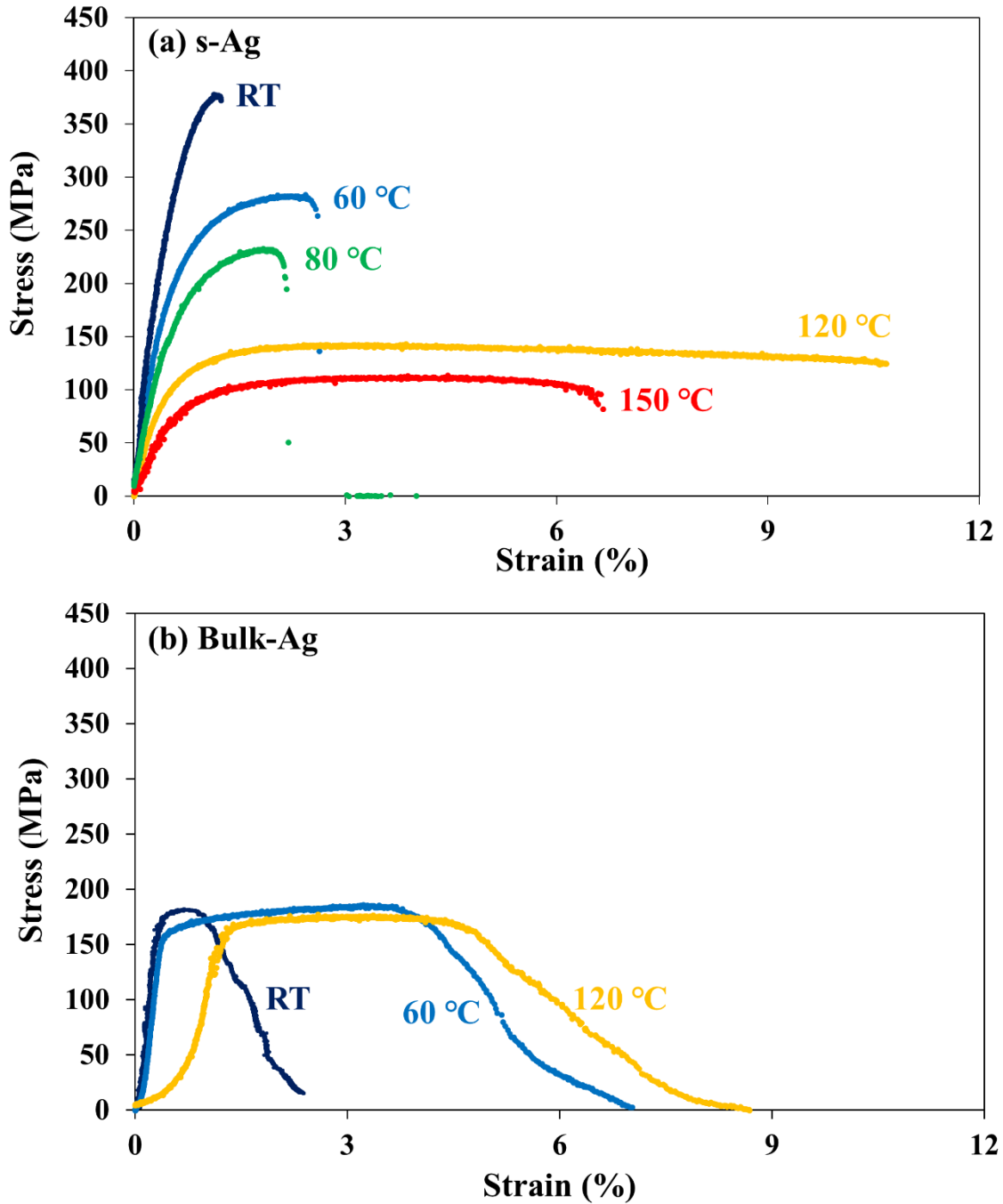


Fig. 2-15 S-S curves for each temperature with (a) s-Ag and (b) bulk Ag [14].

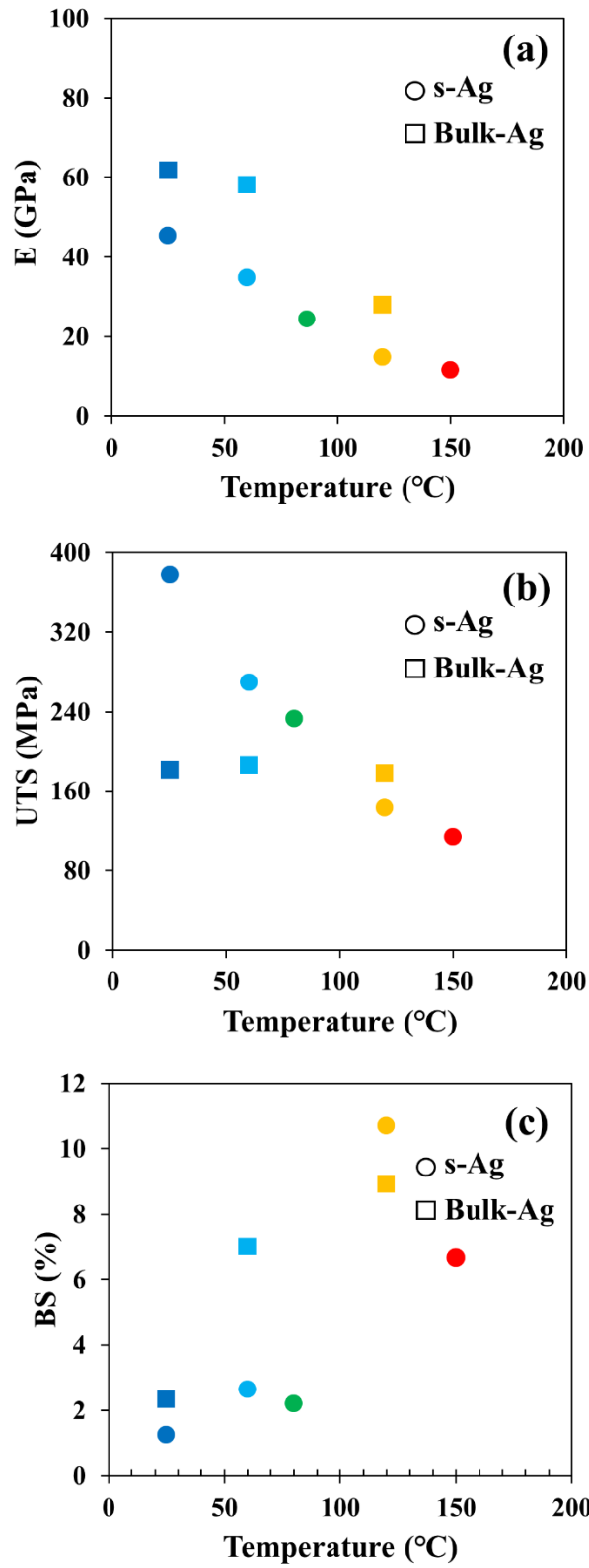
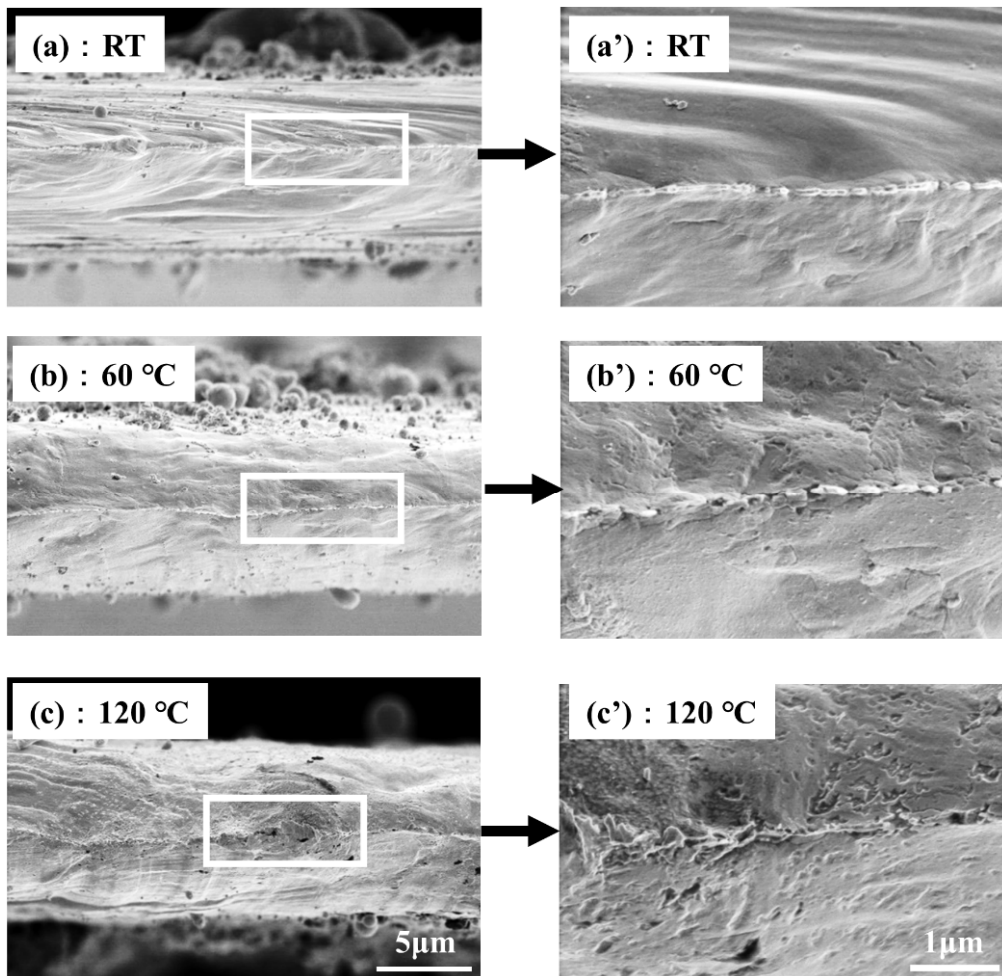


Fig. 2-16 (a) E, (b) UTS, and (c) BS as a function of temperature [14].

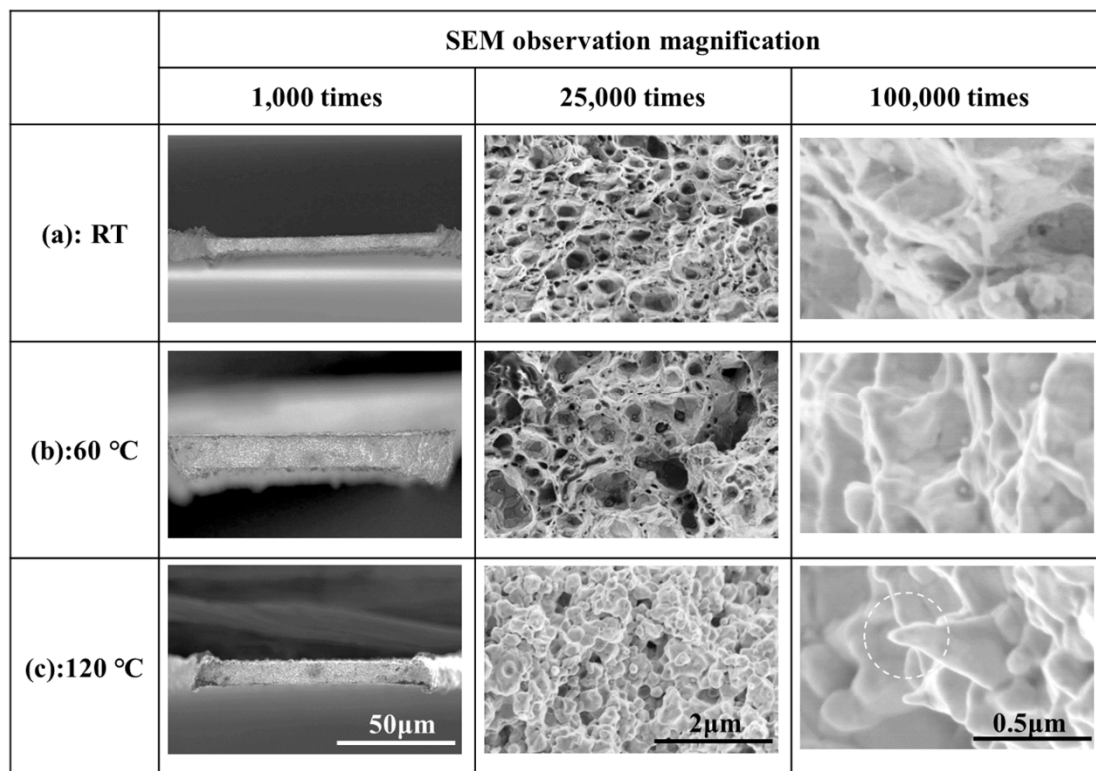
Fig. 2-16 depicts the obtained mechanical properties ((a) E, (b) UTS, and (c) BS) as a function of temperature. The circle plots are indicative of s-Ag, and the square plots are indicative of bulk Ag. Color differences indicate measurement temperature, which is the same as the definition in Fig. 2-15. The E of s-Ag and bulk-Ag negatively correlates with temperature. The mean value of s-Ag at RT shows about 45 GPa, 27% lower than the bulk Ag value. Regarding the temperature dependences on the E, the decreasing rate of E against temperature for s-Ag is similar to that for bulk Ag. The s-Ag UTS value at RT was 370 MPa, which is approximately 2.3 times higher than the bulk Ag value. The average grain size of bulk Ag and s-Ag is 0.8  $\mu\text{m}$  and 0.1  $\mu\text{m}$ , respectively. It has been known that grain size difference influenced the mechanical characteristics of Ag film based on the Hall-Petch law [15, 16]. The results were reasonable in that the UTS of s-Ag was higher than that of bulk Ag because the s-Ag crystal size was smaller than the bulk silver's crystal size. The s-Ag UTS value rapidly and linearly decreases with increasing temperature. On the other hand, that of bulk-Ag slightly decreases with increasing temperature. The temperature dependence on UTS for bulk-Ag is similar to the previous study [17]. The UTS value of s-Ag and bulk Ag overlap at around 120°C. The temperature dependency on BS for s-Ag shows a trend similar to that for bulk Ag in that the BS value positively correlates with increasing the temperature. BS value of s-Ag rises drastically when the temperature increases from 80 to 120°C compared to the bulk Ag results.

## 2-4-2. Fractography



**Fig. 2-17 (a–c) Representative SEM images of bulk Ag fracture surface after tensile tests at RT, 60°C, and 120°C. (a'–c') Enlarged SEM images of each area denoted by white square shown in (a–c) [14].**

Fig. 2-17 (a–c) shows representative SEM images of the fracture surface for bulk Ag and with the magnified images of (a'–c') after the tensile tests at RT, 60°C, and 120°C, respectively. The fracture surface at RT has a prominent protrusion at the middle of the specimen, which indicates that the specimen fractured ductile after necking deformation during tensile loading. Irrespective of temperature elevation, the entire fracture surface morphology is unchanged, although the number of small concave points on the surface increases with temperature elevation. All the bulk Ag specimens fractured plastically within the evaluated temperature range.



**Fig. 2-18 Representative SEM images of the s-Ag fracture surface together with the magnified images after tensile tests at (a) RT, (b) 60°C, and (c) 120°C [14].**

On the other hand, s-Ag specimens show a different trend in fracture with bulk Ag specimens, as shown in Fig. 2-18 (a–c), indicating the representative fracture surfaces after the tests at RT, 60°C, and 120°C. At RT, the fracture surface shows many concaves, and dimples are appeared by locally ductile deformation that can be seen on the fractured surface. Even with increasing temperature to 60°C, no remarkable change is found. The fractured surface at 120°C completely differed from those at RT and 60°C. A convex-concave pattern, like an aggregation of grains, can be found in the front view of the fractured surface. However, in the magnified image of the side view, the fractured surface consists of many sharpened protrusions facing the tensile direction, as depicted in a dashed circle in the right bottom image in Fig. 2-18. The s-Ag specimen contains many Ag nanoparticles, having a higher surface area-to-volume ratio, which provides high surface energy, leading to high binding energy between s-Ag grains. Therefore, only very local plastic deformation inside grains would have happened at low temperatures because of the strengthened grain boundary. A small dimple pattern for each grain would have been produced on the whole fractured surface. Consequently, strengthened specimens would have shown a brittle-like fracture.



By contrast, at high temperatures, since the flow ability of each Ag grain increased, an enormous plastic strain would have been obtained. These facts suggested that s-Ag was deformable in plasticity at high temperatures, like soft metal mechanical property. When operating at a high temperature with WBG devices, the s-Ag die can be deformed by increasing the plastic deformation before cracking, which means that the fracture does not suddenly occur in a brittle manner. That is, the reliability design can be expected to construct based on the fracture in ductile.

## 2-5. NP and NMP tensile mechanical properties of s-Ag film

**Table 2-7 Test No.3 condition.**

Material	Process	Temperature (°C)	Strain speed (s <sup>-1</sup> )
NP s-Ag	300 °C 10 min 60 MPa	RT, 100, and 150 °C	2.5 × 10 <sup>-4</sup>
NMP s-Ag			

Two representative types of commercial paste (NP and NMP) s-Ag at 300°C for 10 min under 60 MPa pressure were employed to investigate the relation between paste trait and these tensile mechanical properties. The experimental condition of test No. 3 is listed in Table 2-7.

### 2-5-1. Microstructure

Fig. 2-19 shows cross-section SEM images of backscattered electron detection with NP and NMP specimens after the sintering process under 60 MPa and 300°C for 10 min. Detailed cross-section treatment is described in Appendix B. Upper and lower side images for each material indicate representative observation results under low and high magnifications, respectively. The image contrast in the high magnification image reflects the crystallinity difference, which equals the grain boundary in the s-Ag layer. Small and spherical shape pores are distributed in the NP specimen, which diameter is around 150 nm at the largest. By contrast, although spherical pores are also found, NMP has large pores and irregular shapes, which might have been made by merging several pores into one. The mean value of  $pr$  for NP and NMP is 5% and 8%, respectively. The mean pore size value for NP and NMP is 0.014  $\mu\text{m}^2$  and 0.049  $\mu\text{m}^2$ , respectively. The mean value of crystal size for NP and NMP is 0.085  $\mu\text{m}^2$  and 0.16  $\mu\text{m}^2$ , respectively. The pore shape parameter ( $psf$ ) is introduced here to characterize each pore shape. The parameter has been described by Anselmetti *et al.* [18]. The  $psf$  was expressed as the following equation:

$$psf = \frac{P}{2\sqrt{\pi A}} \quad (2)$$

where  $P$  is the pore perimeter [ $\mu\text{m}$ ]  $A$  is the pore area [ $\mu\text{m}^2$ ]. The  $psf$  parameter means dimensionless parameter. The mean  $psf$  value was 1.22 in NP and 1.39 in NMP. Each parameter was evaluated by image processing as described in Appendix C.

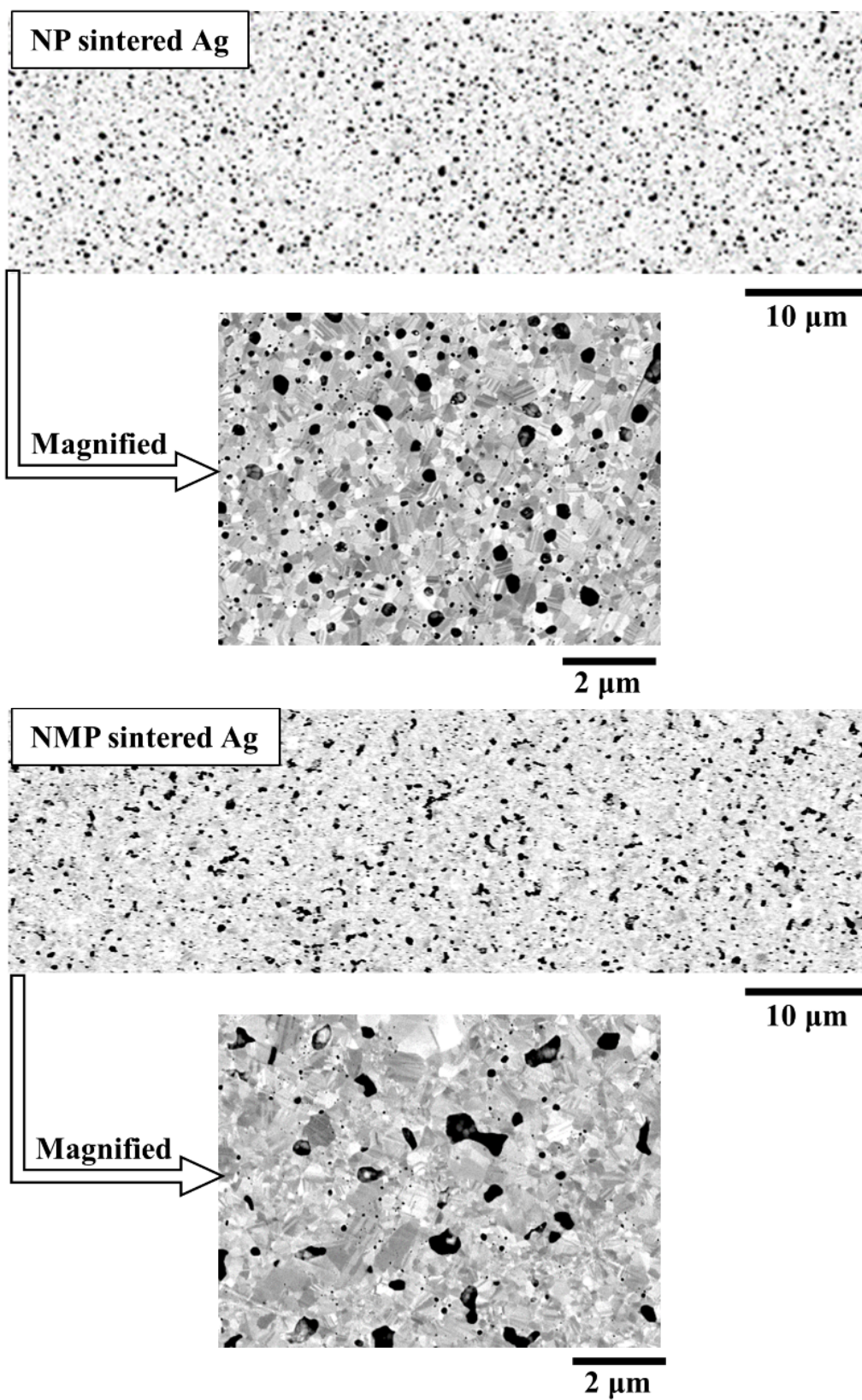


Fig. 2-19 Cross-section SEM observation results of NP and NMP.

### 2-5-2. Stress-strain curve

Fig. 2-20 shows representative *S-S* curves for NP and NMP at RT, 100°C, and 150°C. The blue and green colors of plots in *S-S* curves are indicative of NP and NMP, respectively. Temperature differences accord with the darkness of the color. The dark color means the low-temperature results. For *S-S* curves at RT, both NP and NMP exhibit no clear yielding point, which indicates that specimens fractured in a brittle manner. The tendency well accords with the previous research results [12, 14, 17, 19-24]. BS value is around 1% in both NP and NMP. The UTS of the NP specimen shows around 300 MPa, which is 1.5 times higher than the value in NMP. NP and NMP UTS values are superior to the bulk Ag value of around 150 MPa [17]. That comes from the crystal size difference between bulk Ag and s-Ag. According to the Hall-Petch relations [25, 26], the UTS increased with decreasing the crystal size due to the suppression of dislocation motion within the delicate grain boundary area. In the case of s-Ag with NP and NMP, the mean crystal size was smaller than the bulk annealed Ag crystal size [27], which enhanced the UTS value.

At 100°C for NP, the *S-S* curve exhibits a nonlinear region where the plateau region can be seen from the nominal strain value at around 2%. That means plastic deformation with dislocation slip becomes active. In addition, the little necking region is seen to be a failure. UTS shows around 90 MPa, which value is about 1/3 value of the RT value of UTS. The BS value at 100°C is about ten times higher than the value in RT. The mechanical property completely changes from brittle to ductile for NP specimens at 100°C. The tendency is well accorded that brittle-ductile transition temperature showed around 100°C in the case for small *pr* of s-Ag specimen [14, 23, 28]. By contrast, the NMP *S-S* curve measured at 100°C does not show a broad plateau region as was seen in NP at 100°C. The nominal strain of a few% sees the region before the fracture of the specimen.

At 150°C for NP, the *S-S* curve also exhibits a non-linear curve as was obtained in the *S-S* curve at 100°C in NP. Furthermore, the plateau region increases with increasing the measurement temperature from 100 to 150°C. After the plateau region, the necking behavior appeared to be a complete failure. The UTS value is 30% decreased from the value in NP with 100°C. By contrast, the BS value decreases about 40% lower than the BS value at 100°C. The ductile deformation with dislocation motion started at lower stress with increasing the measurement temperature. For NMP at 150°C, the *S-S* curve firstly shows an apparent non-linear relation as NP *S-S* graphs at 100 and 150°C. However, the NMP plateau region at 150°C is still lower than the NP plateau region at 100 and 150°C. The UTS value of NMP at 150°C is slightly higher than that of NP at 150°C.

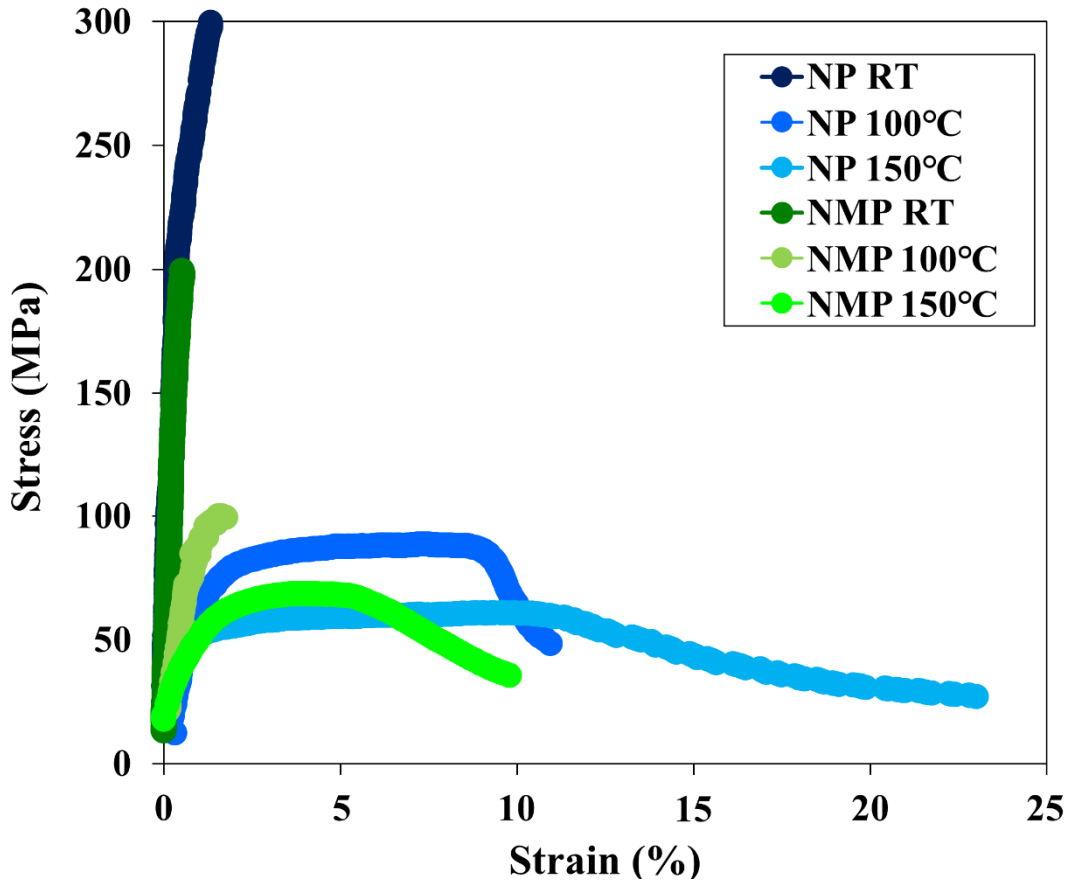


Fig. 2-20 S-S curves for NP (blue colors) and NMP (green colors).

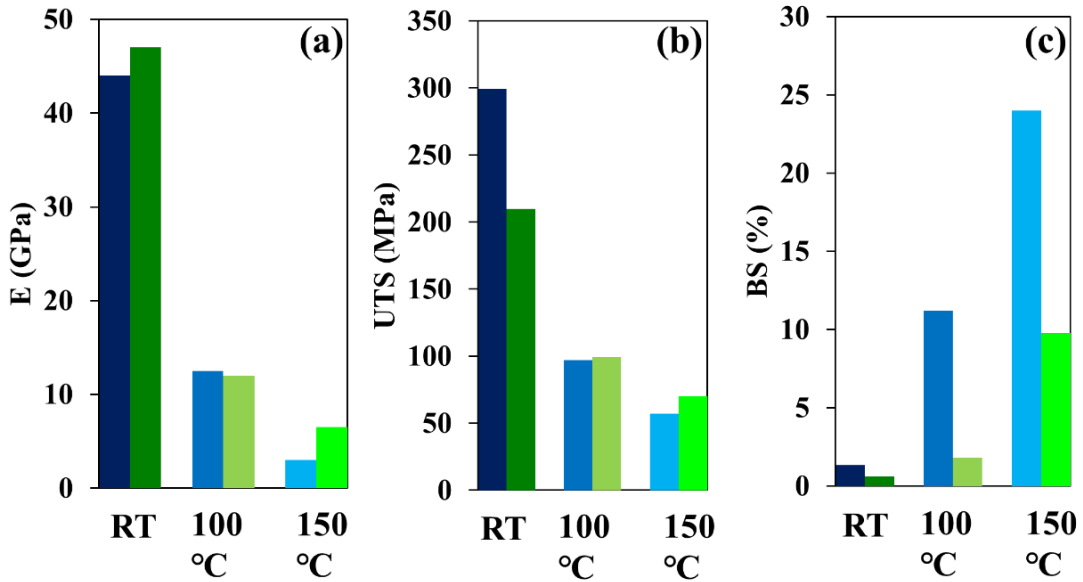


Fig. 2-21 (a) Young's Modulus: E (b) Ultimate tensile strength: UTS (c) Breaking strain: BS.

Fig. 2-21 shows the mechanical properties derived from Fig. 2-20 with (a) E, (b) UTS, and (c) BS at each temperature tested. The mean value of NP and NMP at RT shows about 45GPa, which decreased with increasing the temperature at an approximate rate of 0.35 GPa/°C. For UTS, the value differences between NP and NMP show high value only at RT. UTS value in NP at RT shows 300 MPa, 1.5 times higher than the UTS value in NMP at RT. The UTS values of NP and NMP show around 100 MPa at 100°C and 55 MPa at 150°C, respectively. For BS, only RT results show around 1%, similar between NP and NMP. At 100°C, the NP BS value shows around 10%, which increases about ten times high in comparison with the value of NP at RT. By contrast, the NMP BS value shows around 2%, which is five times smaller than the value of NP at 100°C. At 150°C, the BS value in NP increases by around 25%. The BS value in NMP also increases at around 10%, similar to the NP's value at 100°C.

Fig. 2-22 shows the mechanical properties of (a) E, (b) UTS, and (c) BS as a function of microstructure parameters such as pore size, crystal size, *pr*, and *psf* for NP and NMP. The plot color definition is identical to that in Fig. 2-20 and Fig. 2-21. As depicted in Fig. 2-22, the thick arrow means that the microstructure parameter affected the mechanical properties. All microstructure parameters for NMP show larger than those for NP. For E, the microstructure parameters do not affect the E value irrespective of tested temperature, as shown in Fig. 2-22 (a). For UTS, as shown in Fig. 2-22 (b), the microstructure parameters negatively affect the UTS only in the RT case that showed a brittle fracture. The microstructure parameter does not influence the UTS at 100°C and 150°C, which showed a ductile fracture. That is, dislocation motion was activated by almost identical applied stress irrespective of microstructure parameter differences between NP and NMP. By contrast, the microstructure parameter's influence on BS contradicts UTS, as shown in Fig. 2-22 (c). The BS values at 100°C and 150°C show a negative correlation against microstructure parameters, whereas the BS value at RT shows almost the same value irrespective of microstructure parameters. Microstructure parameters influence UTS at RT regarding the brittle fracture strength and BS at 100°C and 150°C regarding plastic deformation strength. For each case, a small value of microstructure parameters affected well on the improvement of mechanical properties of UTS and BS.

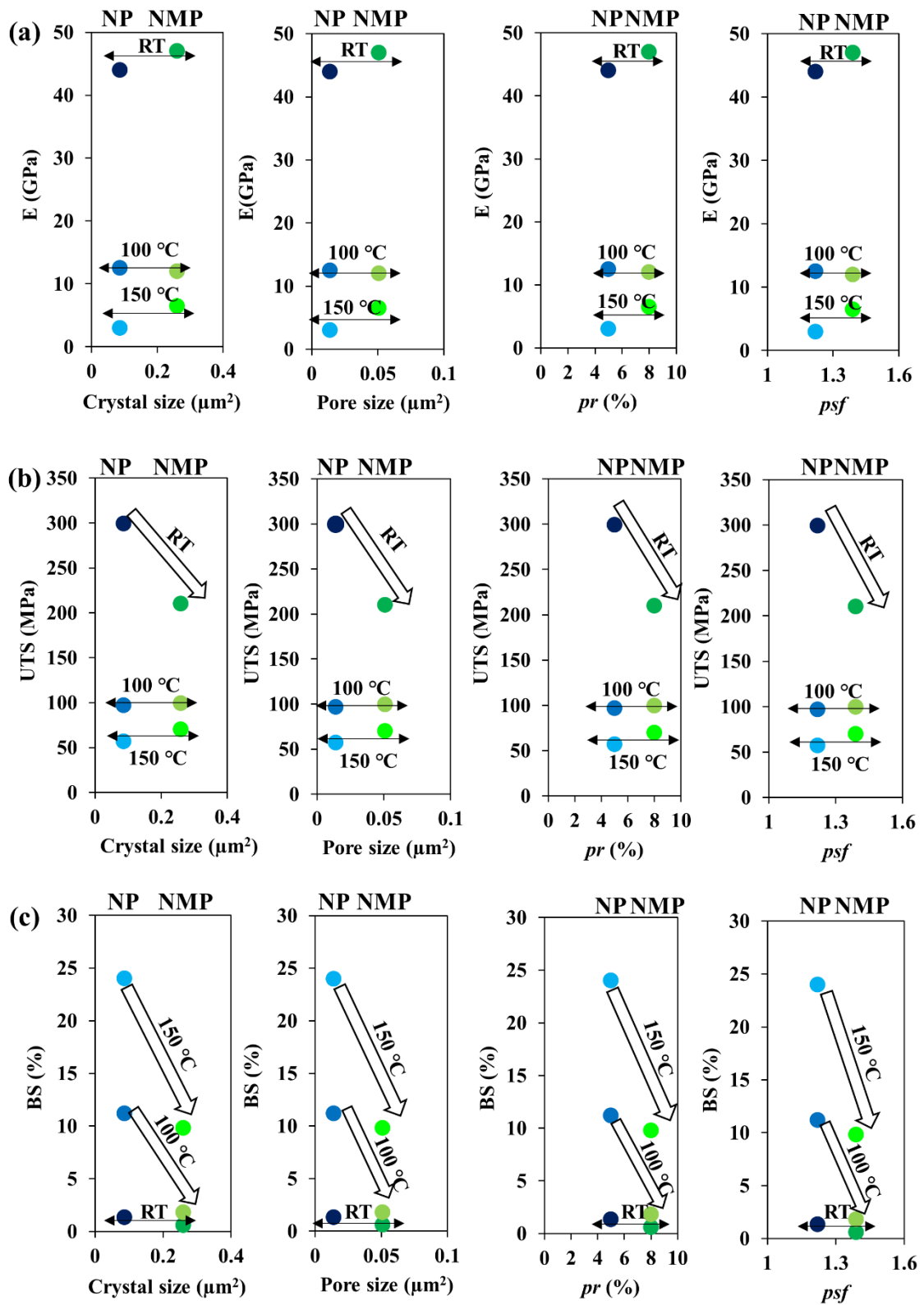
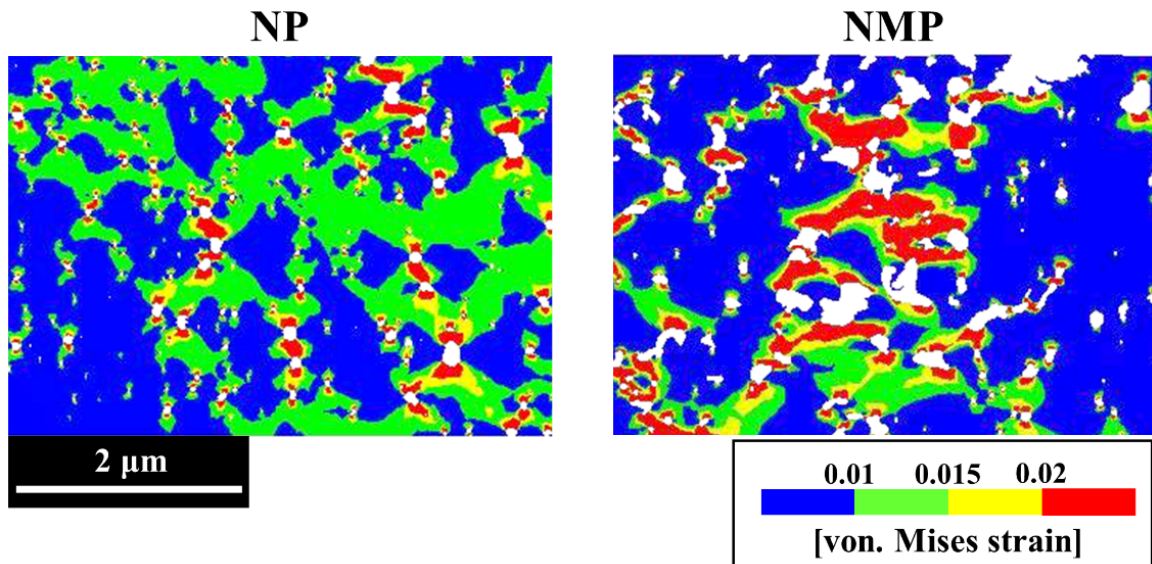


Fig. 2-22 (a) E, (b) UTS, and (c) BS as a function of pore size, crystal size,  $pr$ , and pore shape factor ( $psf$ ) for NP and NMP.

Finite element analysis (FEA) was conducted to explore an appropriate reason that the microstructure influenced mechanical properties, using commercial software, ANSYS 19.0. The von. Mises strain distributions in the NP and NMP are presented in Fig. 2-23. The simulation model was made considering the pore state differences between NP and NMP based on the SEM photographs, as depicted in Fig. 2-19, which were fabricated via image processing software (Synopsys, Simpleware). The model was adopted as a two-dimensional (2D) model because the *pr* value in 2D observation matched the *pr* value in three-dimensional (3D) observation according to the previous study [29]. The left axis was fastened, then the other side was applied by tensile strain at 1%, and the temperature was set to 150°C as a boundary condition in this calculation. Strain intensity area in NP uniformly distributes in the layer due to the small-sized pore existence. The high strain level exceeding 0.02 only distributes surrounding the small-sized pore, as shown in NP strain distribution results in Fig. 2-23. Then, the NP specimen largely deformed with plasticity in total during the tensile test. By contrast, in NMP, high strain intensity exceeding 0.02 distributes surrounding the large-sized pore, which gives rise to local large plastic strain deformation in the layer. Consequently, NMP was considered to be fractured without total significant elongation with plasticity during the tensile test. It can be concluded that minute microstructure in s-Ag can provide better durability against the applied stress.

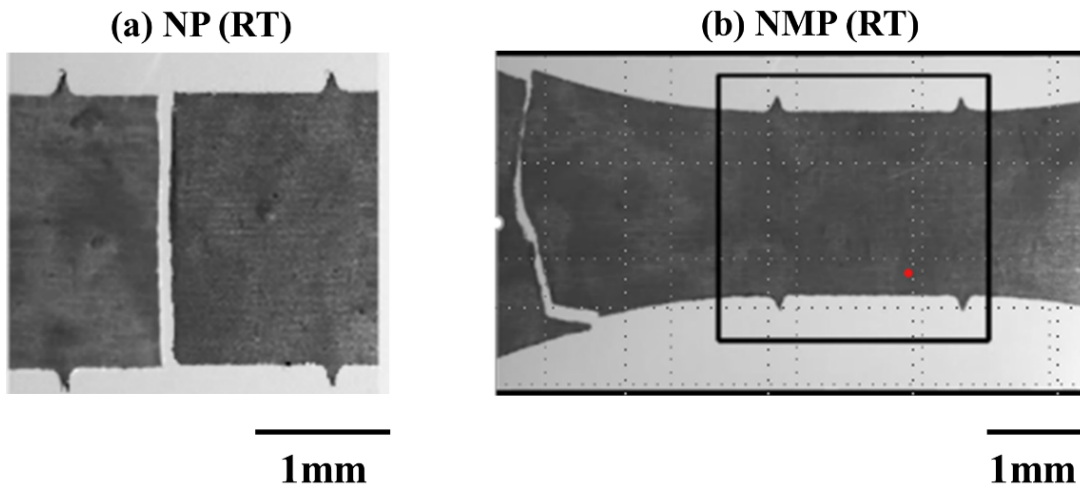


**Fig. 2-23 Strain distribution results from FEA with NP and NMP during tensile tests.**



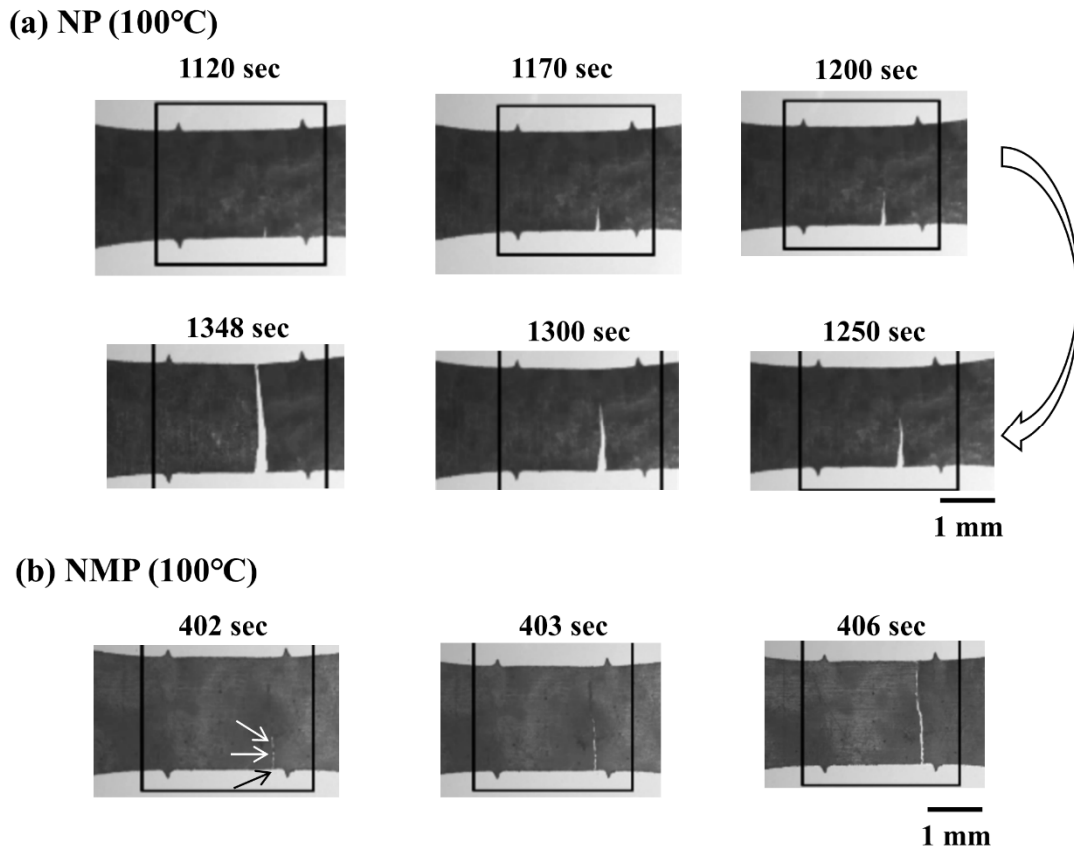
### 2-5-3. Crack propagation & fractography

Crack propagation observations during each tensile test were conducted by a CCD camera above the specimen surface, as shown in Fig. 2-10. Fig. 2-24 shows the CCD photographs after the tensile test at RT in (a) NP and (b) NMP. For NP, the cracking direction is almost orthogonal to the force direction, and the fracture points are within the gauge mark of the specimen's stress intensity area. Pure brittle material has been known to fracture orthogonal to the stress direction [30]. That was, NP specimen fractured in a brittle manner. The cracking direction shows a zigzag wave with NMP at RT. The cracking position is outside the gauge mark area, indicating that pores in the NMP specimen acted strongly as a source of stress concentration.



**Fig. 2-24 CCD photographs of s-Ag specimen surface during the tensile test at RT of (a) NP and (b) NMP.**

Fig. 2-25 shows the CCD photographs after the tensile test at 100°C in (a) NP and (b) NMP. For NP, a time gap between crack initiation time and fracture time exists. After 1120 sec, one crack emerges at the bottom edge of the specimen. That means the specimen released the internal energy to form a new surface after the end of dislocation motions. Then, the crack pathway changes to be slightly inclined from the vertical direction at 1250 sec. After that, the crack keeps progressing almost vertically up to 1348 sec. For NMP, the multiple fracture initiation points simultaneously emerge in a vertical line depicted as three arrows in Fig. 2-25 (b) at 402 sec. After that, each crack propagation is merged within a few seconds to be a complete failure in the specimen. NMP specimen has a small crack propagation resistance compared to the crack resistance in NP.

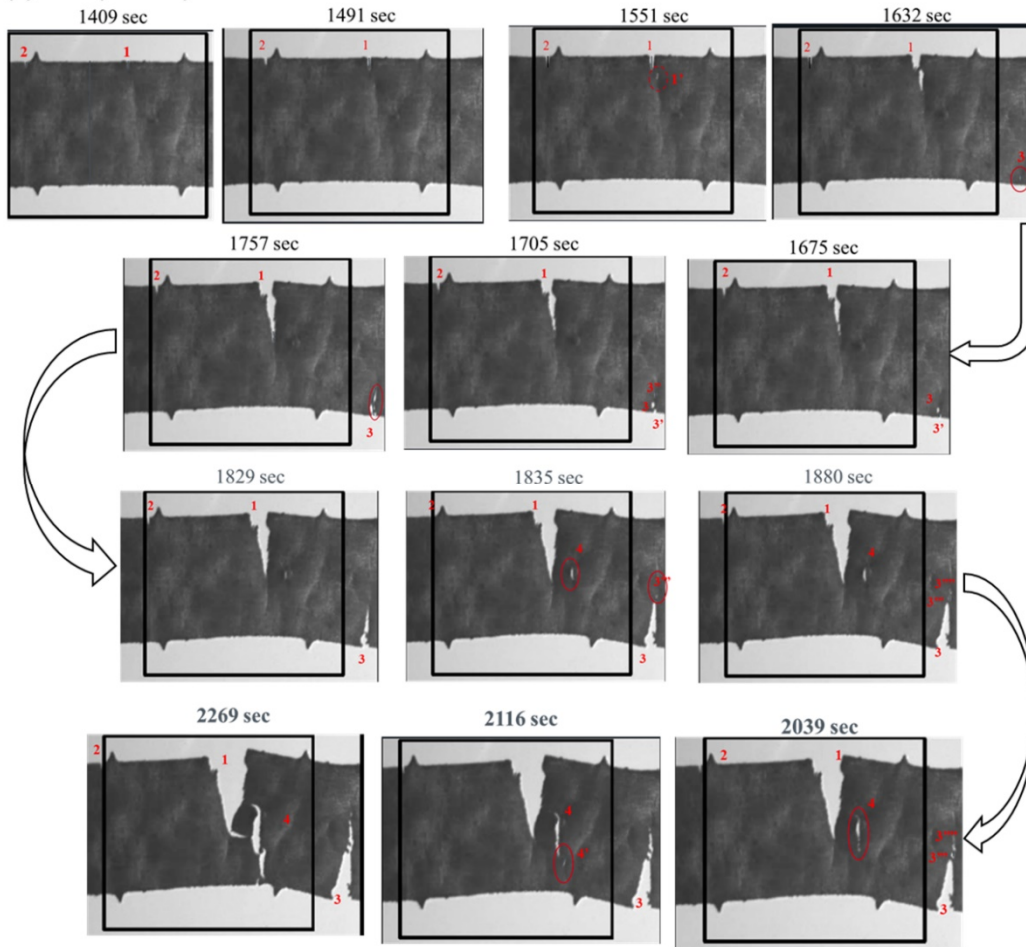


**Fig. 2-25 CCD photographs of s-Ag specimen surface during the tensile test at 100°C of (a) NP and (b) NMP.**

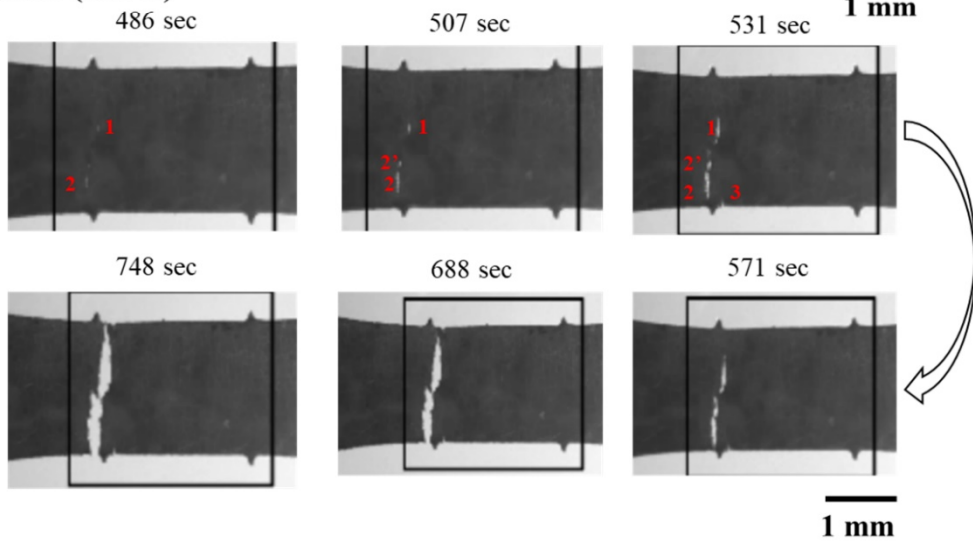
Fig. 2-26 (a) shows the CCD observation results of NP at 150°C. After 1409 sec, two micro-cracks generate at the top edge portion of the specimen. After from 1409 to 1551 sec, two small cracks propagate to the vertical direction. After 1551 sec, a new crack indexed as No. 1', located at the nearest from the end of crack No. 1, emerges. Then, the relation between the new small crack merged with the main crack continued from 1620 to 2269 sec. Nucleation of many cracks has been known that the fracture was accompanied by large plastic deformation [31, 32]. NP fractured with large plastic deformation at 150°C.

Fig. 2-26 (b) shows the CCD observation results for NMP with 150°C. The stress concentration still strongly acts as a crack initiation point regardless of the temperature. After 486 sec, two crack initiations emerge at the inner part of the specimen, not showing the edge portion. Then, the new crack indexed as 2' emerges near the tip of crack 2. Each crack is merged from 507 sec to 748 sec to failure with complete. Finally, the main crack propagates to be a complete failure in the specimen. In the NMP specimen, the crack initiation area shows the edge portion and inner area. The crack merging speed is faster than the merging speed in the NP specimen at 150°C, which resulted in the fast failure.

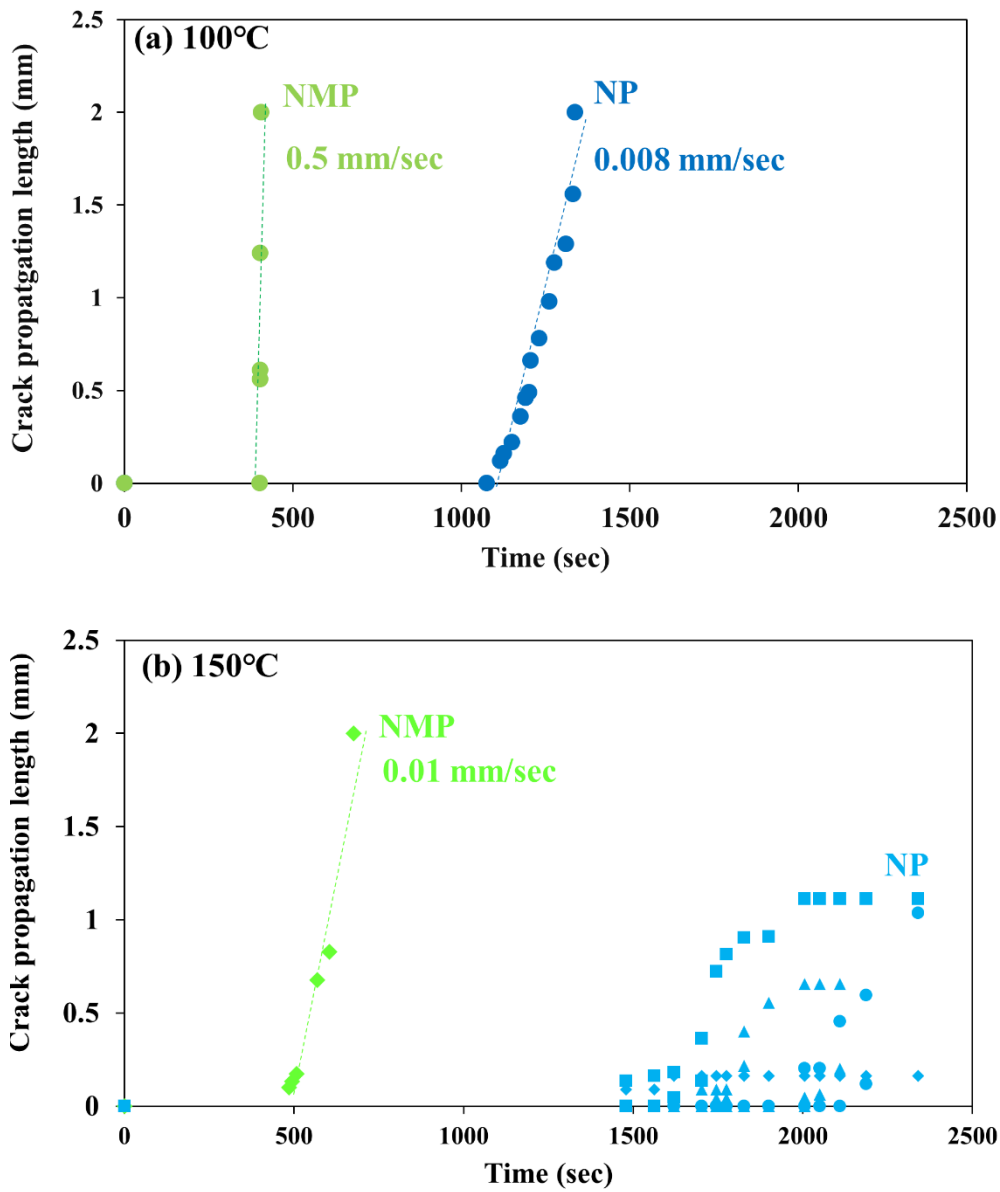
**(a) NP (150°C)**



**(b) NMP (150°C)**



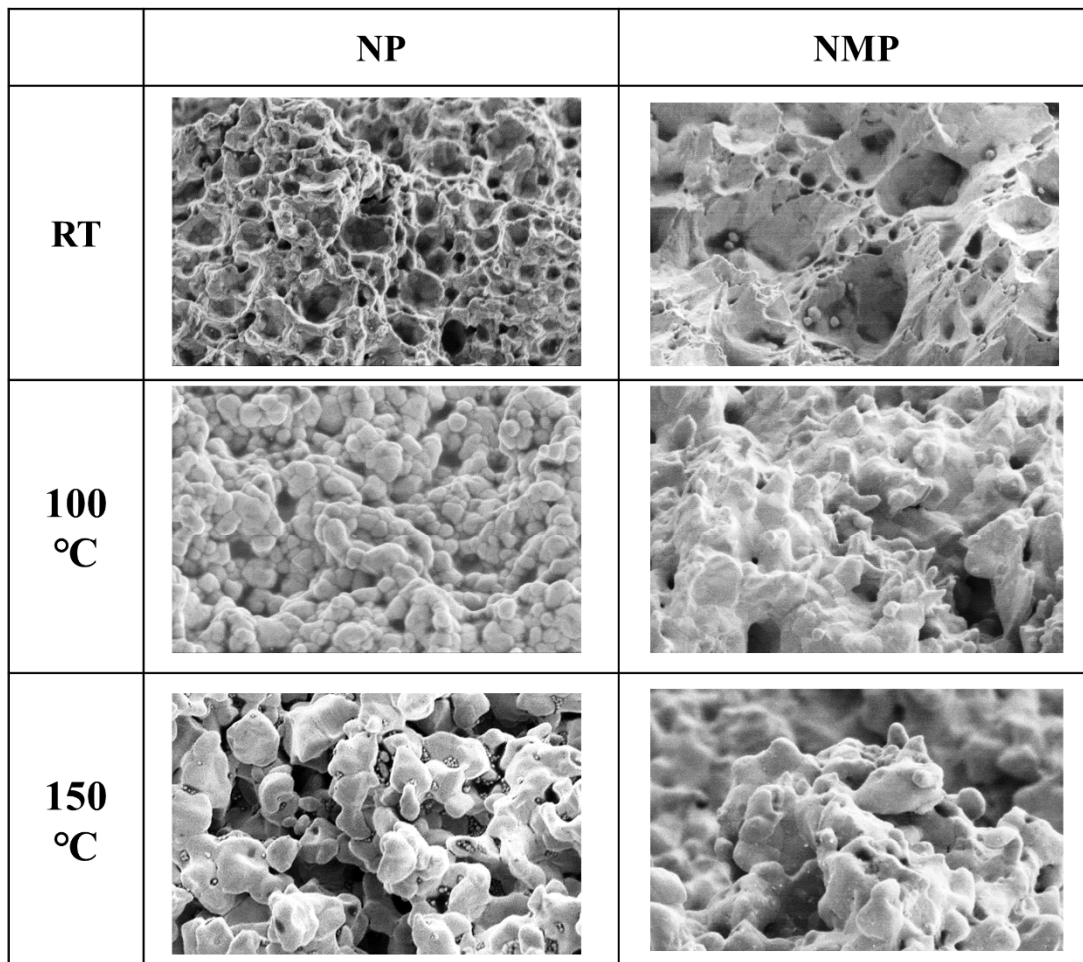
**Fig. 2-26 CCD photographs of s-Ag specimen surface during the tensile test at 150°C of (a) NP and (b) NMP.**



**Fig. 2-27 Crack length during the tensile test as a function of time at (a) 100°C and (b) 150°C for NP and NMP.**

Fig. 2-27 shows the crack propagation length versus time at (a) 100°C and (b) 150°C for NP and NMP. Crack propagation length was defined by the vertical length of the crack as taken from the CCD observation results. The definition of plot color is identical to those in Fig. 2-20, Fig. 2-21, and Fig. 2-22. The figure style differences in NP plots indicate four cracks observed in the CCD images as, shown in Fig. 2-26. For 100°C, crack propagation starts at 402 sec in NMP and 1075 sec in NP. That is, the dislocation slip motion in NP was more active than the dislocation motion in NMP. Consequently, extensive plastic

deformation could be seen in NP. After that, the crack propagation shows at a constant speed in both NP and NMP. The crack propagation speed in NMP is about 0.5 (mm/sec), which is about 70 times faster than the crack propagation speed in NP at 100°C. For 150°C, crack propagation starts propagating from 1480 sec in NP and 500 sec in NMP. Each time value at 150°C is more significant than at 100°C, indicating that dislocation mobility increased with the test temperature [32]. For NMP, only one major crack progresses up to failure. The propagation speed shows constant at 0.01 (mm/sec) at 150°C. The speed is 50 times slower than the value at 100°C, almost equal to the NP value at 100°C. By contrast, NP shows a different trend for each five because multiple cracks were captured during the tensile test. Note that each plot shows non-linear relation against the time, meaning multiple cracks would make nonuniform stress distribution from the interaction between adjacent cracks.



2  $\mu$ m

**Fig. 2-28 Representative SEM images of s-Ag fracture surface at RT, 100°C, and 150°C for NP and NMP.**

Fig. 2-28 shows representative SEM observation results of fracture surface for NP and NMP at RT, 100°C, and 150°C. For NP and NMP at RT, some dimple patterns are observed. A small dimple size in NP is uniformly distributed, originating from the NP's initial microstructure. By contrast, NMP dimple size is nonuniformly distributed from nano to micro size, originating from the NMP microstructure. For NP and NMP at 100°C, the fracture surfaces differ entirely from those at RT in the point that dimples disappeared, but a convex-concave pattern like an aggregation of grains can be observed. In addition, individual grain figures show some protrusion portions around the grain, which indicates that the local plastic deformation occurred with individual Ag grains. For NP and NMP at 150°C, the protrusion portions of Ag grains

become clear. That is, individual plastic deformation was accelerated by increasing the temperature. It was clarified that the crack has progressed along with the grain boundary at higher temperatures, originating from the Ag grain's plastic deformation.



## 2-6. Conclusion

Two types of Ag paste, namely, NP and NMP, were used to investigate the relationship between the microstructure and mechanical properties. NP included Ag particles with 18 nm in mean diameter, and NMP included three types of Ag particles with a mean diameter of 25, 148, and 5063 nm by DLS measurements. The organic components in NP consisted of high molecules, whereas NMP consisted of low molecules clarified by GC/MS measurements. The high molecules of the organic protective in NP were adopted to prevent the high self-aggregation of nanosized Ag particles containing NP.

The s-Ag film tensile mechanical properties were investigated by quasistatic tensile testing at RT to 150°C. Reducing *pr* around 5% could be achieved by pressure-assist sintering with 60 MPa for 10 min at 300°C. The tensile mechanical property showed good results under this condition. The temperature dependence on the s-Ag tensile property indicated that brittle-to-ductile mechanical property transition occurred at around 100°C. The large plasticity deformation in s-Ag specimen at above 100°C can avoid sudden fractures.

NP and NMP tensile mechanical properties were investigated to check the paste-type dependence on tensile mechanical properties. SEM cross-sectional surface images of the NP and NMP after sintering at 60 MPa for 10 min at 300°C revealed that small and spherical pores were distributed in NP. In contrast, relatively large pores with an irregular shape were distributed in NMP. In addition, NP possessed a more miniature structure than NMP. In the *S-S* curves, NP and NMP specimens were found to fracture in a brittle manner at RT. At elevated temperatures, the NP specimen showed a large plateau region in its *S-S* curve, indicating large plastic deformation at 100°C. The NMP specimen showed the same tendency at 150°C. Plastic deformation in NMP specimen was smaller than that in the NP specimen. From the viewpoint of the strain concentration area obtained from FEA analysis results, NMP possessed a large strain concentration area surrounding large pores, which led to local plastic deformation. Consequently, the NMP total deformation was restricted to failure. Therefore, suppressing the microstructure parameter will positively affect the long material durability of film specimens. Based on crack propagation observations by CCD images from the above side of the specimen surface, cracking progressed in a zigzag way from multiple initiations measured at the elevated temperature, which is characterized as ductile mechanical properties. In addition, cross-sectional fracture SEM observations demonstrated that individual Ag grains stretched with a protrusion at high temperatures, which also indicated that s-Ag specimen deformed with plasticity at high temperatures.

## References

- [1] H. Schwarzbauer, "Method of securing electronic components to a substrate," USA Patent US4810672, 1989.
- [2] H. Schwarzbauer, "Method and apparatus for fastening electronic components to substrates," Patent US4903885, 1990.
- [3] H. Schwarzbauer, "Apparatus for fastening electronic components to substrates," USA Patent US5058796, 1991.
- [4] H. Schwarzbauer, R. Kuhnert, "Novel Large Area Joining Technique for Improved Power Device Performance," *IEEE Transactions on Industry Applications*, vol. 27, no. 1, pp. 93-95, 1991, doi: 10.1109/28.67536.
- [5] K. Park, D. Seo, and J. Lee, "Conductivity of silver paste prepared from nanoparticles," *Colloids and Surfaces A: Physicochemical and Engineering Aspects*, vol. 313-314, pp. 351-354, 2008, doi: 10.1016/j.colsurfa.2007.04.147.
- [6] H. Hozoji, T. Morita, and H. Sasaki, "Method for mounting an electronic part on a substrate using a liquid containing metal particles," USA Patent US7393771B2, 2008.
- [7] J. Yeom, S. Nagao, C. Chen, T. Sugahara, H. Zhang, C. Choe, Cai-Fu Li, and K. Suganuma, "Ag particles for sinter bonding: Flakes or spheres?," *Applied Physics Letters*, vol. 114, no. 25, 2019, doi: 10.1063/1.5099140.
- [8] W. Zhang, W. Zhang, X. Qiao, X. Qiu, Q. Chen, and Y. Cai, "Controllable Preparation of Silver Nanostructures and the Effects of Acidity-Basicity of the Reaction System," *Science of Advanced Materials*, vol. 6, no. 2, pp. 304-311, 2014, doi: 10.1166/sam.2014.1716.
- [9] Y. Sun and Y. XIA "Shape-Controlled Synthesis of Gold and Silver Nanoparticles," *Nano technology*, vol. 34, no. 11, pp. 2176-2179, 2003, doi: 10.1002/chin.200310226.
- [10] T. Namazu and S. Inoue, "Tensile and Creep Characteristics of Sputtered Gold-Tin Eutectic Solder Film Evaluated by XRD Tensile Testing," *Sensors and Materials*, vol. 22, no. 1, pp. 13-24, 2010, ISSN: 0914-4935.
- [11] "Semiconductor devices mechanical and climate test methods," IEC International Standard 60749-25, Chap. 5.9, pp. 21, 2003.
- [12] K. Wakamoto, Y. Mochizuki, T. Otsuka, K. Nakahara, and T. Namazu, "Tensile mechanical

- properties of sintered porous silver films and their dependence on porosity," *Japanese Journal of Applied Physics*, vol. 58, no. SD, pp. SDDL08-1-5, 2019, doi: 10.7567/1347-4065/ab0491.
- [13] K. S. Siow, "Are Sintered Silver Joints Ready for Use as Interconnect Material in Microelectronic Packaging?," *Journal of Electronic Materials*, vol. 43, no. 4, pp. 947-961, 2014, doi: 10.1007/s11664-013-2967-3.
- [14] K. Wakamoto, Y. Mochizuki, T. Otsuka, K. Nakahara, and T. Namazu, "Temperature Dependence on Tensile Mechanical Properties of Sintered Silver Film," *Materials*, vol. 13, no. 18, pp. 4061-4071, Sep., 2020, doi: 10.3390/ma13184061.
- [15] G. Saada, "Hall–Petch revisited," *Materials Science and Engineering: A*, vol. 400-401, pp. 146-149, 2005, doi: 10.1016/j.msea.2005.02.091.
- [16] Z. C. Cordero, B. E. Knight, and C. A. Schuh, "Six decades of the Hall–Petch effect – a survey of grain-size strengthening studies on pure metals," *International Materials Reviews*, vol. 61, no. 8, pp. 495-512, 2016, doi: 10.1080/09506608.2016.1191808.
- [17] C. Weber, H. Walter, M. Van Dijk, M. Hutter, O. Wittler, and K.-D. Lang, "Combination of Experimental and Simulation Methods for Analysis of Sintered Ag Joints for High Temperature Applications," in *Proc. 66th Electronic Components and Technology Conference (ECTC)*, Las Vegas, USA, June, 2016, 10.1109/ECTC.2016.394.
- [18] F. S. Anselmetti, S. Luthi, and G. P. Eberli, "Quantitative Characterization of Carbonate Pore Systems by Digital Image Analysis," *AAPG Bulletin*, vol. 82, no. 10, pp. 1815–1836, 1998, doi: 10.1306/1d9bd155-172d-11d7-8645000102c1865d.
- [19] C. Chen, S. Nagao, H. Zhang, T. Sugahara, K. Sugauma, T. Iwashige, K. Sugiura, and K. Tsuruta, "Low-Stress Design for SiC Power Modules with Sintered Porous Ag Interconnection," in *Proc. 66th Electronic Components and Technology Conference (ECTC)*, Las Vegas, NV, USA, Aug., 2016:, doi: 10.1109/ECTC.2016.59.
- [20] R. Shioda, Y. Kariya, N. Mizumura, and K. Sasaki, "Low-Cycle Fatigue Life and Fatigue Crack Propagation of Sintered Ag Nanoparticles," *Journal of Electronic Materials*, vol. 46, no. 2, pp. 1155-1162, 2016, doi: 10.1007/s11664-016-5068-2.
- [21] K. Sugiura, T. Iwashige, K. Tsuruta, C. Chen, S. Nagao, T. Funaki, and K. Sugauma, "Reliability Evaluation of SiC Power Module With Sintered Ag Die Attach and Stress-Relaxation Structure," *IEEE Transactions on Components, Packaging and Manufacturing Technology*, vol. 9, no. 4, pp.

- 609-615, 2019, doi: 10.1109/tcpmt.2019.2901543.
- [22] T. Suzuki, T. Terasaki, Y. Kawana, D. Ishikawa, M. Nishimura, H. Nakako, and K. Kurafuchi, "Effect of Manufacturing Process on Micro-Deformation Behavior of Sintered-Silver Die-Attach Material," *IEEE Transactions on Device and Materials Reliability*, vol. 16, no. 4, pp. 588-596, 2016, doi: 10.1109/tdmr.2016.2614510.
- [23] T. Herboth, M. Guenther, A. Fix, and J. Wilde, "Failure Mechanisms of Sintered Silver Interconnections for Power Electronic Applications " in *Proc. 63rd Electronic Components and Technology Conference*, Las Vegas, USA, May, 2013, doi: 10.1109/ECTC.2013.6575789.
- [24] S. Zabihzadeh, S. Van Petegem, L. I. Duarte, R. Mokso, A. Cervellino, and H. Van Swygenhoven, "Deformation behavior of sintered nanocrystalline silver layers," *Acta Materialia*, vol. 97, pp. 116-123, 2015, doi: 10.1016/j.actamat.2015.06.040.
- [25] E. O. Hall, "The Deformation and Ageing of Mild Steel\_ III Discussion of Results," *Proceedings of the Physical Society. Section B*, vol. 64, no. 9, pp. 747-753, 1951, doi: 10.1088/0370-1301/64/9/303
- [26] E. O. Hall, "The cleavage strength of polycrystals," *Journal of the Iron and Steel Institute*, vol. 174, pp. 25-28, 1951.
- [27] Z. Ning, Q. Wang, D. Zhao, W. Pei, and M. Wen, "Structural Evolution of Bulk Silver during Cold Rolling and Annealing," *Metals*, vol. 12, no. 9, pp. 1525-1531, 2022, doi: 10.3390/met12091525.
- [28] M. Schaal, M. Klingler, and B. W. M. Klingler, "Silver Sintering in Power Electronics: The State of the Art in Material Characterization and Reliability," in *Proc. 7th Electronic System-Integration Technology Conference (ESTC)*, Dresden, Germany, Sept., 2018, doi: 10.1109/ESTC.2018.8546498.
- [29] T. Youssef, W. Rmili, E. Woirgard, S. Azzopardi, N. Vivet, D. Martineau, R. Meuret, G. L. Quilliec, and C. Richard, "Power modules die attach: A comprehensive evolution of the nanosilver sintering physical properties versus its porosity," *Microelectronics Reliability*, vol. 55, no. 9-10, pp. 1997-2002, doi: 10.1016/j.microrel.2015.06.085.
- [30] H. Kosuge, T. Kawabata, T. Okita, and H. Nako, "Accurate Estimation of Brittle Fracture Toughness Deterioration in Steel Structures Subjected to Large Complicated Prestrains," *Crystals*, vol. 10, no. 10, pp. 867-873, 2020, doi: 10.3390/cryst10100867.
- [31] J. Gurland, "Observations on the fracture of cementite particles in a spheroidized 1.05% c steel deformed at room temperature. Acta Metallurgica," *Acta Metallurgica*, vol. 20, no. 5, pp. 735-741,

1972, doi: 10.1016/0001-6160(72)90102-2.

- [32] C. J. McMahon Jr. and M. Cohen, "Initiation of cleavage in polycrystalline iron Amorces de clivage dans le fer polycristallin Einleitung der kristallits paltung in polykristallinem eisen," *Acta Metallurgia*, vol. 13, no. 6, pp. 591-604, 1965, doi: 10.1016/0001-6160(65)90121-5.

### 3. Sintered Silver Die Bonding Reliability

The s-Ag die degradation is commonly assessed by thermal shocked test (TST), which evaluates material's durability against a heating/cooling cycle as introduced in Chapter 1. Materials with different CTE promote thermal out-of-plane deformation surrounding the bonding part, which deteriorate the s-Ag die part by repeated thermal and mechanical stress during TST [1]. The degradation progress during TST has been attributed to the APS distribution in the die layer. In the case of the combination of SiC and Cu bonded with s-Ag, the s-Ag die bonded layer starts to shrink, causing cracks at the edge between s-Ag and SiC. In general, the lifetime of the s-Ag die layer is defined as the delamination percentage of 20% after 1000 cycles in TST [2-4]. If the s-Ag die layer degradation during TST is independently clarified from the aspects of thermal and mechanical stress, then the decisive degradation factor can be focused during TST. In this Chapter, TST and four point bending test (FBT) at RT are compared to check the applied stress direction effect on the s-Ag die layer cracking progress during TST. Then, the developed mechanical bending test, namely, NBT, is proposed. NBT can provide similar out-of-plane deformation with the s-Ag DAAs as TST like. In addition, NBT can operate at high temperature (150°C). s-Ag die layer degradation is assessed by comparing NBTs (0–300 N) at 150°C with 3 min period and TSTs –40 to 150°C with 60 min period for seeking main degradation. Finally, DP defined as the APS divided by the plastic strain of s-Ag material from uniaxial tensile testing at the highest temperature in each condition is proposed for understanding the degradation mechanism classification in the s-Ag die layer.

#### 3-1. Thermal shocked test (TST) and four-point bending test

##### 3-1-1. Experimental methodology

As for the first step, to experimentally understand the s-Ag die attach degradation during TST, the degradation mechanism of s-Ag die attach was investigated by mechanical FBT and TST. s-Ag die attached assemblies (DAAs) have 5% in porosity ( $pr$ ) and are subjected to two types of FBTs: centered bending test (CBT) for bending moment applied to the s-Ag layer and shifted bending test (SBT) for shear force application. FBTs and TST results are compared for seeking the stress mode dependences on crack progress during TST. Fig. 3-1 shows a schematic view of TST, CBT, and SBT. In TST, by temperature cycling between –40 and 150°C, the difference in CTE among respective materials gives rise to specimen deformation upward and downward repeatedly, leading to cyclic bending deformation during the test. In CBT and SBT, four-point bending under the deformation state illustrated as the bending moment diagram

(BMD) and shear force diagram (SFD) is applied to a bar-shaped specimen. In CBT, the specimen with SiC chip edges at the center is symmetrically set at the midpoint of both the loading and supporting points. Between the two loading points, only the bending moment is applied. In SBT, the center of the specimen is set to be at a certain distance from the loading center, which provides both bending moment and shear force applied in the chip edges.

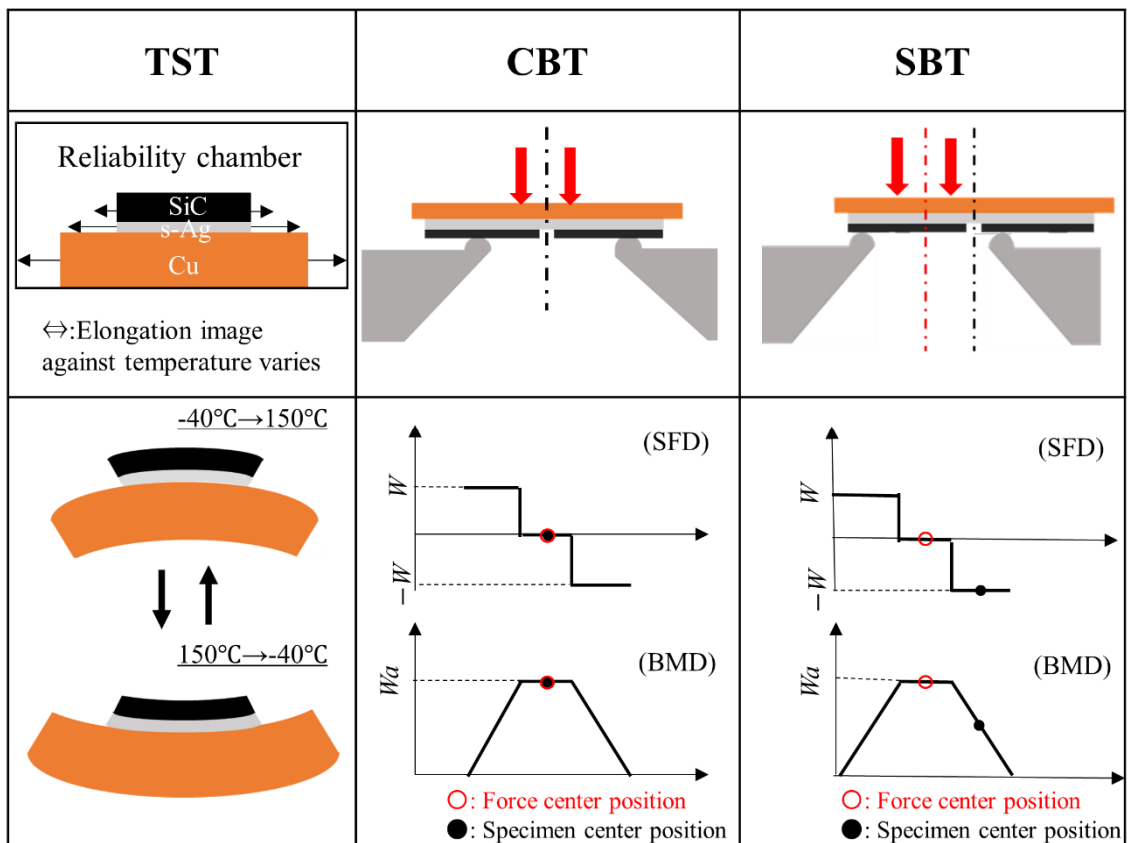


Fig. 3-1 Experiment schematic view of TST, CBT, and SBT [5].

Fig. 3-2 shows a schematic of specimen fabrication for each test and the photograph. For TST, SiC chip measuring 4.8 mm × 4.8 mm × 0.35 mm was bonded with an electroplated copper (Cu) substrate measuring 20 mm × 20 mm × 3 mm by sintering nano paste (NP) with a mean diameter of 18 nm as introduced in Chapter 2. The sintering was conducted at 300°C under 60 MPa pressure for 10 min, as a reference condition as previously introduced in Chapter 2. The temperature rising rate was 150°C/min to prevent semi-sintering before pressuring the Ag layer. The *pr* of s-Ag layer was controlled to be around 5%. The detail of the fabrication protocol was described in Fig. 1-7. For CBT and SBT, two SiC chips were aligned in parallel and bonded with a rectangular Cu substrate by pressure-assisted NP sintering. The sintering condition was the same as that for TST. Then, the assembly was cut by blade dicing to form a bar shape for the bending test. The dimension of each part, including the jig alignment position, is described in Fig. 3-2.

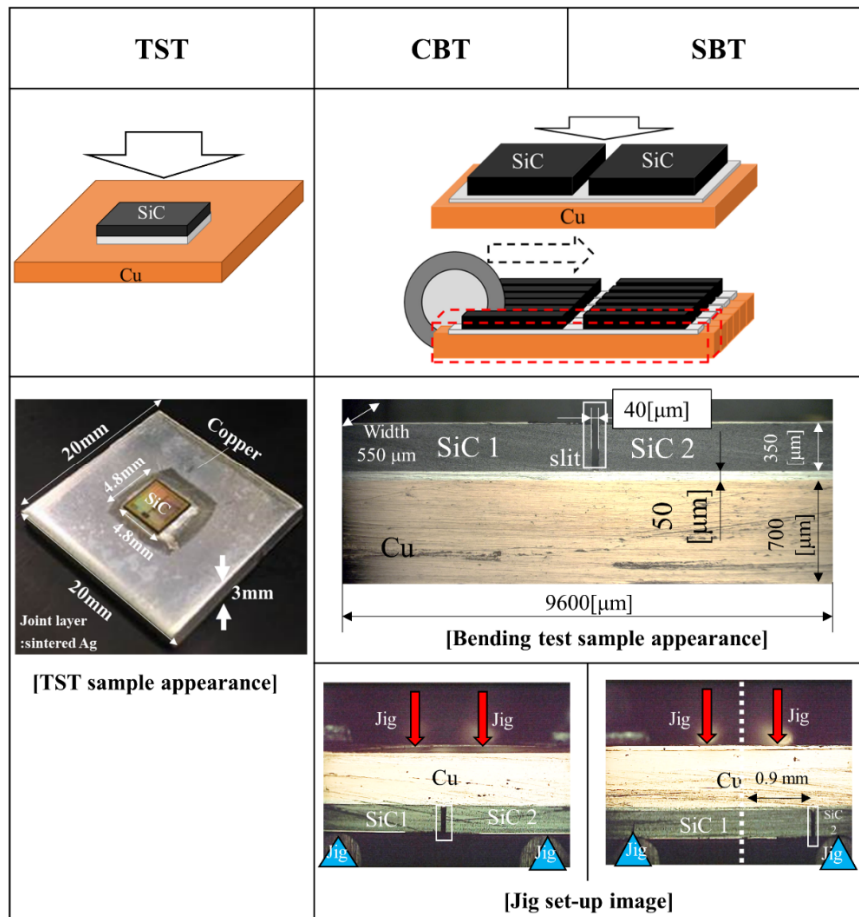


Fig. 3-2 Schematic of specimen fabrication for each test together with the photograph [5].



For TST, commercial equipment, TSA41-EL-A, produced by Espec Japan, was used, as shown in Fig. 3-3. In this chamber, air flow controls the atmosphere temperature, which can control the atmosphere temperature by the variation rate at about 200°C/sec. Assemblies were just placed onto the chamber basket. CBT and SBT were performed by an in-house bending test system shown in Fig. 3-3.

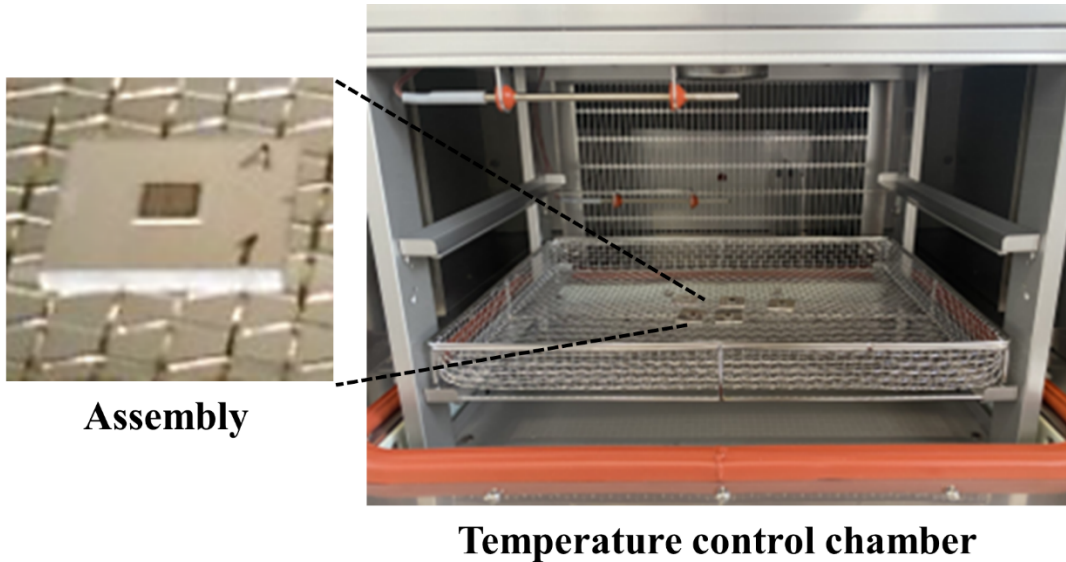


Fig. 3-3 TST chamber.

Table 3-1 Reliability test condition [5].

<b>TST condition</b>	
<b>Atmosphere</b>	<b>-40 to 150°C</b>
<b>Duration time</b>	<b>30 min / 30 min</b>
<b>Mechanical bending test condition (CBT and SBT)</b>	
<b>Atmosphere</b>	<b>Room temperature (RT)</b>
<b>Frequency [Hz]</b>	<b>10</b>
<b>Wave form</b>	<b>Sine curve of load (Peak value: 0~26N)</b>

The CBT and SBT conditions are listed in Table 3-1. The equipment consists of a piezoelectric (PZT) actuator for bending force application, a load cell for bending force measurement, a set of specimen's holding jigs for fastening a specimen at the four points during the test, and a laser displacement meter for bending deflection measurement. The detailed tester specifications can be seen in the previous papers [6-8].

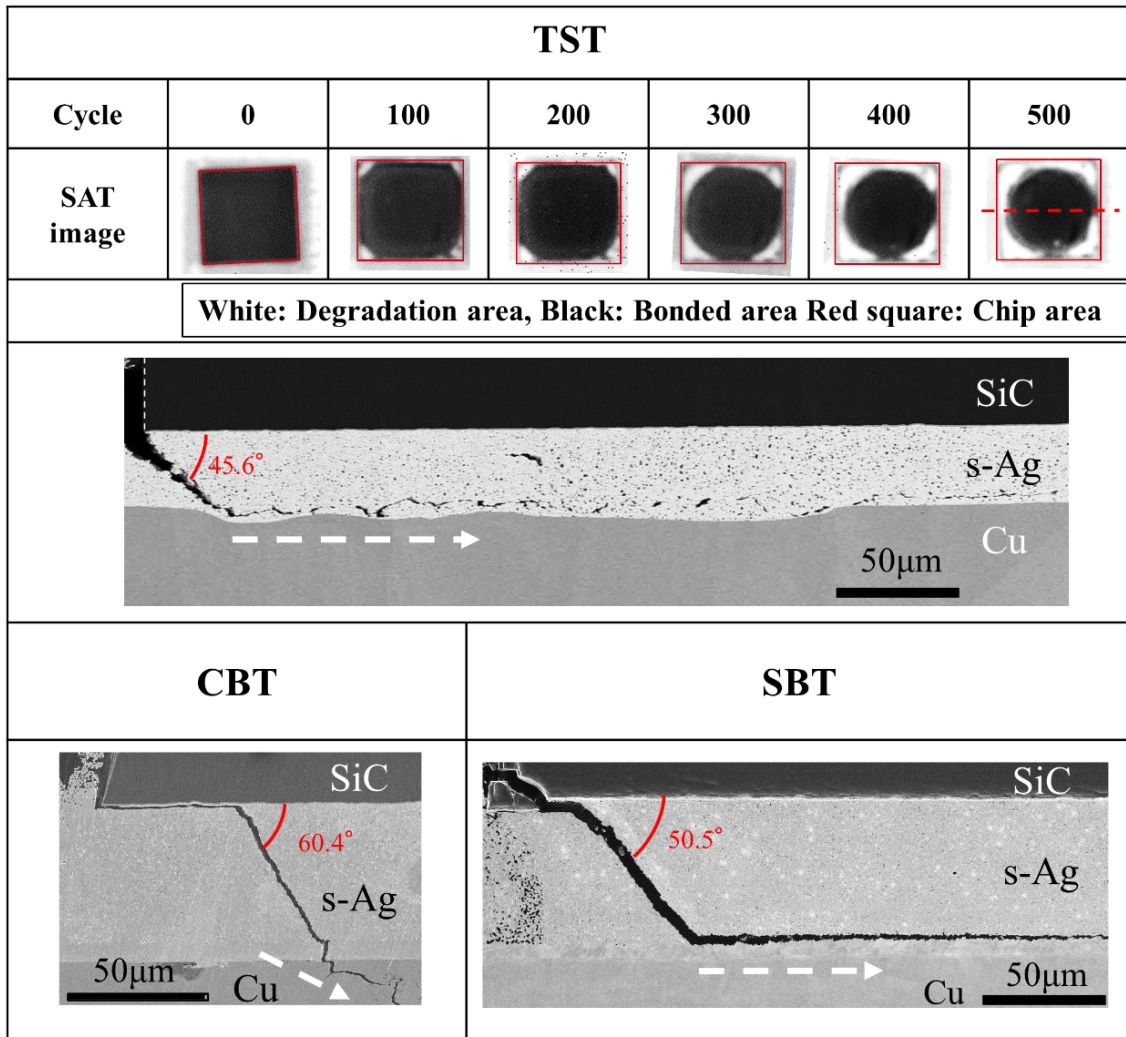
### 3-1-2. Fracture mode

Fig. 3-4 shows representative scanning acoustic tomography (SAT) images at 100 cycles intervals in 0~500 cycles during TST. Also, cross-sectional scanning electron microscopy (SEM) images are shown after 500 cycles for TST, 190,000 cycles for CBT, and 46,000 cycles for SBT. The specimen, after 500 cycles of TST, was cut at the center, indicated as the red dashed line on the SAT image for cross-sectional SEM observation. In the SAT images of TST, the specimen shows a black-colored portion only in the initial state, indicating the whole area is completely bonded. All the images were obtained using an ultrasonic probe with 25 MHz. After 100 cycles, a white-colored portion can be seen at every corner, indicating that delamination has started there almost simultaneously. With increasing the number of cycles, each white-colored area increases gradually. At around 400 cycles, those portions have been connected to each other. In the cross-sectional SEM image, after 500 cycles of TST, a crack initiated at the corner of the SiC chip and propagated into the s-Ag layer at around 45°. When the crack tip reached the s-Ag and Cu substrate interface, the propagation direction changed horizontally along the substrate surface. All the specimens tested showed the same degradation phenomenon, although those data are skipped here.

For CBT, a crack was initially introduced at the same corner as the TST specimen. After that, the crack propagated horizontally along the SiC bottom surface. After the crack proceeded by approximately 50  $\mu\text{m}$ , it turned to the s-Ag inside at an inclined angle of around 60° from the horizontal plane. When the crack tip reached the s-Ag and Cu interface, it did not turn in the horizontal direction but kept penetrating the Cu substrate.

For SBT, a crack was initiated at the SiC chip's corner, as did the other two specimens. Soon after, the crack proceeded into the s-Ag layer at an inclined angle of around 50°. In the vicinity of the s-Ag and Cu interface, the propagation direction changed to the horizontal direction, as did the TST crack. The similarity between SBT and TST suggests that shear force plays an essential role in imitating cracking direction in TST.

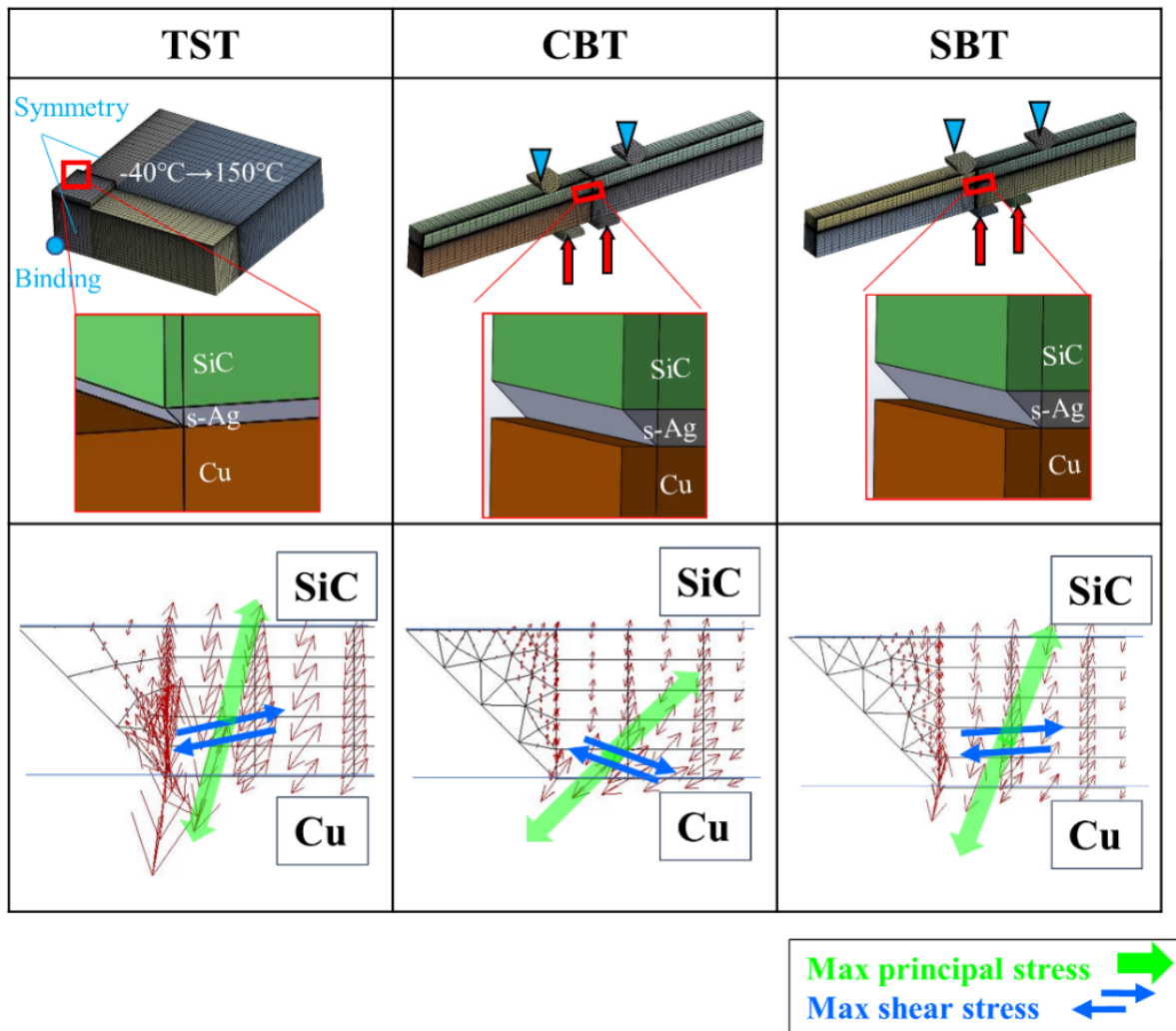
However, the s-Ag porous structure after TST differed from that after CBT and SBT. Before TST, only tiny pores were observed in the s-Ag layer with a *pr* of 5%. After 500 cycles in TST, the growth and coalescence of pores are clearly seen. In contrast, even after 190,000 cycles in CBT and 46,000 cycles in SBT, the internal structure of the s-Ag layer is significantly unchanged from the initial state.



**Fig. 3-4** Representative scanning acoustic tomography (SAT) images at 100 cycle intervals in 0~500 cycles for TST along with cross-sectional scanning electron microscopy (SEM) images after 500 cycles for TST and after 190,000 cycles for CBT and 46,000 cycles for SBT, respectively [5].

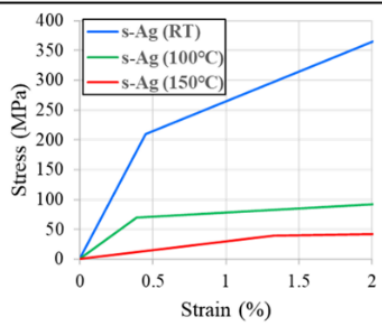
### 3-1-3. Stress direction

Finite element analysis (FEA) was conducted to understand the difference in crack propagation direction in the s-Ag layer between the three tests, using commercial software, ANSYS 19.0. Fig. 3-5 depicts representative FEA results along with the models. Stress distribution in the s-Ag layer around the corner of the SiC chip edge was calculated. Since the maximum shear force direction could not be directly displayed in the calculation, it was estimated by rotating by  $45^\circ$  from the maximum principal stress direction calculated. A one-quarter model configuration was adopted in the TST simulation, and the cyclic temperature as a driving force for the calculation was set at  $-40$  to  $150^\circ\text{C}$ . In both the CBT and SBT simulations, the face load of 26 N and 0 N were applied to the specimen model from the bottom and top surface where the loading and supporting jigs contact, respectively. The material characteristic values used for FEA are listed in Table 3-2. Only for s-Ag, the elastic-plastic behavior was considered. In the TST mode FEA, the maximum principal stress is found to face the direction slightly inclined from the out-of-plane direction, providing the maximum shear stress slightly inclined from the in-plane direction. The SBT mode FEA shows almost a similar trend to the TST. However, the maximum shear stress direction in the CBT mode tilts into the substrate surface compared to that in the TST and SBT modes. In general, the fatigue crack of metal is well known to propagate along the maximum shear stress direction.[9] In the cases of TST and SBT, the crack direction after the crack tip reaches the substrate accorded with the maximum shear stress direction in the s-Ag layer. The similarity in stress distribution between the TST and SBT modes would have given rise to the similar crack propagation phenomenon in those tests.



**Fig. 3-5 Representative FEA results along with the models [5]. (Upper side: Modeling overview. Downside: Maximum principal stress and sheared stress direction distribution in the s-Ag die layer. Thick annotation means representative direction for each test.)**

**Table 3-2 Material mechanical properties used in FEA [5].**

<b>Material</b>	<b>Young's Modulus (GPa)</b>	<b>Poisson's Ratio</b>	<b>CTE (<math>\times 10^{-6}</math>)</b>
<b>SiC</b>	<b>412</b>	<b>0.17</b>	<b>3.0</b>
<b>Copper</b>	<b>118</b>	<b>0.35</b>	<b>16.8</b>
<b>64 Ti</b>	<b>115</b>	<b>0.35</b>	<b>-</b>
<b>s-Ag</b>		<b>0.35</b>	<b>19.5</b>
<b>Cemented carbide</b>	<b>630</b>	<b>0.21</b>	<b>-</b>

### 3-1-4. Failure mechanism

Fig. 3-6 (a) and (b) show the crack length in the out-of-plane and in-plane directions as a function of the number of cycles, respectively. The length of the crack introduced into each specimen was divided into the out-of-plane crack length (OCL) and in-plane crack length (ICL), which definitions are illustrated in Fig. 3-6. A specimen's lifetime was defined as the state when the ICL reached 250  $\mu\text{m}$ . The dashed and solid plots indicate the incline and in-plane crack parts, respectively. In Fig. 3-6 (a), the OCL value for TST rapidly increases to 300 cycles from the start. The value for SBT and CBT also increased rapidly from 1,000 to 10,000 cycles, respectively, compared to the initial state. After that, the OCL value for TST and SBT looks kept constant, which means that the crack propagated along the horizontal direction into the s-Ag layer. By contrast, the OCL value for CBT shows a gradual increase trend throughout the test, indicating that the crack direction was unchanged during the CBT. In Fig. 3-6 (b), the ICL value for TST and SBT linearly increases in the sold plot part with increased cycles. The fatigue crack propagation speed

indicated as an approximation line can be estimated to be 0.52 and 0.014  $\mu\text{m}/\text{cycle}$  for TST and SBT, respectively. The propagation speed for CBT in the final section is estimated to be  $7 \times 10^{-4} \mu\text{m}/\text{cycle}$ , which is 20~740 times slower than that for TST and SBT. By comparing the crack propagation speed in TST with that in SBT, the value for TST was approximately 4,000 times faster than that for SBT. The OCL value reaches the lifetime length of 250  $\mu\text{m}$  at around 500 and 50,000 cycles for TST and SBT, respectively. That is, the lifetime assessment period for SBT is approximately 1,400 times shorter than that for TST. This fact implies that if the fracture mechanism of SBT is the same as that of TST, SBT can be a lifetime acceleration test for the die-attach s-Ag material.

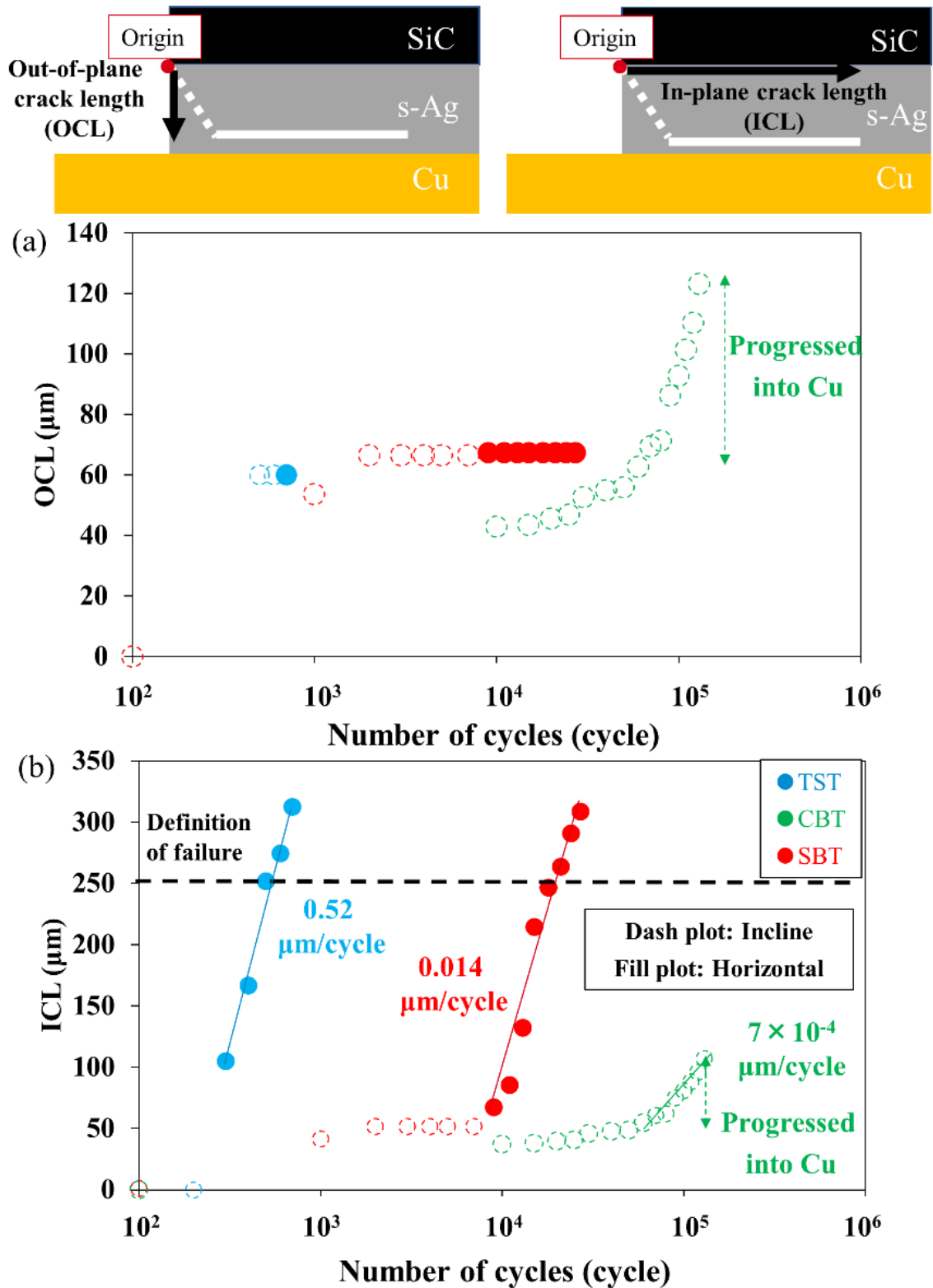
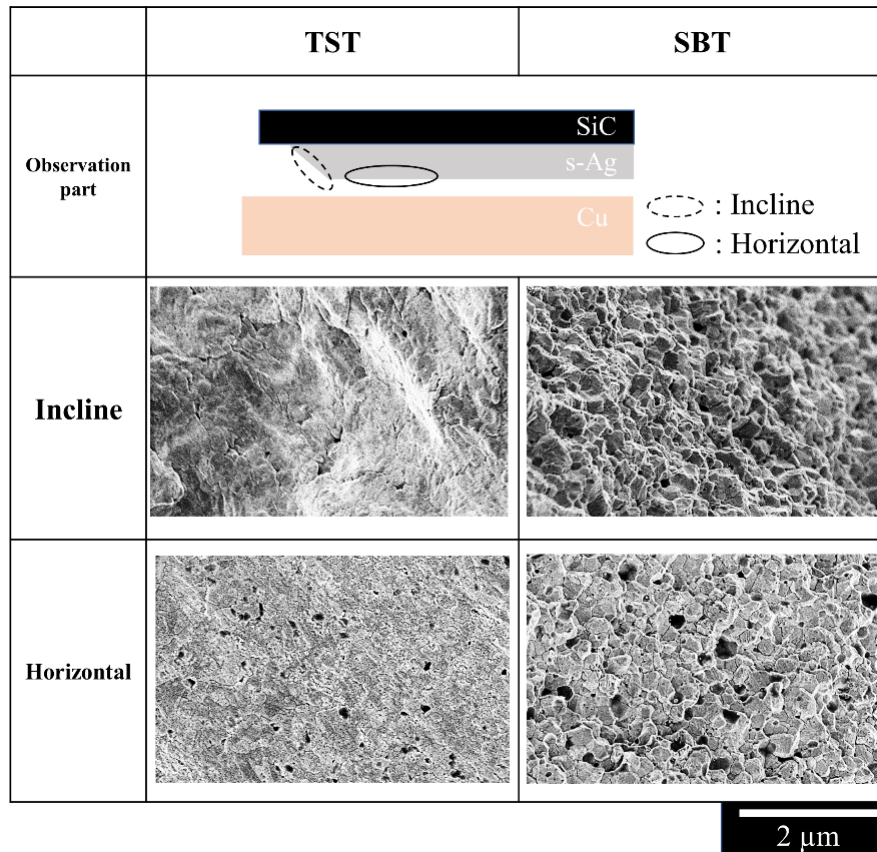


Fig. 3-6 Crack length as a function of the number of cycles (a) Out-of-plane crack length (OCL) (b) In-plane crack length (ICL) [5].



The fracture surface was observed with SEM to discuss the fracture mechanism of the s-Ag layer after TST and SBT. Fig. 3-7 shows a representative fracture surface at the inclined and horizontal cracking portions after TST and SBT. The inclined portion of the s-Ag fracture surface after TST shows a smooth surface, whereas that after SBT shows a rough surface. The difference in morphology between the two portions can also be confirmed from these magnified photos. The fracture behavior of s-Ag film is known to change from brittle to ductile at around 100°C. Since temperature changes range from -40 to 150°C during TST, the dislocation glide was probably introduced in the s-Ag grains, while creep deformation happened at the high-temperature region in the TST cycles. Consequently, a crack originating from plastic deformation would have propagated just after pore growth and dislocation glide happened at the crack tip. In contrast, SBT was conducted at ambient temperature, so the s-Ag layer fractured in a brittle manner. That is, by mechanical cyclic loading, stress concentration at the grain boundary was probably generated during SBT, resulting in the intergranular fracture of the s-Ag layer.



**Fig. 3-7 Representative fracture surface at the inclined and horizontal portions after TST and SBT [5].**

The crack propagation direction in SBT was close to that in TST. However, the failure mechanism in the s-Ag layer differed from each other. The discussion on the possibility of SBT as the lifetime acceleration test for TST should not be concluded until the evenness of fracture mode between the two tests has been confirmed experimentally. As for the next step, a mechanical bending test at high temperatures should be conducted for approaching TST failure mode associated with plastic deformation. In addition, mechanical bending deformation, including out-of-plane deformation as TST-like, would be more suitable for comparing results.

## 3-2. TST and nine-point bending test (NBT)

### 3-2-1. Experimental methodology

This section introduces a new mechanical bending test technique called the nine-point bending test (NBT). Fig. 3-8 shows a TST and NBT schematic and out-of-plane deformation distribution obtained from FEA using commercial software, ANSYS 19.0. The simulation aim is to verify the similarity of out-of-plane deformation with substrate between TST and NBT. For TST, a cyclic temperature between  $-40^{\circ}\text{C}$  and  $150^{\circ}\text{C}$  was set to the ambient atmosphere as a driving force. For NBT, a cyclic point force between 0 and 300 N was set on the bottom face of the load pin as a driving force. The eight supporting pins were placed onto the substrate at a  $45^{\circ}$  in-plane interval with a 7 mm in radius. s-Ag deforms plastically under applied stress at elevated temperatures [3, 10]. Therefore, the simulation temperature of NBT was set to keep at  $150^{\circ}\text{C}$  to induce local plastic deformation in the s-Ag die layer by applied mechanical force. The input material property is identical as listed in Table 3-2. The stress-free temperature in both TST and NBT was set to  $120^{\circ}\text{C}$ , which was determined based on the previous literature [1].

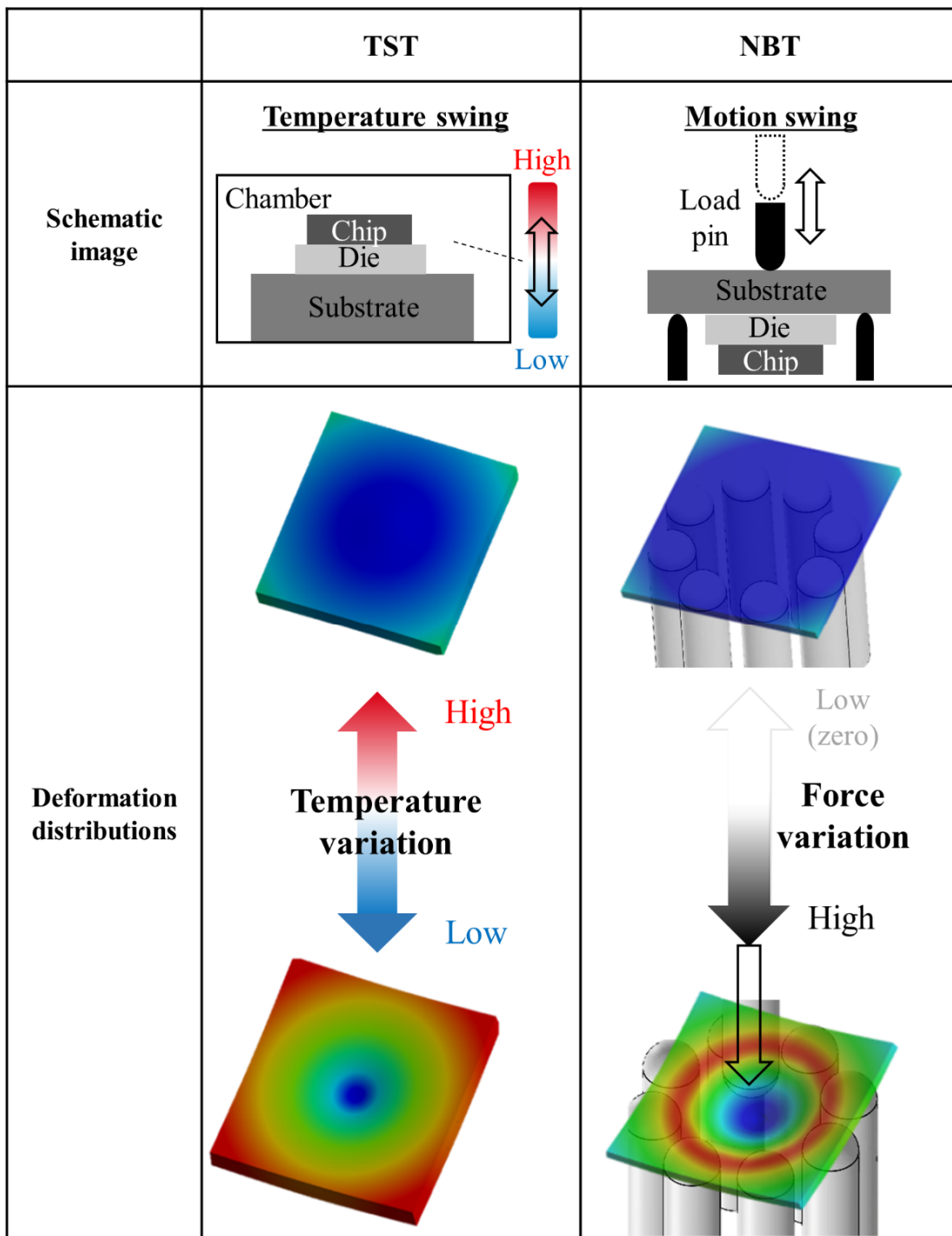


Fig. 3-8 Schematic of TST and NBT along with out-of-plane deformation distribution.

For TST, a concentric out-of-plane deformation happened because of the difference in CTE between SiC and Cu. By decreasing the temperature to  $-40\text{ }^{\circ}\text{C}$ , the out-of-plane deformation with a concentric concave morphology was obtained. On the contrary, by increasing the temperature to  $150\text{ }^{\circ}\text{C}$ , the deformation with a concentric convex morphology was obtained. The difference in the deformation direction was attributed to whether the target temperature was above or below  $120\text{ }^{\circ}\text{C}$ , a stress-free temperature. For NBT, a concentric concave pattern was observed in all the applied force conditions. The deflection at the center portion was proportional to the applied force. Based on the FEA results above, the common thing between the two tests was to give a concentric out-of-plane deformation. In the experiment, by heating and cooling cycles during TST, the s-Ag layer will deform mechanically in the out-of-plane direction, and simultaneously it will suffer from thermal damage. That is, during TST, both thermal and mechanical damages will be introduced in the s-Ag layer. On the other hand, by mechanical cycling loading during NBT, the s-Ag layer will suffer from mechanical damage only. The author aims to apply additional damages to the s-Ag layer through TST and NBT to understand its degradation mechanism in the experiment. The FEA results suggest that the two tests will provide a similar deformation and a different type of damage with the s-Ag layer.

Fig. 3-9 (a) shows photographs of the NBT experiment system. A universal test system (Instron Japan, 68TM-5) comprising a temperature variation chamber, a load cell, a brushless AC servomotor, a flow heater, a displacement sensor, and the load and support jigs we designed were used. The load jig motion was controlled by external commercial software, Instron Blue Hill Universal, where the applied stress was controlled. A round-shaped cemented carbide pin was embedded at the center of the loading jig made of stainless steel alloy. A screw was embedded on the lateral surface of the base jig to fix the load pin position. For the support jig, eight pins identical to the load pin were arranged in a regular octagonal position in-plane to maintain a 7 mm distance from the center of the support jig made of stainless steel alloy. A 20 mm square-hole metal guide plate made of aluminum alloy was placed at the center of the base jig to guide the specimen position. The NBT system cross-section and assembly are illustrated in Fig. 3-9 (b). A stainless-steel spring was placed under the bottom surface of each support pin to make a uniform contact between each support pin and the substrate surface. The height of each pin was lifted to the contact position using the spring's reaction force. The height of each pin can be fixed by fastening the side screw. The detailed setup procedure is described in Appendix D.

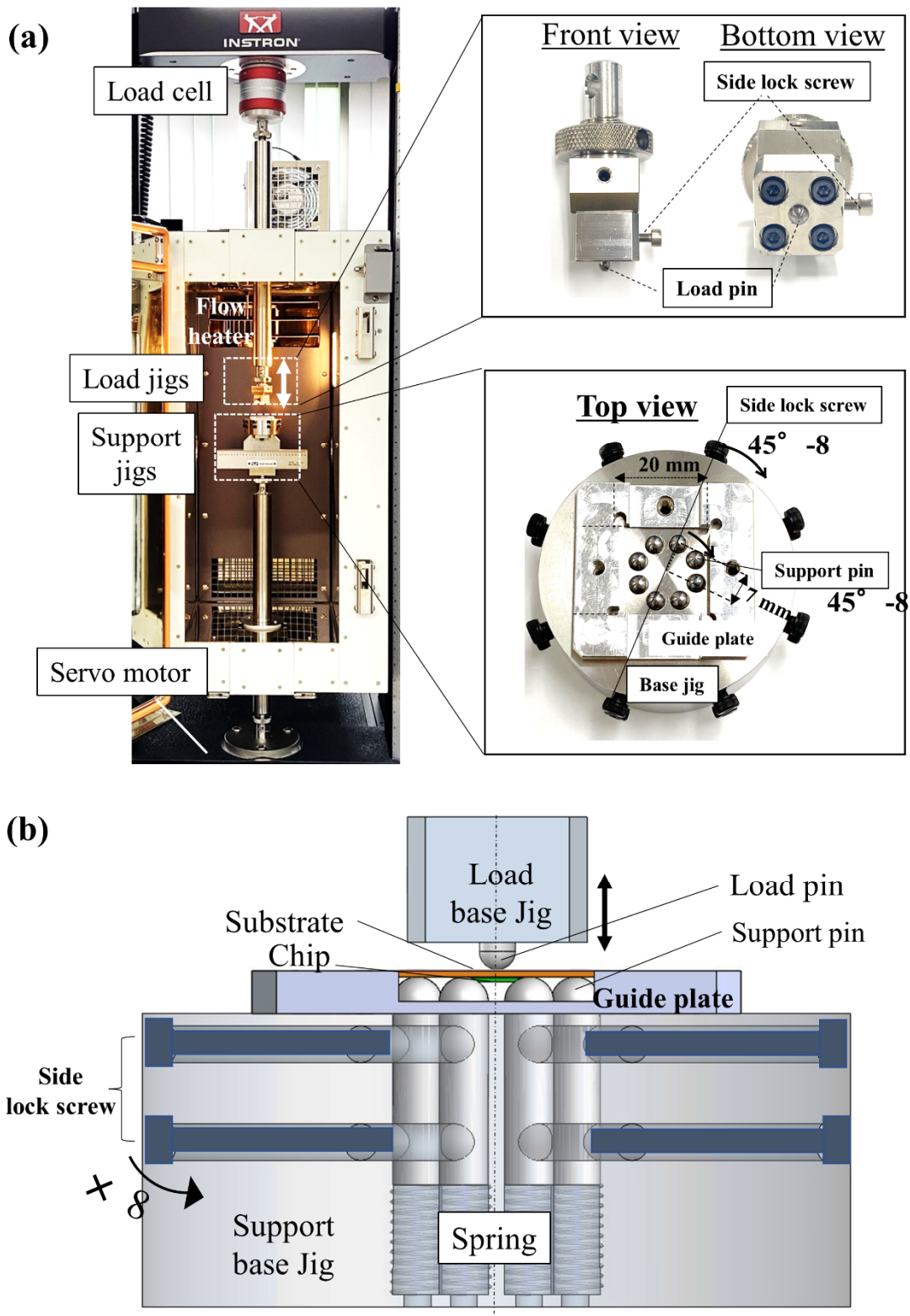


Fig. 3-9 Photographs of (a) NBT experiment components and (b) Cross section sketch view of NBT together with the s-Ag assemble.

### 3-2-2. Experimental condition

The test conditions are listed in Table 3-3. TSTs were conducted under five different conditions with several temperature profiles ranging from  $-40$  to  $150^{\circ}\text{C}$ . The temperature transition time between the lowest and highest for each TST condition was set to be 25 sec. As a reference structure for TST, a 4.8 mm square SiC chip with 0.35 mm thick was s-Ag bonded with a 20 mm square copper substrate with 2 mm thick at the process temperature of  $300^{\circ}\text{C}$  for 10 min under 60 MPa pressure of NP and NMP s-Ag bonded layer with 50  $\mu\text{m}$  thick. The s-Ag layers of 50 and 100  $\mu\text{m}$  thick were used with the Cu substrates of 1 and 2 mm thick to investigate the thickness effect on s-Ag degradation. For NBT, Ti-6Al-4V (64 Ti) with Ag sputtered substrate was adopted. The exact Ag sputtering condition is referred to in Appendix E. The reason why used 64Ti for NBT was attributed to the excellent mechanical property of 64 Ti. The mechanical property of Young's modulus is almost identical to Cu material. However, the yield stress is about three times higher than the primary value of Cu yield stress [11]. Therefore, 64Ti substrate can allow bending deformation without fatigue plastic deformation during the NBT. The test temperature was kept at a constant value of  $150^{\circ}\text{C}$  by heat flow regulated by the feedback signal of the resistance thermometer installed in the chamber. NBT was performed after 60 min to stabilize the temperature in this experiment. SiC chip bonding conditions and other assembly configurations for NBT were identical to those for TST. The maximum applied force varied from 240 to 300N. In NBT, under the maximum loads of 300, 270, and 240N, the traveled times from 0N to the maximum value for each condition were 90, 84, and 72 sec, respectively. The strain rate values were estimated to be  $6\sim 8\times 10^{-4}\text{ sec}^{-1}$  based on actual experimental conditions and FEA simulation results, almost the same in all the test conditions. All the tests were performed immediately after setting the specimens to avoid introducing any damage providing material's unevenness before the tests.

Table 3-3 Experiment condition.

	Temperature pattern		s-Ag material	s-Ag BLT ( $\mu\text{m}$ )	Cu thickness (mm)
	TST	Temperature ( $^{\circ}\text{C}$ )	Waveform (Rectangular)		
(I)	-40-150	60min period (30/30 min)	NP NMP 60MPa 300 $^{\circ}\text{C}$ 10min	50	2
(II)				50	1
(III)				100	2
(IV)				-40-100	50
(V)	150	Storage (60,000 min)		50	2

	Force pattern		s-Ag material	s-Ag BLT ( $\mu\text{m}$ )	$^{64}\text{Ti}$ thickness (mm)
	NBT	Force [N]	Waveform (Triangle)		
(I)	0-300	3min period	NP NMP 60MPa 300 $^{\circ}\text{C}$ 10min	50	1
(II)	0-270	2.7min period			
(III)	0-240	2.4min period			

### 3-2-3. Results of TST and NBT

Fig. 3-10 shows representative SAT images for TST and NBT. All the images were obtained using an ultrasonic probe with 25 MHz, which is identical to section 3.1. The color difference is attributed to the reflective acoustic intensity. The white color depicts the delamination area corresponding to the high reflective intensity caused by air inside, whereas the black color depicts the bonded area. In TST (I), a standard condition for s-Ag DAA with NP, the delamination starts steadily at the corner of the die after 400 cycles. The delamination proceeds with increasing the number of cycles. Mainly it randomly proceeds from 800 to 1000 cycles. For NMP, the delamination starts after 200 cycles, which randomly proceeds until 1000 cycles. The delamination area for NMP is found to be larger than that for NP in each cycle. The delamination for both NP and NMP starts at the corner of the die after 200 cycles in TST (II), which difference from TST (I) is in the thinner Cu substrate thickness. With increasing the number of cycles, the delamination area increases, but the rate is more significant than that in TST (I). TST (III) with thicker s-Ag layer thickness for both NP and NMP than those s-Ag thickness in TST (I) shows delamination after 400 cycles. This trend is similar to TST (II). One of the common phenomena obtained in TST (II) and (III) is at the point where delamination occurred at around four corners only. By reducing the Cu substrate thickness or increasing the s-Ag layer thickness, the stress leading to the delamination during TST would have decreased in TST (IV), which difference from TST (I) is in the maximum temperature. Almost no delamination was observed in NP, whereas partial delamination happened in NMP, although the delamination area was smaller than in TST (I). Small  $\Delta T$  gave rise to a small delamination area, as with the previous results [2, 3]. In TST (V), indicating temperature holding testing, no delamination was observed at all throughout the test for both s-Ag materials. A temperature variation would be necessary for the delamination.

In NBT (I), the delamination in NP is seen at the two corners after 400 cycles, and then on the one-side edge, a significant delamination happens. With increasing the number of cycles, the delamination area gradually increases. In the case of NMP, after 200 cycles, the first delamination is seen in the one-side edge, and the area increases with increasing the number of cycles. In the NBT (II) and (III) conditions, a similar trend is seen to NBT (I). Also, in every condition, NP showed a smaller delamination area than NMP at every cycle. All SAT results are displayed in Appendix F.



No.	s-Ag	0 cycle	200 cycle	400 cycle	600 cycle	800 cycle	1000 cycle	
I	NP							
	NMP							
II	NP							
	NMP							
III	NP							
	NMP							
IV	NP							
	NMP							
V	NP		<b>Temperature storage</b>					
	NMP							

(a)

No.	s-Ag	0 cycle	200 cycle	400 cycle	600 cycle	800 cycle	1000 cycle
I	NP						
	NMP						
II	NP						
	NMP						
III	NP						
	NMP						

(b)

Fig. 3-10 Representative SAT images after (a) TST and (b) NBT.

No.	s-Ag	SAT Cut line View	Cross section SEM image	100 $\mu\text{m}$
I	NP			
	NMP			
II	NP			
	NMP			
III	NP			
	NMP			
IV	NP			
	NMP			
V	NP			
	NMP			

(a)

No.	s-Ag	SAT Cut line View	Cross section SEM image	100 $\mu\text{m}$
I	NP			
	NMP			
II	NP			
	NMP			
III	NP			
	NMP			

(b)

NP			
State	Initial	TST	NBT
NMP			

(c)

Fig. 3-11 Representative cross-section SEM analysis results after 1000 cycles of (a) TST, (b) NBT, and (c) Microstructure image analysis results in red frame regions depicted in the SEM cross-section images (Red: Pore).

Fig. 3-11 (a) and (b) representative cross-sectional SEM observation results for TST and NBT after 1000 cycles, respectively. The cutting line and observation direction are indicated in the SAT images. All cross-sectional SEM images except for TST (IV) and (V) showed a similar cracking behavior toward the middle of the bonded region. Firstly, a crack was initiated at the top left corner of the s-Ag layer. Then it propagated into the s-Ag layer at an inclined angle of approximately  $45^\circ$  to the substrate surface. After that, the propagation direction was changed to the horizontal direction along with the substrate surface, which is probably associated with the maximum shear stress direction in the s-Ag layer [5]. Although those “straight” cracks were commonly found in all conditions other than TST (V). Other “wavy” cracks were observed in TST (I), (II), and (IV). In TST (I) and (II) for both NP and NMP, a straight crack was found to change to a wavy crack, propagating out-of-plane in the middle of the bonded section, irrespective of s-Ag materials. Note that a crystal grain morphology was different in only the wavy cracking region. As illustrated in Fig. 3-11 (c), pores indicated as red-colored portions and crystal grains are found to grow after 1000 cycles in TST (I) for both NP and NMP. Since the number of pores was reduced, multiple pores would have merged into one originating from growing crystal grains in a harsh environment. However, in TST (IV) for NMP, only a wavy crack was found instead of a straight crack. In the DAA, the morphology of the crystal grain was unchanged. Therefore, the wavy crack might have happened coincidentally. Only an inclined short crack was found in TST (IV) for NP. In TST (III) for both NP and NMP, only a straight crack was seen, indicating that no damages based on crystal grain growth were introduced. In TST (V), no cracks were found either straight or wavy for NP and NMP. In the case of NBT, all the DAAs showed only straight cracking and unchanged crystal grain morphology before and after the tests. According to the Ostwald ripening law [12, 13], microstructure aging becomes active with increasing holding time at high temperatures. Accordingly, mechanical force application with a short period of 3 min would not have been enough to give rise to pore growth in the s-Ag layer.

Note that the white-colored portion corresponding to the delamination area in SAT images includes straight cracking and wavy cracking because the 25 MHz ultrasonic probe used here covers the entire s-Ag layer to be observed.

3-2-4. Delamination analysis

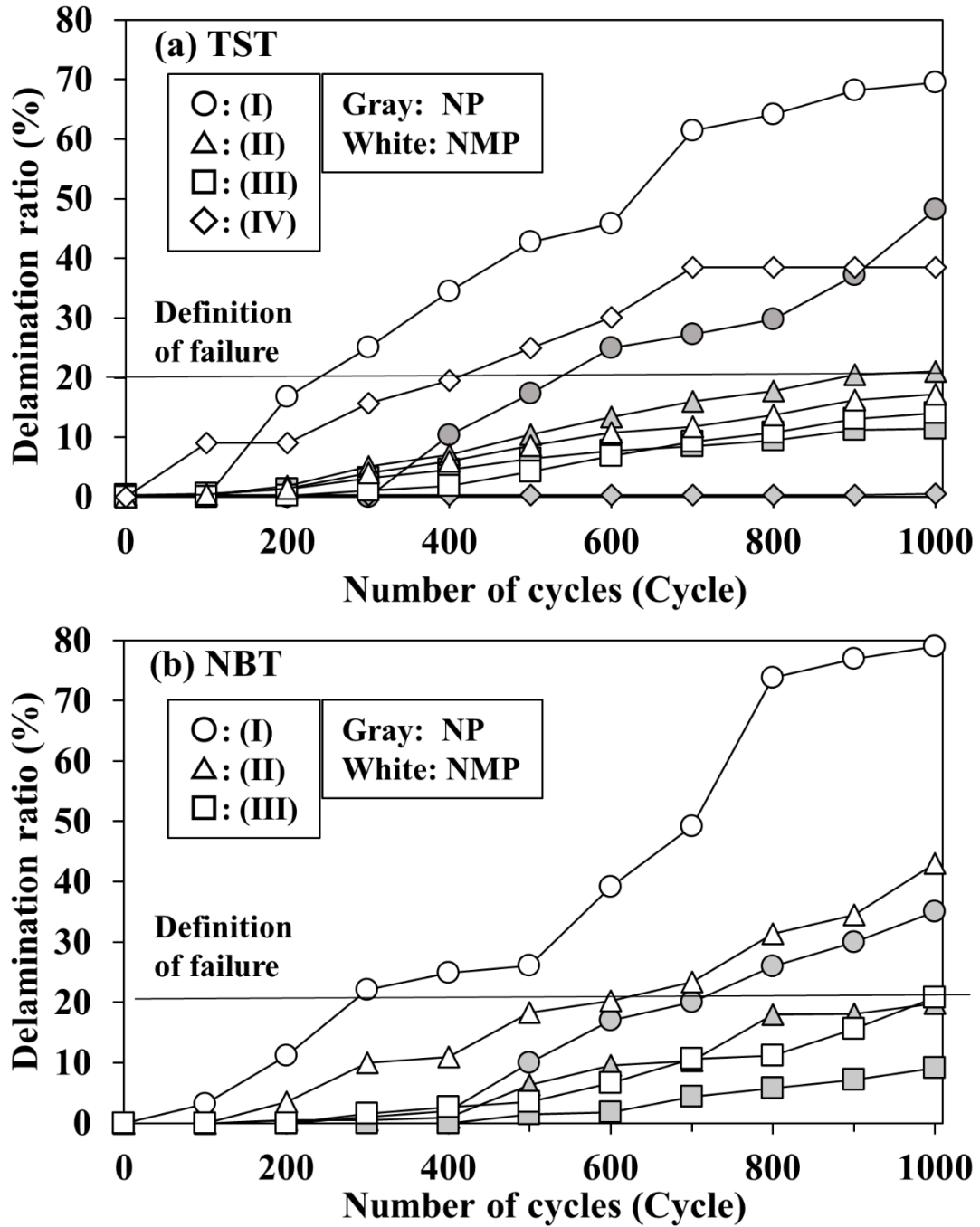


Fig. 3-12 Delamination ratio as a function of the number of cycles of (a) TST and (b) NBT.

Fig. 3-12 (a) and (b) depict the relationship between the number of cycles and delamination ratio after TST and NBT, respectively. The delamination ratio is defined as the ratio of the white-colored area corresponding to the delaminated area in a SAT image to the entire SiC die area. All the data in Fig. 3-12

were based on SAT images in Fig. 3-10. Gray and white colored plots indicate NP and NMP, respectively, and the difference in plot style indicates the difference in test conditions. In Fig. 3-12 (a), the delamination ratio for NP in TST(I) is almost 0% even after 300 cycles. Then, it monotonically increases to around 50% after 1000 cycles at a constant rate of roughly 0.7% per cycle. For NP in TST (II) and (III) with a thin substrate and a thick s-Ag layer, respectively, those delamination ratios increase from 200 to 1000 cycles, and the increasing rates show almost half of the rate in TST (I). For NP in TST (IV), however, almost no delamination happened throughout the TST. For NMP in TST (I), the delamination is found to start after 200 cycles. The delamination ratio under each cycle takes larger values, reaching 70% after 1000 cycles. The increasing rate for NMP was roughly twice that for NP. For NMP in TST (IV), the delamination ratio increased from 300 to 1000 cycles, reaching 40% in 1000 cycles, although the NP DAA showed almost no delamination. The difference between the two comes from the difference in degradation mode. A wavy crack was observed in the NMP DAA under the TST (IV), which would have produced a large delamination ratio. However, NMP in TST (II) and (III) has no significant differences between NMP and NP. This tendency implies that under fewer stress conditions originating from a thin substrate or thick s-Ag layer, a crack introduced inside the s-Ag layer propagated slowly, whether the crack form is wavy.

The NBT results in Fig. 3-12 (b) showed a similar trend to the TST results. The delamination ratio increased with increasing the number of cycles. In every NBT condition, the delamination ratio for NMP was larger by over twice that for NP. In the case of NBTs, a crack propagation speed depended on the magnitude of applied force to the DAAs with NP and NMP. In NBT, under several conditions, the numbers of cycles to failure were below 1,000 cycles, which were obtained at a constant frequency of 0.0056 Hz. In the bending-mode fatigue test at 10 Hz with RT, the s-Ag's lifetime was around 50,000 cycles [5]. Another experiment where the three-point bending-mode fatigue test was conducted at 1 Hz at 125 °C showed a failure at around 7,000 cycles [14]. Those comparisons imply that the lifetime of s-Ag strongly depends on frequency during the fatigue test, indicating a solid strain rate dependency on fatigue.

Fig. 3-13 (a) and (b) show the Weibull plot of the delamination ratio for NP and NMP obtained in TST and NBT, respectively. The definition of plot style is identical to that in Fig. 3-12. Here, five specimens per condition were subjected to TST and NBT, and the delamination ratio for each specimen after 1000 cycles in Fig. 3-12 was employed for drawing the Weibull plot. The median rank method was used for delamination probability calculations [2]. In many conditions, the delamination ratio takes a linear relationship with delamination probability on the Weibull statistics sheet, which indicates that the data for

each condition can be fitted well using a single two-parameter Weibull distribution function. According to the analysis of the strength of brittle materials, only one fracture mechanism existed in a series of DAAs under the same test condition. However, only TST (I) for NP and NMP and TST (IV) for NMP possessed a clear inflection point, as it is indicated using a solid line shown in Fig. 3-13 (a). That is, those data could be fitted using two straight lines. Generally, considering the strength of brittle materials with a statistical approach, the fact that two straight lines well fit the data in the Weibull plot means that a series of the DAAs failed under two different fracture modes. As shown in Fig. 3-13 (b), no inflection point was found in all the data obtained in NBT, indicating that all the DAAs under the same test condition fractured under a sole mechanism.

In this study, the definition of die attach failure was set to be 20% in the delamination ratio. When a s-Ag material with random particle size was used under a wide range of temperature changes and high-stress application, the s-Ag DAAs exceeded the life at the early stage of the test, as shown in Fig. 3-12. Also, even under the same condition, some DAAs exceeded the life after 1000 cycles, as shown in Fig. 3-13. Those experimental facts indicate that the range of the optimum condition for designing the s-Ag layer without failure can be specified if the physical phenomena causing its degradation could be understood correctly.



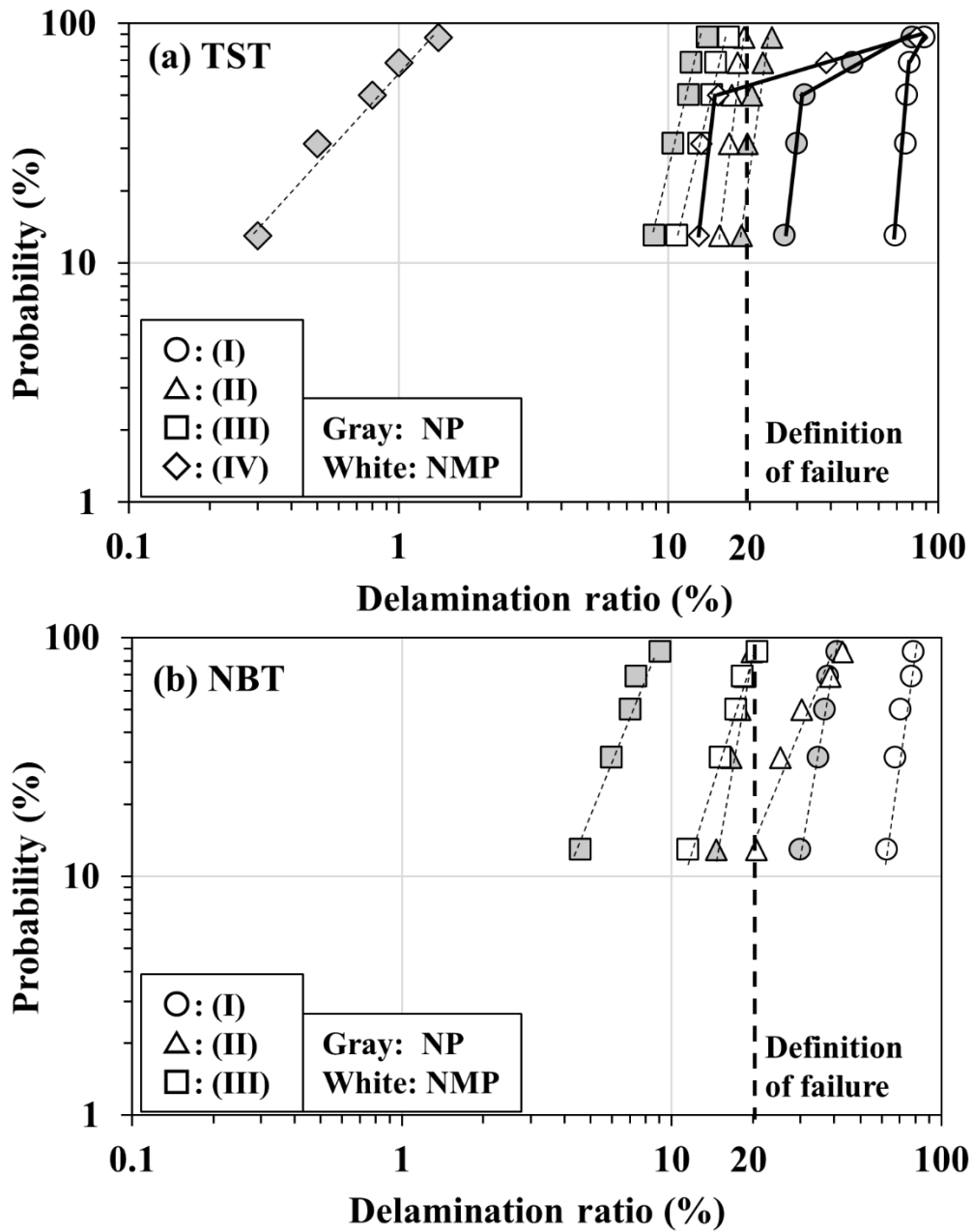


Fig. 3-13 Weibull plot of delamination ratio after 1000 cycles of (a) TST and (b) NBT.

### 3-2-5. Damage parameter validation

The multiple degradation mechanisms shown in Fig. 3-13 should be understood in more detail for further improvement of the reliability of s-Ag die attach. In general, the accumulated APS has been utilized as an appropriate parameter to describe the degradation of the s-Ag layer [3, 14-20]. The APS value can describe the s-Ag's plastic flowability, which would affect the degradation of s-Ag die attach during TST

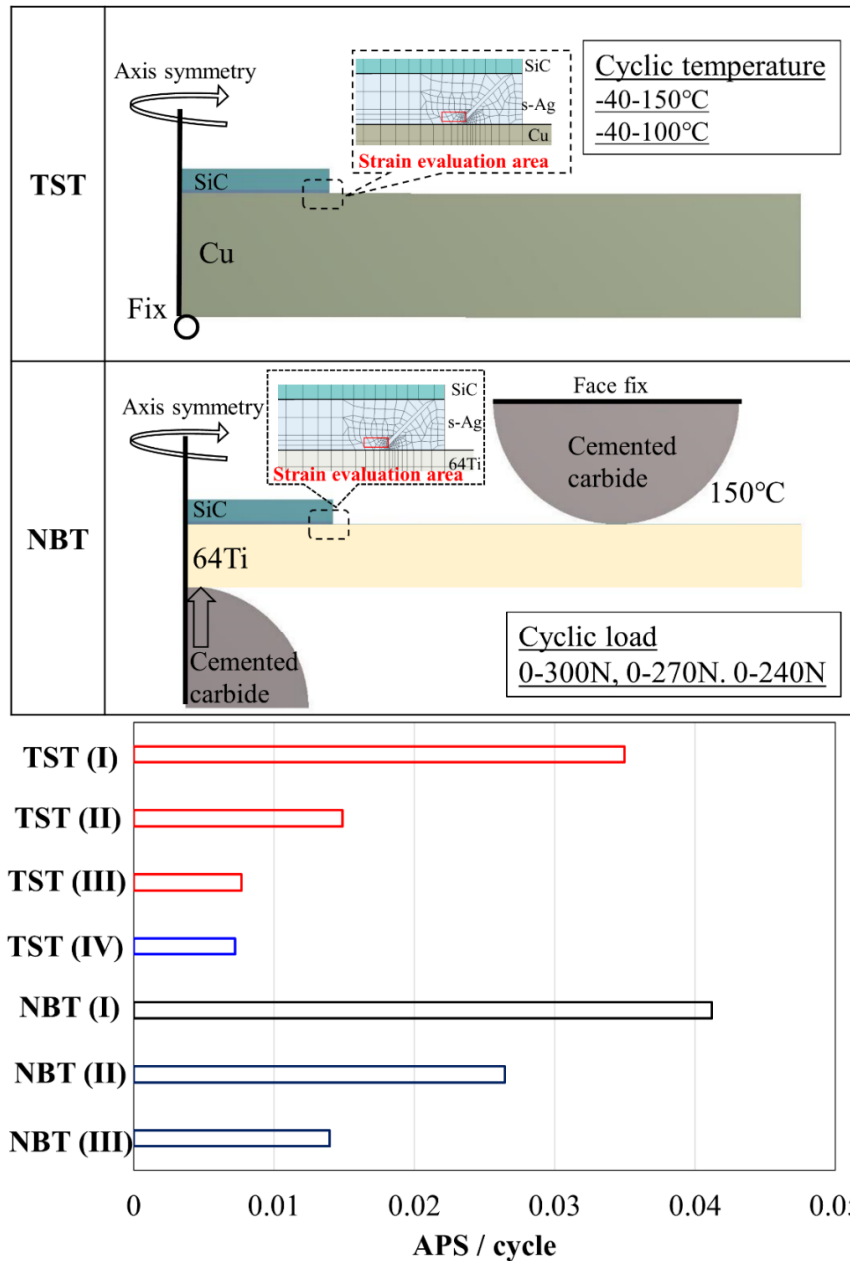
and NBT. However, NP and NMP had a different temperature dependence on tensile mechanical properties as mentioned in the Chapter 2. That is, APS cannot intrinsically consider the s-Ag plastic resistivity difference by applied stress. That is, APS cannot intrinsically consider the s-Ag plastic resistivity difference by applied stress. For a comprehensive understanding of multiple degradation mechanism classification for s-Ag die attach with NP and NMP, the author proposes a new parameter of DP, which is defined as the ratio of the APS to plastic strain,  $\varepsilon_p$ , originating from uniaxial tensile testing at the highest temperature in each condition. The DP can be given as follows:

$$DP = \frac{APS}{\varepsilon_p} \quad (3)$$

Here, the APS around a tip of a crack introduced into the s-Ag layer is considered for DP calculation. The APS divided by  $\varepsilon_p$  of the s-Ag material for each condition indicates the possibility of cracking originating from plastic flow around a tip of a crack in the s-Ag layer, which can be regarded as the percentage of a crack that can propagate from the stress intensity area in the s-Ag layer, for example, crack tips. Considering that the endurance until fracture differs for each s-Ag material, the APS around a tip of a crack should be normalized by using  $\varepsilon_p$  of each s-Ag material under each condition, which indicates that the degradation can be expressed irrespective of the difference in s-Ag material. Therefore, DP is an appropriate parameter compared with APS in making an overall description of s-Ag degradation under certain mechanism.

Fig. 3-14 shows the two dimension (2D) FEA models for TST and NBT produced in commercial software of ANSYS 19.0. The 2D models were reasonable due to the symmetrical assembly configuration of all DAAs used in the experiment. The axis symmetry condition was set on the left edge of the models. Temperature and force variations were set as boundary conditions for TST and NBT, respectively, based on those experimental conditions listed in Table 3-3. An inclined crack was initially made into the s-Ag layer based on the experimental results [5]. To avoid the singularity, the mean APS value for each condition took the average values at 88 nodes located within a  $20 \mu\text{m} \times 10 \mu\text{m}$  squared area around a tip of the crack as depicted in Fig. 3-14. In addition, the crack shape would also affect the APS value. However, in this study, the crack shape was set to the same configuration as shown in Fig. 3-14 for simplistically focusing on the DAAs configuration and external boundary condition dependences on the calculated APS value. Each material characteristic input was identical to our previous studies [5, 20]. The bar graph compares the averaged APS values under each condition as a representative result. The value for TST (I) was 0.035,

which was the largest among the TST conditions. Decreasing the substrate thickness to half, the TST (II) value decreased to 0.015, around 40% of the TST (I) value. By increasing the s-Ag layer thickness to twice, TST (III) value was reduced to 0.008, which was comparable to the TST (IV) value. NBT (I) took an immense value of 0.041 in all the conditions treated here, which was larger by 0.006 than the TST (I) value. With decreasing applied force, the value decreased proportionately.



**Fig. 3-14 FEA geometry, mesh configuration, boundary condition, and FEA calculation results of averaged APS value in the evaluation area.**

Based on Fig. 3-14, the DP values were calculated as shown in Fig. 3-15. The definition of a fill color is identical to that in Fig. 3-13. Frame color definition is identical to that in Fig. 3-14. The DP values were separately derived considering the  $\varepsilon_p$  difference between NP and NMP at each temperature. Under conditions except for TST (IV), the DP values of NMP were roughly 1.7 times higher than those of NP. All the DP values are listed in Table 3-4, which was used to derive Fig. 3-15.

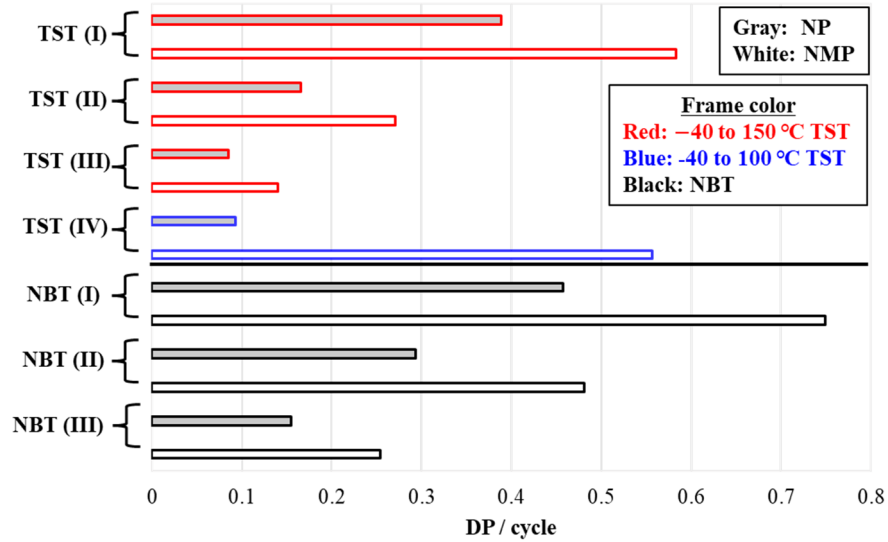


Fig. 3-15 Damage parameter numerical results of all experiments.

Table 3-4 DP parameter derivation list.

Item	APS	$\varepsilon_p$	DP
TST (I)	0.035	0.095	0.37
		0.055	0.64
TST (II)	0.015	0.095	0.16
		0.055	0.27
TST (III)	0.008	0.095	0.08
		0.055	0.14
TST (IV)	0.007	0.078	0.09
		0.013	0.56
NBT (I)	0.041	0.095	0.43
		0.055	0.75
NBT (II)	0.026	0.095	0.28
		0.055	0.48
NBT (III)	0.014	0.095	0.15
		0.055	0.25

Fig. 3-16 shows the delamination ratio after 1000 cycles as a function of APS and DP. The delamination ratio used here is the value at the delamination probability of 63.2% for each condition in Fig. 3-13. The plot color and style definition are identical to that in Fig. 3-12 and Fig. 3-13. The difference in plot frame color is identical to that in Fig. 3-15. APS and delamination ratio relation have a positive correlation in double logarithmic graph. However, the plots are scattered between NP and NMP as indicated in the arrows shown in Fig. 3-16 (a). Only APS associated with plastic flowability was not suitable for classifying failure mode differences among experiments. By contrast, the plots were well fitted using two linear approximation lines in the double logarithmic graph of the delamination ratio and DP relation as shown in Fig. 3-16 (b). The difference in delamination ratio between the two lines was at most 10% at the DP value of around 0.09. In addition, at the DP value around 0.6, the two lines cross, indicating the same delamination ratio value. In both lines, the DP value lower than 0.18 fulfills the delamination ratio lower than 20%, which is a condition for s-Ag die attach regarded as fracture. Red frame plots showing TST (I)–(III) at  $-40^{\circ}\text{C}$  to  $150^{\circ}\text{C}$  on NP and NMP were close to the upper straight line, which indicates that high-temperature cycling test with long holding time would cause cracking originating from material aging in the s-Ag layer Fig. 3-13. During testing, the s-Ag mechanical property weakens because of pore growth originating from crystal grain growth, corresponding to an increase of the DP value. Consequently, the delamination ratio value with aging would result in a higher value than that without aging. By contrast, black frame plots showing NBT (I)–(III) at  $150^{\circ}\text{C}$  and blue frame plots showing TST (IV) from  $-40^{\circ}\text{C}$  to  $100^{\circ}\text{C}$  were close to the lower straight line. Under those conditions, material aging would not occur.

By using the proposed DP, the delamination ratio data could be divided into aging and non-aging during testing. Therefore, the DP would work well to find a condition that s-Ag material can show long-term durability against thermal and mechanical cyclic loading.

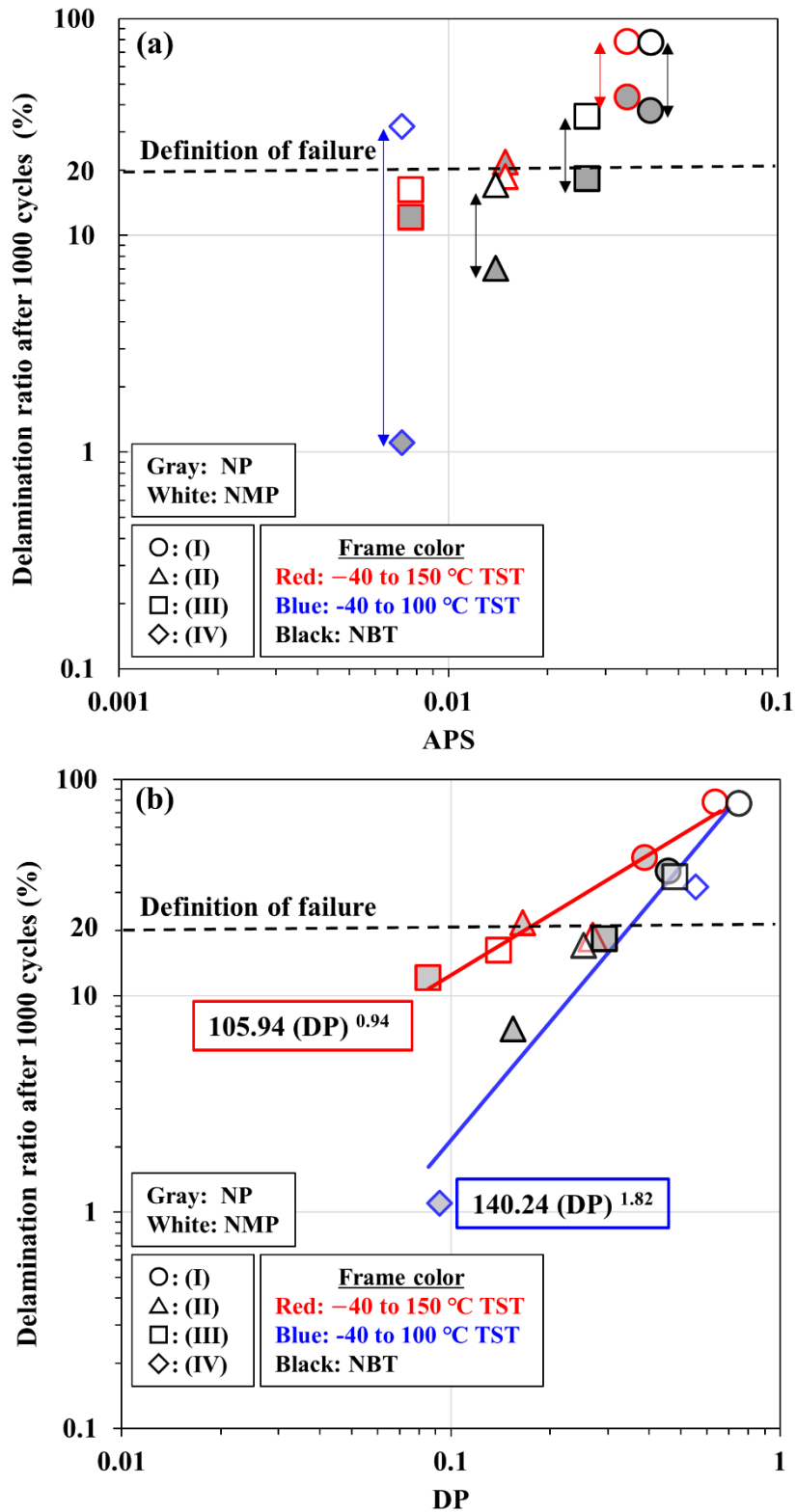


Fig. 3-16 Delamination ratio after 1000 cycles as a function of APS (Upper graph) and DP (Downside graph).

### 3-3. Conclusion

In this Chapter, the degradation mechanism of s-Ag DAAs is experimentally investigated by TST and mechanical bending test (FBT and NBT). For FBT, a bar-shaped specimen is subjected to two types of FBTs (centered bending test] for bending moment application and shifted bending test [SBT] for shear force application). A crack path in SBT was similar as TST, which indicated that the maximum shear mechanical stress played an important role in imitating the same s-Ag cracking morphology after TST. However, the crack propagation speed per cycle in TST was 4,000 times faster than the propagation speed during SBT. The lifetime assessment period of SBT was approximately 1,400 times shorter than that of TST. The fracture surface of the s-Ag layer after TST was smoother than that after SBT, which indicated that the s-Ag layer during TST fractured with plastic deformation at the elevated temperature side, whereas, SBT fracture mechanism almost originated from a brittle fracture with a granular fracture. The difference would come from the environmental differences of temperature and induced time. Bar-shaped specimens with FBTs were obtained by uniaxial bending tests, which could not reflect the out-of-plane deformation during TST.

NBT can mechanically provide the same deformation as TST like. NP and NMP were sintered at 300°C for 10 min under 60 MPa pressure. TSTs were conducted under thermal cyclic loading between -40°C and 150°C with a trapezoid waveform for 60 min per a cycle. NBTs were conducted under cyclic mechanical loading between 0 and 300 N with a triangular waveform for 3 min per a cycle at 150°C. SAT evaluated the die-attach delamination during TST and NBT. NP DAAs showed less delamination than NMP DAAs after TST and NBT. Small temperature and force variation led to small delamination. The thick s-Ag layer and thin substrate showed the small delamination of s-Ag after TST. Cross-sectional observation demonstrated that mechanical cracking and material aging in the s-Ag layer coexisted after TST under the condition of -40°C to 150°C. The DP proposed in this study worked well to fit the delamination area ratio after 1000 cycles, which indicated that the degradation can be categorized into two groups.

## References

- [1] T. Herboth, M. Guenther, R. Zeiser, and J. Wilde, "Investigation of Stress States in Silicon Dies Induced by the Low Temperature Joining Technology," in *Proc. 14th International Conference on Thermal, Mechanical and Multi-Physics Simulation and Experiments in Microelectronics and Microsystems, (EuroSimE)*, Wroclaw, Poland, April, 2013, doi: 10.1109/EuroSimE.2013.6529945.
- [2] T. Herboth, M. Guntherl, M. Gunther, and J. Wilde, "Assessment of Thermo-Mechanical Stresses in Low Temperature Joining Technology," in *Proc. 13th International Conference on Thermal, Mechanical and Multi-Physics Simulation and Experiments in Microelectronics and Microsystems, (EuroSimE)*, Cascais, Portugal, April, 2012, doi: 10.1109/ESimE.2012.6191762.
- [3] T. Herboth, M. Guenther, A. Fix, and J. Wilde, "Failure Mechanisms of Sintered Silver Interconnections for Power Electronic Applications " in *Proc. 63rd Electronic Components and Technology Conference*, Las Vegas, USA, May, 2013, doi: 10.1109/ECTC.2013.6575789.
- [4] M. Schaal, M. Klinger, B. Metais, R. Grüninger, S. Hoffmann, and B. Wunderle, "Reliability Assessment of Ag Sintered Joints Using a SiC Semiconductor and Determination of Failure Mechanism in the Field of Power Electronics," in *Proc. 21st International Conference on Thermal, Mechanical and Multi-Physics Simulation and Experiments in Microelectronics and Microsystems (EuroSimE)*, Cracow, Poland, July, 2020, doi: 10.1109/EuroSimE48426.2020.9152674.
- [5] K. Wakamoto, Y. Kumakiri, T. Otsuka, K. Nakahara, and T. Namazu, "Comparison of sintered silver die attach failure between thermal shock test and mechanical cycling test," *Japanese Journal of Applied Physics*, vol. 61, pp. SD1029-1-7, 2022, doi: 10.35848/1347-4065/ac5b23.
- [6] T. Namazu, T. Ishikawa, and Y. Hasegawa, "Influence of polymer infiltration and pyrolysis process on mechanical strength of polycarbosilane-derived silicon carbide ceramics," *Journal of Materials Science*, vol. 46, no. 9, pp. 3046-3051, 2010, doi: 10.1007/s10853-010-5182-0.
- [7] T. Namazu, K. Kuwahara, M. Fujii, S. Kanetsuki, S. Miyake, and S. Inoue, "Mechanical Reliability of Reactively Alloyed NiAl as a Structural Material," *Sensors and Materials*, vol. 28, no. 2, pp. 141-152, 2016. Doi:10.18494/SAM.2016.1164.
- [8] T. Namazu and S. Inoue, "Tensile and Creep Characteristics of Sputtered Gold-Tin Eutectic Solder Film Evaluated by XRD Tensile Testing," *Sensors and Materials*, vol. 22, no. 1, pp. 13-24, 2010, ISSN: 0914-4935.



- [9] H. W. Liu, "SHEAR FATIGUE CRACK GROWTH: A LITERATURE SURVEY," *Fatigue Fract. Engng. Mater. Struct.*, vol. 8, no. 4, pp. 295-311, 1985, doi: doi.org/10.1111/j.1460-2695.1985.tb00429.x.
- [10] K. Wakamoto, Y. Mochizuki, T. Otsuka, K. Nakahara, and T. Namazu, "Temperature Dependence on Tensile Mechanical Properties of Sintered Silver Film," *Materials*, vol. 13, no. 18, pp. 4061-4071, Sep., 2020, doi: 10.3390/ma13184061.
- [11] C. S. Chenyang Wang, G. Xu, Z. Jing, J. Liu, and Y. Su, "Microstructure and Mechanical Property Improvement of Laser Additive Manufacturing Ti-6Al-4V via the Niobium Addition," *Materials Transactions*, vol. 61, no. 4, pp. 723-728, 2020, doi: 10.2320/matertrans.MT-M2019370.
- [12] H. Zhang, C. Chen, J. Jiu, S. Nagao, and K. Sugauma, "High-temperature reliability of low-temperature and pressureless micron Ag sintered joints for die attachment in high-power device," *Journal of Materials Science: Materials in Electronics*, vol. 29, no. 10, pp. 8854-8862, 2018, doi: 10.1007/s10854-018-8903-9.
- [13] P. Gadaud, V. Caccuri, D. Bertheau, J. Carr, and X. Milhet, "Ageing sintered silver: Relationship between tensile behavior, mechanical properties and the nanoporous structure evolution," *Materials Science and Engineering: A*, vol. 669, no. 4, pp. 379-386, 2016, doi: 10.1016/j.msea.2016.05.108.
- [14] J. Heilmann, I. Nikitin, U. Zschenderlein, D. May, K. Pressel, and B. Wunderle, "Reliability experiments of sintered silver based interconnections by accelerated isothermal bending tests," *Microelectronics Reliability*, vol. 74, pp. 136-146, 2017, doi: 10.1016/j.microrel.2017.04.016.
- [15] J. Heilmann, K. Pressel, and B. Wunderle, "Accelerated reliability testing and modeling of subsystems based on sintered silver thermal interface materials," in *Proc. 20th International Workshop on Thermal Investigations of ICs and Systems*, Greenwich, UK, Sep., 2014, doi: 10.1109/THERMINIC.2014.6972540.
- [16] J. Heilmann, I. Nikitin, U. Zschenderlein, D. May, K. Pressel, and B. Wunderle, "Advances and Challenges of Experimental Reliability Investigations for Lifetime Modeling of Sintered Silver Based on Interconnection," in *Proc. 17th International Conference on Thermal, Mechanical and Multi-Physics Simulation and Experiments in Microelectronics and Microsystems (EuroSimE)*, Montpellier, France, April, 2016, doi: 10.1109/EuroSimE.2016.7463347.
- [17] J. Heilmann, J. Arnold, and B. Wunderle, "Acceleration of lifetime modeling by isothermal bending fatigue tests," in *Proc. 16th International Conference on Thermal, Mechanical and Multi-Physics*

*Simulation and Experiments in Microelectronics and Microsystems*, Budapest, Hungary, April, 2015, doi: 10.1109/EuroSimE.2015.7103151.

- [18] D. J. Yu, X. Chen, G. Chen, G. Q. Lu, and Z. Q. Wang, "Applying Anand model to low-temperature sintered nanoscale silver paste chip attachment," *Materials & Design*, vol. 30, no. 10, pp. 4574-4579, 2009, doi: 10.1016/j.matdes.2009.04.006.
- [19] P. Rajaguru, H. Lu, and C. Bailey, "Sintered silver finite element modelling and reliability based design optimisation in power electronic module," *Microelectronics Reliability*, vol. 55, no. 6, pp. 919-930, 2015, doi: 10.1016/j.microrel.2015.03.011.
- [20] F. Forndran, J. Heilmann, M. Metzler, M. Leicht, and B. Wunderle, "A Parametric Simulative Study for Lifetime Prediction of Sintered Silver Die Attach Under Different Accelerated Testing Conditions," in *Proc. 22nd International Conference on Thermal, Mechanical and Multi-Physics Simulation and Experiments in Microelectronics and Microsystems (EuroSimE)*, St. julian, Marta, Apr., 2021, doi: 10.1109/EuroSimE52062.2021.9410830.

## 4. Sintered Silver Degradation Mechanism

### 4-1. Pore growth condition

#### 4-1-1. MD simulation

The cause of categorizing into two groups in Fig. 3-16 will be considered from the viewpoint of microstructure physics. The point is to clarify the main physical reason why the relationship between the relation between delamination ratio and DP was divided into two groups. To first explore the right reason for the s-Ag aging, molecular dynamics (MD) simulations were carried out. MD calculations have been widely adopted to analyze the physical movements of atoms and molecules by the following steps:

1. Determine the initial atomic position velocity, and boundary condition.
2. Calculation of force acting on each atom.
3. Update of atomic position and velocity.
4. Data analysis.

For the s-Ag case, the Ag particle diffusion during the sintering process has been studied to understand the sintering mechanism by MD simulation [1, 2]. In this study, molecular dynamics (MD) simulations were carried out by free software, LAMMPS. The simulation model configuration and boundary condition are shown in Fig. 4-1, together with the boundary condition.

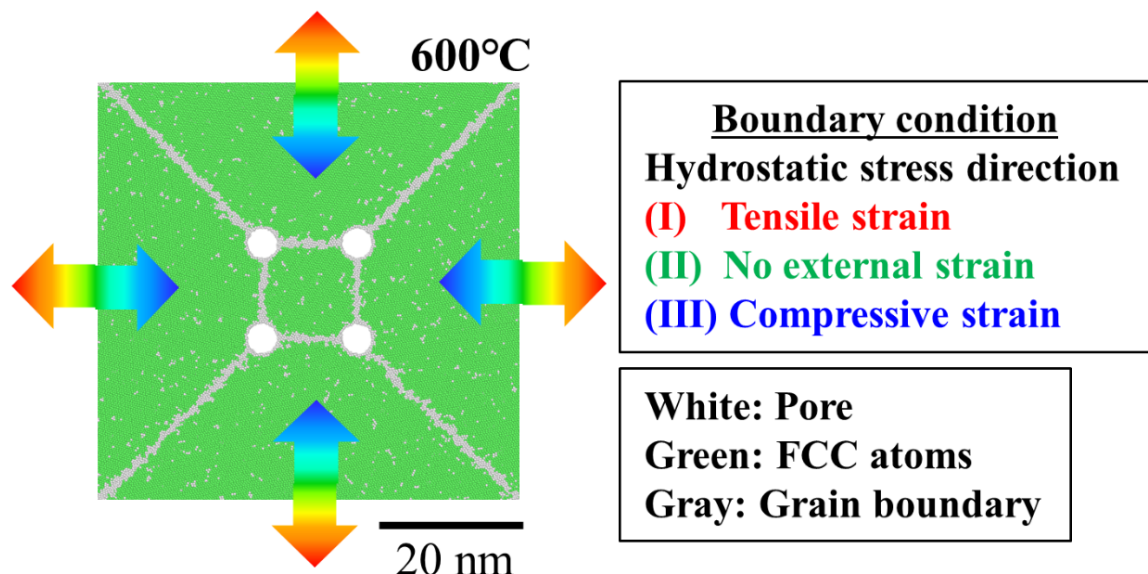


Fig. 4-1 MD calculation condition.

Four equal circular pores were symmetrically placed at each vertex point of the standard square positions surrounded by five grains. The symmetry configuration can stably calculate MD. In addition, different-sized crystals can observe crystal growth associated with Oswald ripening law [3,4]. The model includes four trapezoidal crystals with  $822 \text{ nm}^2$  in surface area and one square shape of grain with  $170 \text{ nm}^2$  in surface area. The grain boundaries were made of the misorientation angle setting between adjacent regions. The overall model configuration is  $58.8 \text{ nm}$  in X and Y directions and  $2.04 \text{ nm}$  in the Z direction. Periodic boundary condition in the Z direction was set. MD calculations are limited to treating up to microsecond time scales [5], which are significantly shorter than the actual pore growth time scales during experiments. The calculation temperature was set at  $600^\circ\text{C}$ , which was higher than the temperatures in the experiment to visualize the pore growth within the MD calculation time scale. The calculation time step was set to be  $1 \text{ fs}$ , and the entire calculation time was set up to  $3 \text{ ns}$ . A hydrostatic strain was selected from  $2\%$  in the compression direction to  $2\%$  in the tensile direction. A random crystallographic orientation was employed based on previous literature [6-8]. An embedded atom method (EAM) was adopted, which is commonly used for the Ag calculation [2, 9].

Fig. 4-2 (a) shows the MD simulation results after  $0.1 \text{ ns}$  passed. The upper and bottom images show pore configuration and hydrostatic stress distribution, respectively. The pore shape and size are found not to be changed so much under every strain condition. Hydrostatic stress is distributed uniformly at each state because the period time under an applied hydrostatic strain was very short. As shown in the graph on the relationship between applied strain and pore growth ratio, the pore size is found to be unchanged throughout the simulation. After  $3 \text{ ns}$  passed, as shown in Fig. 4-2 (b), however, the pore configuration is changed, which is strongly dependent on the applied strain value. Under the compressive strain condition, the pore size and composition were still similar to the initial state, whereas, under the tensile strain condition, those were changed because more atoms moved around grain boundaries by deformation and diffusion. As a result, the configuration of pores got asymmetry. Fig. 4-2 (b) suggests that high tensile stress generated along the grain boundaries accelerated atomic diffusion, leading to pore growth along the boundaries. In the relationship between applied strain and pore growth ratio, pore size was little changed under compressive strain applied. With increasing tensile strain, the pore size rapidly increased. At a tensile strain of  $2\%$ , the mean pore size grew to almost twice the initial state of that.

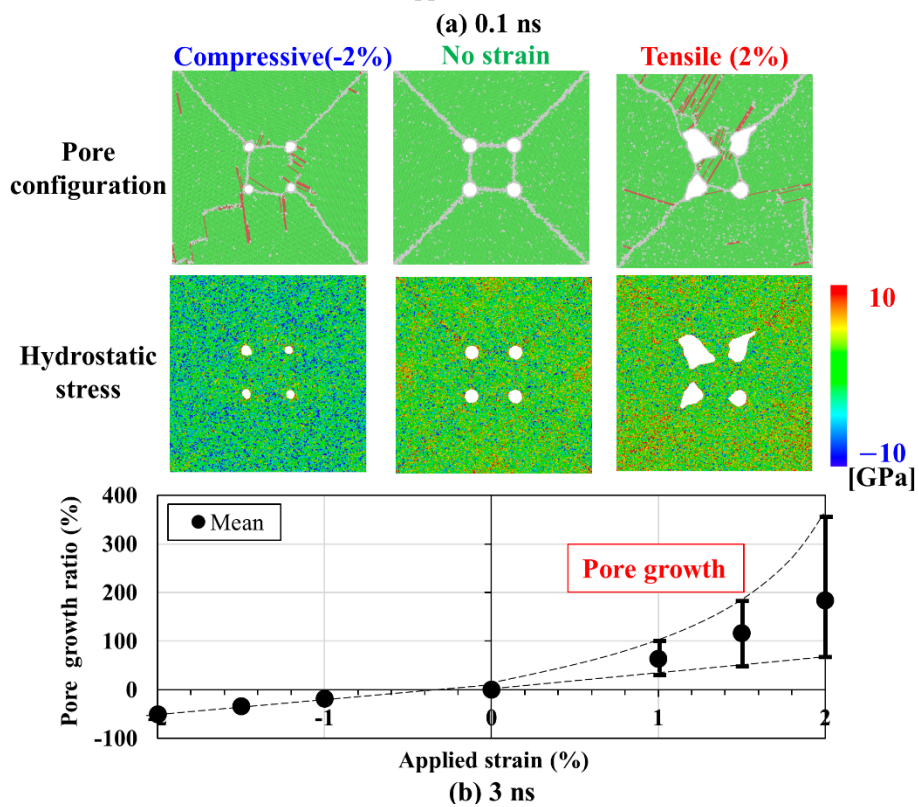
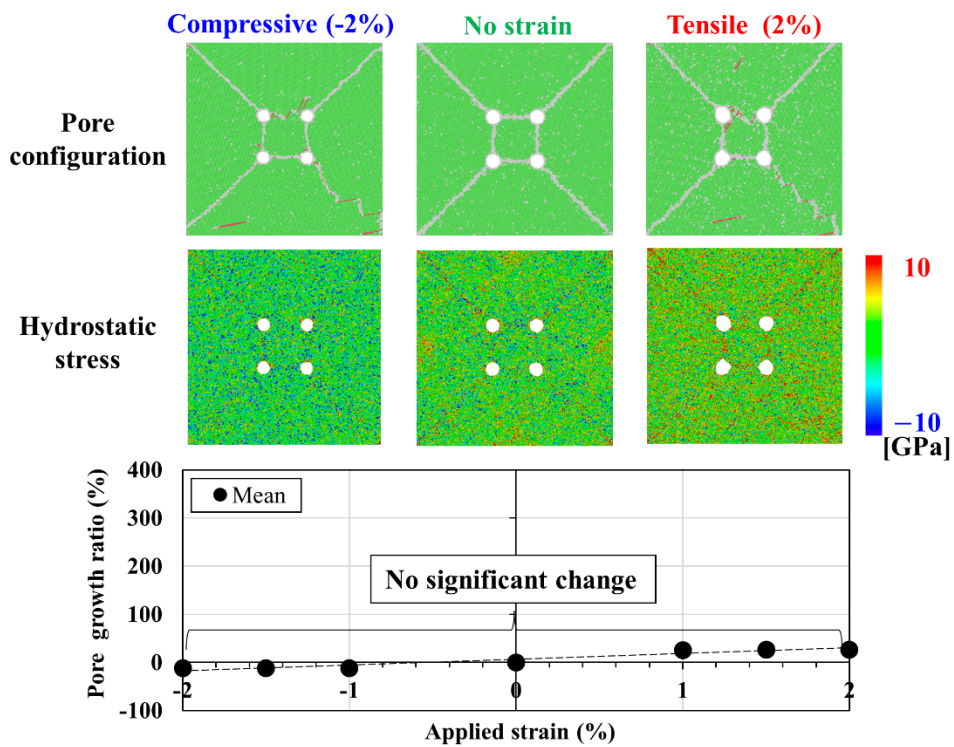


Fig. 4-2 Molecular dynamics simulation of (a) 0.1 and (b) 3 ns. (Upper side image: Pore configuration. Downside image: Hydrostatic stress distribution. Bar graph: Pore size growth ratio as a function of applied strain.)

#### 4-1-2. Stress direction

FEA was conducted to examine the stress component around a crack tip and inside the s-Ag layer in the die attach, considering straight crack and wavy crack, respectively, as shown in Fig. 3-11.

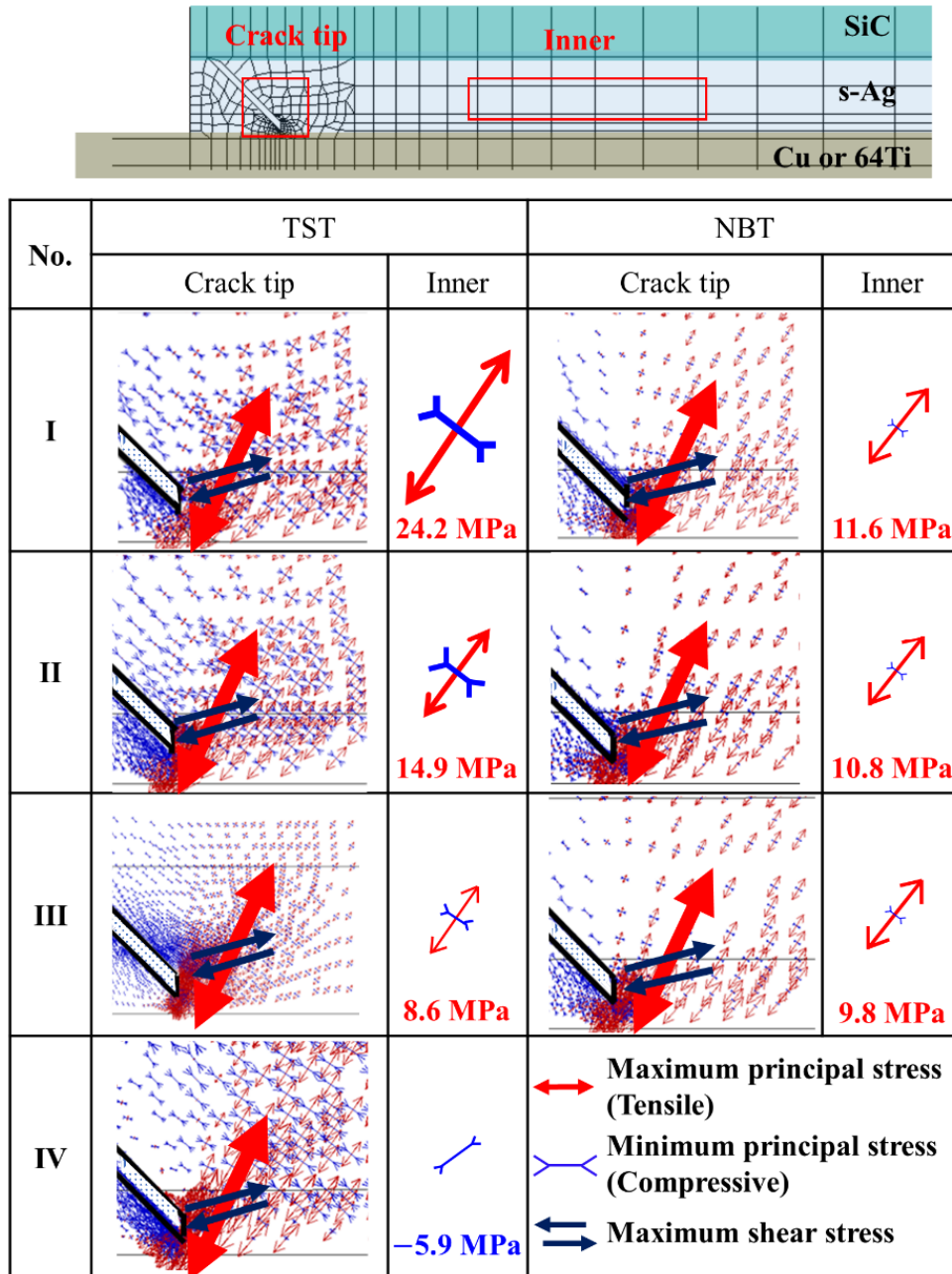


Fig. 4-3 Stress distribution at around a crack tip along with representative stress component and direction inside the s-Ag layer.

Fig. 4-3 shows stress distributions around a crack tip, representative stress components and direction inside the s-Ag layer. In this FEA model, pore is not considered in the s-Ag layer; thus, the averaged stress direction in the layer can be considered because the porosity level of NP and NMP was low in accordance with the cross-sectional SEM observations Fig. 2-19. Of course, the stress direction distribution would be changed by increasing the pore size and distribution during tests. However, this simulation aims to initially understand the main stress component in the s-Ag die layer during TST and NBT in the initial stage when the pore is not still grown up. The red and blue arrows indicate the maximum and minimum principal stresses, respectively. A set of black arrows indicate the maximum shear stress. At a crack tip, the stress direction shows almost the same in all the test conditions. The maximum principal stress is in tension, which is found to face a slightly inclined vertical direction. The minimum principal stress is in compression. The maximum shear stress direction determined by rotating the maximum principal stress direction by  $45^\circ$  is close to the horizontal line, which would have worked to change the crack propagation direction to horizontal along the s-Ag and substrate boundary in the experiment [10]. In the inner region, the maximum principal stress in tension dominates, and the angle tilts approximately  $30^\circ$  from the vertical axis except for TST (IV). The maximum principal tensile stress value is written in Fig. 4-3 for each condition, which was calculated by taking an average of the stress values in the red-squared region. In TST and NBT, those values were calculated at the highest temperature and the induced force, respectively, for each condition. The value for TST (I) was 24.2 MPa, which decreased to 14.9 MPa for TST (II) with decreasing Cu substrate thickness to half. For TST (III), the value decreased to 8.6 MPa, almost one-third of that for TST (I), with increasing the s-Ag layer thickness to twice that for TST (I). The compressive stress was dominant for TST (IV) since the highest temperature was 100, lower than 120 providing non-stress with the s-Ag layer [11]. For NBT (I), the value of tensile stress as the maximum principal stress was 11.6 MPa, which decreased to 10.8 MPa and 9.8 MPa with decreasing the applied force from 300 N to 270 and 240 N, respectively.

From the MD simulation results above, it was confirmed that the condition necessary for pore growth requires the application of tensile stress in the s-Ag layer. The FEA results suggested that tensile stress as the maximum principal stress was produced at an inclined crack tip and inside the s-Ag layer during both TST and NBT under almost all conditions. In several cases in this study's experiment, the thermal and mechanical cycling tests were conducted under the condition that pores quickly grew in the s-Ag layer.

## 4-2. Degradation criterion

### 4-2-1. Classical pore growth physics

The pore growth model combined “Thermo dynamics” and “kinematic law” is considered to determine a criterion for pore growth. The pore growth can be derived as following steps based on previous literature [12-15]. This calculation is supposed to show that the free energy change ( $dG$ ) and an atom ( $dN$ ) diffuses in the distance ( $l$ ) within time ( $t$ ). The thermodynamics force ( $f$ ) acted on each atom is estimated as the following equation:

$$f \cong -\frac{1}{l} \left( \frac{dG}{dN} \right) \quad (4)$$

The average speed ( $v$ ) of atom is derived from Einstein equation as the following equation:

$$v = \frac{fD}{kT} \quad (5)$$

where  $D$  is the diffusion coefficient,  $k$  is the Boltzmann coefficient, and  $T$  is the absolute temperature. Suppose the atomic transfer with diffusion occurs within the diffusion cross-section area ( $\alpha$ ), which can be assumed that the atom unit volume is  $\Omega$ . Then, the volume variation ( $dV$ ) can be derived as the following equation:

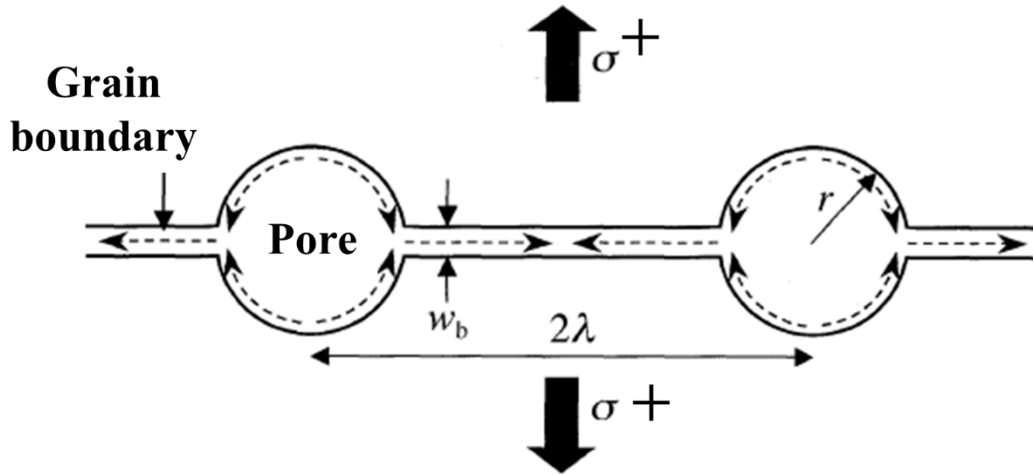
$$dV = \Omega dN = v\alpha dt \quad (6)$$

Combine from equation (4) to (6), the pore growth equation is derived as the following equation:

$$\frac{dV}{dt} = \Omega \frac{dN}{dt} = v\alpha = \frac{\alpha f D}{kT} = -\frac{D}{kT} \frac{\alpha}{l} \left( \frac{dG}{dN} \right) \quad (7)$$

Accordingly, if the free energy variation ( $\Delta G$ ) is calculated, the pore growth rate can be clarified. The physics model is considered to calculate the  $\Delta G$  under the applied stress to the pore, as depicted in Fig. 4-4. This model configuration supposes that spherical pores with radius  $r$  (volume  $V$ ) are located in a line by  $2\lambda$  interval distance. The external force of  $\sigma$  is applied to the grain boundary. It can be assumed that the pore is a sphere shape because the surface diffusion at the pore surface is sufficiently rapid compared to the grain boundary diffusion [12-15].





**Fig. 4-4 Classical pore growth physical model overview.**

When the pore  $\Delta n$  (atom increments) per  $\Delta t$  (time increments) diffuses from the pore surface to the grain boundary, the radius of the pore increases by  $\Delta r$  (radius increments) due to diffusion and migration of  $\Delta n$  from the pore surface to the grain boundary within  $\Delta t$  (time) per pore. The  $\Delta V$  (pore volume increment) is derived as the following equation:

$$dV = \Omega dN = 4\pi r^2 dr \quad (8)$$

In addition to the potential energy change of the external force as the Gibbs free energy change ( $\Delta G$ ), the surface energy change of the pore (the Helmholtz free energy change of the object) is also considered. Surface energy per area is assumed as  $\gamma$ . Then the  $\Delta G$  is derived as the following equation with surface energy variation and external force potential variation:

$$dG = 8\pi r \gamma dr - 4\pi r^2 \sigma dr = -4\pi r^2 \left( \sigma - \frac{2\gamma}{r} \right) dr \quad (9)$$

The average diffusion distance is estimated as the following equation:

$$l \cong \frac{\lambda - r}{2} \quad (10)$$

The diffusion cross section is estimated as the following equation:

$$\alpha \cong 2\pi r w \quad (11)$$

Then, combine the equations among (7), (9), (10), and (11), the pore growth rate under tensile stress is derived as the following equation:

$$\begin{aligned}
\frac{dV}{dt} &= -\frac{D}{k_B T} \frac{\alpha}{l} \left( \frac{dG}{dN} \right) = -\frac{D}{k_B T} \frac{\alpha}{l} \left\{ -4\pi r^2 \left( \sigma - \frac{2\gamma}{r} \right) \frac{dr}{dN} \right\} = \frac{D}{k_B T} \frac{\alpha}{l} \left\{ -4\pi r^2 \left( \sigma - \frac{2\gamma}{r} \right) \frac{\Omega}{4\pi r^2} \right\} \\
&= \frac{D\Omega}{k_B T} \frac{\alpha}{l} \left( \sigma - \frac{2\gamma}{r} \right) = \frac{D\Omega}{k_B T} \frac{2\pi r w_b}{\frac{\lambda - r}{2}} \left( \sigma - \frac{2\gamma}{r} \right) \\
&= \frac{4\pi D w_b \Omega}{k_B T} \left( \frac{r}{\lambda - r} \right) \left( \sigma - \frac{2\gamma}{r} \right) \tag{12}
\end{aligned}$$

It is worth noting that the positive or negative with pore growth rate is determined by the relationship between applied stress ( $\sigma$ ) and surface energy per pore radius ( $2\gamma/r$ ). The pore volume variation is derived as the following equation:

$$dV = \frac{4\pi D w_b \Omega}{k_B T} \left( \frac{r}{\lambda - r} \right) \left( \sigma - \frac{2\gamma}{r} \right) dt \tag{13}$$

#### 4-2-2. Pore growth criterion map

Equation (13) is utilized for determining the pore growth criterion stress plane. A pore included in the s-Ag layer is not a perfect sphere, as shown in Fig. 3-11 (c). For making the following calculations simple, s-Ag pore was considered as an equivalent sphere. In this study, the criterion that pore grew was set to be 250 nm in equivalent sphere diameter, considering pore growth after TST as shown in Fig. 3-11. Under that condition, the  $dV$  between the initial and grown states can be expressed geometrically as the following equation:

$$dV = \frac{4\pi}{3} \{ (250 \times 10^{-9})^3 - r^3 \} \tag{14}$$

**Table 4-1 Input parameter for deriving the equation (15).**

<b><math>\lambda</math> (nm)</b>	<b>500</b>
<b><math>w</math> (nm)</b>	<b>0.14</b>
<b><math>\Omega</math> (m<sup>3</sup>)</b>	<b><math>1.2 \times 10^{-29}</math></b>
<b><math>\gamma</math> (J/m<sup>2</sup>)</b>	<b>1.14 [2]</b>
<b><math>k</math> (J/K)</b>	<b><math>1.38 \times 10^{-23}</math></b>

By substituting the equation (14) and other parameter values, listed in Table 4-2 into the equation (13), the pore growth criterion stress of  $\sigma$ , around a pore can be given by:

$$\sigma\left(D \cdot \frac{dt}{T}, r\right) = \frac{2.28}{r} \left( \frac{5 \times 10^{-7} - r}{\frac{D \cdot dt}{T} \cdot r} \right) (4.5 \times 10^{-5} - 2.8 \times 10^{15} \cdot r^3) \quad (15)$$

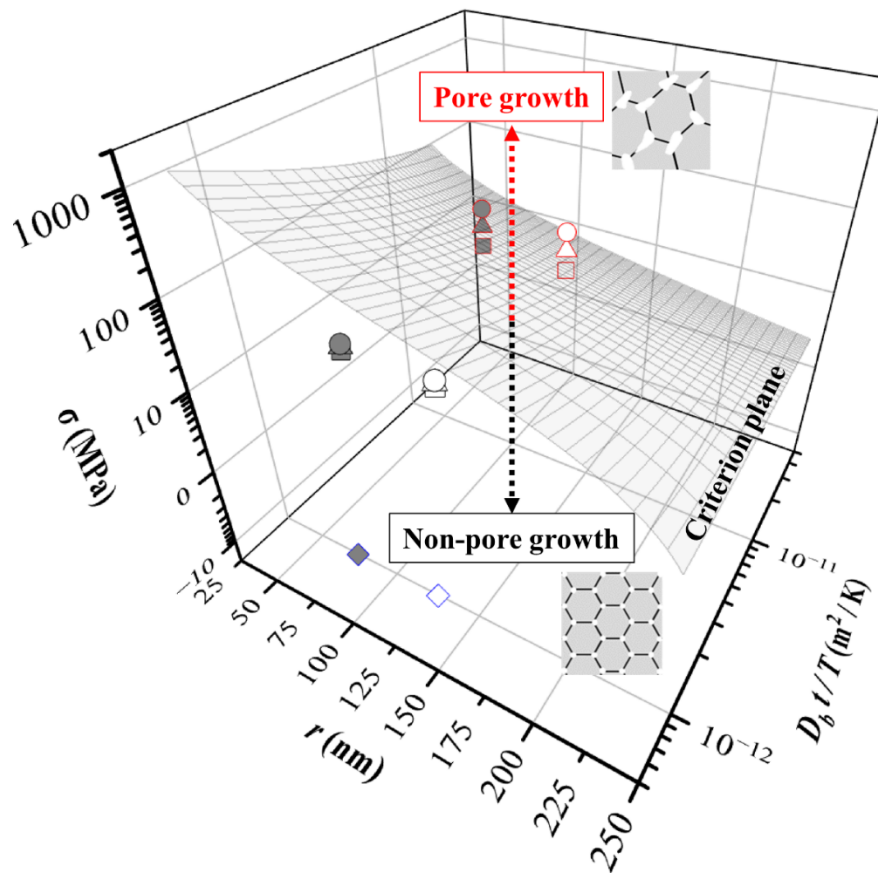
Fig. 4-5 shows the relationships between stress,  $\sigma$ , around a pore, initial pore size,  $r$ , and diffusion effect,  $Dt/T$ , where  $t$  is the time at the highest temperature applied during TST and the time at the stress applied during NBT. Here, the hatched plane shown in the figure is indicative of the critical stress condition where a pore starts growing, which was made by calculating the equation (15). The plane is found to be located in the tensile stress region, as the MD results suggested in Fig. 4-2. The  $\sigma$  necessary for pore growth depends on  $Dt/T$  and  $r$ , which is found to decrease with increasing the two values. Increasing the  $Dt/T$  indicates activating diffusion around a pore by increasing the temperature or stress-induced time. Accordingly, pore growth can quickly occur even without applying large stress. Also, the critical stress plane suggests that if a pore is initially large, a small stress for growing the pore from  $r$  to 250 nm, set as the critical size, is unnecessary.

For giving the plots originating from the experimental results in Fig. 4-5, the stress,  $\sigma$ , was estimated using each parameter listed in Table 4-2. Since pores were not included in the FEA calculations in Fig. 4-3, stress concentration should be considered if the  $\sigma$  around a pore needs to be estimated. Here, the  $\sigma$  around a pore was calculated by multiplying the FEA stress values in Fig. 4-3 by the stress intensity factor  $\alpha = 2.2$  surrounding a pore, as referred to the previous study [16].  $Dt/T$  was determined by considering the experimental condition in TST and NBT [17, 18]. Based on the cross-sectional SEM images, the  $r$  was set to be 80 nm and 130 nm for NP and NMP, respectively, which are the median values for each. The plot color and style definition are identical in Fig. 4-5 to those in Fig. 3-16. The experimental plots placed on the 3D graph could be categorized into two, located over and beneath the critical stress plane for pore growth. That is, the plots for TST (I)–(III) are placed over the plane, whereas those for NBT (I)–(III) and TST (IV) is placed beneath the plane. Note that the two groups divided by the critical stress plane are identical to those divided using the DP shown in Fig. 3-16. This result means that the s-Ag subjected to severe environments over the critical stress plane shows aging originating from pore growth. Therefore, it can be concluded that the DP proposed in this study is effective for separately evaluating the s-Ag degradation phenomena originating from only cracking and the combination of cracking and aging based

on pore growth.

**Table 4-2 Input parameter for plotting.**

$\sigma$ : (MPa)	Inner stress of Fig. 4-3 $\times \alpha$ ( $\alpha=2.2$ ) [16]
$r$ : (nm)	80 (NP) 140 (NMP)
$D$ : (m <sup>2</sup> /sec)	$D(\infty) \times e^{-\frac{E_a}{kT}}$ $D(\infty)=1.2 \times 10^{-5}$ $E_a = 70 \text{ kJ/mol}$ [2,17,18]
$T$ : (°C)	TST: 150, 100 °C NBT: 150 °C
$t$ : (sec)	TST: $1.8 \times 10^6$ NBT: $1.8 \times 10^5$



**Fig. 4-5 Pore growth criterion plane together with plots of each test condition as a function of initial pore size  $r$ , and diffusivity with  $Dt/T$ —showing s-Ag die attach reliability criterion.**

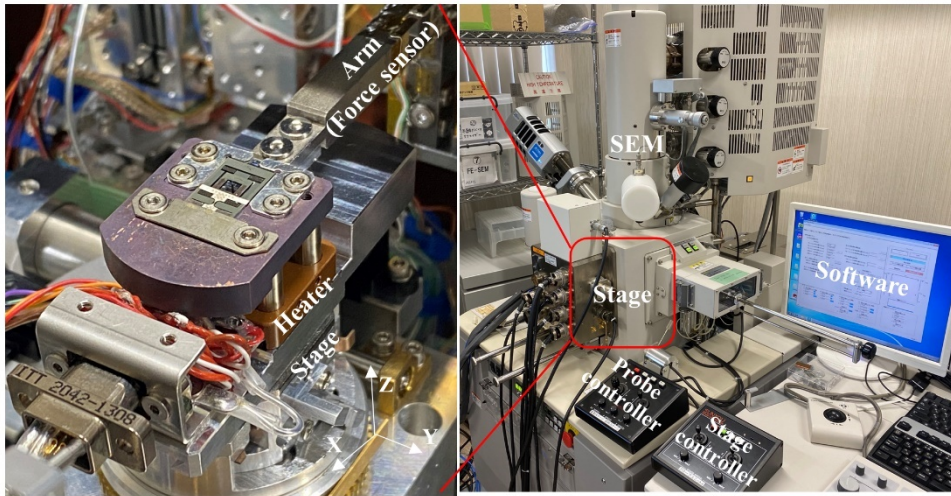
### 4-3. In-situ s-Ag pore growth observation

This section describes the pore growth transition for experimentally understanding the s-Ag pore growth mechanism in more detail. The In-situ SEM tensile testing system was adopted to clarify the s-Ag pore growth transition phenomena. Fig. 4-6 shows an In-situ SEM tensile testing overall photographs and an enlarged view of the test specimen part. This system comprises the conventional SEM system (Hitachi High-Technology, S-4800) and the original tensile testing system (SUNYOU, NPS T21066). The original tensile system includes the force sensor arm ( $3\text{ N}\pm 3\text{mN}$ ) attached to the probe (diameter:  $300\ \mu\text{m}$ ), the micro heater, and two actuators for driving the stage and force sensor motion. Two actuators are driven by the PZT motor (stroke:  $40\ \mu\text{m}$ , resolution:  $1\ \text{nm}$ , speed:  $0.05\text{-}0.5\ \mu\text{m}/\text{sec}$ ) and the stepping motor (stroke:  $15\text{mm}$ , resolution:  $0.5\ \mu\text{m}$ , speed:  $5\ \mu\text{m}/\text{sec}$ ). The basic specimen appearance is identical to Fig. 2-8 using Si spring configuration. The specimen is mechanically chucked and fastened by two screws to bind the specimen onto the stage, as shown in Fig. 4-7 (b). Also, two half-frame metal plates can guide the specimen's position. The probe located under the Si frame hole can be motion-controlled with the red arrow direction by the external software, as shown in Fig. 4-7 (b). The experiment condition is listed in Table 4-3. The s-Ag specimen was fabricated by the NP at  $300^\circ\text{C}$  for 10 min under the process pressure of 60MPa. The experiment temperature was set at  $300^\circ\text{C}$ , which was higher than the temperatures in the TST. The diffusivity with *the*  $Dt/T$  value, as introduced in section 4-2-2 at  $300^\circ\text{C}$  conditions, reaches the value order at  $10^{-11}$  under 20 minutes considering the input parameter as listed in Table 4-2. Consequently, the proposed tensile test condition potentially gives rise to the s-Ag's pore growth under tensile stress with a quasistatic speed condition, which is the same strain speed order value of TST and NBT.

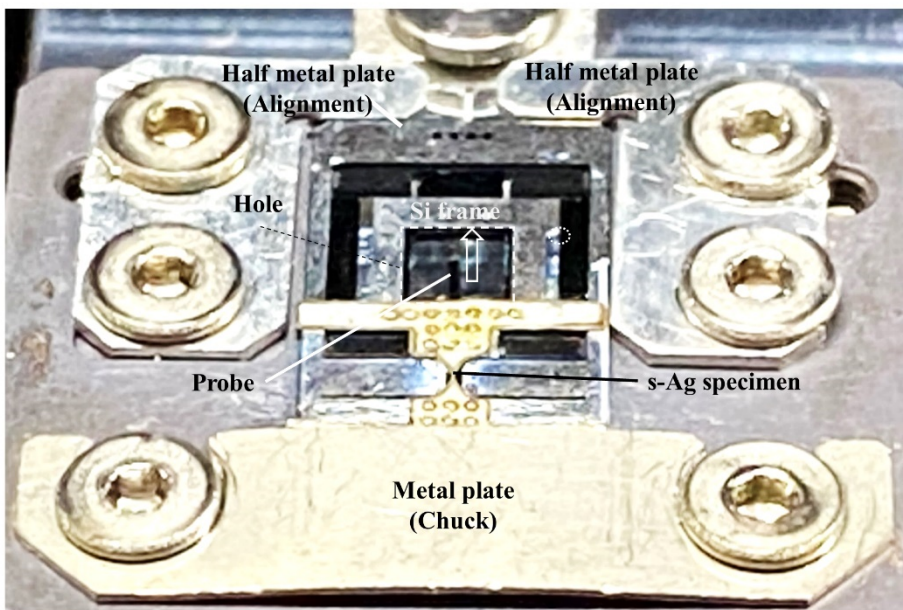
**Table 4-3 Experiment condition**

<b>Material</b>	<b>Process</b>	<b>Atmosphere (pa)</b>	<b>Temperature (<math>^\circ\text{C}</math>)</b>	<b>Strain speed (<math>\text{s}^{-1}</math>)</b>
<b>NP s-Ag</b>	<b>300 <math>^\circ\text{C}</math> 10 min 60 MPa</b>	<b><math>8 \times 10^{-4}</math></b>	<b>300</b>	<b><math>8 \times 10^{-4}</math></b>

**(a) In-situ SEM tensile testing system overview**



**(b) In-situ SEM tensile testing specimen set up image**



**Fig. 4-6 In-situ SEM tensile tester photographs (a) Overall photograph (b) Specimen attachment appearance.**

Fig. 4-7 shows a specimen process procedure schematic view. First, the s-Ag film with a 20  $\mu\text{m}$  thick specimen cut by an ultraviolet laser marker (KEYENCE Japan, 3-Axis UV Laser Marker MD-U1000) as shown in the top line in Fig. 4-7. The s-Ag specimen was introduced into the focused ion beam (FIB) tester (Hitachi High-Technology, SMI3050) to prepare the crack path for microstructure observations during tensile testing. Second, the notch acted as a stress concentration point was fabricated by the gallium (Ga) ion implantation, as illustrated in the middle line of Fig. 4-7. However, the s-Ag specimen's pore at around the crack tip can not observe well from the top view due to the surface roughness of the specimen surface at this stage. Therefore, the Ga ion is irradiated with an incline angle of  $30^\circ$  from the horizontal axis, as shown in the bottom right image of Fig. 4-7. The surface smoothness is enough for observing the pore from the top view on the s-Ag specimen surface by the SEM tester. The FIB beam condition is listed in Table 4-4.

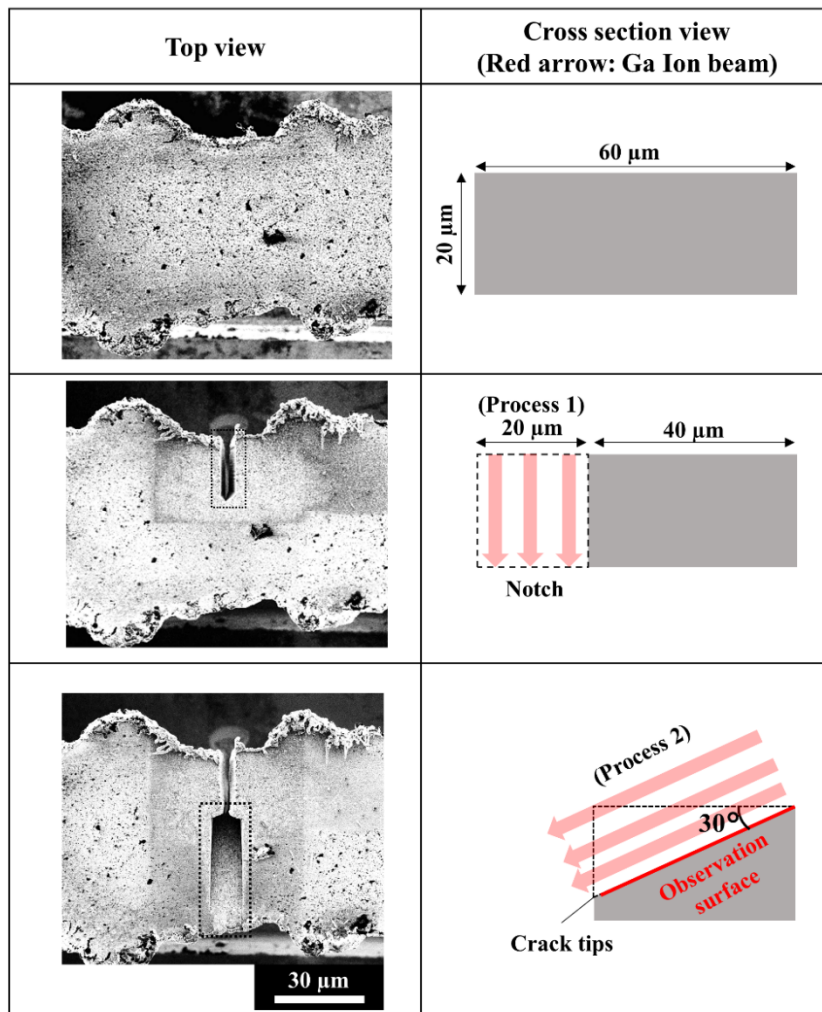


Fig. 4-7 Specimen fabrication steps

**Table 4-4 FIB process condition**

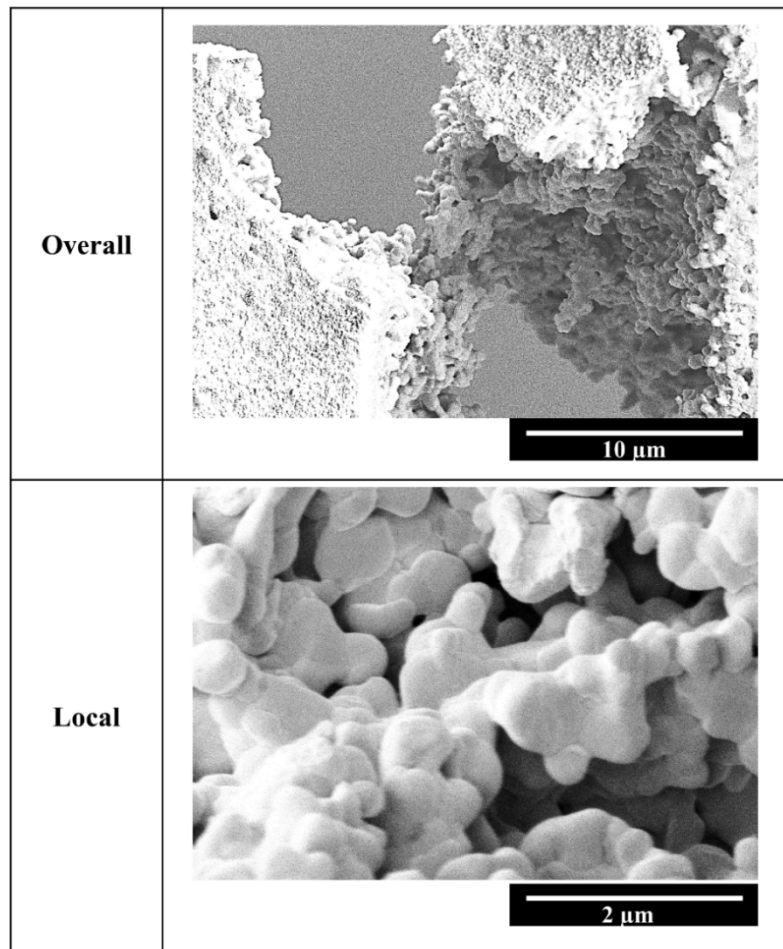
	<b>Process 1</b>	<b>Process 2</b>
<b>Acceleration voltage</b>	<b>30 kV</b>	
<b>Beam current</b>	<b>13 nA</b>	<b>0.7 nA</b>
<b>Beam diameter</b>	<b>2000 <math>\mu\text{m}</math></b>	<b>60 <math>\mu\text{m}</math></b>

Fig. 4-8 shows snapshot SEM observation photographs during tensile testing. The SEM observation area was set at  $10\ \mu\text{m} \times 7\ \mu\text{m}$ . The right line in Fig. 4.8 shows an enlarged view of the snapshot image as a characteristic morphology image in the SEM observations. The pore is almost uniformly distributed in the SEM images, as shown in step 1 of the s-Ag specimen's initial state. The crack tips and neighbor pore relations are shown in an enlarged dash-square area of the step 1 SEM image. Then, the crack progresses upwards, and the pore is gradually grown, which shortens the distance between the crack tip and the grown pore, as shown in step 2 enlarged view. The local stress intensity is considered to be high in this area from the high stress distribution surrounding the high local pr, as shown in Fig. 2-23. Consequently, the local pore growth rate is considered to be high in this region. After that, the crack and the pore are merged into one new crack, as shown in step 3 images. The location relation between the new crack and the next neighbor pores are shown in the enlarged view of step 3 (b). The neighbor pore to the crack tip indexed as Pore 1 grew up at step 4. Finally, the crack is merged with Pore 1 into the new crack, as shown in step 5. In addition, Pore 2 and Pore 3 are also grown up to compensate for the distance between the grown pore and the main crack, as was the almost same tendency from steps 2 to 3. The In-situ SEM observation results during tensile force at  $300^\circ\text{C}$  clarify that the overall crack propagation speed was not shown at a constant speed because the pore surrounded by the crack is simultaneously grown originating from the local high stress concentration at high temperatures. Consequently, the overall crack propagation speed with a pore growth case would be high compared to the speed of straight crack progress only.



Step	3 $\mu\text{m}$ SEM image	1 $\mu\text{m}$ Enlarged view (Dash square area)
1		
2		
3		(a)
		(b)
4		
5		

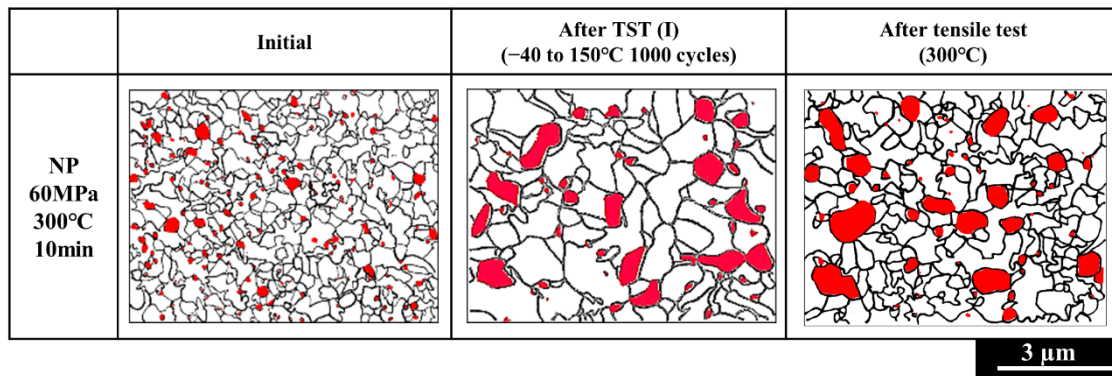
Fig. 4-8 In-situ SEM observation results



**Fig. 4-9 Fracture surface SEM images (Upper side: Overall SEM image. Downside: Fracture surface image with local area)**

Fig. 4-9 shows SEM observation results after the fractured s-Ag specimen. Upperside and downside images indicate the overall and local SEM observation results, respectively. The crack direction shows a wavy path, as shown in the overall observation result. In addition, many protrusion shapes of grain can be observed on the fracture surface. These protrusions indicate that the local plastic deformation would be actively occurred during tensile testing. The fracture surface morphology of the local area shows a granular surface like, which shows almost the same result at the temperature of 150°C with Fig. 2-28. The local plastic deformation of individual s-Ag particle would be occurred during the In-situ tensile testing at 300°C.

Fig. 4-10 shows microstructure image analysis results after cross-section treatment, as Appendix B explains. In addition, the initial microstructure of s-Ag and TST(I):  $-40$  to  $150^{\circ}\text{C}$  after 1000 cycles are also shown as a reference structure, which was already shown in Fig. 3-11. Pores indicate a red-colored portion in Fig. 4-11. Both pore size and crystal size were found to be grown after the Insitu-SEM test at  $300^{\circ}\text{C}$ . The grown pore is located along with the grain boundary region. The microstructure characteristic shows a similar trend with the results of TST (I) after 1000 cycles. That is, the pore growth during TST is experimentally clarified that pore diffused to grow at the grain boundary in high temperatures by applied tensile stress [17, 18].

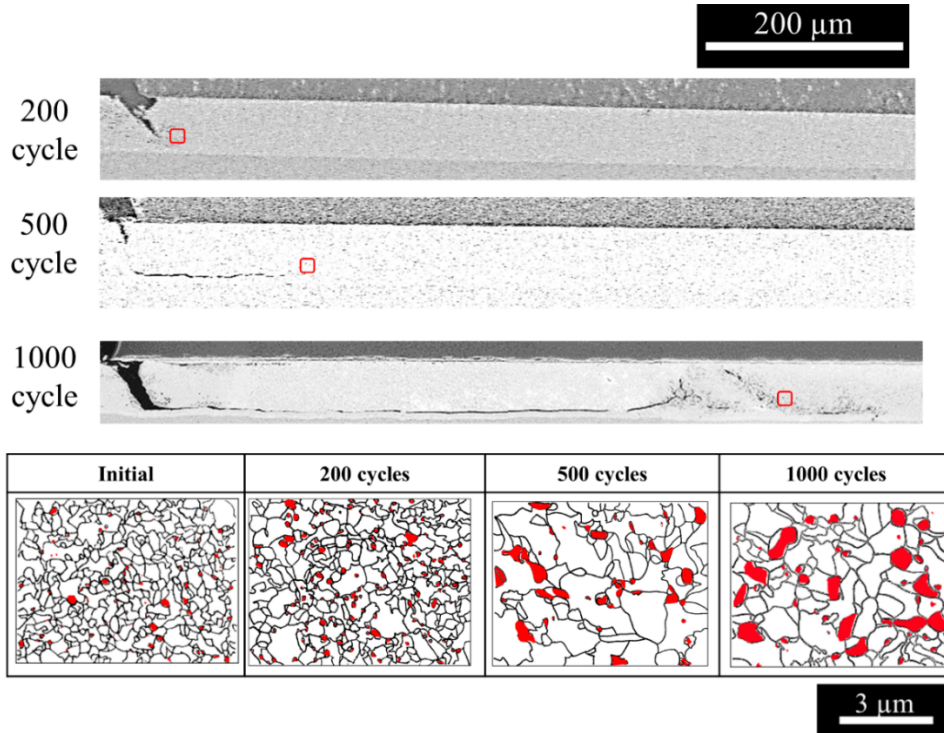


**Fig. 4-10 Microstructure image analysis comparison results of initial, after TST 1000 cycles ( $-40$  to  $150^{\circ}\text{C}$ ), and after the In-situ tensile testing at  $300^{\circ}\text{C}$ . (Red: Pore.)**

#### 4-4. Overall s-Ag die layer degradation mechanism

Fig. 4-11 shows a representative cross-section SEM image of TST (I) with NP DAAs after 200, 500, and 1000 cycles to clarify fracture mode transition with pore growth case in TST. After 200 cycles in NP DAAs, the inclined crack starts at the left corner edge of the s-Ag layers. Then the crack stops in the middle of the s-Ag layer. The microstructure of s-Ag has not changed from the initial state. After 500 cycles, the cracking path horizontally progresses along with the substrate, not showing the wavy cracking. However, pore growth associated with crystal growth started after 500 cycles, as shown in the microstructure analysis results. The merging speed between the crack and the neighbor pore would gradually increase around this cycle due to the high stress intensity around the pore. After 1000 cycles, the crack mode shows mixed modes, such as straight cracking and wavy cracking. Significantly grown pores are closely located in the

inner portion of the wavy crack to form like a pre-crack. The other observation results are referred with Appendix G, H and I.

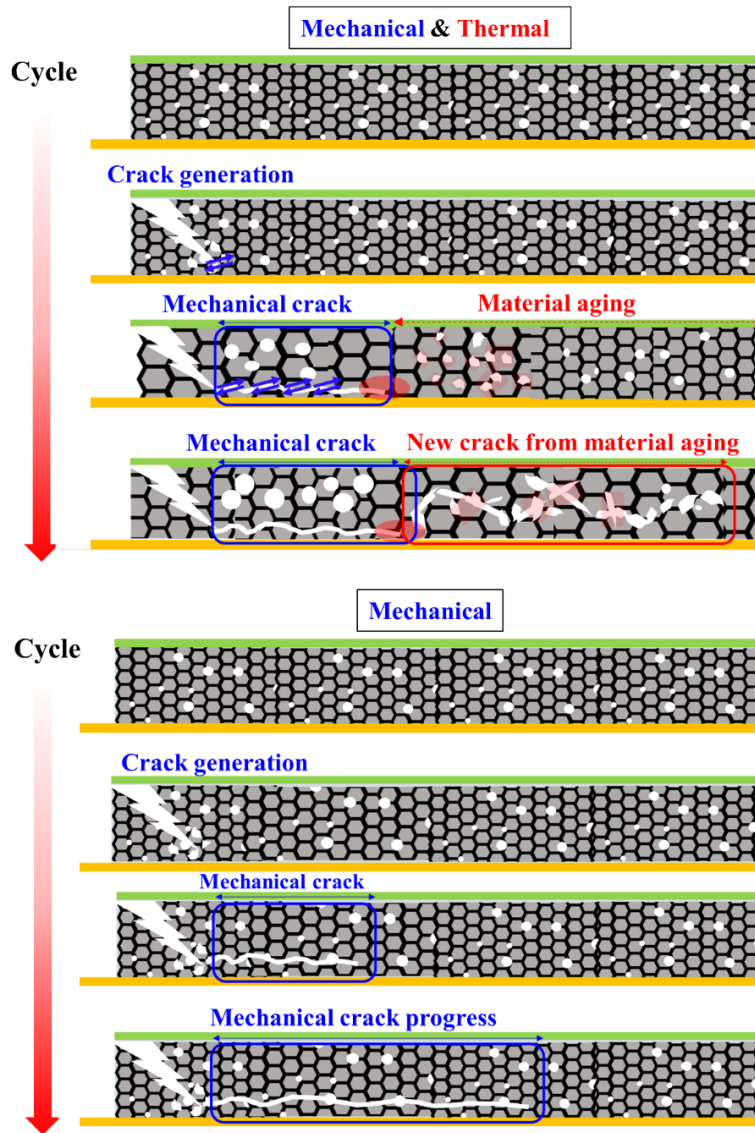


**Fig. 4-11 Representative cross-section SEM image of TST (I) with NP after 200, 500, and 1000 cycles. Microstructure image analysis results in red frame regions depicted in the SEM cross-section images (Red: Pore).**

Fig. 4-12 shows an overall fracture mode schematic image as a function of cycles based on the cross-sectional observation results and pore growth discussed in Chapter 4. The upper images illustrate the fracture mode caused by mechanical and thermal stresses associated with TST at temperatures ranging from  $-40$  to  $150^{\circ}\text{C}$ . The lower images show the fracture mode caused by only mechanical stress related to NBT.

First, a crack generates at the upper left corner edge of the s-Ag die layer, where the stress is concentrated after specific cycles. Then, the crack progresses with an incline angle in both cases. Second, cracking progresses along with the horizontal way associated with the maximum shear stress direction at the tip of the crack. The horizontal crack speed is well associated with the value of DP, which is defined in section 3-2-5. Apparent cracking behavior is observed regardless of the test type up to the middle stage at around

500 cycles. However, in the case of thermal and mechanical stresses, material aging associated with pore growth is due to tensile tension at a high temperature at the inner part of the s-Ag layer, as shown in the third line illustration of the upper side. Finally, conventional mechanical crack with a straight direction would merge with new cracking originating from pore growth, which accelerates and destabilizes the overall cracking speed. In the case of mechanical stress only, the crack still progresses with a straight line at a steady speed because the overall horizontal crack speed would not be affected by the pore growth at the s-Ag layer inside.



**Fig. 4-12 Overall fracture mode schematic images as a function of cycles (Upper side: Thermal and mechanical stress. Lower side: Mechanical stress.)**

## 4-5. Conclusion

In this Chapter, the cause of categorizing into two groups in Fig. 3-16 was considered from the viewpoint of microstructure physics. First, in exploring the cause of pore formation, MD calculations were performed to seek the cause of pore growth. MD simulations indicated that when a certain amount of tensile stress was applied to the pore configuration under a certain time and at a high temperature, more atoms moved through the grain boundary to promote pore growth. Based on the stress distribution results from FEAs, the tensile stress was induced at the s-Ag layer of DAAs during TST and NBT except for that at  $-40^{\circ}\text{C}$  to  $100^{\circ}\text{C}$ . The pore growth criterion plane was derived from the equation originating from the classical pore growth theory. The criterion plane signified about the relationship between stress,  $\sigma$ ; around a pore; initial pore size,  $r$ ; and diffusion effect,  $Dt/T$ , where  $t$  is the time at the highest temperature applied during TST and the time at the stress applied during NBT.  $\sigma$  necessary for pore growth depends on  $Dt/T$  and  $r$ , which can decrease with the increase of the two values. Increasing  $Dt/T$  indicated the activation of diffusion around a pore by increasing temperature or stress-induced time. Based on the criterion plane, TSTs were plotted over the criterion plane, whereas NBTs were plotted beneath the criterion plane. The two groups divided by the critical stress plane were identical to the two groups divided by using the DP shown in Fig. 3-16. Therefore, the DP proposed in this study worked well for separately evaluating the s-Ag degradation phenomena originating from cracking only and the combination of cracking and aging based on pore growth or not. The In-situ SEM tensile testing with  $300^{\circ}\text{C}$  at quasistatic speed can reveal the relation between the s-Ag pore growth and the crack tip. The pore growth occurred around the crack tip, where the local stress intensity was considered to be high. After that, the crack tips and the grown pore are merged into the new crack. In addition, the pore growth was occurred with the grain boundary after the In-situ SEM testing, which shows similar morphology to the TST. It was experimentally revealed that the tensile stress gave rise to the pore growth during TST at high temperatures.

## References

- [1] L. Ding, R. L. Davidchack, and J. Pan, "A molecular dynamics study of sintering between nanoparticles," *Computational Materials Science*, vol. 45, no. 2, pp. 247-256, 2009, doi: 10.1016/j.commatsci.2008.09.021.
- [2] H. A. Alarifi, M. Atis, C. Ozdogan, A. Hu, M. Yavuz, and Y. Zhou, "Molecular Dynamics Simulation of Sintering and Surface Premelting of Silver Nanoparticles," *Materials Transactions*, vol. 54, no. 6, pp. 884-889, 2013, doi: 10.2320/matertrans.MD201225.
- [3] H. Zhang, C. Chen, J. Jiu, S. Nagao, and K. Suganuma, "High-temperature reliability of low-temperature and pressureless micron Ag sintered joints for die attachment in high-power device," *Journal of Materials Science: Materials in Electronics*, vol. 29, no. 10, pp. 8854-8862, 2018, doi: 10.1007/s10854-018-8903-9.
- [4] P. Gadaud, V. Caccuri, D. Bertheau, J. Carr, and X. Milhet, "Ageing sintered silver: Relationship between tensile behavior, mechanical properties and the nanoporous structure evolution," *Materials Science and Engineering: A*, vol. 669, no. 4, pp. 379-386, 2016, doi: 10.1016/j.msea.2016.05.108.
- [5] S. Malolar and H. Hakkinen, "Prospects and challenges for computer simulations of monolayer-protected metal clusters," *Nature Communications*, vol. 12, no. 2197, pp. 1-4, 2021, doi: 10.1038/s41467-021-22545-x.
- [6] J. Heilmann, I. Nikitin, U. Zschenderlein, D. May, K. Pressel, and B. Wunderle, "Reliability experiments of sintered silver based interconnections by accelerated isothermal bending tests," *Microelectronics Reliability*, vol. 74, pp. 136-146, 2017, doi: 10.1016/j.microrel.2017.04.016.
- [7] D. Kim, S. Lee, C. Chen, S. J. Lee, S. Nagao, and K. Suganuma, "Fracture mechanism of microporous Ag-sintered joint in a GaN power device with Ti/Ag and Ni/Ti/Ag metallization layer at different thermo-mechanical stresses," *Journal of Materials Science*, vol. 56, no. 16, pp. 9852-9870, 2021, doi: 10.1007/s10853-021-05924-z.
- [8] S. Nishimoto, S. A. Moeini, T. Ohashi, Y. Nagatomo, and P. McCluskey, "Novel silver die-attach technology on silver pre-sintered DBA substrates for high temperature applications," *Microelectronics Reliability*, vol. 87, pp. 232-237, 2018, doi: 10.1016/j.microrel.2018.06.010.
- [9] S. M. Foiles, M. I. Baskes, and M. S. Daw, "Embedded-atom-method functions for the fcc metals Cu, Ag, Au, Ni, Pd, Pt, and their alloys," *Phys. Rev. B. Condens Matter*, vol. 33, no. 12, pp. 7983-

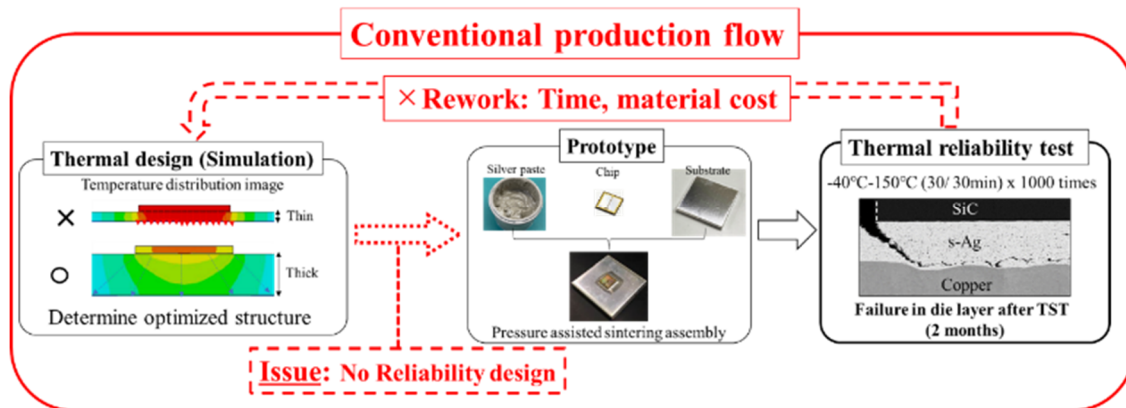
- 7991, 1986, doi: 10.1103/physrevb.33.7983.
- [10] K. Wakamoto, T. Otsuka, K. Nakahara, and T. Namazu, "Comparison of sintered silver die attach failure between thermal shock test and mechanical cycling test," *Japanese Journal of Applied Physics*, vol. 61, p. SD1029-1-7, 2022, doi: 10.35848/1347-4065/ac5b23.
- [11] T. Herboth, M. Guenther, R. Zeiser, and J. Wilde, "Investigation of Stress States in Silicon Dies Induced by the Low Temperature Joining Technology," in *Proc. 14th International Conference on Thermal, Mechanical and Multi-Physics Simulation and Experiments in Microelectronics and Microsystems, EuroSimE 2013*, Wroclaw, Poland, 14-17 April, 2013, doi: 10.1109/EuroSimE.2013.6529945.
- [12] S. Onaka, M. Kato, S. Soeta, and T. Mori, "A New Approach for Diffusional Growth of Grain-Boundary Voids," *Transactions of the Japan Institute of Metals*, vol. 29, pp. 284-291, 1988, doi: 10.2320/matertrans1960.29.284.
- [13] S. Onaka and M. Kato, "Unified Analysis for Various Diffusion-controlled Deformation and Fracture Processes," *ISIJ International*, vol. 31, no.4, 1991, doi: 10.2355/isijinternational.31.331.
- [14] M. Kato, "Selected Topics in Strength of Materials V—High-temperature Deformation, Fatigue and Fracture—," *Materia Japan*, vol. 47, no. 9, pp. 469-474, 2008, doi: 10.2320/materia.47.469.
- [15] R. W. Balluffi and L. L. Seigle, "Growth of Voids in Metals during Diffusion and Creep," *Acta Metallurgica*, vol. 5, pp. 449-454, 1957, doi: 10.1016/0001-6160(57)90063-9.
- [16] S. Tammas-Williams, P. J. Withers, I. Todd, and P. B. Prangnell, "The Influence of Porosity on Fatigue Crack Initiation in Additively Manufactured Titanium Components," *Scientific Reports*, vol. 7, no. 1, pp. 7308-7320, Aug., 2017, doi: 10.1038/s41598-017-06504-5.
- [17] R. E. Hoffman and D. Turnbull, "Lattice and Grain Boundary Self-Diffusion in Silver," *Journal of Applied Physics*, vol. 22, no. 5, pp. 634-639, 1951, doi: 10.1063/1.1700021.
- [18] W. K. Lee, R. L. Eadie, and G. C. Weatherly, "A STUDY OF THE SINTERING OF SPHERICAL SILVER POWDER-II. THE INITIAL STAGE," *Acta Metallurgica*, vol. 26, pp. 1837-1843, 1978, doi: 10.1016/0001-6160(78)90096-2.



## 5. Conclusions

Given the increasing demand for high-power-density power module products, a new die-attach material with high heat conductivity and melting point could be utilized as a WBG die-attach material. The s-Ag bonding technique has attracted so many researchers. The driving force of Ag sintering originates from the reduction of high surface energy with each Ag particle, which allows us to die bonding at low temperature ranging from 200°C–300°C. However, pores are inevitably included in the s-Ag layer to make a gas pathway to outside during sintering. Furthermore, the physical property of s-Ag exceeded the conventional die material of solders.

Fig. 5-1 show the conventional power module production flow overview from a thermal design, prototyping, and thermal reliability test. First, material configuration was determined on the basis of simulation results to satisfy the specification requested from customers. At that stage, products could virtually optimize the power module configurations. Second, prototype a product in accordance with the simulation results. The initial bonding state is checked by SAT, that is, the bonding area shows no delamination. Finally, the bonded layer is commonly assessed through a reliability test. Furthermore, TST that evaluates heating and cooling between low and high temperatures includes severe reliability tests for products. The TST temperature profile has been commonly adopted between  $-40^{\circ}\text{C}$  and  $150^{\circ}\text{C}$  with a trapezoid waveform for 60 min per a cycle and then repeated up to 1000 cycles. The total assessment time costs about 2 months for one testing. After 1000 cycles, the die delamination ratio should be suppressed under 20%. The most compelling issue was the lack of knowledge against the s-Ag die failure of physics during TST. Therefore, if the reliability design could not be performed properly, then it would be meaningless regardless of how the virtual side is designed. Furthermore, if the production process goes back to the origin state and revise the configuration, then die failure would reoccur after the TST. The production cycle continues with infinity by only wasting of resources.



**Fig. 5-1 Conventional production flow overview.**

This study experimentally investigated the s-Ag mechanical reliability for clarifying the s-Ag degradation mechanism during TST. In this study, two types of pastes (NP [Ag particle: 18 nm] and NMP [Ag particle: 23, 148, and 5023 nm]) were used as the starting s-Ag material. The sintering condition was set to 300°C for 10 min under 60 MPa pressure to reduce the pore. After sintering, NP possessed a pore-sized microstructure and grain compared with those in NMP originating from the only nanosized Ag particle. NP and NMP films were conducted by quasistatic tensile testing at RT, 100°C, and 150°C. NP possessed a large ductility region at 100°C and 150°C. Consequently, minute microstructure affected good durability against applied tensile stress. The mechanical reliability evaluation was expanded from films to DAAs. The results of the FBT indicated that s-Ag die layer degradation was attributed to the maximum shear stress at high temperature. In understanding the overall s-Ag degradation mechanism, the author newly proposed that NBT can apply out-of-plane deformation as TST like. The degradation of the s-Ag layer after TSTs and NBTs was evaluated by SAT for the delamination ratio. Cross-sectional SEM was utilized to observe the s-Ag layer failure mode. In ordering the s-Ag delamination ratio between TSTs and NBTs, a new parameter of DP was proposed. DP is defined as the ratio of the accumulated plastic APS to plastic strain,  $\epsilon_p$ , originating from uniaxial tensile testing at the highest temperature in each condition. The SAT results reveal that less stress conditions originating from the use of a thin substrate or thick s-Ag layer during TST and applying less force variation suppressed the s-Ag delamination ratio in NP and NMP DAAs. Cross-sectional SEM observation demonstrates that mechanical cracking and material aging in the s-Ag layer coexist after TST at -40°C to 150°C. The proposed DP could separately approximate the delamination ratio between wavy-crack-included and non-included samples. The MD and FEA

simulations indicated that some tensile stress and temperature were necessary for pore growth inside the s-Ag layer. In addition, the pore growth was observed along with the crystal boundary after In-situ SEM tensile testing with 300°C at a quasistatic speed. It was clarified that the pore growth during TST originated from the tensile stress at high temperatures. The DP was useful for separately evaluating s-Ag degradation with and without aging originating from pore growth. The evaluation method using the DP can lead to future reliability design methodology for die attach.

Fig. 5-2 shows the new production flow overview. The most divergent points from conventional methodology could indicate the reliability evaluation methodology into the new production flow. In the new production flow, after the evaluation of virtual designing, the calculation of the DP process and evaluation of DAA delamination by NBT are newly added. During DP evaluation, the film specimen of the die material was fabricated, and then tensile testing was performed to investigate  $\varepsilon_p$  for deriving DP. In addition, APS is calculated by FEA in accordance with the external condition of the reliability experiments. Planned DAAs will satisfy the definition of failure or not by comparing the calculated DP with the graph shown in Fig. 3-16 in the case of s-Ag at that stage. If DP value exceeds 0.18, then the process should go back to the origin stage to reconstruct the configuration. By unifying the awareness of the user and production sides, the cycle of material development will leap forward at an accelerated pace. After the prototype DAAs, the bonding state is checked by SAT, confirming no delamination in the bonded layer. Then, DAAs are evaluated by using the NBT proposed in this study, resulting in fast die delamination evaluation. NBT can work well for screening the DAAs with very short time within 2 or 3 days. If the die layer satisfies with lifetime, then TST is performed for DAAs. However, the process will not return to the origin state because the die delamination design can be already attained. Therefore, the production cycle can be achieved rapidly and efficiently because of the production flow based on the die failure of physics.

Further validations are necessary for the application of next-generation die materials used for sintered Cu bonding, cold-rolled Ag solid-state bonding, and transient liquid-phase bonding. Each material DP and delamination ratio relation should be performed. Combining WBG devices and excellent physical properties of die material will lead to new concepts of application products. This fruition will drastically change human life with convenience, which satisfies the social needs.

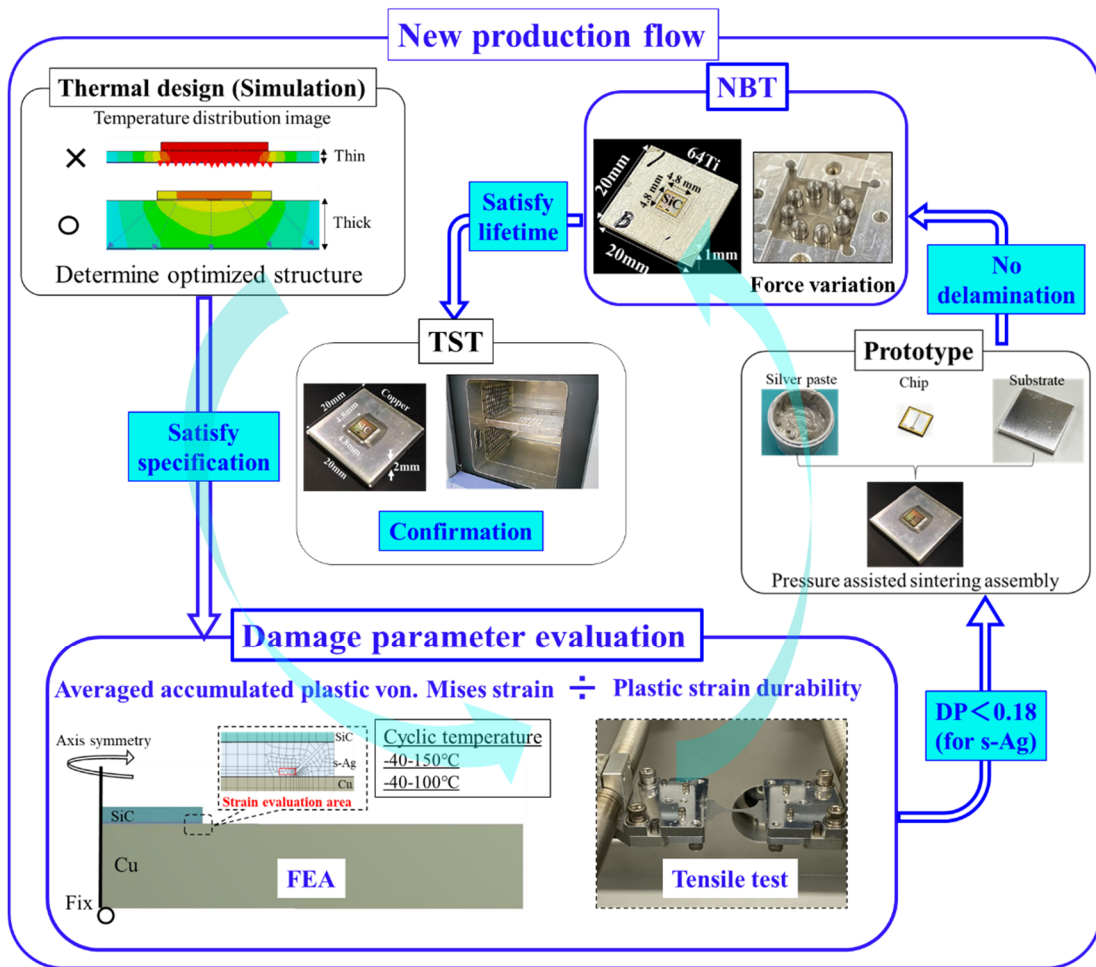


Fig. 5-2 New production flow overview.

# Appendix

## A. Packaging product trends

Fig. A-1 shows the products' appearance together with each product's cross-sectional structure. The trend is shifted from single-side cooling to double-side cooling packaging for enhancing power density. On the contrary, the double-side cooling package cost is high. Then, an advanced single-side cooling module is also one of the candidate structures, as depicted in Fig. A-1. In the near future, the die part will be entirely replaced from solder material to sintered Ag material to enhance the cooling performance.

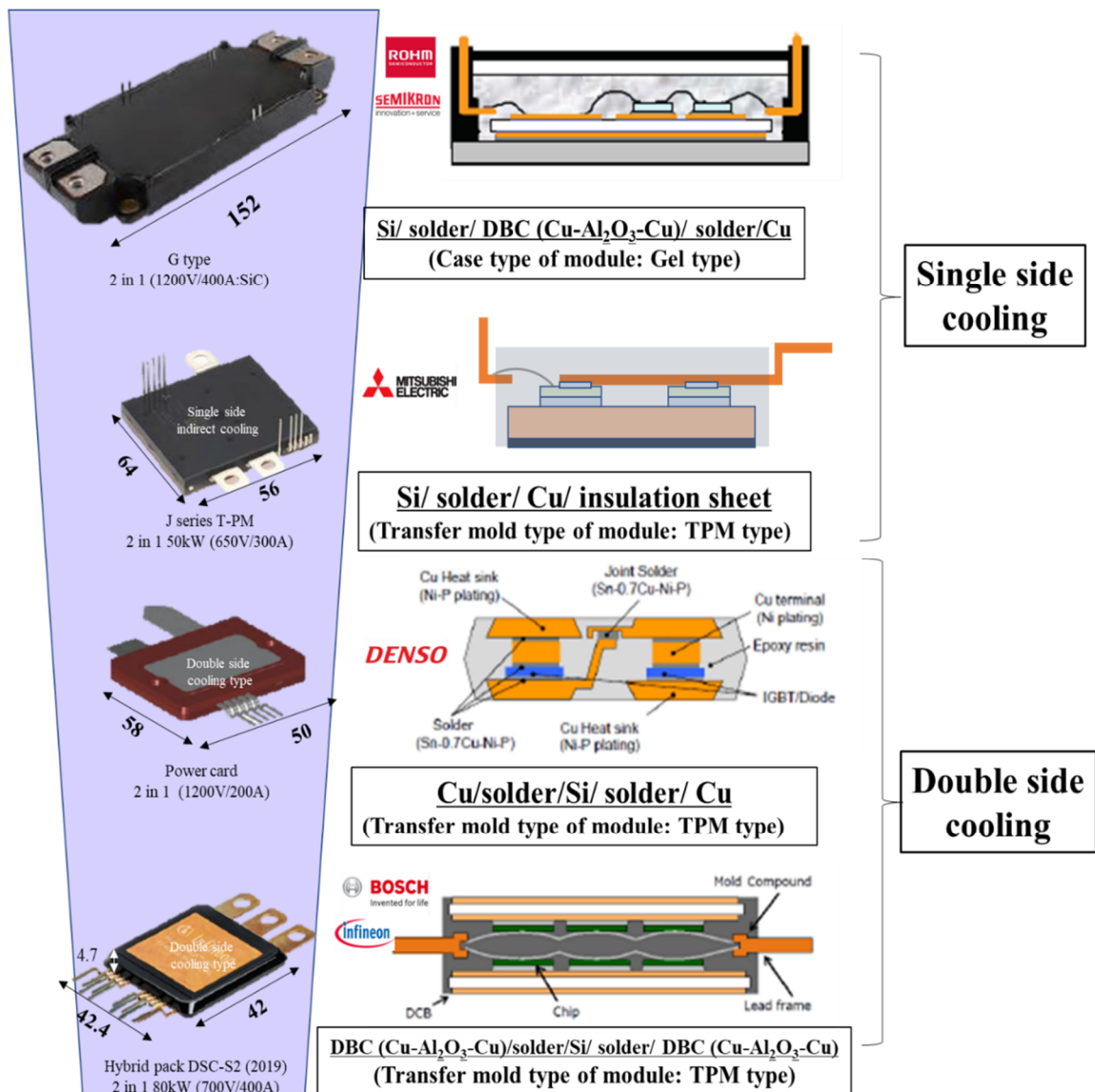


Fig. A-1 Packaging appearance with cross section sketch view.

## B. Micro structure observation methodology

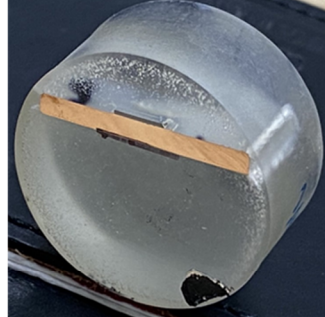
The microstructure of the s-Ag analysis methodology is introduced here to characterize the pore and crystal states of NP and NMP s-Ag specimens, as shown in Fig. B-1. To get analytical results with high quality, the preprocessing for smoothing surface of specimen should be paid much attention at most. Fig. B-1 shows the flow for observing the s-Ag microstructure. For the first step, the sample is cross-cut by a blade dicing machine (Struers, Accutom-10). The holders clump the specimen. Then the sample was cut by the rotated blade. For the second step, the sample is encapsulated with a resin block. The resin powder (KULZER, Technovit 4004 powder) and cure resin liquid (KULZER, Technovit 4004 liquid) are mixed in the cup. Then, the specimen is dipped in the liquid resin so that the observation surface contacts well with the bottom surface of the cup. After around 10 min, liquid resin is chemically reacted to be cured. After confirmation of the solidity in the resin block, then the solid resin block can be detached from the cup. For the third step, the resin-encapsulated surface was polished with abrasive in the water base suspensions (Struers, Labosystem). Then, the buffing polish was carried out by mono-crystalline diamond slurry solutions. Flat ion milling is utilized for the fourth step to planarize the sample surface (Hitachi High-Technology, IM4000). In this treatment, the Argon ion beam irradiates against the sample surface at an angle. Then, the sample and beam center position are eccentrically aligned to get a wide irradiation area of the sample. Irradiation angle can be set from 0 to 90°. When set the angle is above 80°, the ion beam irradiation direction is almost parallel to the surface. Consequently, reduced unevenness formation can be obtained. For the fifth step, microstructure observation is utilized by two testers. First is the field emission scanning electron microscope (FE-SEM) tester (Hitachi High-Technology, S-4800). In this tester, a secondary electron or backscattering electron launched from the target sample is utilized to detect surface morphology from nanoscale. Second is the focus ion beam (FIB) tester (Hitachi High-Technology, SMI3050). Gallium (Ga) ions are generated from a Ga liquid metal ion source by the electric field of the extraction electrode and accelerated by the cathode electric field. The generated ion beam is focused on the sample by two sets of electrostatic lenses (condenser and objective lenses). When irradiated at the solid surface, the secondary electrons are generated from the surface, which can produce an image contrast according to the crystallographic orientation of each grain. The image is called a scanning ion microscope (SIM) image. Although electron beam irradiation by FE-SEM is also obtained in such a contrast image, the contrast degree is lower than the contrast in the SIM image.

## 1~4. Preprocessing

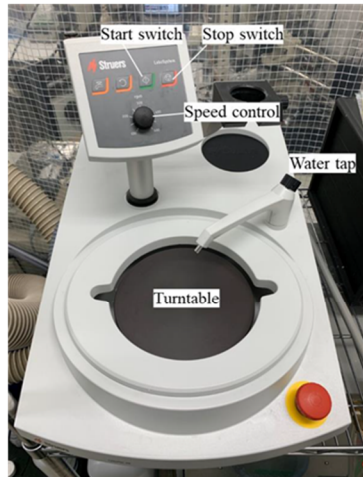
1. Cutting



2. Encapsulation



3. Grinding



4. Ion milling



## 5. Analysis

FIB tester



FE-SEM



Fig. B-1 Micro structure analysis methodology flow.

Table B-1 is listed of each process condition performed in this study.

**Table B-1 Processing condition.**

Process	Treatment specification
1. Cutting	Rotation: 3000 rpm Moving speed: 0.05mm /sec
2. Encapsulation	Cure resin liquid: 5 ml Resin powder: 1.5 g
3. Polishing	Step.1 Water polish: 300rpm, #300, #800, #1200, and #2000) Step:2 Diamond colloid polish: 150rpm: Diamond diameter: 9 $\mu$ m, 3 $\mu$ m, 1 $\mu$ m
4. Ion milling	Flat milling Beam irradiation angle: 80° Acceleration voltage: 4.5 kV Ar gas flow: 0.07 cm <sup>3</sup> /sec Irradiation time: 20 min
5. FIB	Acceleration voltage: 4.5 kV Beam diameter: 13nm Beam current: 10 $\mu$ A Surface sputtering: Continuous scan for 20 sec
5. SEM	Acceleration voltage: 1.5 kV Extra voltage: 4.5 kV Detection: Secondary ion Beam current: 10 $\mu$ A (Tilting angle: 30° for fracture surface)



### C. Image analysis methodology

Fig. C-1 shows the image processing methodology from raw SIM or SEM images to distinguish pore and crystal boundaries for numerical analysis.

1. Obtaining the SIM observation results (10 $\mu\text{m}$  window view).
2. Extract pores from the SIM image by myself with care.
3. The crystal line is strengthened by myself.
4. Overlay pore image and crystal grain boundary line image.
5. Numerical analysis by image software (WaferMaster, Picman).

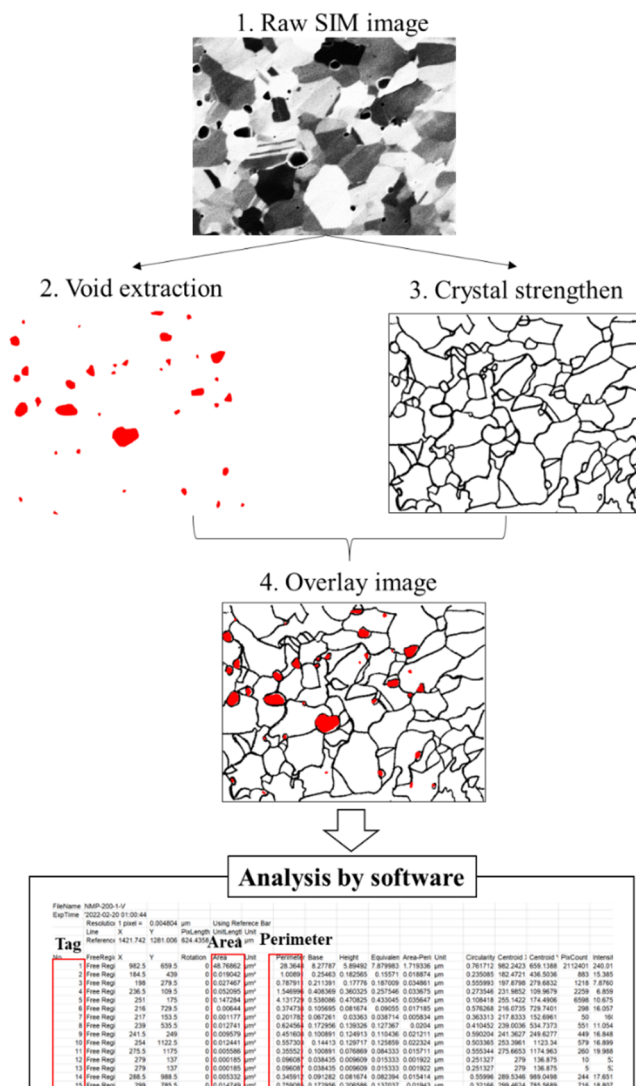


Fig. C-1 Image analysis flow.

## D. NBT set up methodology

This Appendix section describes the NBT setup as a procedure to stabilize contact between pins and substrate surface. Fig. D-1 shows the NBT system photograph and illustration of the cross-section schematic view following each setup procedure.

### Experiment methodology step

1. Each spring was installed into the support jig basement holes, respectively. A guide plate with a hole was placed onto the support jig by fastening two screws. The guide plate displacement was centered at the support jig surface, which could guide for centering the interconnection on the base jig.
2. Die attached assemble (DAA) was flipped to place onto the freestanding pins guided by the hole metal plate. (Spring state was the natural length.)
3. A metal plate was placed from the above direction for the contact between flipped DAA and each pin. This compressive stress shrank each spring through each pin. Even if the substrate deforms with warpage, the spring can be shrunk to absorb the substrate height differences. Then, the screw was fastened from the top side to keep the position. Finally, two screws per pin were fastened from the side parts. Each pin height could be completely optimized at this stage.
4. Finally, the metal plate was detached to be ready for performing NBT.

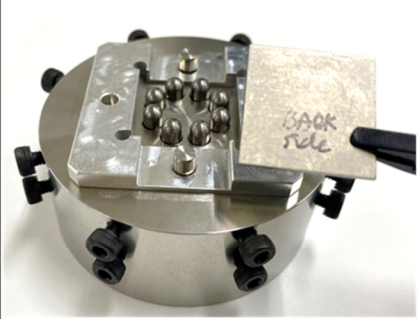
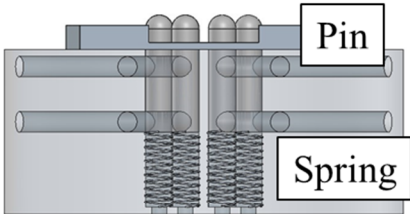
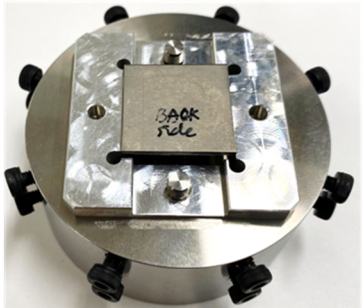
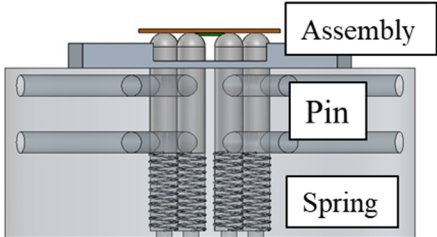

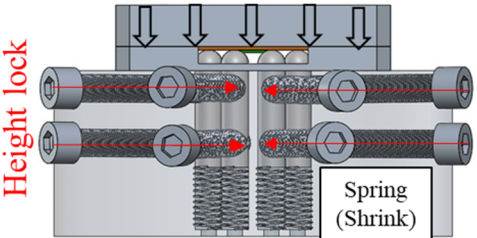
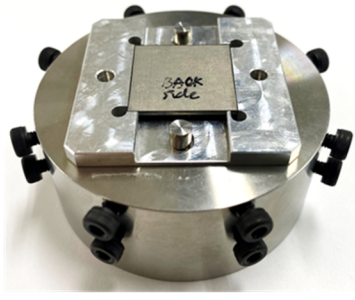
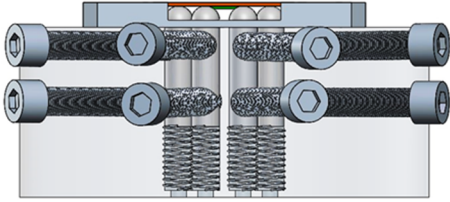
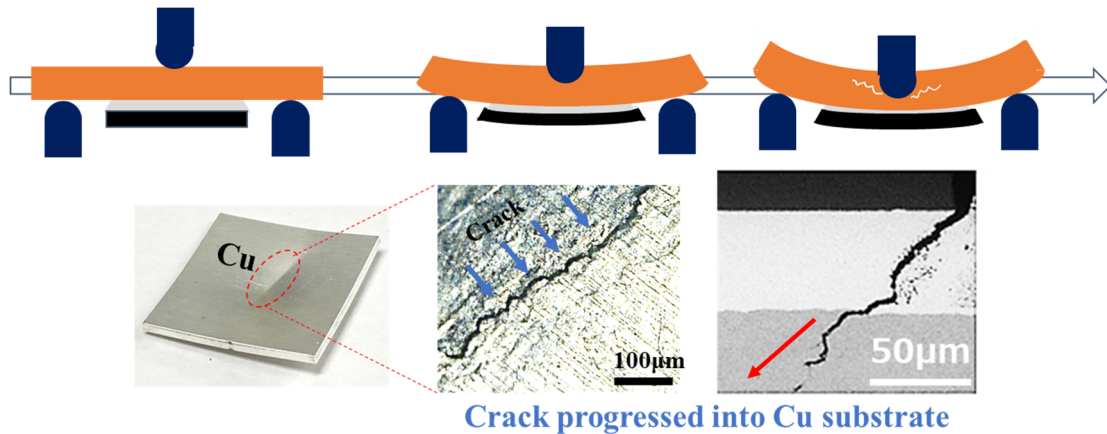
Step	Sample photograph (Bird view)	Front view (Skelton image with CAD)
1		 <p data-bbox="995 712 1206 757">Pin / Spring</p>
2		 <p data-bbox="903 1066 1273 1111">Assembly / Pin / Spring</p>
3		 <p data-bbox="826 1413 1337 1458">Assembly / Pin / Spring (Shrink)</p>
4		

Fig. D-1 NBT setup procedure schematic view.

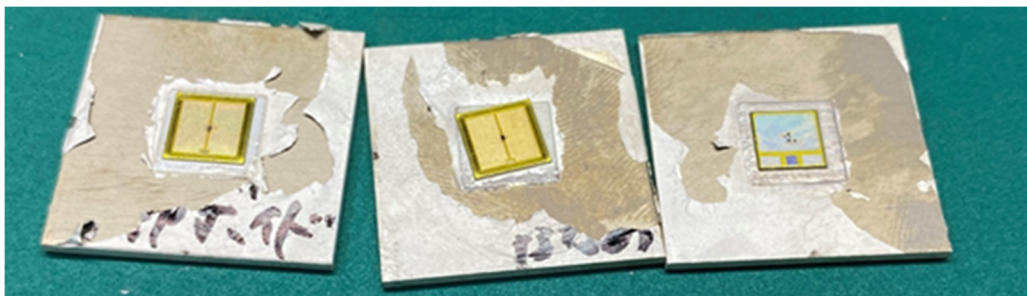
## E. NBT interconnection optimization

For NBT, bonding optimization is so important. First, the copper substrate for bonding was employed as was used in TST. However, the substrate was broken up during NBT due to the plastic deformation accumulation in the Cu substrate, as illustrated in Fig. E-1.



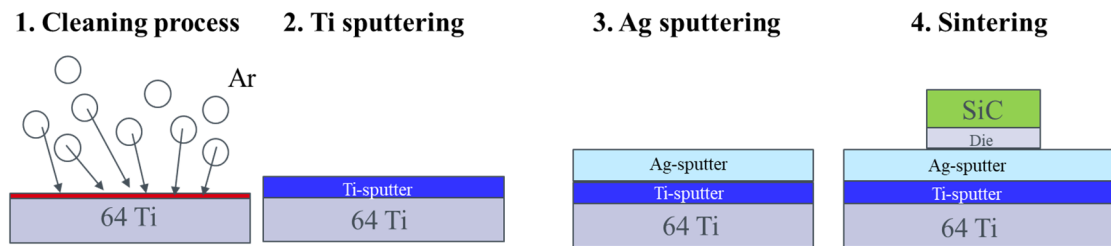
**Fig. E-1 NBT failure experiment with Cu substrate interconnections.**

Then, the substrate material was changed from Cu to 64Ti. As stated in Chapter 3, 64Ti has a high yield stress, but the same Young's modulus as Cu, which equals 64Ti, has a wide elastic range. For obtaining enough bonding strength between the s-Ag layer and 64Ti substrate, Ag plating on the substrate was necessary. However, Ag plating on 64Ti could not be s-Ag bonded, as shown in Fig. E-2. Hence the 64Ti substrate surface quickly oxidized, then the adhesion between the Ag electro plate film and 64Ti substrate became so weak. As a result, delamination occurred during the SiC chip bonding with temperature elevation. Therefore, it is essential to prevent making an oxidized layer onto the 64Ti substrate surface during the fabrication of Ag electroplating. During the air atmosphere, the electroplating process is severe for preventing oxidation on the 64Ti substrate.



**Fig. E-2 Ag electro plating failure with 64Ti substrate.**

Then, the sputtering process was employed under high vacuum conditions to improve the adhesivity between Ag and 64Ti surface. Optimized process flow of sputtering Ag on the 64Ti was illustrated in Fig. E-3. First, the 64Ti substrate was cleaned by Ar gas irradiation. Then, Ti was sputtered onto the 64Ti surface. After that, Ag sputtering was performed on the surface. SiC chip die bonding treatment was the same as the conventional treatment. As shown in Fig. 3-10 (b), the perfect bonding could be confirmed.



**Fig. E-3 Optimized process procedure for Ag sputtered on 64Ti substrate.**

F. AT results of all images after TST, NBT

Appendix F presents all SAT images according to Fig. 3-10.

(I) TST (-40-150°C, s-Ag (50µm thick), Cu (2mm thick))

NP	0 cycle	100 cycle	200 cycle	300 cycle	400 cycle	500 cycle	600 cycle	700 cycle	800 cycle	900 cycle	1000 cycle
1											
2											
3											
4											
5											

NMP	0 cycle	100 cycle	200 cycle	300 cycle	400 cycle	500 cycle	600 cycle	700 cycle	800 cycle	900 cycle	1000 cycle
1											
2											
3											
4											
5											

Fig. F-1 SAT images of TST (I). (Upper images: NP DAAs and downside images: NMP DAAs)

(II) TST (-40-150°C, s-Ag (50μm thick), Cu (1mm thick))

NP	0 cycle	100 cycle	200 cycle	300 cycle	400 cycle	500 cycle	600 cycle	700 cycle	800 cycle	900 cycle	1000 cycle
1											
2											
3											
4											
5											

NMP	0 cycle	100 cycle	200 cycle	300 cycle	400 cycle	500 cycle	600 cycle	700 cycle	800 cycle	900 cycle	1000 cycle
1											
2											
3											
4											
5											

Fig. F-2 SAT images of TST (II). (Upper images: NP DAAs and downside images: NMP DAAs)

(III) TST (-40-150°C, s-Ag (100μm thick), Cu (2mm thick))

NP	0 cycle	100 cycle	200 cycle	300 cycle	400 cycle	500 cycle	600 cycle	700 cycle	800 cycle	900 cycle	1000 cycle
1											
2											
3											
4											
5											

NMP	0 cycle	100 cycle	200 cycle	300 cycle	400 cycle	500 cycle	600 cycle	700 cycle	800 cycle	900 cycle	1000 cycle
1											
2											
3											
4											
5											

Fig. F-3 SAT images of TST (III). (Upper images: NP DAAs and downside images: NMP DAAs)



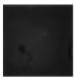









(IV) TST (-40-100°C, s-Ag (50μm thick), Cu (2mm thick))

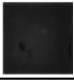









NP	0 cycle	100 cycle	200 cycle	300 cycle	400 cycle	500 cycle	600 cycle	700 cycle	800 cycle	900 cycle	1000 cycle
1											
2											
3											
4											
5											

NMP	0 cycle	100 cycle	200 cycle	300 cycle	400 cycle	500 cycle	600 cycle	700 cycle	800 cycle	900 cycle	1000 cycle
1											
2											
3											
4											
5											

Fig. F-4 SAT images of TST (IV). (Upper images: NP DAAs and downside images: NMP DAAs)

**(V) Temperature storage test (150°C), s-Ag(50μm thick), Cu (2mm thick)**

NP	Initial	→	After
1		<b>Temperature storage test (150°C) → 60,000 min</b>	
2			
3			
4			
5			

NMP	Initial	→	After
1		<b>Temperature storage test (150°C) → 60,000 min</b>	
2			
3			
4			
5			

**Fig. F-5 SAT images of temperature holding test (V). (Upper images: NP DAAs and downside images: NMP DAAs)**

(I) NBT (0-300N, s-Ag (50μm thick), 64Ti (1mm thick))

NP	0 cycle	100 cycle	200 cycle	300 cycle	400 cycle	500 cycle	600 cycle	700 cycle	800 cycle	900 cycle	1000 cycle
1											
2		NA					NA				
3		NA					NA				
4		NA									
5		NA									

NMP	0 cycle	100 cycle	200 cycle	300 cycle	400 cycle	500 cycle	600 cycle	700 cycle	800 cycle	900 cycle	1000 cycle
1											
2											
3		NA									
4		NA									
5		NA									

Fig. F-6 SAT images of NBT (I) images. (Upper images: NP DAAs and downside images: NMP DAAs.)

(II) NBT (0-270N, s-Ag (50μm thick), 64Ti (1mm thick))

NP	0 cycle	100 cycle	200 cycle	300 cycle	400 cycle	500 cycle	600 cycle	700 cycle	800 cycle	900 cycle	1000 cycle
1											
2		NA									
3		NA									
4		NA									
5		NA									

NMP	0 cycle	100 cycle	200 cycle	300 cycle	400 cycle	500 cycle	600 cycle	700 cycle	800 cycle	900 cycle	1000 cycle
1											
2		NA									
3		NA									
4		NA									
5		NA									

Fig. F-7 SAT images of NBT (II) images. (Upper images: NP DAAs and downside images: NMP DAAs.)

(III) NBT (0-240N, s-Ag (50 $\mu$ m thick), 64Ti (1mm thick))

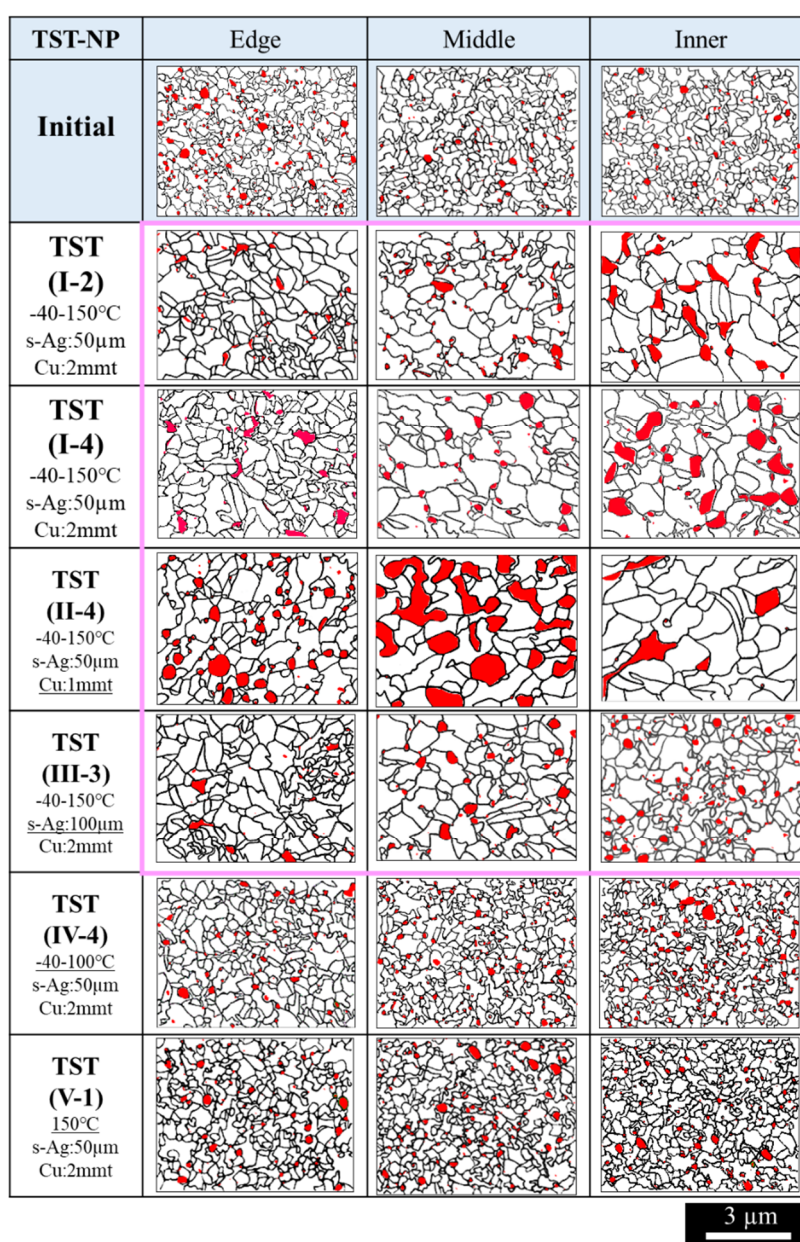
NP	0 cycle	100 cycle	200 cycle	300 cycle	400 cycle	500 cycle	600 cycle	700 cycle	800 cycle	900 cycle	1000 cycle
1											
2		NA					NA				
3		NA									
4		NA					NA				
5		NA									

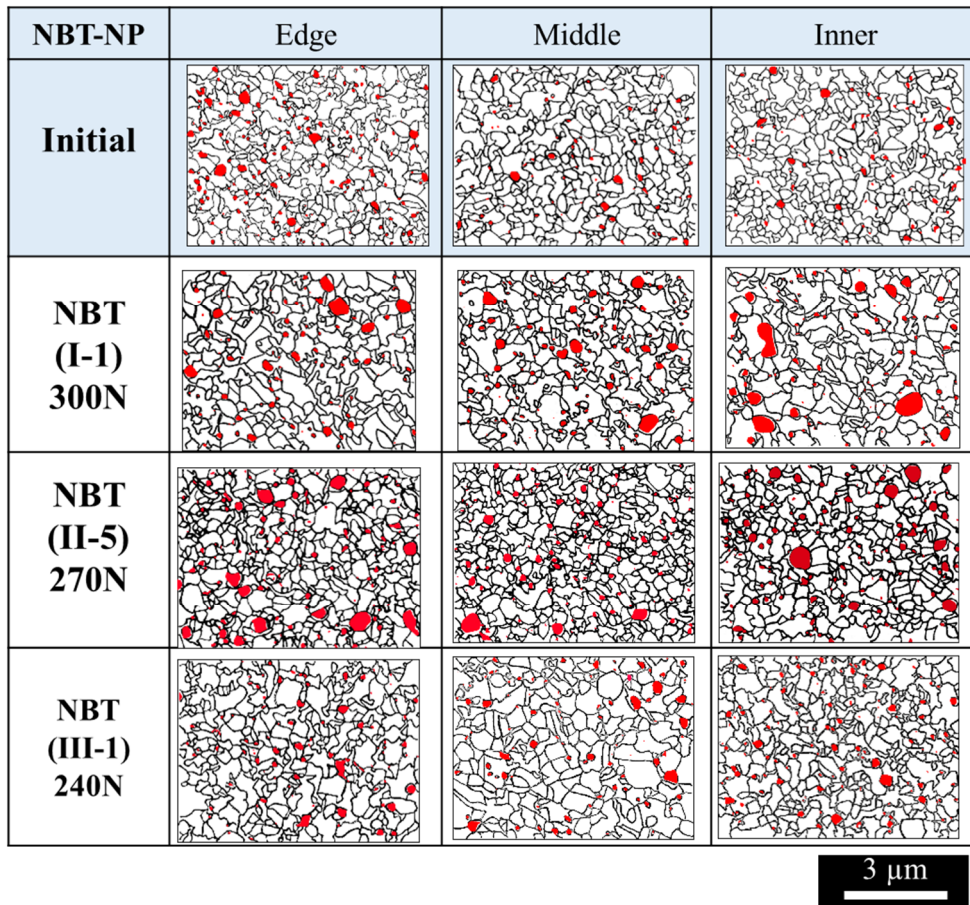
NMP	0 cycle	100 cycle	200 cycle	300 cycle	400 cycle	500 cycle	600 cycle	700 cycle	800 cycle	900 cycle	1000 cycle
1											
2		NA									
3		NA									
4		NA									
5		NA									

Fig. F-8 SAT images of NBT (III) images. (Upper images: NP DAAs and downside images: NMP DAAs.)

## G. Micro structure analysis results of all images after TST and NBT

Fig. G-1 depicts NP's representative SIM image analysis results with each portion with edge, middle, and inner after 1000 cycles in TST and NBT. The index number corresponds to the SAT images. The Greek number means TST condition, and Arabic numerals correspond with the sample number as depicted in Appendix F. Pink frame indicates pore and crystal growth. Significant pore and crystal growth could be observed in TST of (I) and (II) with  $-40$  to  $150^{\circ}\text{C}$ . Significant crystal growth could be observed in TST of (III) with  $-40$  to  $150^{\circ}\text{C}$ . Whereas NBT results showed no considerable pore or crystal growth.





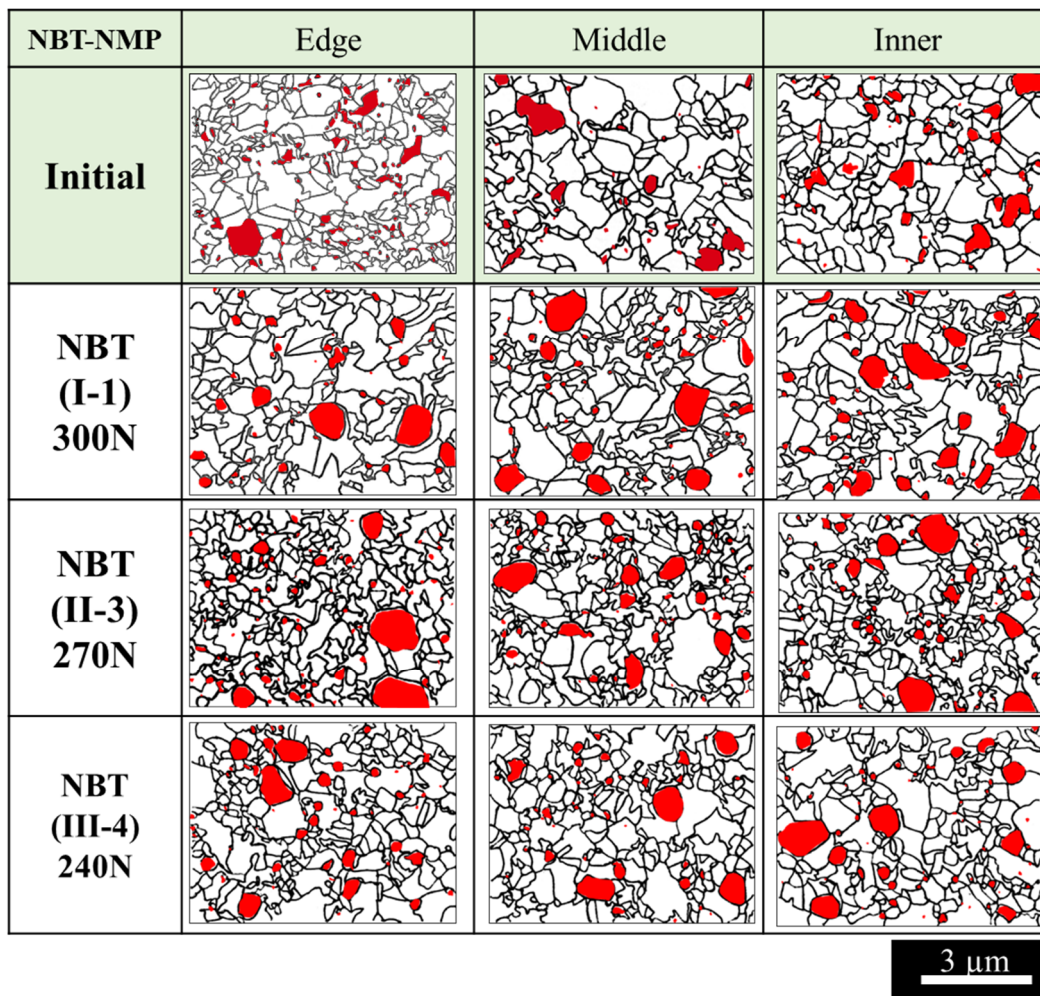
**Fig. G-1 SIM image analysis results after 1000 cycles of TSTs and NBTs with NP DAAs. (Red portion: Pore. Pink frame: Pore growth.)**

Fig. G-2 depicts NMP's representative SIM image analysis results with each portion with edge, middle, and inner after 1000 cycles in TST and NBT. Pink frame meaning and sample number definition are identical to those in NP results. Significant pore growth can be observed in TST of (I) and (II) with  $-40 \sim 150^{\circ}\text{C}$ .

TST-NMP	Edge	Middle	Inner
<b>Initial</b>			
<b>TST (I-2)</b> -40-150°C s-Ag:50μm Cu:2mmt			
<b>TST (II-2)</b> 40-150°C s-Ag:50μm Cu:1mmt			
<b>TST (III-3)</b> -40-150°C s-Ag:100μm Cu:2mmt			
<b>TST (IV-4)</b> -40-100°C s-Ag:50μm Cu:2mmt			
<b>TST (IV-5)</b> -40-100°C s-Ag:50μm Cu:2mmt			
<b>TST (V-1)</b> 150°C s-Ag:50μm Cu:2mmt			

3 μm

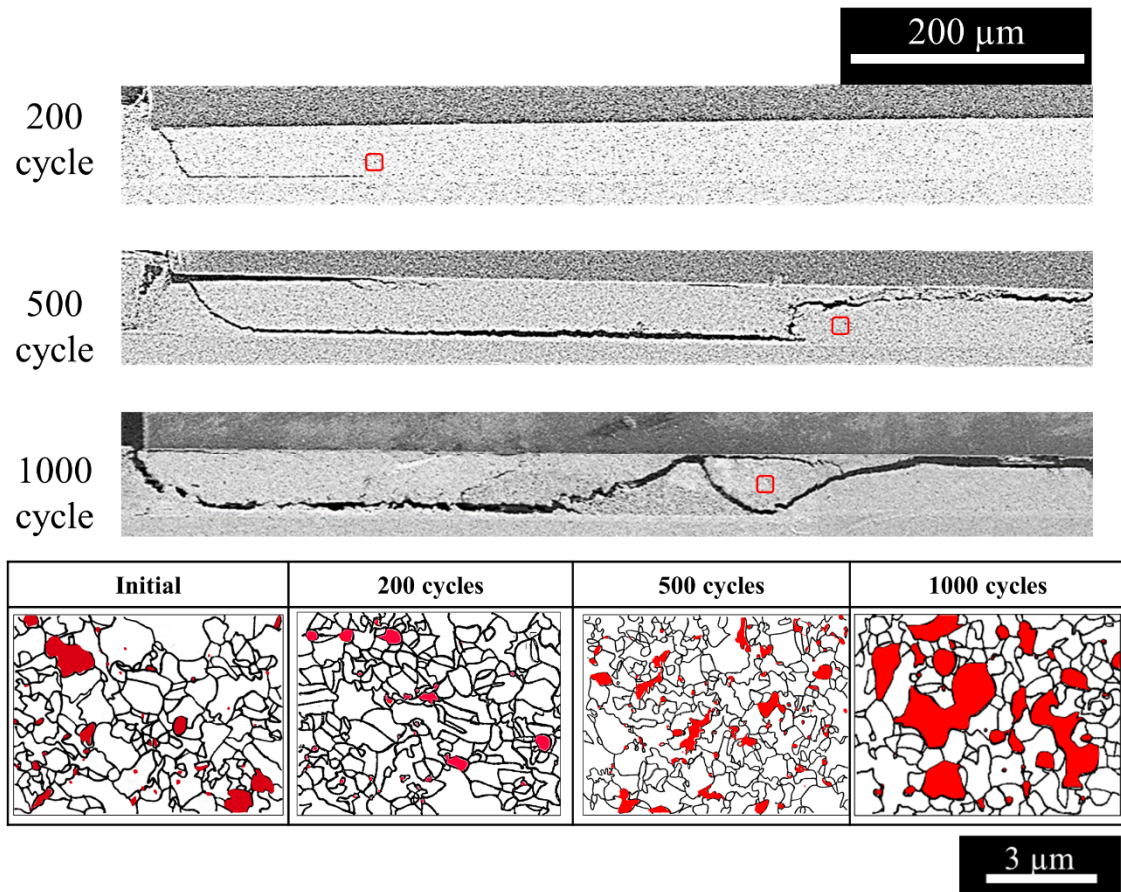




**Fig. G-2 SIM image analysis results after 1000 cycles of TSTs with NMP DAAs (Red portion: Pore. Pink frame: Pore growth.)**

## H. Fracture mode transition

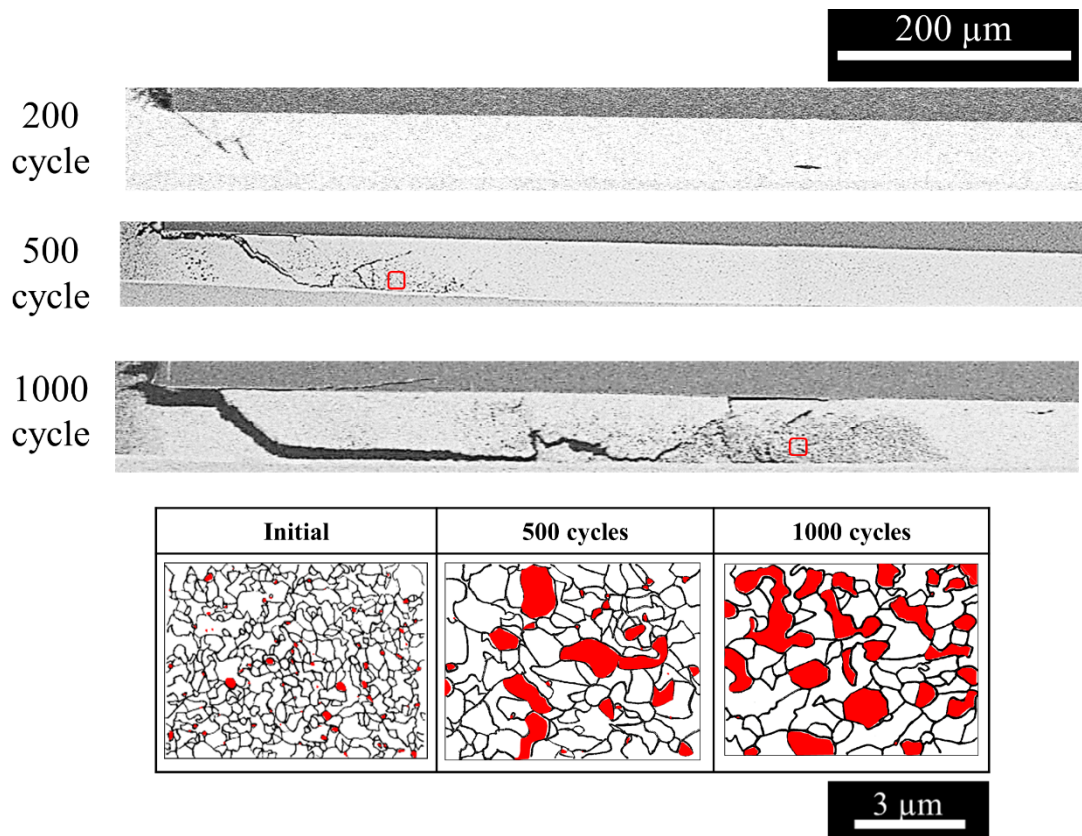
Fig. H-1 shows representative cross-section SEM images of TST (I) in NMP after 200, 500, and 1000 cycles. For 200 cycles, an inclined crack appeared at the left edge of the s-Ag layer, and then the crack was horizontally propagated along with the substrate. After 500 cycles, the crack is horizontally progressed with a straight, then, the crack direction is changed to an upwards direction in the middle. The local microstructure is not changed up to 500 cycles. After 1000 cycles, the straight crack changes to a wavy crack in the middle. In addition, a pore is significantly grown around the wavy crack region. It was confirmed that significant pore growth would happen after 1000 cycles, as is the same condition with the NPDAAs.



**Fig. H-1 Representative cross-section SEM image of TST (I) with NMP after 200, 500, and 1000 cycles. Microstructure image analysis results in red frame regions depicted in the SEM cross-section images (Red: Pore).**

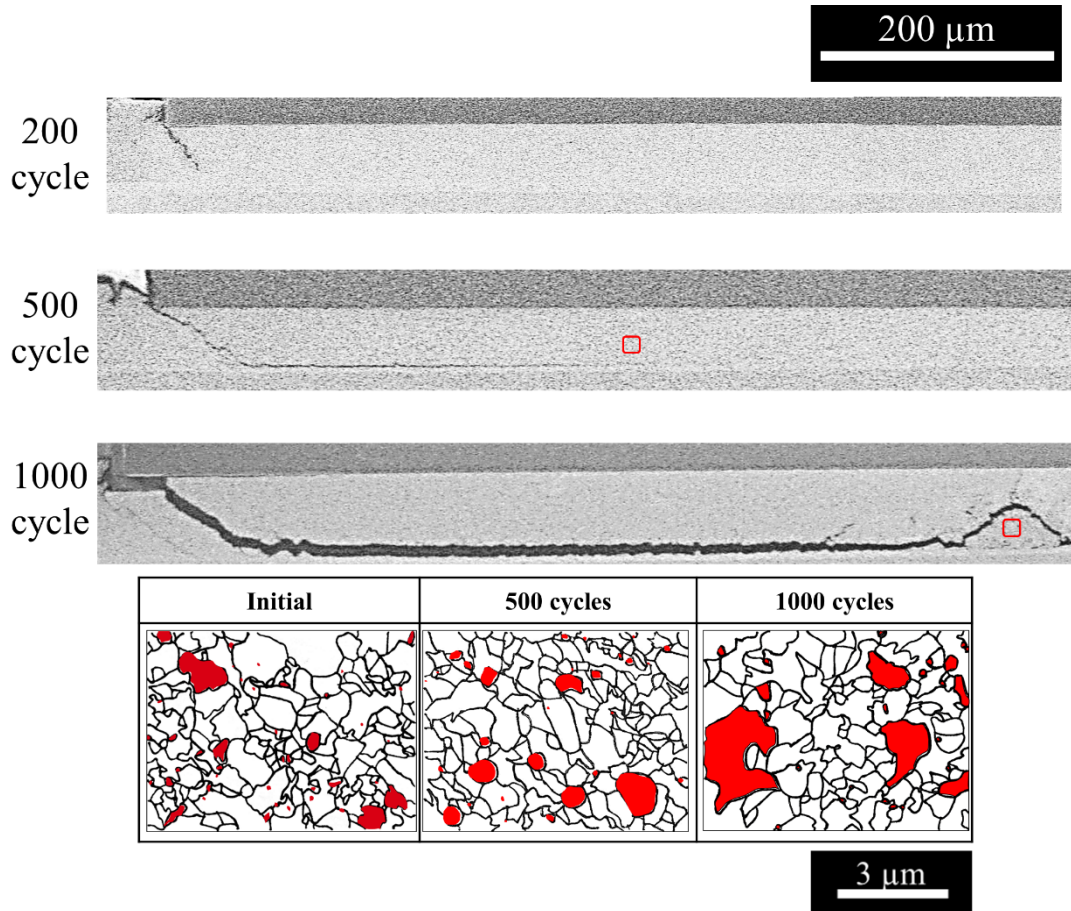
## I. Fracture mode transition after TST(II)

Fig. I- depicts representative cross-section observation results of TST (II) after 200, 500, and 1000 cycles in NP DAAs. An incline crack was generated at the corner of the chip part in 200 cycles, as was the same morphology as in TST (I), as shown in Fig. 4-6. However, a wavy crack was already seen in 500 cycles at the end of the incline crack portion. Then the wavy crack area enlarged at 1000 cycles. Significant pore growth has already been seen in 500 cycles. That would be associated with the straight crack speed difference between TST (I) and TST (II). The straight cracking speed in TST (II) is lower than the speed in TST (I). Then, the time for stress concentration at the front of the crack gets long. As a result, the pore growth would be readily given rise in the TST (II) case. From the viewpoint that delamination ratio in the TST (II) was smaller than the delamination ratio in the TST (I), as shown in Fig. 3-12, the mechanical crack mainly contributed to the overall delamination area.



**Fig. I-1 Representative cross-section SEM image of TST (II) with NP after 200, 500, and 1000 cycles. Microstructure image analysis results in red frame regions depicted in the SEM cross-section images (Red: Pore).**

Fig. I-2 shows microstructure analysis results of SIM images. The overall tendency of TST (II) in NP was similar with NP of TST (I) that crystal, pore size increases with increasing the number of cycles. NMP pore is grown up at 1000 cycles of inner portion. That is, 500 cycles of TST (I) and (II) in NP was the inflection point that the s-Ag locally aged or not. In NMP, aging was occurred after 1000 cycles at least in both TST (I) and (II).



**Fig. I-2 Representative cross-section SEM image of TST (II) with NMP after 200, 500, and 1000 cycles. Microstructure image analysis results in red frame regions depicted in the SEM cross-section images (Red: Pore).**

# Achievements

## List of Papers

1. K. Wakamoto, T. Otsuka, K. Nakahara, and T. Namazu, "Degradation Mechanism of Silver Sintering Die Attach Based on Thermal and Mechanical Reliability Testing," *IEEE Transactions on Components, Packaging and Manufacturing Technology*. vol. 13, no. 2, pp.197-210, Feb, 2023, doi: 10.1109/TCPMT.2023.3242423.
2. K. Wakamoto, T. Otsuka, K. Nakahara, and T. Namazu, "Nine Point Bending Test Technique for Understanding of Sintered Silver Die Bonding Failure Mechanism," *Experimental techniques*. (Under review)
3. K. Wakamoto, "Sintered Silver Die-attach Thermal Reliability Evaluation toward High Power Density Power Module Products," *Journal of JSEM*. vol. 22, no.2 pp. 91-95, June, 2022, doi: 10.11395/jjsem.22.91.
4. K. Wakamoto, Y. Kumakiri, T. Otsuka, K. Nakahara, and T. Namazu, "Comparison of sintered silver die attach failure between thermal shock test and mechanical cycling test," *Japanese Journal of Applied Physics*, vol. 61, pp. SD1029-1-7, 2022, doi: 10.35848/1347-4065/ac5b23.
5. K. Wakamoto, T. Otsuka, K. Nakahara, and T. Namazu, "Degradation Mechanism of Pressure-Assisted Sintered Silver by Thermal Shock Test," *Energies*, vol. 14, no. 17, pp. 5532-5546, 2021, doi: 10.3390/en14175532.
6. K. Wakamoto, Y. Mochizuki, T. Otsuka, K. Nakahara, and T. Namazu, "Temperature Dependence on Tensile Mechanical Properties of Sintered Silver Film," *Materials*, vol. 13, no. 18, pp. 4061-4071, Sep., 2020, doi: 10.3390/ma13184061.
7. K. Wakamoto, Y. Mochizuki, T. Otsuka, K. Nakahara, and T. Namazu, "Tensile mechanical properties of sintered porous silver films and their dependence on porosity," *Japanese Journal of Applied Physics*, vol. 58, no. SD, pp. SDDL08-1-5, 2019, doi: 10.7567/1347-4065/ab0491.

## **List of international conference presentation**

1. K. Wakamoto, T. Otsuka, K. Nakahara, and T. Namazu, “Sintered Silver Degradation Assessment by Thermal and Mechanical Cyclic Tests,” in *Proc. 6th International Conference on Materials and Reliability (ICMR)*, Yamaguchi, Japan, Dec., 2022. (Oral)
2. K. Wakamoto, T. Otsuka, K. Nakahara, and T. Namazu, “Nine Point Bending Test Technique for Evaluating the Sintered Silver Die Degradation,” in *Proc. 19th International Conference on Precision Engineering (ICPE)*, Nara, Japan, Nov., 2022. (Oral)
3. K. Wakamoto, T. Otsuka, K. Nakahara, and T. Namazu, “Degradation Mechanism Comparison of Sintered Silver Die in Thermal and Mechanical Cycling Tests,” in *Proc. 35th International Microprocesses and Nanotechnology Conference (MNC)*, Tokushima, Japan, Nov., 2022. (Oral)
4. K. Wakamoto, T. Otsuka, K. Nakahara, and T. Namazu, “Evaluating Sintered Silver Die-attach Thermal Cycling Degradation by Nine Point Cycling Bending Test,” in *Proc. 54th International Conferences on Solid State Devices and Materials (SSDM)*, Chiba, Japan, Sep., 2022. (Oral)
5. K. Wakamoto, T. Otsuka, K. Nakahara, and T. Namazu, “Comparison in Sintered Silver Die Attach Failure between Thermal Shocked Test and Four-point Bending Test,” in *Proc. 34th International Microprocesses and Nanotechnology Conference (MNC)*, online, Nov., 2021. (Online oral)
6. K. Wakamoto, T. Otsuka, K. Nakahara, and T. Namazu, “Pore Size and Shape Dependences on Quasi-Static Tensile Characteristics of Sintered Silver Films,” in *Proc. 33rd International Microprocesses and Nanotechnology Conference (MNC)*, online, Nov., 2020. (On-demand)
7. K. Wakamoto, Y. Mochizuki, T. Otsuka, K. Nakahara, and T. Namazu, “The Influence of Mechanical Property on the Heat-Cycle Reliability of Sintered Silver Die Attach,” in *Proc. 32nd International Symposium on Power Semiconductor Devices and ICs (ISPSD)*, Vienna, Austria, Sep., 2020. (Poster)
8. Maiko Hatano, Keisuke Wakamoto, Takukazu Otsuka, and Ken Nakahara, “Improved heat-cycle reliability induced by thick sintered-silver die attach,” in *Proc. 20th International Conference on*

*Electronics Packaging*, Tokyo, Japan, April, 2020. (Accepted and canceled due to Covid-19)

9. Keisuke Wakamoto, Yo Mochizuki, Takukazu Otsuka, Ken Nakahara, and Takahiro Namazu, “Mechanical Property of Nano Porous Sintered Silver: Toward Reliability Estimation,” in *Proc. 3rd International Conference on Materials Science and Engineering*, Frankfurt, Germany, Oct., 2019. (Oral)
10. Yo Mochizuki, Keisuke Wakamoto, Takukazu Otsuka, Ken Nakahara, and Takahiro Namazu, “Degradation Mechanism of Sintered Porous Silver Film at Elevated Temperatures,” in *Proc. 32nd International Microprocesses and Nanotechnology Conference*, Hiroshima, Japan, Oct., 2019. (Poster)
11. Keisuke Wakamoto, Yo Mochizuki, Takukazu Otsuka, Ken Nakahara, and Takahiro Namazu, “Influence of Porosity on Tensile Mechanical Properties of Sintered Porous Silver Films,” in *Proc. 31st International Microprocesses and Nanotechnology Conference*, Sapporo, Japan, Nov., 2018. (Poster)

### **List of domestic conference presentation**

1. K. Wakamoto, T. Otsuka, K. Nakahara, and T. Namazu, “Degradation Mechanism of Sintered Silver Die Attach by Thermal and Mechanical Cycling Testing,” The Japan Institute of Electronics Packaging 37th Annual General Meeting, Yokohama, Mar., 2023. (Oral)
2. K. Wakamoto, T. Otsuka, K. Nakahara, and T. Namazu, “Sintered Silver Die Degradation Evaluation by Nine Point Bending Test Technique,” *The Japan Society of Mechanical Engineers Annual General Meeting*, Toyama, Sep., 2022. (Oral)
3. K. Wakamoto, T. Otsuka, K. Nakahara, and T. Namazu, “Degradation Mechanism of Sintered Silver Bonding Layer by Thermal Cyclic Loading,” *The Japan Institute of Electronics Packaging 36th Annual General Meeting*, Online, Mar., 2022. (On-demand oral)
4. K. Wakamoto, T. Otsuka, K. Nakahara, and T. Namazu, “Understanding of correlation between sintered silver porous structure and its thermal-mechanical reliability,” The Japan Society of Mechanical Engineers, *The 12th Micro/Nano Engineering Symposium*, Online, Nov., 2021. (On-

- demand oral)
5. K. Wakamoto, T. Otsuka, K. Nakahara, and T. Namazu, "Micro pore structure dependence on pressured-type sintered silver tensile mechanical properties," *The Japan Society of Mechanical Engineers Annual General Meeting*, Online, Sep., 2021. (On-demand-oral)
  6. K. Wakamoto, Y. Kumakiri, S. Kammachi, T. Otsuka, K. Nakahara, and T. Namazu, "Temperature Dependency on Thermal Reliability Test Result by Sintered Silver Interconnection," *The Japan Society of Mechanical Engineers Annual General Meeting*, Online, Sep., 2020. (On-demand-oral)
  7. S. Kammachi, Y. Mochizuki, K. Wakamoto, T. Otsuka, K. Nakahara, and T. Namazu, "Quasi-Static Tensile and Fatigue Tests of Sintered Silver Film," *The Japan Society of Mechanical Engineers Annual General Meeting*, Online, Sep., 2020.
  8. Y. Kumakiri, K. Wakamoto, T. Otsuka, K. Nakahara, and T. Namazu, "Study on Degradation Mechanism of Sintered Ag Mechanical Joint," *The Japan Society of Mechanical Engineers Annual General Meeting*, Online, Sep., 2020.
  9. K. Wakamoto, Y. Mochizuki, T. Otsuka, K. Nakahara, and T. Namazu, "The Influence of Sintered Silver Mechanical Property on the Heat Cycle Reliability Life Time," *The Japan Institute of Electronics Packaging 34th Annual General Meeting*, Online, Mar., 2020. (Accepted and canceled due to Covid-19)
  10. M. Hatano, K. Wakamoto, T. Otsuka, and K. Nakahara, "Effect of Silver Sinter Bonding Film Thickness on Thermal Reliability," *The Japan Institute of Electronics Packaging 34th Annual General Meeting*, Online, Mar., 2020. (Accepted and canceled due to Covid-19)
  11. K. Wakamoto, Y. Mochizuki, T. Otsuka, K. Nakahara, and T. Namazu, "Tensile Mechanical Fatigue Properties of Sintered Porous Silver Films," *The Japan Society of Mechanical Engineers Annual General Meeting*, Akita, Sep., 2019. (oral)
  12. Y. Mochizuki, K. Wakamoto, T. Otsuka, K. Nakahara, and T. Namazu, "Porosity Dependence of Tensile Mechanical Properties of Sintered Nano silver Thin Films," *The Japan Society of Mechanical Engineers Tokai Branch Meeting*, Gifu, Mar., 2019.
  13. K. Wakamoto, Y. Mochizuki, T. Otsuka, K. Nakahara, and T. Namazu, "Tensile Mechanical



Properties of Sintered Porous Silver Films,” *The Japan Society of Mechanical Engineers Annual General Meeting*, Osaka, Sep., 2018. (Oral)

### **Book Publication List**

1. K. Wakamoto, R. Matsumoto, and T. Namazu, “SiC Power Module Design: Performance, Robustness and Reliability,” *The Institution of Engineering and Technology (IET) Book*, Chapter 10, Nov., 2021, doi: 10.1049/PBPO151E\_ch10.

### **Award List**

1. Research Encouragement Award of The Japan Institute of Electronics Packaging 36th Annual General Meeting.
2. Best Oral Presentation Award of 6th International Conference on Materials and Reliability.

## Acknowledgements

I would like to express my sincere gratitude toward the numerous people who have helped me along the course of this Ph.D. thesis.

As for my first sincere acknowledgment, I would like to appreciate my main supervisor, Professor, Takahiro Namazu. You motivated me to enroll in KUAS as a Ph.D. student to establish the s-Ag reliability from the viewpoint of mechanical engineering. After joining your laboratory, I could learn so many mechanical engineering techniques through so many cutting-edge testers. This experience was invaluable and irreplaceable. You always inspired me to move forward during my doctor thesis to progress in the right way by providing me with so many challenging opportunities. What I learned from you the most is the importance of breaking past my own limitations through ongoing and regular effort. I would like to keep up strong spirits learned from your laboratory in the future to grow up myself more. Lastly, I will always be grateful for the many instructions you provided me with about the fundamental research skills of writing of technical papers, presentations, and organizing the way of project with professionals. All these skills are essential for being a self-standing researcher. Keeping this in mind, I would like to be a genuine researcher in the future.

I would like to appreciate my co-supervisor, Dean, Professor, Osamu Tabata. I was always given so much encouragement and advice from you. You always pointed me toward the right direction in my thesis work with simple but powerful phrases that underlie so many hints and truths. Even though I could not fully catch up to the truth behind all of your advice, I have recalled those words time and time again as I was confronted with difficulties. Then, the knowledge of their true meaning enabled me to overcome numerous difficulties. The words of encouragement I received from you have been a great motivation to pursue my research goal. Thank you so much.

I would like to also appreciate my co-supervisor, Professor, Alberto Castellazzi. Thank you so much for having such a great interest in my doctor thesis. Your valuable insights into my doctoral presentation has always encouraged me. Your overarching views on power electronics research has provided priceless research value toward my own work.

I would like to appreciate Professor, Kazuo Oki as my co-supervisor. I was really impressed by the question you posed to me during my 2nd doctoral presentation: "If you satisfy your research goal, what will the world become?" The question continues to remind me that research should always be motivated by the bigger picture. I felt encouraged by you at that moment. Thank you so much again.

I would like to give a special appreciation to Professor, Juergen Wilde of Freiburg University, IMTEK. Firstly, I really appreciate you for agreeing to my requests for discussions even when you did not know me at the time. You are my research role-model who established the s-Ag die reliability estimations from the view point of mechanical reliability. Therefore, I was honored beyond words when you agreed to have discussions with me. Every discussion with you helped inspire me even further. Having a fruitful discussion with you was one of my biggest motivators in my doctor thesis, which simultaneously helped bring my research quality up to worldwide standards. Thank you so much again.

I would like to appreciate Associate Professor, Ryosuke Matsumoto as my supervisor lecturer. Without your advice on the material microstructure physics, I could not have imaged the pore growth physics in the s-Ag. Especially, your assistance with MD simulation was one of the pivotal data for my doctor thesis. Visualizing atomic motion in the structure helps attract more attention toward my thesis.

I would also appreciate Professor, Shugo Miyake of Kobe City College of Technology. I was able to obtain the s-Ag utilization as a functional die attachment technology because of your expert knowledge on thermophysical properties. Thank you so much for discussing with me about the microstructure and thermophysical relations.

I would like to appreciate the people of the Rohm company. This doctor thesis project would not have been possible without the cooperation of Rohm company.

I would like to extend my first special appreciation toward Ph.D. Ken Nakahara, general manager, Research and Development Center. Thank you so much for setting up an attractive research theme for the company. It is not too much to say that your presence motivated me to pursue a Ph. D. Without your profound understanding of my research, I could not have done my research both in the company and in the college institute. You always said that simplifying the phenomena is the best approach that guarantees an answer, and you always told me that achieving the ideal situation of reliability design flow for outsmarting competitive companies equals taking a lead in the world. These pivotal words of advice have always given me opportunities to think about the right way to do my research. I have cherished many precious memories with you during this doctor thesis, if I had to pick one, it would be the advice you gave me after the company conference on “New Technologies and New Products” Q &A section from the advisory board person, where you said to me “Do not accept questioner’s comments, you should insist on what needs to be said, regardless of whether the opponent is great or not.” I deeply regretted that I could not have strongly answered the questioner’s comments about making my presentation lower quality than

usual. However, according to your advice, that moment turned out to be a turning point in my life when it came to the quality of my presentations. Your advice has helped me grow and mature as a researcher. Thank you so much.

I would like to appreciate my group manager Mr. Takukazu Otsuka, Research and Development Center. You provided me with so much technical advice about s-Ag die bonding with your vast experience. Above all, the 64Ti bonding optimization would not have been achieved without your timely advice. Also, thank you so much for being my daily motivator. No matter how busy you were, you always consulted with me, from research topics to private consultations. I was able to enjoy every moment of my work because I had the privilege of belonging to your research group. Thank you very much.

I would like to appreciate Mr. Kazunori Fuji as my senior researcher, Research and Development Center. In NBT jigs, many ideas were delivered to me from Fuji-san. Without your support, I could not make an excellent NBT system. I have learned a lot from your deep knowledge about production technique. Thank you so much.

I would like to appreciate Ph.D. Maiko Hatano as a chief researcher, Research and Development Center. The NMP material you introduced to me was the basement s-Ag material matched with my doctor thesis. Also, the technical discussion I had with you about improving die reliabilities were invaluable. Chapter 3 results can be taken on your previous research basement results. After you moved to the other research group, we had lesser time to discuss everything. But I hope we can talk again in the near future. Again, thank you so much for advising and supporting me.

I would like to appreciate my senior Mr. Tatsuya Miyazaki, chief researcher, Research and Development Center. You always cared about my thesis topics, and cheered me up on so many occasions. The discussion about the material failure of physics stimulated my imagination and helped me in acquiring the knowledge considering about my thesis topic. Thank you so much again.

I would like to give many thanks to my colleagues. Ph.D. Kento Kariya, researcher, Research and Development Center, thank you so much for taking a discussion with me about your way of thinking about DP with regards to die-failure physics. I was really motivated by your vast knowledge about calculation science. Thank you so much for discussing with me.

Ph.D. Masaya Ukita, researcher, Research and Development Center. Thank you so much for your assistance on NBTs. Also, I am honored to have been your mentor representative when you were a newcomer. I hope that I have inspired you in one way or the other.

Mr. Natsuya Yoshida, researcher, Research and Development Center, thank you so much for helping me in establishing a detachment methodology of s-Ag film to make a tensile test specimen. While seeking the appropriate conditions for self-standing films, I remembered so many experiments conducted with you about changing substrate material and configuration. And you were my first mentee in the company. I hope I have assisted you in some way in your career.

Mr. Yo Mochizuki, Research and Development Center, you did so many experiments on the tensile mechanical property of s-Ag film when you were the master course student in the Aichi Institute of Technology. You were always sincere toward me, and for that I am extremely honored. I clearly recall the moment you presented the mechanical property of s-Ag and bulk silver differences using Hall-Petch equations to me. I was surprised that s-Ag exhibited a brittle characteristic at RT, despite having a low porosity rate. As I look back on my research, those moments were the origin of this study. Chapter 2 data covers your contributions toward this study. Thank you so much again.

Also, I would like to thank Mr. Masahiro Takakusa, Ms. Haruko Ooe, and Ms. Natsumi Hayashi for assisting me in obtaining SAT data after TST. Many of the SAT images in Chapter 3 owes itself to your daily support and assistance. Also, thank you so much for making the interconnection samples.

I would like to extend a special thanks to my doctor course student colleague, Mr. VIGENDRAN Mugilgeethan. You assisted me on MD calculation with a strong passion. Chapter 4's MD calculation results helped me a lot when it came to understanding pore motion mechanism. Without MD calculation results, I could not finalize my consideration against s-Ag microstructure aging physics. Thank on your tireless effort.

My PhD student colleagues, Mr. Lee Yonghwa, Mr. Ali Walid Bin, and Mr. Kwak Jaedon, thank you so much for encouraging and each other. The dinner with all my PhD students was so memorable. I wish I could have dinner with all again in some time to share individual's status of career.

I would like to appreciate my lab mates. Mr. Yuga Kumakiri of Namazu laboratory, OB student. You always supported me with experimental techniques. When I entered KUAS, you guided me on so many technical skills of Namazu laboratory's tester. You also gave me so many experimental ideas with your flexible brain. It was always fun and helpful to me. I feel nostalgic about our many discussions on the appropriate way to set up the bending test. Thank you so much.

Mr. Shingo Kammachi, Mr. Kento Kodama, Mr. Hiromichi Ando, and Mr. Tomohito Kino of Namazu laboratory, OB students. I will never forget the laboratory time that we spent. Let us hang out again in the

near future.

Mr. Daisuke Yasugi, master course student of Namazu laboratory colleague, you were practically the only person in charge of all experiments on the Namazu laboratory. Also, you helped me with using the tester or troubleshooting no matter how busy you were. Thank you so much for your patience. Your thesis theme is partly related to my work, which helps me partially understand some of the difficulties you face. But you never gave up on your experiments for extracting something from difficult situations. I believe your thesis theme will play a pivotal role in the die reliability field. I always hope for your future success. Also, every discussion I had with you was so much fun for me. Thank you.

Ms. Michiko Shindo, Namazu laboratory researcher, I would like to extend my appreciation towards you for your diligent care toward laboratory environments. Also, you always cheer me up and understand my situation. I will never forget the kindness you showed me. Thank you so much.

Mr. Hiroya Saegusa and Mr. SINGH Abhiraj (Abbi-kun), undergraduate school students with my lab colleagues, all of you guys always warmly welcomed me. I did not have the pleasure of directly working with you, however, I really felt comfortable going out for lunch or dinner with all of you. Should you face some difficulty in the near future, please feel free to contact me.

Finally, I would like to thank my family. To my wife, Tsubasa, I am so sorry for not spending enough time with you even though it is a holiday in the doctor thesis period. Moreover, the emotional weight of being apart was unbearable at times, which puts us in a bad mood. However, you always kept supporting me. Without your support, I could not have written this thesis paper. I am looking forward to spending time with you after the end of the doctor thesis period.

As for my wife's mother and father, thank you so much for your patience and understanding regarding my situation. You always cared for me as if I were your real son. You made me feel welcome and comfortable with you. I would like to maintain a good relationship with the both of you. Thank you so much.

Dr. Atsushi Fukao, whom I consider to be my second father, you cared about me so much, not only as family but also as one of the researchers. Your curiosity, encouragement, and positive words were always a primary motivation for my progress. Thank you so much.

My mother, you are always my biggest supporter. When I doubted myself, you always cheered me up, and guided me about the numerous positive outcomes for the future. Thank you so much for always believing in me. You may not understand my doctor thesis in detail, but please feel honored for this

achievement of mine. Take care of yourself and be relieved for me.

As for my father, you graciously invited me to go out to dinner with my wife Tsubasa. I always felt comfortable to talk to you about my work, career, and other aspects of my life. I wish I could continue to show you my growth.

I would like to stress that this dissertation paper rests on the undying support and assistance of many people, some of whom I have yet to express my gratitude towards. I am beyond grateful to all of you.

Lastly, I would like to say again, "Thank you so much everyone!"

Keisuke Wakamoto

March 2023